INTERNATIONAL JOURNAL

of

COMPUTERS COMMUNICATIONS & CONTROL

ISSN 1841-9836

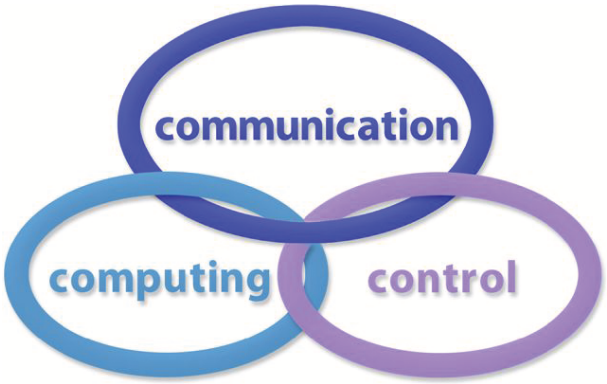

A Bimonthly Journal
With Emphasis on the Integration of Three Technologies

Year: 2015 Volume: 10 Issue: 1 (February)

This journal is a member of, and subscribes to the principles of, the Committee on Publication Ethics (COPE).

CCC Publications - Agora University Editing House

CCC Publications

http://univagora.ro/jour/index.php/ijccc/

BRIEF DESCRIPTION OF JOURNAL

Publication Name: International Journal of Computers Communications & Control.
Acronym: IJCCC; **Starting year of IJCCC:** 2006.
Abbreviated Journal Title in JCR: INT J COMPUT COMMUN.
International Standard Serial Number: ISSN 1841-9836.
Publisher: CCC Publications - Agora University of Oradea.
Publication frequency: Bimonthly: Issue 1 (February); Issue 2 (April); Issue 3 (June); Issue 4 (August); Issue 5 (October); Issue 6 (December).
Founders of IJCCC: Ioan DZITAC, Florin Gheorghe FILIP and Mişu-Jan MANOLESCU.
Logo:

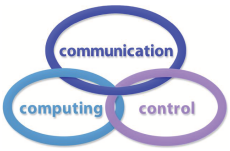

Indexing/Coverage:

- Since 2006, Vol. 1 (S), IJCCC is covered by Thomson Reuters and is indexed in ISI Web of Science/Knowledge: Science Citation Index Expanded.
- Journal Citation Reports (JCR - Science Edition), IF = 0.694 (JCR2013).
  Subject Category:
  - Automation & Control Systems: Q4 (46 of 59);
  - Computer Science, Information Systems: Q3 (96 of 135).
- Since 2008, 3(1), IJCCC is covered in Scopus, SJR2013 = 0.231, H index = 13.
  Subject Category:
  - Computational Theory and Mathematics: Q4;
  - Computer Networks and Communications: Q3;
  - Computer Science Applications: Q3.
- Since 2007, 2(1), IJCCC is covered in EBSCO.

Focus & Scope: International Journal of Computers Communications & Control is directed to the international communities of scientific researchers in computer and control from the universities, research units and industry.

To differentiate from other similar journals, the editorial policy of IJCCC encourages the submission of original scientific papers that focus on the integration of the 3 "C" (Computing, Communication, Control).

In particular the following topics are expected to be addressed by authors:

- Integrated solutions in computer-based control and communications;
- Computational intelligence methods (with particular emphasis on fuzzy logic-based methods, ANN, evolutionary computing, collective/swarm intelligence);
- Advanced decision support systems (with particular emphasis on the usage of combined solvers and/or web technologies).

Editorial Address:
Agora University/ R&D Agora Ltd. / S.C. Cercetare Dezvoltare Agora S.R.L.
Piata Tineretului 8, Oradea, jud. Bihor, Romania, Zip Code 410526
Tel./ Fax: +40 359101032
E-mail: ijccc@univagora.ro, rd.agora@univagora.ro, ccc.journal@gmail.com
Journal website: http://univagora.ro/jour/index.php/ijccc/

Gheorghe Păun
Institute of Math. of Romanian Academy
Bucharest, PO Box 1-764, Romania
gpaun@us.es

Mario de J. Pérez Jiménez
Dept. of CS and Artificial Intelligence
University of Seville, Sevilla,
Avda. Reina Mercedes s/n, 41012, Spain
marper@us.es

Dana Petcu
Computer Science Department
Western University of Timisoara
V.Parvan 4, 300223 Timisoara, Romania
petcu@info.uvt.ro

Radu Popescu-Zeletin
Fraunhofer Institute for Open
Communication Systems
Technical University Berlin, Germany
rpz@cs.tu-berlin.de

Imre J. Rudas
Óbuda University
Budapest, Hungary
rudas@bmf.hu

Yong Shi
School of Management
Chinese Academy of Sciences
Beijing 100190, China &
University of Nebraska at Omaha
Omaha, NE 68182, U.S.A.
yshi@gucas.ac.cn, yshi@unomaha.edu

Athanasios D. Styliadis
University of Kavala
Institute of Technology
65404 Kavala, Greece
styliadis@teikav.edu.gr

Gheorghe Tecuci
Learning Agents Center
George Mason University
U.S.A.
University Drive 4440, Fairfax VA
tecuci@gmu.edu

Horia-Nicolai Teodorescu
Faculty of Electronics and
Telecommunications
Technical University "Gh. Asachi" Iasi
Iasi, Bd. Carol I 11, 700506, Romania
hteodor@etc.tuiasi.ro

Dan Tufiş
Research Institute for Artificial Intelligence
of the Romanian Academy
Bucharest, "13 Septembrie" 13, 050711,
Romania
tufis@racai.ro

Lotfi A. Zadeh
Director,
Berkeley Initiative in Soft Computing (BISC)
Computer Science Division
University of California Berkeley,
Berkeley, CA 94720-1776
U.S.A.
zadeh@eecs.berkeley.edu

DATA FOR SUBSCRIBERS
Supplier: Cercetare Dezvoltare Agora Srl (Research & Development Agora Ltd.)
Fiscal code: 24747462
Headquarter: Oradea, Piata Tineretului Nr.8, Bihor, Romania, Zip code 410526
Bank: BANCA COMERCIALA FEROVIARA S.A. ORADEA
Bank address: P-ta Unirii Nr. 8, Oradea, Bihor, România
IBAN Account for EURO: RO50BFER248000014038EU01
SWIFT CODE (eq.BIC): BFER

INTERNATIONAL JOURNAL OF COMPUTERS COMMUNICATIONS & CONTROL
ISSN 1841-9836, Volume 10, Issue 1, February, 2015.

Contents

INTERNATIONAL JOURNAL OF COMPUTERS COMMUNICATIONS & CONTROL
ISSN 1841-9836, 10(1):8-21, February, 2015.

Method for Visual Detection of Similarities in Medical Streaming Data

J. Bernatavičienė, G. Dzemyda, G. Bazilevičius,
V. Medvedev, V. Marcinkevičius, P. Treigys

Jolita Bernatavičienė*, Gintautas Dzemyda,
Gediminas Bazilevičius, Viktor Medvedev,
Virginijus Marcinkevičius, and Povilas Treigys
Vilnius University
Institute of Mathematics and Informatics
Lithuania, LT-08663 Vilnius, Akademijos, 4
Jolita.Bernataviciene@mii.vu.lt, Gintautas.Dzemyda@mii.vu.lt,
Gediminas.Bazilevicius@mii.vu.lt, Viktor.Medvedev@mii.vu.lt,
Virginijus.Marcinkevicius@mii.vu.lt, Povilas.Treigys@mii.vu.lt
*Corresponding author: Jolita.Bernataviciene@mii.vu.lt

Abstract: The analysis of medical streaming data is quite difficult when the problem is to estimate health-state situations in real time streaming data in accordance with the previously detected and estimated streaming data of various patients. This paper deals with the multivariate time series analysis seeking to compare the current situation (sample) with that in chronologically collected historical data and to find the subsequences of the multivariate time series most similar to the sample. A visual method for finding the best subsequences matching to the sample is proposed. Using this method, an investigator can consider the results of comparison of the sample and some subsequence of the series from the standpoint of several measures that may be supplementary to one another or may be contradictory among themselves. The advantage of the visual analysis of the data, presented on the plane, is that we can see not only the subsequence best matching to the sample (such a subsequence can be found in an automatic way), but also we can see the distribution of subsequences that are similar to the sample in accordance with different similarity measures. It allows us to evaluate differences among the subsequences and among the measures.
Keywords: Streaming data, similarity measures, multivariate time series, visualization, multidimensional scaling.

1 Introduction

Time series data are widely available in different fields including medicine, finance, and science. A time series is a collection of chronologically performed observations of the values of a feature that characterizes the behaviour of a particular object. There are many topics in time series data mining, i.e., similarity search, clustering, classification, anomaly detection, motif discovery, etc. The similarity problem can be defined as a comparison of two time series to determine whether they are similar or not. Usually, the choice of a similarity measure can affect the result of data mining tasks. By a similarity measure we mean a method, which compares two time series and returns the value of their similarity. If the object is characterized by several features, we have a multivariate time series (MTS) [1].

In this paper, we investigate the similarity search in multivariate physiological time series. A physiological time series is a series of some medical observations over a period of time. Such a type of data can be collected using devices (or sensors) that collect personal medical features, such as heart rate, blood pressure, etc. An example of such data can be the intensive care multivariate online-monitoring time series [2]. A sensor is an instrument that detects or measures a physical or environmental characteristic or state, transmits and/or records the reading in some form (e.g.,

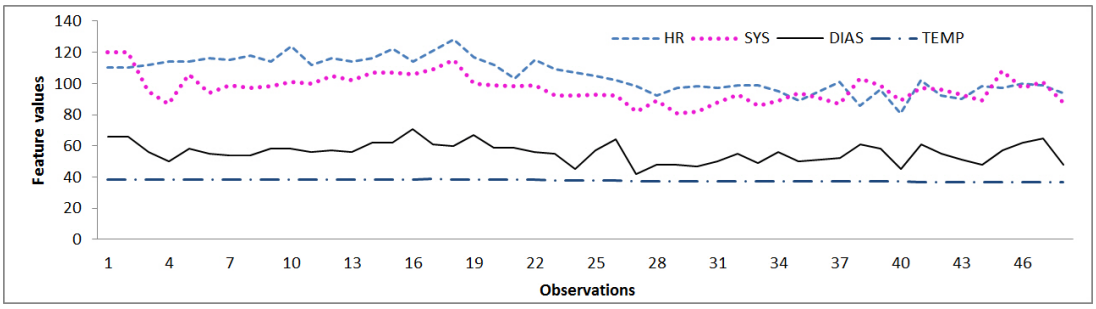

Figure 1: Example of the multivariate time series

a visual display, audio signal, digital transmission, etc.). A sensor converts the physical quantity to electric output. For example, a pressure sensor converts pressure to electric output. Remote monitoring of health parameters such as the pulse rate, oxygen level in blood or blood pressure can be very helpful for early detection of diseases, resulting in reduction of treatment time.

Most methods, used to analyse medical data, focus primarily on analysing the univariate time series. However, because of parameter dependences and variation over time, examination of all medical data together in a multivariate time series can provide more information about the data and patient, to make a better diagnosis and treat the patient [3].

Therefore, this paper deals with the multivariate time series analysis with a view to compare the current situation with that of in chronologically collected historical data, and to find subsequences of the multivariate time series most similar to the sample, corresponding, e.g. to the current situation. An example of MTS of four features (heart rate HR, non-invasive systolic arterial blood pressure SYS, non-invasive diastolic arterial blood pressure DIAS, temperature TEMP) is presented in Figure 1.

Let us have a multivariate time series of n features and T_a observations:

$$X^a = \begin{pmatrix} x^a_{11} & \cdots & x^a_{1T_a} \\ \vdots & \ddots & \vdots \\ x^a_{n1} & \cdots & x^a_{nT_a} \end{pmatrix}.$$

Denote the sample of n features and T_b observations as

$$X^b = \begin{pmatrix} x^b_{11} & \cdots & x^b_{1T_b} \\ \vdots & \ddots & \vdots \\ x^b_{n1} & \cdots & x^b_{nT_b} \end{pmatrix}.$$

Here $T_a > T_b$. In fact, X^a and X^b are matrices.

As a result, we need to find the optimal place of X^b on X^a. The place is defined by some time moment $T_* : 1 \leq T_* \leq T_a - T_b + 1$. Our procedure analyses the multivariate time series X^a by using the moving time window the width of which is adapted to the current situation X^b (width is equal to T_b) and comparing the content of this window with the sample, in the sense of several similarity measures, at the same time.

Visual method of finding the best subsequences matching to the sample is proposed in this paper. As it is indicated in [4], the goal of visual analytics research is to turn the information overload into an opportunity, i.e. decision-makers should be enabled to examine massive, multidimensional, multisource, time varying information stream to make effective decisions in time critical situations.

There are attempts to apply visual analysis for the streaming data. The example is the Visual Content Analysis of Real-Time Data Streams project [5] at the Pacific Northwest National Laboratory. Its goal was to allow users to quickly grasp dynamic data in forms that are intuitive and natural without requiring intensive training in the use of specific visualization or analysis tools and methods. The project has prototyped five different visualization prototypes that represent and convey dynamic data through human-recognizable contexts and paradigms such as hierarchies, relationships, time and geography.

In this paper, we suggest using the specific visualization tools and methods (multidimensional data visualization [6]) that are effective and also do not require intensive training of the users. Moreover, we show a possibility of making the decision, based on five criteria of similarity of the sample with the subsequence of real-time data stream by representing the similarity as a point on a plane. Dimensionality reduction and visual analysis of multidimensional data [6] have been applied when comparing the best found subsequences in X^a.

The proposed method is described in Section 2. Similarity measures for multivariate time series and comparative analysis of the measures are presented in Section 3. Multidimensional data visualization is reviewed in Section 4, where the emphasis is put on the multidimensional scaling. Comparative analysis of similarity measures for multivariate time series is presented in Section 5. An example, illustrating the proposed method, is presented in Section 6.

2 Visual Method for Finding the Best Subsequences Matching to the Sample

In our method, the multivariate time series X^a are analysed by using the moving time window. The width of this window is adapted to the current situation (sample) X^b and is equal to T_b. The content of this window is compared with the sample, in the sense of several similarity measures at the same time. It includes the dimensionality reduction procedure that allows us to observe multidimensional data visually.

The visual method for finding the best subsequences, matching to the sample, can be generalized as follows:

1. Let us have: - a multivariate time series X^a of n features and T_a observations; - sample X^b of n features and T_b observations; - m similarity measures $S_i, i = 1, \ldots, m$.

2. The sample X^b is compared with all subsequences of X^a by using m similarity measures $S_i, i = 1, \ldots, m$. The subsequences are obtained by moving the time window in the X^a from beginning to end. The content of such a window is a matrix of n rows. Denote it by X^c. The width of the window (the number of columns of X^c) is adapted to the current situation (sample) X^b (its width is equal to T_b). For each measure, k subsequences are chosen most similar to the sample. Therefore, the total number of subsequences for a further analysis is equal to km.

3. Each comparison of the sample with a subsequence, chosen in the way defined in the step above, produces a m-dimensional point $\overline{S}_q = (S_{q1}, S_{q2}, \ldots, S_{qm})$, where, in our case, $q = 1, \ldots, km$. Let us derive two additional points: - $\overline{S}_0 = (S_{01}, S_{02}, \ldots, S_{0m})$ is the array of values of all similarity measures, computed for the subsequence, that is ideally coincident with the sample (the array of the best values of m similarity measures); - $\overline{S}_C = (S_{C1}, S_{C2}, \ldots, S_{Cm})$ is the weight center of $\overline{S}_q = (S_{q1}, S_{q2}, \ldots, S_{qm}), q = 1, \ldots, km$. Therefore, the total number of m-dimensional points for discovering the most similar subsequences to the sample is equal to $km+2$. Afterwards, the normalization of the components

of these points is performed by z-score. Denote the obtained matrix of normalized points by Z. It consists of $km + 2$ rows and m columns.

4. The points from matrix Z are mapped on the plane using the Multidimensional Scaling [6] (or are other algorithm of nonlinear projection of multidimensional points on the plane). Denote the resulting matrix by Y, that contains $km + 2$ rows, corresponding to different comparisons of the sample with other subsequences, and 2 columns. Each row is coordinates of the point on the plane.

5. The investigator analyses the information presented graphically, where all m-dimensional points are represented as the points on a plane, and makes decisions. In general, the most similar subsequence to the sample can be the subsequence, the corresponding point of which on a plane is closest to the projection of $\overline{S}_0$ on the plane. However, more subsequences may be considered as similar to the sample. The points on the plane, corresponding to such subsequences, must be closer to the projection of $\overline{S}_0$ on a plane than to the projection of $\overline{S}_C$. These rules can be checked automatically in the program realization of this method, however participation of the investigator is valuable, because it gives a possibility to him to cognize the data deeper.

The advantage of this method is that the investigator can consider the results of comparison from the standpoint of several measures that may be supplementary to one another or contradictory among themselves. Therefore, the similarity of subsequences with the sample will be evaluated from different standpoints. The method is universal, because different sets of similarity measures can be chosen, depending on the problem, but the scheme of decision remains the same. Moreover, the involvement of the dimensionality reduction and visual analysis of multidimensional data in the proposed method renders the opportunity to the investigator to participate in the final decision, when comparing the best found subsequences of the multivariate time series with the sample. However, the decision on their similarity can also be made automatically.

3 Similarity Measures for Multivariate Time Series

To detect events in real multivariate time series, it is necessary to compare time series using the appropriate similarity measure [7]. Different techniques and similarity measures are introduced and used for comparison of multivariate time series of different nature [8], [9]. Multivariate time series can be reduced to univariate time series and their similarity can be measured, using a univariate time series approach [10]. That may lead to a great loss of information, therefore, we concentrate on the multivariate time series approach here. Five similarity measures $S_i, i = 1, \ldots, 5$, used in this paper for multivariate time series, are presented below.

Let us compare two multivariate time series:

$$X^a = \begin{pmatrix} x^a_{11} & \cdots & x^a_{1T_a} \\ \vdots & \ddots & \vdots \\ x^a_{n1} & \cdots & x^a_{nT_a} \end{pmatrix} \text{ and } X^b = \begin{pmatrix} x^b_{11} & \cdots & x^b_{1T_b} \\ \vdots & \ddots & \vdots \\ x^b_{n1} & \cdots & x^b_{nT_b} \end{pmatrix}.$$

The Frobenius norm is often used in the matrix analysis [11]. This similarity measure is based on the Euclidean distance. The Frobenius norm of a matrix X^b is defined by the formula:

$$\left\|X^b\right\|_F = \sqrt{\sum_{p=1}^{n}\sum_{q=1}^{T_b}(x^b_{pq})^2} = \sqrt{tr((X^b)'X^b)}, \tag{1}$$

where tr is the sum of elements on the diagonal of the square matrix. The Frobenius norm is used to compare the similarity of two matrices. The similarity of X^b and X^c is defined by the formula $Frob = \left\|X^b - X^c\right\|_F$. The best possible value of the Frobenius norm is 0.

The correlation coefficient between two matrices of the same size (*Matrix Correlation Coefficient*) can also be used as a similarity measure [12]:

$$r = \frac{\sum_{p=1}^{n}\sum_{q=1}^{T_b}(x_{pq}^b - \bar{X}^b)(x_{pq}^c - \bar{X}^c)}{\sqrt{\sum_{p=1}^{n}\sum_{q=1}^{T_b}(x_{pq}^b - \bar{X}^b)^2 \sum_{p=1}^{n}\sum_{q=1}^{T_b}(x_{pq}^c - \bar{X}^c)^2}}, \tag{2}$$

where $\bar{X}^b$ and $\bar{X}^c$ are the means of X^b and X^c, respectively. This measure is the Pearson correlation coefficient adapted to matrices and calculated using the MATLAB *corr2* function [12]. The best possible value of the matrix correlation coefficient is 1.The correlation coefficient between two matrices has found wide applications in the image analysis, molecular biology, etc.

The third similarity measure for multivariate time series is the *Principal Component Analysis (PCA) similarity factor* [9], [13]. PCA is a well-known and wide used technique for dimensionality reduction of data. It is a linear transformation that projects the original data to a new coordinate system with the minimal loss of information. In multivariate cases, the information is the structure of the original data, i.e. the correlation between the features and alteration of the correlation structure among them. To create a projection, PCA selects coordinate axes of the new coordinate system one by one according to the greatest variance of any projection. The PCA similarity factor is defined by the following formula:

$$S_{PCA}(X^b, X^c) = tr(L'MM'L), \tag{3}$$

where L and M are matrices that contain the first l principal components of X^b and X^c, respectively. It means that the principal components are computed by the standard algorithm using the matrices $(X^b)'X^b$ and $(X^c)'X^c$, and then l principal components with the highest eigenvalues are selected. The best possible value of the PCA similarity factor is l. In our experiments $l = 1$.

Dynamic time warping (DTW) [14] is the most widely used technique for comparison of time series data, where extensive a priori knowledge is not available. The Euclidean distance reflects the similarity in time, while the dynamic time warping (DTW) reflects the similarity in shape. DTW searches for the best alignment between two time series, attempting to minimize the distance between them. The advantage of DTW is that it can handle unequal series and distortions. *Multidimensional Dynamic Time Warping (MDTW)* is presented in [15]. Some distance matrix is defined: $\{d(p,q) = \sum_{k=1}^{n}(x_{kp}^b - x_{kq}^c)^2,\ p,q = 1,\ldots,T_b\}$. Then the matrix D of cumulative distances is calculated as in the traditional DTW algorithm [15]:

$$D(p,q) = \begin{cases} d(1,1), \text{if } p = 1, q = 1, \\ d(p,q) + D(p-1,q), \text{if } p = 2,\ldots,T_b, q = 1, \\ d(p,q) + D(p,q-1), \text{if } p = 1, q = 2,\ldots,T_b, \\ d(p,q) + min \begin{cases} D(p-1,q) \\ D(p,q-1), \\ D(p-1,q-1) \end{cases} \text{in other cases.} \end{cases} \tag{4}$$

(p,q) defines the pair of the pth observation in X^b and the qth observation in X^c. Finally, the minimal path and the distance along the minimal path are obtained using matrix D. The path must start at the beginning of each time series at $(1,1)$ and finish at the end of both time series

at (T_b, T_b). See [13] for details. The best possible value of MDTW is 0. On the other hand, DTW can lead us to unintuitive alignments, where a single point on one time series maps onto a large subsection of another time series [16], [17]. Also, DTW can fail to find the obvious and natural alignments in two time series because of a single feature (i.e. peak, valley, infection point, plateau, etc.). One of the causes is due to the great difference between the lengths of the compared series.

In this paper, the fifth similarity measure for multivariate time series is *Eros (Extended Frobenius norm)* [9]. Eros is based on the principal component analysis and computes the similarity between two MTS items by measuring how close the corresponding principal components are using the eigenvalues as weights. In our case, X^b and X^c are two multivariate time series items of n features and T_b observations. $V^b = [v_1^b, \ldots, v_n^b]$ and $V^c = [v_1^c, \ldots, v_n^c]$ are two right eigenvector matrices obtained by applying a singular value decomposition (SVD) to the covariance matrices M^b and M^c of features in X^b and X^c respectively. The *Eros similarity* of X^b and X^c is defined as follows:

$$Eros(X^b, X^c, w) = \sum_{i=1}^{n} w_i |\langle v_i^b, v_i^c \rangle|, \tag{5}$$

where $\langle v_i^b, v_i^c \rangle$ is the inner product of v_i^b, and v_i^c, w is a weight vector, based on eigenvalues of the MTS data set (see more in detail in [9]), $\sum_{i=1}^{n} w_i = 1$.

4 Multidimensional Data Visualization

The method, proposed in Section 2 for finding the best subsequences matching to the sample, is based on the visual presentation and analysis of multidimensional points the coordinates of which are the values of similarity measures, computed for a pair of subsequences. The visualization technology is introduced below.

For an effective data analysis, it is important to include a human into the data exploration process and combine the flexibility, creativity, and general knowledge of the human with the enormous storage capacity and computational power of today's computer. Visual data mining aims at integrating the human in the data analysis process, applying the human's perceptual abilities to the analysis of large data sets, available in today's computer systems. Visualization finds a wide application in the medical data analysis, too [18], [19].

The goal of the projection method is to represent the input data items in a lower-dimensional space so that certain properties of the structure of the data set were preserved as faithfully as possible. The projection can be used to visualize a data set, if rather a small output dimensionality is chosen. One of these methods is the principal component analysis (PCA). The well-known principal component analysis [6] can be used to display the data as a linear projection on a subspace of the original data space such that best preserves the variance in the data. PCA cannot embrace nonlinear structures, consisting of arbitrarily shaped clusters or curved manifolds, since it describes the data in terms of a linear subspace. Therefore, several methods have been proposed for reproducing nonlinear higher-dimensional structures on a lower-dimensional display: multidimensional scaling and its modifications [6], [20], [21], [22], Isomap [23], locally linear embedding [24], etc. Various neural network approaches are used for this aims as well (see e.g. [25], [26], [27]).

Multidimensional scaling (MDS) is a group of methods that project multidimensional data to a low (usually two) dimensional space and preserve the interpoint distances among data as much, as possible. Let us have the m-dimensional points $\overline{S}_q = (S_{q1}, S_{q2}, \ldots, S_{qm}), q = 1, \ldots, t, (\overline{S}_q \in$

R^m). The pending problem is to get the projection of these points onto the plane R^2. Two-dimensional points $Y_1, Y_2, \ldots, Y_t \in R^2$ correspond to them. Here $Y_q = (y_{q1}, y_{q2}), q = 1, \ldots, t$. Denote the distance between the points $\overline{S}_q$ and $\overline{S}_p$ by d^*_{qp}, and the distance between the corresponding points Y_q and Y_p on the projected space by d_{qp}. In our case, the initial dimensionality is m, and the resulting one is 2 (2-D). Naturally, 1-D and 3-D projections could be considered, too. However, in the 1-D case, we lose knowledge that can be obtained from 2-D or 3-D views. Advantages of 3-D can be achieved when special means to present such data on the screen are applied. Therefore, 2-D projections of the multidimensional data are commonly used.

There exists a multitude of variants of MDS with slightly different so-called stress functions. In our experiments, the raw stress is minimized $E_{MDS} = \sum_{q<p}^{t} (d^*_{qp} - d_{qp})^2$, seeking to find the optimal coordinates of points $Y_1, Y_2, \ldots, Y_t$.

5 Comparative Analysis of Similarity Measures for Multivariate Time Series

The data from PhysioNet/Computing in Cardiology Challenge are used for the experimental analysis (*http://www.physionet.org/challenge/2012/*). The records were collected in the Intensive Care Unit. In the experiments we used a set X^a, containing multivariate time series of 50 patients of the same age, i.e. if to follow the notation of Section 1, we have 50 different multivariate time series $X^a_i, i = 1, \ldots, 50$, each consisting of 48 observations (columns) of $n = 4$ features (rows: non-invasive diastolic arterial blood pressure, non-invasive systolic arterial blood pressure, heart rate, temperature). $X^a = \{X^a_i, i = 1, \ldots, 50\}$.

In general, the sample X^b (the current situation) does not belong to X^a. However, seeking for more precise conclusions in this research, we have chosen X^b in X^a at random of the length $T_b = 8$. Moreover, we have chosen X^b such that its contents belongs to the same patient, i.e. X^b does not consist of the parts of different patients' records.

The goal is to go through time windows X^c (of the size of X^b) in X^a and compare them with X^b. For each similarity measure the optimal place of X^b on X^a has been found. By the optimal place of X^b, in accordance with the chosen similarity measure, we assume X^c such that produces the best value of this similarity measure when comparing X^b and X^c. Then the values of remaining measures were computed for the same X^c. Due to the specific character of data (50 patients), the place of X^c on X^a may be denoted as follows: $i[T_{start}; T_{end}]$, where i is the order number of a patient, $i = 1, \ldots, 50, T_{start}$ and T_{end} are start and end positions of X^c on X^a. The illustration results are presented in Table 1.

Let us choose the sample at random. In our case, $X^b = 1[23 - 30]$. It was compared with all the other available subsequences X^c of the analysed data set X^a. Considering that the sample taken for the analysis is selected from X^a and striving for the independence of investigation results on this case, we choose X^c only such that has no more than 5 common observations with X^b.

Five subsequences $X^c \neq X^b$, that are most similar to the sample, were selected according to each similarity measure. Therefore, we get five collections of five most similar subsequences. The total number of the selected subsequences is 25 and some of them coincident according to different measures. For each collection, the values of all similarity measures are computed and presented in Table 1. The best values obtained for all similarity measures are marked in bold.

Table 1 shows that different measures often mark different (not the same) subsequences as similar. All the measures acquire their best values in the case of identical coincidence of X^b and X^c. Thus, a further task is to summarize the obtained results and to develop a method for selecting of the most similar subsequence X^c to the sample X^b. The analysis of subsequences, found by

Table 1: Most similar subsequences according to each similarity measure; sample $X^b = 1[23-30]$

	No.	X^c	Similarity measures				
			r	*Eros*	*Frob*	*MDTW*	S_{PCA}
Ideal coincidence	0	1[23-30]	1	1	0	0	1
r	1	1[16-23]	**0.9639**	0.1745	4.4224	**16.9434**	0.7175
	2	48[37-44]	0.9575	0.1302	**2.5551**	19.2153	0.6874
	3	1[17-24]	0.9504	**0.6067**	3.9967	17.0556	**0.8480**
	4	42[16-23]	0.9455	0.3440	3.8527	30.8482	0.1680
	5	1[19-26]	0.9430	0.2969	3.1215	18.8935	0.8474
Eros	6	10[30-37]	0.0013	**0.9423**	6.5985	59.1889	**0.9847**
	7	25[31-38]	-0.3214	0.9099	7.1453	62.7647	0.6705
	8	49[35-42]	-0.2209	0.9064	8.0460	41.6136	0.5461
	9	17[9-16]	**0.6266**	0.8979	**4.6676**	**39.8056**	0.4329
	10	40[16-23]	0.1164	0.8948	7.7252	55.2800	0.5772
Frob	11	48[37-44]	**0.9575**	0.1302	**2.5551**	19.2153	0.6874
	12	48[36-43]	0.9366	**0.4445**	2.8003	**18.6496**	**0.9789**
	13	1[36-43]	0.8931	-0.2531	2.9396	31.2548	0.9206
	14	48[35-42]	0.9169	-0.2479	3.0346	23.2913	0.9148
	15	48[38-45]	0.8943	0.1853	3.0886	25.6391	0.5152
MDTW	16	34[39-46]	-0.0158	0.4709	7.2486	**8.8982**	0.3182
	17	22[14-21]	0.1724	0.6900	6.5888	9.6141	0.5765
	18	29[4-11]	0.5061	-0.0177	4.9202	9.6744	0.6974
	19	12[12-19]	**0.6511**	-0.3166	**4.8690**	10.1095	**0.9553**
	20	15[3-10]	0.5351	0.2744	7.4371	11.0668	0.2524
S_{PCA}	21	10[32-39]	-0.1145	0.0688	7.5452	96.4585	**0.9920**
	22	16[33-40]	-0.0749	**0.2350**	9.2904	67.8260	0.9896
	23	10[33-40]	-0.0695	0.0074	7.6335	93.8404	0.9896
	24	10[34-41]	0.0036	-0.4202	7.5849	70.1514	0.9892
	25	4[5-12]	**0.4171**	0.1522	**6.9828**	**57.2766**	0.9890

different measures shows that matrix correlation coefficient and Frobenius norm measures try to find the most similar subsequence according to the values of the subsequence elements. MDTW tends to compare the data change dynamics: the scales of features of the subsequences can be different, but MDTW can indicate these sequences as similar. S_{PCA} and *Eros* measures do not also depend on the scale and are less sensitive to abrupt signal changes. It is very important in the medical data analysis.

The correlation analysis (see Table 2) has the depicted a strong inverse correlation between the Frobenius norm and the matrix correlation coefficient. For the investigation, 50 randomly selected samples $X_i^b, i = 1, \ldots, 50$ consisting of $T_b = 8$ successive observations were selected; from each X_i^a one subsequece X_i^b was selected as a sample. For each selected sample and for each similarity measure 25 most similar subsequences were identified in the whole X^a. Just like above, we choose X^c only such that has no more than 5 common observations with X^b. The total number of comparisons of X^b and X^c is 1250. According to these data, the correlation matrix of similarity measures has been computed. It is presented in Table 2. As the results shows, there is a very strong inverse correlation (-0.7355) between the Frobenius norm *Frob* and the matrix correlation coefficient r.

Because of the strong inverse correlation between the Frobenius norm and the matrix corre-

Table 2: Correlation matrix of similarity measures

	r	*Eros*	*Frob*	*MDTW*	S_{PCA}
r	1.0000	-0.1917	**-0.7355**	-0.2127	-0.1652
Eros	-0.1917	1.0000	0.1819	0.1731	-0.1748
Frob	-0.7355	0.1819	1.0000	0.1071	0.1055
MDTW	-0.2127	0.1731	0.1071	1.0000	0.0454
S_{PCA}	-0.1652	-0.1748	0.1055	0.0454	1.0000

lation coefficient, the Frobenius norm was casted away. It has been done with a view to reduce the general impact of the correlated parameters on the investigation results. In such a way, outcasting of the Frobenius norm measure evens the impact of the rest measures.

For the second investigation 50 randomly selected samples $X_i^b, i = 1, \ldots, 50$ consisting of $T_b = 8$ successive observations have been selected. One sample X_i^b is selected from each X_i^a. For each selected sample and for each similarity measure (4 similarity measures are investigated now), 20 most similar subsequences were identified in the whole X^a. Just like previously, we choose X^c only such that has no more than 5 common observations with X^b. The total number of comparisons of X^b and X^c is 1000. According to the obtained data, for each sample X_i^b and for four measures, a 4-dimensional point is constructed: $\overline{S}_q^i = (S_{q1}^i, S_{q2}^i, S_{q3}^i, S_{q4}^i), q = 1, \ldots, 20$. Coordinates of the point are the values of different measures. For example, the ideal subsequence match is assumed as $\overline{S}_0 = (1, 1, 0, 1)$. Further, the Euclidean distance is calculated between the ideal match $\overline{S}_0$ and all the rest $\overline{S}_q^i$ of similar subsequences. Then the subsequences are sorted according to the shortest distance and the first 5 subsequences are treated as similar (from the total 5x50 subsequences). Table 3 summarizes the investigation results, i.e. shows the most often found similar subsequences.

Table 3: Most often found similar subsequences according to each similarity measure

Frequencies	r	*Eros*	*MDTW*	S_{PCA}
Total 250	93	32	91	34
Percentage from 250 subsequences	31	11	30	11

As can be seen from Table 3, the matrix correlation coefficient and MDTW measures are the best.

In addition, the Frobenius norm measure can be considered together with these two measures because of its high correlation with the matrix correlation coefficient measure. Moreover, a high correlation of the Frobenius norm with the matrix correlation coefficient does not mean that they yield very similar results. The experiment below illustrates this fact. Ten most similar subsequences were found for the chosen sample, using these two similarity measures for multivariate time series. The obtained subsequences are presented in Table 4 in decreasing order of their goodness, depending on the similarity measure. Coincident subsequences are presented in different tint of grey colour. We see three coincident subsequences only with quite different order numbers.

Table 4: Comparison of the Frobenius norm with the matrix correlation coefficient

	No.	r	*Frob*
Sample 1[23-30]	1	1[16-23]	48[37-44]
	2	48[37-44]	48[36-43]
	3	1[17-24]	1[36-43]
	4	42[16-23]	48[35-42]
	5	1[19-26]	48[38-45]
	6	48[36-43]	1[35-42]
	7	1[18-25]	20[15-22]
	8	42[35-42]	1[19-26]
	9	42[17-24]	1[34-41]
	10	1[7-14]	48[40-47]

6 Experimental Illustration of the Visual Method for Finding the Best Subsequences, Matching to the Sample

The performance of the proposed method is illustrated by the example. Like in Section 5, the data from PhysioNet/Computing in Cardiology Challenge (http://www.physionet.org/challenge) are used for the experimental analysis.

1. Sample $X^b = 1[23-30]$ has been chosen.

2. The sample is compared with all the subsequences of X^a by using 5 similarity measures, given in Section 3. In accordance with each measure, 10 subsequences, most similar to the sample, are chosen. Therefore, the total number of subsequences for a further analysis is equal to 50.

3. Each comparison of a sample to a subsequence, chosen in the way defined in the step above, produces the 5-dimensional point $\overline{S}_q = (S_{q1}, S_{q2}, \ldots, S_{q5})$, where $q = 1, \ldots, 50$. Let us derive two additional points:

   - $\overline{S}_0 = (S_{01}, S_{02}, \ldots, S_{05})$ is the array of values of all the similarity measures computed for the subsequence that is ideally coincident with the sample (the array of the best values of m similarity measures); in our case, $\overline{S}_0 = (1, 1, 0, 0, 1)$;
   - $\overline{S}_C = (S_{C1}, S_{C2}, \ldots, S_{Cm})$ is the weight center of $\overline{S}_q = (S_{q1}, S_{q2}, \ldots, S_{q5}), q = 1, \ldots, 50$; in our case, $\overline{S}_C = (0.39298, 0.31968, 5.98348, 35.26159, 0.715413)$.

   Therefore, the total number of 5-dimensional points for discovering the most similar subsequences to the sample is equal to 52. Afterwards, the normalization of the components of these points is performed by z-score. The obtained matrix Z of normalized points consists of 52 rows and 5 columns.

4. The points from matrix Z are mapped on the plane using the Multidimensional Scaling. The resulting matrix is Y, the rows of which correspond to different comparisons of the sample with other subsequences and are the coordinates of points on the plane.

5. Figure 2 presents graphically all 52 5-dimensional points from Y on a plane for decision making. In general, the subsequence best matching to the sample can be the subsequence the corresponding point of which on a plane is closest to the projection of $\overline{S}_0$ on a plane.

However, more subsequences are similar to the sample. The points on the plane, corresponding to such subsequences, must be closer to the projection of $\overline{S}_0$ on the plane than to the projection of $\overline{S}_C$. If we draw a circle with the center on the projection of $\overline{S}_0$ on the plane and the radius that is equal to the distance between the projections of $\overline{S}_0$ and $\overline{S}_C$, we can visually detect subsequances most similar to the sample. In Figure 2, the colour of the point corresponds to the similarity measure according to which the subsequence falls among the most similar ones:

- Red points - matrix correlation coefficient,
- Green points - Eros,
- Yellow points - Frobenius norm,
- Blue points - MDTW,
- Magenta points - S_{PCA}.

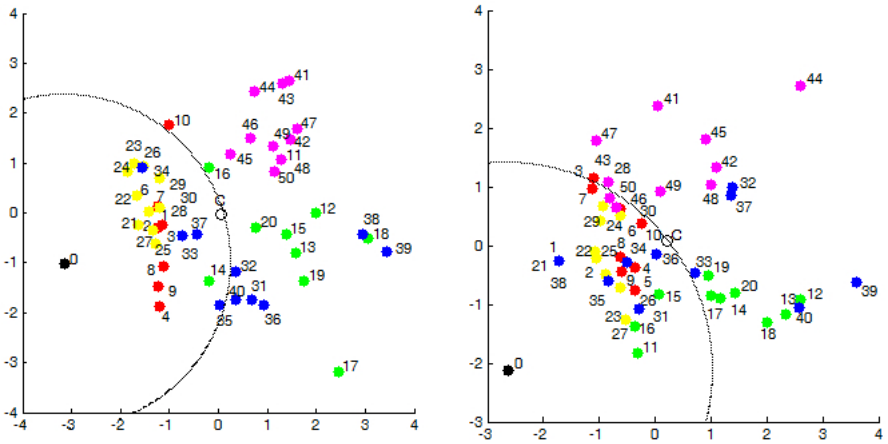

(a) (b)

Figure 2: Results for the visual analysis: a) sample 1[23-30]; b) sample 5[15-22]

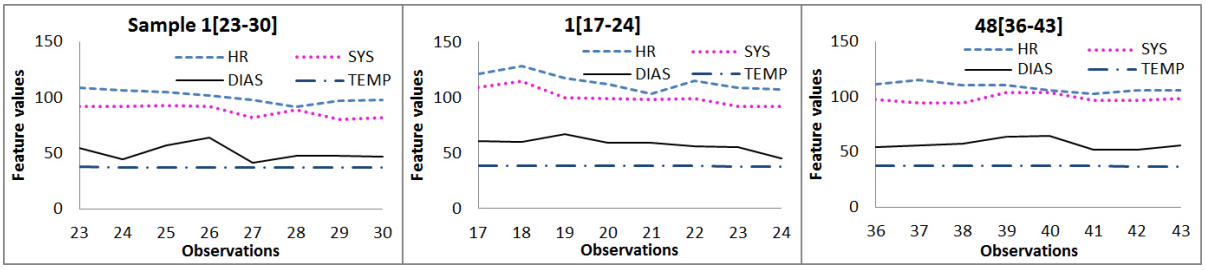

Figure 3: Two subsequences most similar to the sample 1[23-30]

In Figure 2a, two best similarity measures, in accordance with which the subsequence falls among the most similar ones, are the matrix correlation coefficient and Frobenius norm measures. In Figure 2b, these two measures are exceptional again, however MDTW and Eros have influenced the appearance of subsequences in the most similar subsequence list. A relatively small number of the most similar subsequences is produced by S_{PCA}, only. Therefore, all the measures are important and can be successfully used jointly .

Finally, the sample and two found most similar subsequences are presented, as an example, in Figure 3.

7 Conclusions

This paper deals with the multivariate time series analysis seeking to compare the current situation (sample) with that in chronologically collected historical data and to find subsequences of the multivariate time series most similar to the sample. The visual method for finding the best subsequences matching to the sample has been proposed. Using this method, the investigator can consider the results of comparison of the sample and some subsequence of the series from the standpoint of several measures that can be supplementary to one another or contradictory among themselves.

The analysis of medical streaming data is quite a difficult problem. The data are very specific to an individual patient. It may cause the problem of reliability of the decision if the problem is to estimate the health-state situations in real time streaming data in accordance with the previously detected and estimated streaming data of various patients. The usage of a larger number of similarity measures (not a single fixed measure) can increase the efficiency of decisions on the health state of the patient based on the streaming data of other patients.

The advantage of the visual analysis of the data, presented on the plane, is that we can see not only the subsequence best matching to the sample (such a subsequence can be found in the automatic way), but also we can see the distribution of subsequences that are similar to the sample in accordance with different similarity measures. It allows us to evaluate differences among the subsequences and among the measures.

Five similarity measures were integrated in this research. Note that the correlation coefficient between two matrices is quite effective and easily interpreted among other measures, that are usually used for multivariate streaming data analysis. However, the best efficiency of applications of this measure is achieved when combining it with other measures.

This method is universal and can be used in the analysis of streaming data of various nature (not only medical data). It is necessary to select the proper set of similarity measures depending on the problem solved only.

Bibliography

[1] Batal I., Sacchi L., Bellazzi R., Hauskrecht M. (2009); Multivariate Time Series Classiffcation with Temporal Abstractions, *Florida Artificial Intelligence Research Society Conference, Twenty-Second International FLAIRS Conference*, ISBN 978-1-57735-419-2, 344–349.

[2] Borowsky M., Imhof M., Schettlinger K., Gather U. (2008); Multivariate Signal Filtering from Intensive Care Online-Monitoring Time Series, avialable at `https://www.statistik.tu-dortmund.de/fileadmin/user_upload/Lehrstuehle/MSind/SFB_475/C/2008_-_Borowski_Imhoff_Schettlinger_Gather_-_Multivariate_Signal_Filtering_from_Intensive_Care_Online_Monitoring_Time_Series_-_Biosignalverarbeitung_2008.pdf`.

[3] Ordonez P., des Jardins M., Feltes C., Lehmann C., Fackler J. (2008); Visualizing Multivariate Time Series Data to Detect Specific Medical Conditions. *Proceedings of AMIA (American Medical Informatics Association) 2008 Annual Symposium*, ISBN 978-1-61567-435-0, 6: 530–534.

[4] Keim D.A , Mansmann F., Schneidewind J., Ziegler H. (2006); Challenges in Visual Data Analysis, *Proc. Intl Conf. Information Visualization (IV)*,ISBN 0-7695-2602-0/06, 9–16.

[5] Chin G., Singhal M., Nakamura G., Gurumoorthi V., Freeman-Cadoret N. (2009); Visual analysis of dynamic data streams, *Information Visualization*, ISSN 1473-8716, 8(3): 212-229.

[6] Dzemyda G., Kurasova O., Žilinskas J. (2013); *Multidimensional Data Visualization: Methods and Applications (Springer Optimization and Its Applications, 75)*, Springer, ISBN 978-1-4419-0235-1.

[7] Ye N. (2003); *The Handbook of Data Mining*, Mahwah, NJ: Lawrence Erlbaum, ISBN 0-8058-4081-8.

[8] Karamitopoulos L., Evangelidis G., Dervos D. (2008); Multivariate Time Series Data Mining: PCA-based Measures for Similarity Search, *Proceedings of The 2008 International Conference on Data Mining*, USA, ISBN 1-60132-062-0, 253–259.

[9] Yang K., Shahabi C. (2004); A PCA-based Similarity Measure for Multivariate Time Series, *MMDB '04 Proceedings of the 2nd ACM international workshop on Multimedia databases*, ISBN 1-58113-975-6, 65–74.

[10] Xun L., Zhishu L. (2010); The Similarity of Multivariate Time Series and Its Application, *2010 Fourth International Conference on Management of e-Commerce and e-Government (ICMeCG)*, ISBN 978-0-7695-4245-4, 76–81.

[11] Moon T., Striling W. (2000); *Mathematical Methods and Algorithms for Signal Processing*, Prentice Hall, ISBN 978-0201361865.

[12] *MATLAB R2014a and Image processing toolbox*, Natick, Massachusetts: The MathWorks Inc., 2014, avialable at `http://www.mathworks.se/help/images/ref/corr2.html`.

[13] Krzanowski W. (1979); Between-groups Comparison of Principal Components, *JASA*, ISSN 0162-1459, 74(367): 703–707.

[14] Berndt D., Clifford J. (1994); Using Dynamic Time Warping to Find Patterns in Time Series, *KDD Workshop*, 359–370.

[15] Sanguansat P. (2012); Multiple Multidimensional Sequence Alignment Using Generalized Dynamic Time Warping, *WSEAS Transactions on Mathematics*, e-ISSN 2224-2880, 11(8): 668–678.

[16] Fu T.-C. (2011); A Review on Time Series Data Mining, *Engineering Applications of Artificial Intelligence*, ISSN 0952-1976, 24: 164–181.

[17] Keogh E., Pazzani M. (2001); Derivative Dynamic Time Warping, *First SIAM International Conference on Data Mining (SDM2001)*, Chicago, USA, ISBN 978-0-89871-495-1, 1–11.

[18] Bernatavičienė J., Dzemyda G., Kurasova O., Marcinkevičius V., Medvedev V. (2007); The Problem of Visual Analysis of Multidimensional Medical Data, *Springer optimization and its applications 4, Models and algorithms for global optimization*, New York, Springer, ISBN 0-387-36720-9, 277–298.

[19] Klawonn F., Lechner W., Grigull L. (2013); Case-Centred Multidimensional Scaling for Classification Visualisation in Medical Diagnosis, *Health Information Science,Lecture Notes in Computer Science*, ISBN 978-3-642-37898-0, 7798: 137–148.

[20] Borg I., Groenen P. (1997); *Modern Multidimensional Scaling: Theory and Applications*, Springer, ISBN 0-387-94845-7.

[21] Bernatavičienė J., Dzemyda G., Marcinkevičius V. (2007); Conditions for Optimal Efficiency of Relative MDS, *Informatica*,ISSN 0868-4952, 18(2): 187-202.

[22] Bernatavičienė J., Dzemyda G., Marcinkevičius V. (2007); Diagonal majorization algorithm: properties and efficiency, *Information technology and control*, ISSN 1392-124X, 36(4): 353–358.

[23] Tenenbaum J.B., de Silva V., Langford J.C. (2000); A Global Geometric Framework for Nonlinear Dimensionality Reduction, *Science*, ISSN 0036-8075, 290(5500): 2319–2323.

[24] Karbauskaitė R., Dzemyda G., Marcinkevičius V. (2010); Dependence of Locally Linear Embedding on the Regularization Parameter, *TOP*, ISSN 1134-5764, 18(2): 354–376.

[25] Medvedev V., Dzemyda G. (2006); Optimization of the local search in the training for SAMANN neural network, *Journal of global optimization*, ISSN 0925-5001, 35(4): 607–623.

[26] Bernatavičienė J., Dzemyda G., Kurasova O., Marcinkevičius V. (2006); Optimal Decisions in Combining the SOM with Nonlinear Projection Methods, *European Journal of Operational Research*, ISSN 0377-2217, 173(3): 729–745.

[27] Medvedev V., Dzemyda G., Kurasova O., Marcinkevičius V. (2011); Efficient Data Projection for Visual Analysis of Large Data Sets Using Neural Networks, *Informatica*, ISSN 0868-4952, 22(4): 507–520.

INTERNATIONAL JOURNAL OF COMPUTERS COMMUNICATIONS & CONTROL
ISSN 1841-9836, 10(1):22-29, February, 2015.

Control System for Auto Moving Vehicle using for Artificial Turf Ground Performance Test

M.J. Chung

Myung Jin Chung*
Mechatronics Engineering Department
Korea Polytechnic University, Republic of Korea
*Corresponding author: mjchung@kpu.ac.kr

Abstract: Recently, use of artificial turf has been increasing in a variety of international games as well as the change of school playgrounds to artificial turf from clay. Artificial turf is needs to obtain a standard certification to hold international games. This standard certification is based on a shock performance test during a specified period. The control system of the auto moving vehicle using for artificial turf ground performance tests is proposed and the control algorithm was adopted to improve the trajectory following performance of the auto moving vehicle. The control algorithm was optimized by computer simulation. Each part of the control system was developed and integrated into the auto moving vehicle. Experiments were conducted to verify the performance of the control system. From the performance test, the control system had a positioning resolution of $0.05m$, maximum velocity of $1m/sec$, and a trajectory following error of $\pm 1.3deg$ for operating conditions.
Keywords: control system, auto moving vehicle, artificial turf, positioning, velocity, trajectory following.

1 Introduction

The use of artificial turf has been increasing from the variety of international games held on it and the change of school playgrounds to artificial turf from clay. Artificial turf ground is required to meet the standards of certification to play international games. This standard certification is given by the Federation International Football Association (FIFA) rules determined by a shock performance test during a specified period. FIFA rules are described in the "FIFA Quality Concept − Handbook of Test Methods and Requirements for Artificial Turf Football Surfaces." Shock performance test technology is growing due to the development of automobile crash safety performance test technology. However, the application area of shock performance test technology is limited to the automobile industry. [1] Data acquisition and analysis technologies are limited to the automobile industry as well. Currently, the shock performance test for artificial turf ground is conducted by manually moving the test system around the testing area of the artificial turf. It is a time consuming process and the repeatability of the measured data is poor. [2] Therefore, an auto measuring system having functions including auto moving, auto testing, and auto data acquisition and analysis is required for the shock performance test.
Researches associated with auto moving vehicles and auto shock performance tests are conducted in the area of automobile crash safety performance tests, respectively. [3]- [5] Researches on the combined control of auto moving vehicles and auto shock performance test are rarely conducted in the area of artificial turf. [6]- [7] In addition, improvement of the trajectory following performance of the auto moving vehicle is required for application in the auto measuring system for the shock absorbing performance test of artificial turf.
In this work, the control system of the auto moving vehicle using for the artificial turf ground performance test is proposed and the control algorithm was adopted to improve the trajectory following performance of the auto moving vehicle. The control algorithm was optimized by computer simulation. Each part of the control system was developed and integrated into the

auto moving vehicle. Experiments were conducted to verify the performance of the developed control system of the auto moving vehicle.

2 Configuration

The configuration of auto measuring system for shock absorbing performance test of artificial turf ground is as follows: auto moving vehicle for moving the auto shock performance testing module, auto shock performance testing module for raising and dropping the reference weight, data acquisition module for measuring the force and acceleration of the reference weight, and wireless communication module for transferring the measured data from the data acquisition module to the remotely positioned PC as shown in Fig. 1. The auto moving vehicle is operated as described in Fig. 2. The auto moving vehicle containing the auto shock performance testing module follows the reference trajectory of the artificial turf ground, and stops for shock performance testing. When the auto moving vehicle stops, the auto shock performance testing module raises and drops the reference weight. Then, the data acquisition module measures the force and acceleration of the reference weight and the wireless communication module transfers the measured data from the data acquisition module to the remotely positioned PC. In the remote PC, measured data is analyzed and graphically displayed. The control system of the auto moving vehicle consists of two BLDC hub motors and drivers, six Ni batteries, digital magnetic compass sensor, ZigBee transmitter and receiver, and a main controller as shown in Fig. 3.

3 Requirements

The requirements of the auto measuring system for the shock absorbing performance test of artificial turf include the auto vehicle moving along the reference trajectory of the artificial turf ground, auto shock performance testing at the reference position, auto data acquisition of measured data, and the auto transferring of the measured data to the remotely positioned PC via wireless communication. The requirements of the auto moving vehicle also include a positioning resolution of $0.05m$, maximum velocity of $1m/sec$, and a trajectory following error of $\pm 2.0deg$ along the reference trajectory of the artificial turf with an area of $100m$ by $200m$. The control system of auto moving vehicle is required to have a robust trajectory following performance.

4 Design and Development

The control system of the auto moving vehicle consists of two BLDC hub motors and drivers, six Ni batteries, digital magnetic compass sensor, ZigBee transmitter and receiver, and a main controller. Two $250watt$ BLDC hub motors and two BLDC motor drivers are used for moving the $40kg$ auto shock performance testing module as shown in Fig. 4. The specifications of the BLDC hub motor and driver are listed in Table 1. Six Ni batteries with capacities of $40AH$ are connected in parallel. A digital magnetic compass sensor with a 0.5% resolution is used to detect the trajectory following direction of the auto moving vehicle as shown in Fig. 5. The main controller uses a 16bit microprocessor for signal processing and control algorithm as shown in Fig. 5. In the main controller, by comparing the reference direction signal and the digital magnetic compass, the motor driving sensor signal is generated, fed to the BLDC motor driver, and used to control its velocity and position. The position data is calculated with the digital magnetic compass sensor signal and the BLDC motor hall sensor signal. The wireless communication module consists of the ZigBee transmitter and receiver with a real-time transferring speed of $115Kbps$ and a transferring distance of $1km$ as shown in Fig. 6. This module receives the

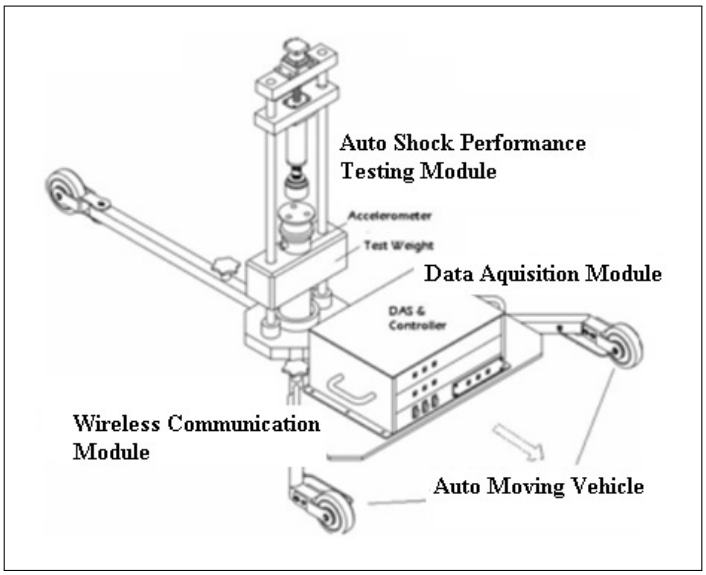

Figure 1: Configuration of auto measuring system

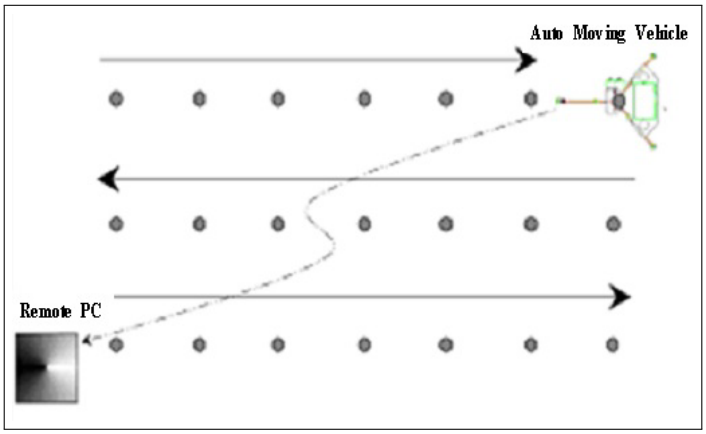

Figure 2: Operation procedure of auto moving vehicle

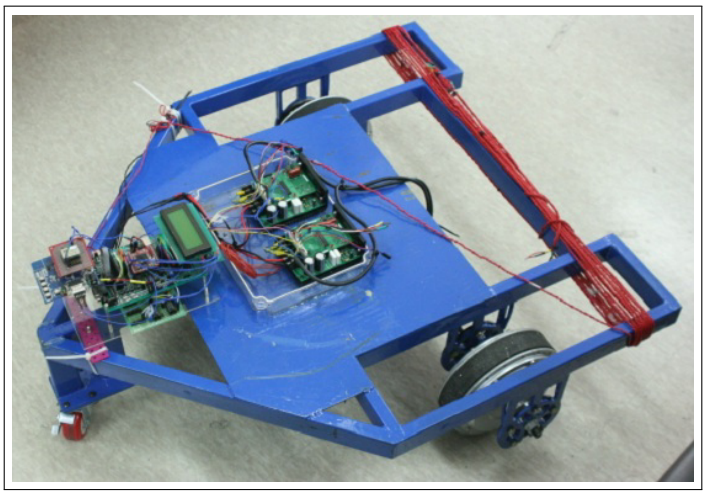

Figure 3: Control system of auto moving vehicle

operating signal from the remote PC and transmits the measured data to the remote PC for analysis.

Figure 4: BLDC hub motor and driver

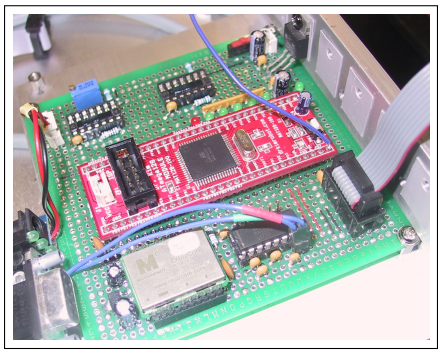

Figure 5: Compass sensor and main controller

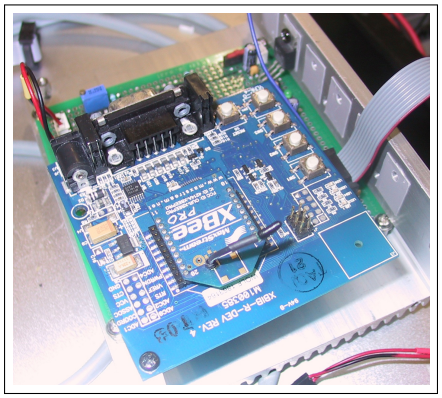

Figure 6: Wireless communication module

5 Control Algorithm

The control algorithm was adopted to improve the trajectory following performance of the auto moving vehicle and was optimized by using a computer simulation. The auto moving vehicle

Table 1: Specifications of the BLDC hub motor and driver

	Parameters	Value	Unit
Motor	Power	250	Watt
	Input voltage	36	Volt
	Rated RPM	3000	RPM
	Hub wheel size	200	mm
Driver	Rated voltage	48	Volt
	Rated current	10	A
	Velocity control method	PWM	-
	Switching Frequency	10	kHz

can be described by the mathematical modeling of the motor and body of the auto measuring system. Electric model of the motor is given by:

$$V - Ri - L\frac{di}{dt} - K_b\dot{\theta} = 0 \tag{1}$$

$$T_w = K_T i \tag{2}$$

where V is a voltage applied to the motor, R is a resistance of the motor, i is a current flowing through the motor, L is an inductance of the motor, K_b is a constant of back EMF, T_w is the torque generated by the motor, and K_T is the constant of torque, respectively.
Dynamic model of the motor and body of auto measuring system is given by: [8]

$$2(mr^2 + I_w)\ddot{\theta} = 2T_w + R_H r \tag{3}$$

$$Mr^2\ddot{\theta} = R_H r \tag{4}$$

where m is a mass, r is a radius, and I_w is the moment of inertia of the motor, M is the mass of the body, and R_H is the horizontal force acting on the motor by the body of the auto measuring system, respctively.
From Eq. (1) - (4), the relationship of angular velocity (Ω) and applied voltage (V) is geiven by:

$$T_w(s) = \frac{K_T}{Ls + R}[V(s) - K_b\Omega(s)] \tag{5}$$

$$\frac{\Omega(s)}{T_w(s)} = \frac{2}{[(2m + M)r^2 + 2I_w)]s} \tag{6}$$

From Eq. (5) and (6), simulink block diagram of the control system of the auto moving vehicle can be constructed as shown in Fig. 7. In this block diagram, a PID controller was adopted to optimize the trajectory following performance of the auto moving vehicle. The control signal generated by the PID controller is given by:

$$u(t) = K_p e(t) + K_i \int_0^t e(\tau)d\tau + K_d\frac{de(t)}{dt} \tag{7}$$

where u is a control signal, K_p is a proportional, K_i is a integral, and K_d is a derivative coefficient, respectively. In this system, K_i value is sensitive to the deviation range of the directional angle.

6 Experimental Results

The auto measuring system including the developed control system of the auto moving vehicle was used as an experimental setup for performance verification as shown in Fig. 8. In this experimental setup, the angle of the digital magnetic compass sensor was set at 0 degrees at the starting point and the signal processing time was set at $50msec$. Fig. 9 shows the experimental results of the auto moving vehicle according to the control signal for a $40m$ straight line following motion. In this experiment, the positioning resolution was $0.05m$, maximum velocity was $1m/sec$, and the deviation range of the directional angle was $\pm 1.3deg$, respectively.

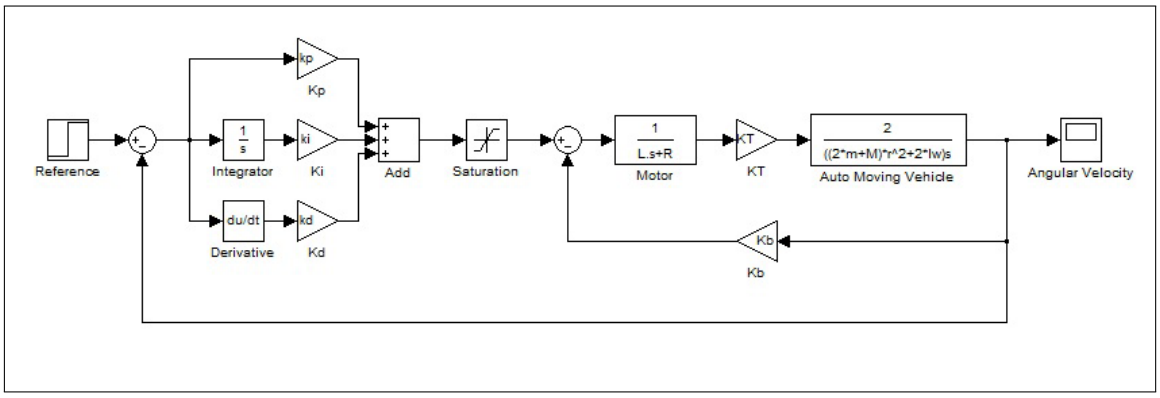

Figure 7: Simulink block diagram for PID controller simulation

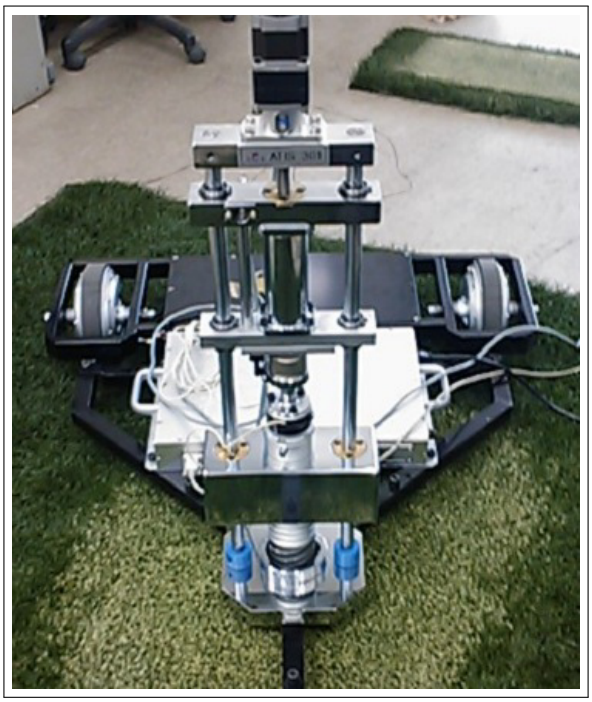

Figure 8: Experimental setup of the developed auto moving vehicle

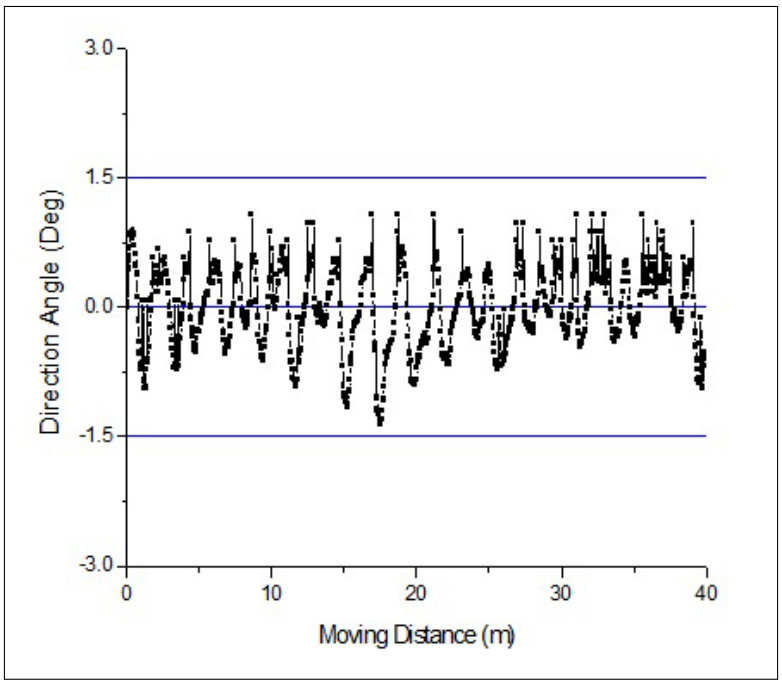

Figure 9: Experimental result of the auto moving vehicle

7 Conclusions

From this work, the control system of the auto moving vehicle using for artificial turf performance tests was proposed and a control algorithm to improve the trajectory following performance of the auto moving vehicle was adopted. The control algorithm was optimized by computer simulation. Each part of the control system was developed and integrated into the auto moving vehicle. Experiments were conducted to verify the performance of the developed control system of the auto moving vehicle. From the performance test, the developed control system of the auto moving vehicle had a positioning resolution of $0.05m$, maximum velocity of $1m/sec$, and a trajectory following error of $\pm 1.3deg$ for operating conditions.

Bibliography

[1] Park, J.W.; Lee, J.H.; Kim, J.W. (2003); Mathematical Model of Shock Absorber for Performance Prediction of Automobile, *J. Korean society of marine engineers*, ISSN 1226-9549, 27(4): 467-478.

[2] Nunome, H. et al (2007); A Valid Shock Absorbency Test For Artificial Turf, *J. of Biomechanics*, ISSN 0021-9290, 40: 740.

[3] Choo, Y.G. (2013); A Study on Designing Autonomous Parking Assistance using Fuzzy Controller, *J. of the Korean Society of Manufacturing Technology*, ISSN 1598-6721, 12(1): 70-76.

[4] Tsiotras P.; Diaz R.S. (2014); Real-Time Near-Optimal Feedback Control of Aggressive Vehicle Maneuvers, *Optimization and optimal control in automotive systems*, ISSN 0170-8643, 1(1): 109-130.

[5] Hossain, M.; Nabors, D.T. (2005); Testing and Evaluation of Used Automobile Tires and Recycled Tire-Derived Materials for Low-Cost Crash Cushions, *J. of Materials in civil engineering*, ISSN 0899-1561, 17(1): 36-44.

[6] Chung, M.J.; OH, S.G. (2008); Development of Auto Measuring System for Shock Absorbing Performance Test of Artificial Turf Ground, *Int. Conference on Control, Automation and Systems*, Print ISBN 978-89-950038-9-3, IEEE: 847-850.

[7] Chung, M.J.; OH, S.G.; Kang, K.W. (2010); A Study on the Evaluation of Shock Absorbing Performance for Domestic Artificial Turf Ground, *Int. Journal of Modern Physics*, ISSN 0217-9792, 24(15-16): 2567-2572.

[8] Chung, M.J.; Park, H.B.; Choi, K.H. (2012); Mathematical Model Based Attitude Control of Inverted Pendulum Type Mobile Robot, *Conference on Institute of Control, Robotics and Systems*, ICROS: 147-150.

INTERNATIONAL JOURNAL OF COMPUTERS COMMUNICATIONS & CONTROL
ISSN 1841-9836, 10(1):30-37, February, 2015.

A Comprehensive Approach to Off-line Advanced Error Troubleshooting in Intelligent Manufacturing Systems

L.S. Csokmai, R.C. Ţarcă, C. Bungău, G. Husi

Lehel Szabolcs Csokmai, Constantin Bungău*,
Radu Cătălin Ţarcă
Mechatronics Department, University of Oradea
Romania, 410087 Oradea, Universitatii St., 1
cs.lehel@gmail.com, rtarca@uoradea.ro
*Corresponding author: bungau@uoradea.ro

Géza Husi
Department of Electrical Engineering and Mechatronics
University of Debrecen
Hungary, Debrecen, Dembinszky Ut.
husigeza@eng.unideb.hu

Abstract: The errors recovery in the production systems will be always an open issue. Therefore, the FMSs have to be endowed with tools and techniques allowing an automatic recovery of errors. The objective of this work consists in proposing an off-line version of the software framework for error troubleshooting in a flexible manufacturing system [1]. The main difference between the on-line and off-line version is that the error database is stored on the mobile device and the frame marker device is connected directly to the FMS components without the need of the PC.). Our framework system is designed to solve the failures in the functioning of the FMS and to generate self-training from previous experience.
Keywords: frame maker, FMS(flexible manufacturing system), error, troubleshooting, advanced decision systems.

1 Introduction

To improve their products quality, many companies used the Six Sigma approach to capture measureand eliminate the defects in manufacturing process in last years.

Nowadays, in flexible manufacturing systems, smart products and FMSs components (equipped with embedded smart devices) are wirelessly networked and remotely monitored in a real-time, using for this intelligent control systems.

Consequently, using these systems, we can achieve real time data gathering, remote monitoring and analysing the results acquired from smart product and FMS components, the purpose being: to control the manufacturing quality and to detect quality degradation, that will allows assessment of the failure situation and taking of appropriate corrective actions accordingly.

The error handling issue can be observed from two points of views. The former (out-of order) is related to the hole system-level point of view and deals with unexpected events as: FMS's components breakdowns, changes in task priorities, and all others which can be identified by the system's controller. The latter (out-of-ordinary events) is related to the errors at the cell level. Exceptions (differences between the actual and the expected state of the system) in a flexible manufacturing cell can be classified as: (1) unexpected events [2] (like time-out on expected process report or occurrence of unexpected reports), (2) errors [3] (like positioning errors), (3) unpredictable failures [9] (such as resource's out of orders, cameras failures, equipment failures, tool breakages, human errors, material handling problems, collisions, obstructions and handling failures).

The diagnosis issue is widely spread in the FMS research community. The diagnosis task can be split in the following sub-tasks [5], [6], [9]:

- Detection, the goal of this task is to identify that something is not going as expected;
- Isolation, the goal of this task is to determine the exact location of the disturbance;
- Identification, the goal of this task is to determine the disturbance magnitude and impact;
- Error Diagnosis and Prognosis, that means to identify the responsible for the system degradation and the future degradation consequences;
- Error or Failure Recovery a procedure that allows to restart the error of failure in a way that either eliminates or minimizes it.

From the perspective of the automated control system, real-time status and data gathering of the various FMS components or manufacturing process and information transfer to the manufacturing process control centre or a corrective maintenance intervention upon FMSs components represents the close loop control and management of the manufacturing system (Figure 1).

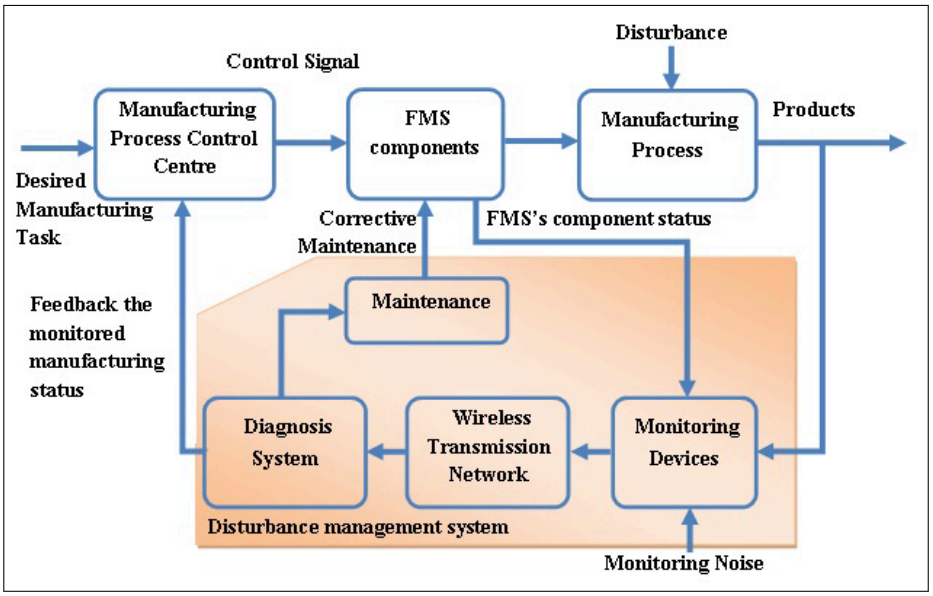

Figure 1: Disturbance management system

Figure 1 illustrates the informational flow in a disturbance management system. The monitoring devices is continuously observe the FMSs component status and manufacturing process, performing a comparison with the existing states and plans to verify if a deviation occurs.

If a deviation is detected, a diagnostic is generated, so the causes for the disturbance are identified; then its dynamics is evaluated, the possible actions to be executed to prevent a dynamic evolution of the disturbances consequences [7] ; all these with the aim to recover the system from this status.

If the diagnostic is generated, the diagnostic system starts a self-repair procedure; if it is not possible, the system requests a corrective maintenance intervention to the maintenance department. In the same time this department generates updates info about occurred disturbances.

In [8] was developed a prototype system, using RFID monitoring system and ZigBee wireless transmission as a close loop, to monitor the manufacturing process for a FMS.

In [9] is presented a new disturbance management system approach, based on ADACOR holonic control architecture [10].

2 System Structure

To monitoring the FMS system developed at the University of Oradea and presented in figure 2, our researchers have conceived and realized an off-line frame marker device for error troubleshooting.

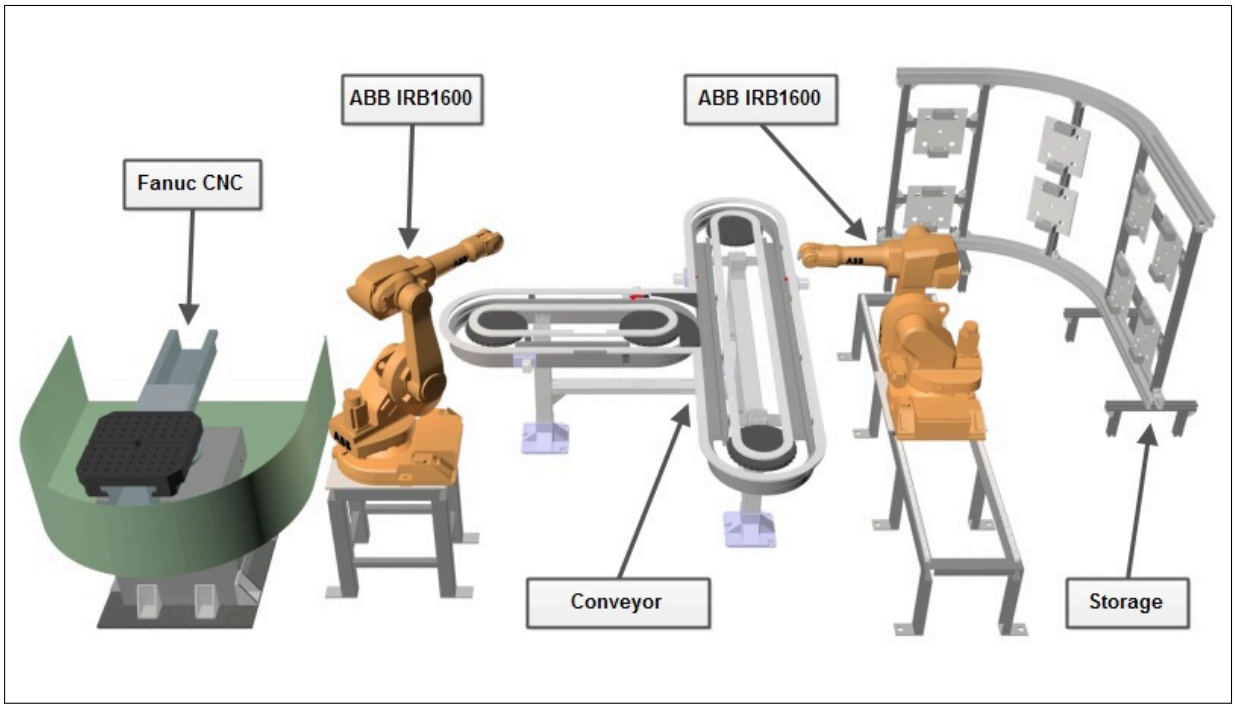

Figure 2: FMS structure

The main components of the FMS are: the 5-axis machine-tool TMA AL 550 equipped with Fanuc CNC, two ABB IRB 1600 robots with SCHUNK PNG 100 grippers, an ASRS (to storage pallet with work-piece, finite product and tools) and a conveyor.

3 Frame Maker Device

The starting point in using frame markers to detect errors in FMS is the ease of recognition of their patterns fiducial markers by Vuforia SDK Frame Marker software which can run on any smart phone. These fiducial markers (called frame markers) present a very predictable and specific pattern and are generated by Frame Marker Device (FMD) realized by authors.

The frame marker's ID, used to recognize the marker in its environment by the camera during run-time, is generated by FMD which has three zones as follows: a continuous outline black square, an area with light and dark blocks which follow the outline border and the last one - the inside area - a black square (figure 3). The position and arrangement of blocks from second zone are distinct, offering possibility to develop a computer vision algorithm for frame markers detection. The ID is encoded four times (on each edge of the frame) using a different base pattern of dark and light blocks. This redundancy increases the robustness of marker in detection and tracking.

To realise the code generator device of the FMD two major components were used::

- LED stripe with 36 LEDs individually addressable;

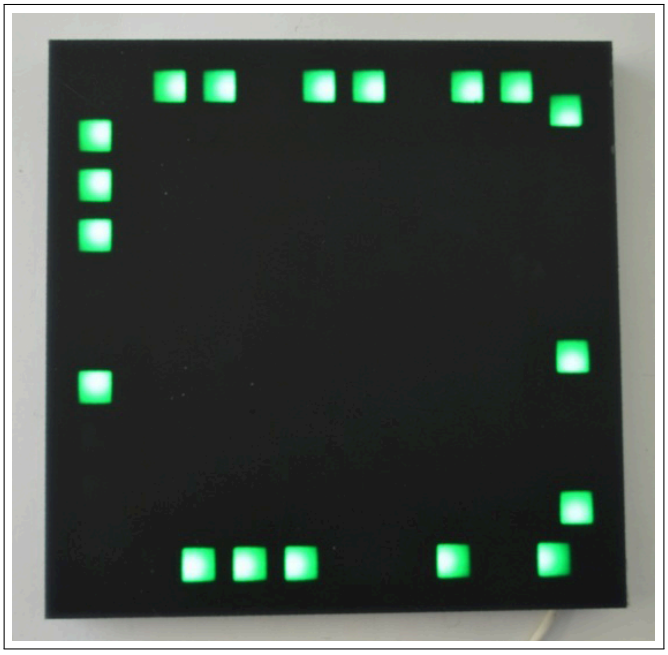

Figure 3: Frame Marker Device

- as signal generator for LED stripe was used an ATmega 1280 micro-controller .

Each LED is powered separately because of the high energy consumption. If all 36 LEDs are set to white colour the consume should be around 12 Watts (2.5 Amps and 5 Volts) Each LED is provided with an control chip (shift register) which uses one pin for input and one for output. From this reason the used protocol is very timing-specific and the micro-controller has to work with high repeatability (100nS timing precision) and at least on 8MHz. For each LED, the colour can be set with 8-bit PWM precision (24-bit colour / LED).

The ATmega 1280 micro-controller can be programmed with the Processing/Wiring open source programming language and the integrated development environment (IDE). The programming language is built on Java but uses a simplified syntax.

4 Structure of the off-line error troubleshooting system

The structure of the off-line error troubleshooting system is presented in figure 4.

The Frame Maker Device is connected through Factory Server to each FMS component's control module, and also receive information about the FMS's components status directly from the monitoring devices.

If any error appears in FMS (e.g. failure at any FMSs component, or at the FMS control modules or at the communications level) the error troubleshooting system will try to solve this problem searching in the error database for a possible solution. If the error can be manage automatically by the system it will be solve by FMS software. If not, the code generator maker of the frame marker device will generate and deliver an error code to the FMD and the operator will be notified about the need of troubleshooting the error through a visual and sound alarm.

The error ID can be read, from the frame maker device, using a portal device CCD camera, which should be directed toward the FMD (figure 5). The image acquired by CCD camera is decoded by Vuforia SDK to an error ID. On the portable device screen will appear an error message, with a brief description (which corresponds to that error ID figure 6).

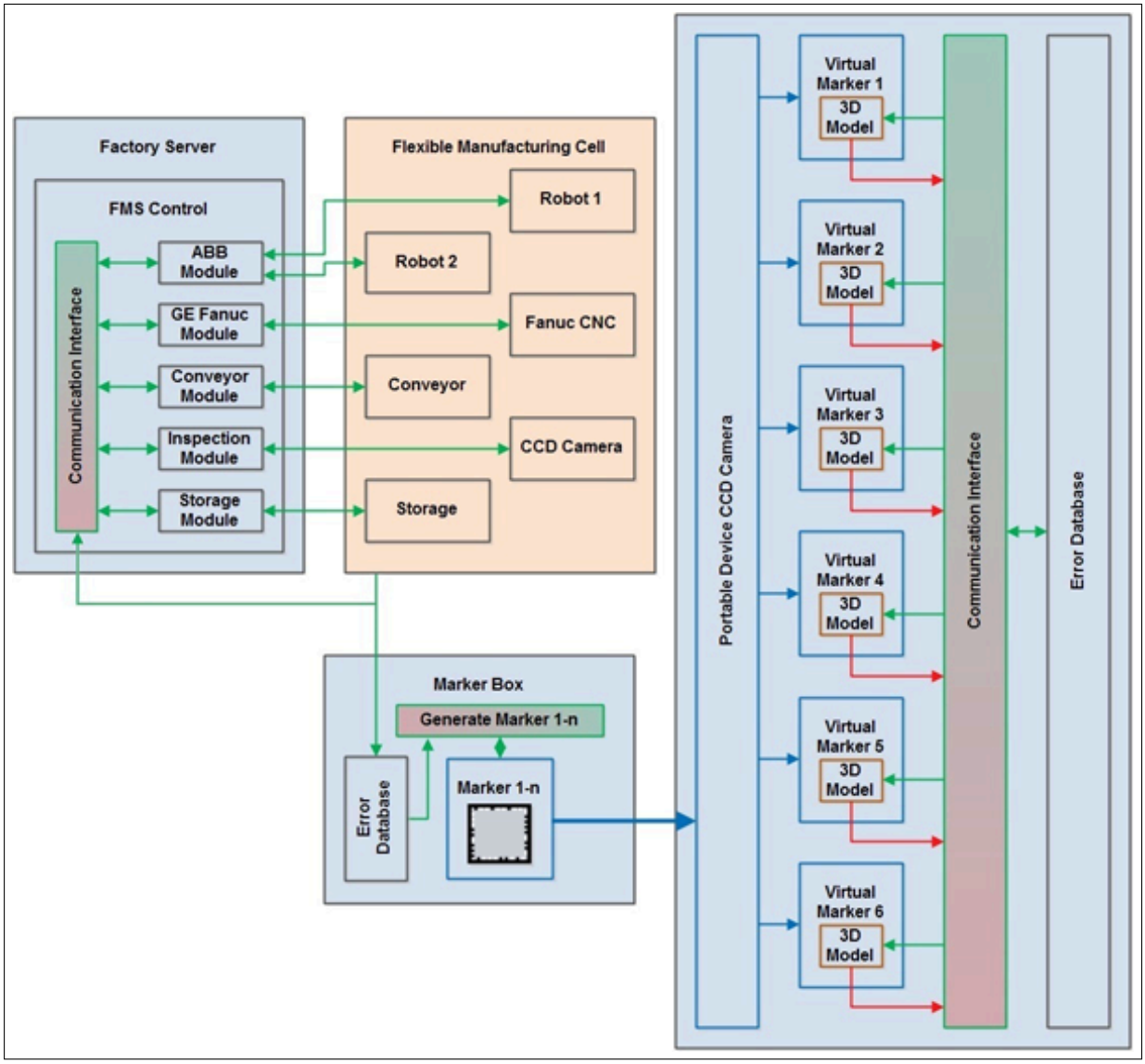

Figure 4: Structure of the off-line error troubleshooting system

Errors types for different cases of failures is presented in figure 7 (with red for ABB IRB robot, with blue for ASRS system, with purple for conveyor).

In some cases when the portable device screen is touched, detailed information of the error can be supplied, if exists.

After one error was successfully corrected, the operator should communicate the intervention via WiFi with FMS's Error Database.

Another application was also developed by authors: to check the functional status of FMS components by orienting the portable device towards the marker device; if a message on a green background appears on portable device screen, it means that the FMS component works properly; in case that a message on a purple background appears on screen, it means that the FMS component is off-line.

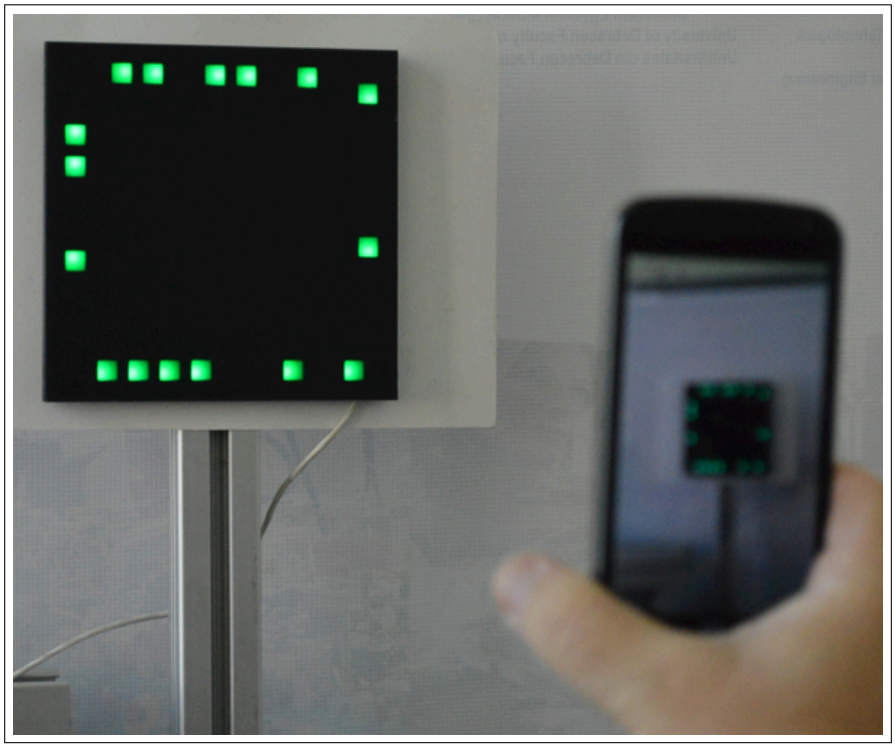

Figure 5: Image acquired by CCD camera

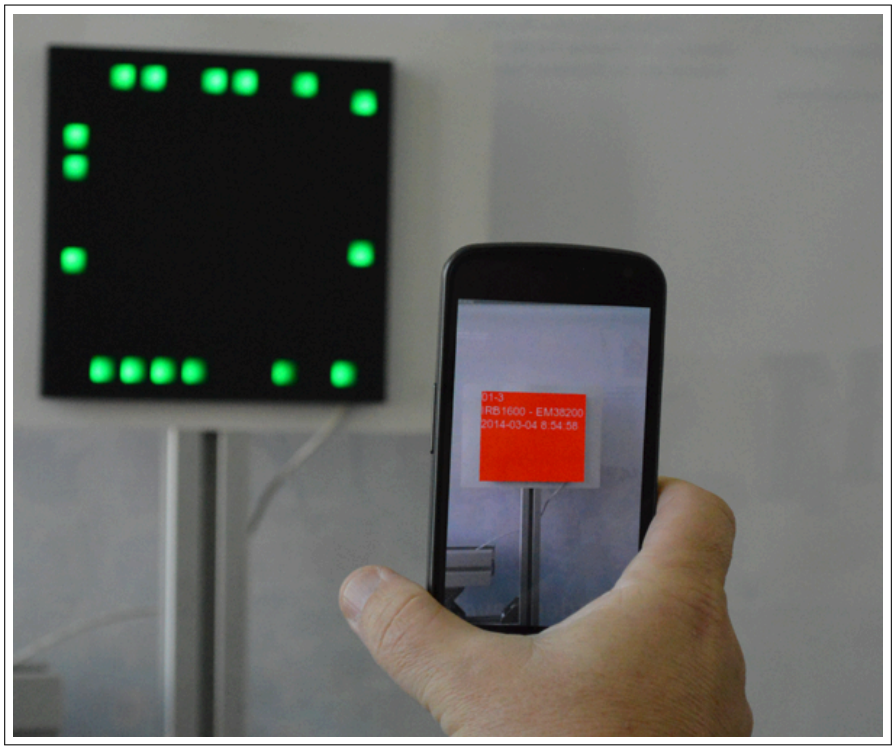

Figure 6: Error message

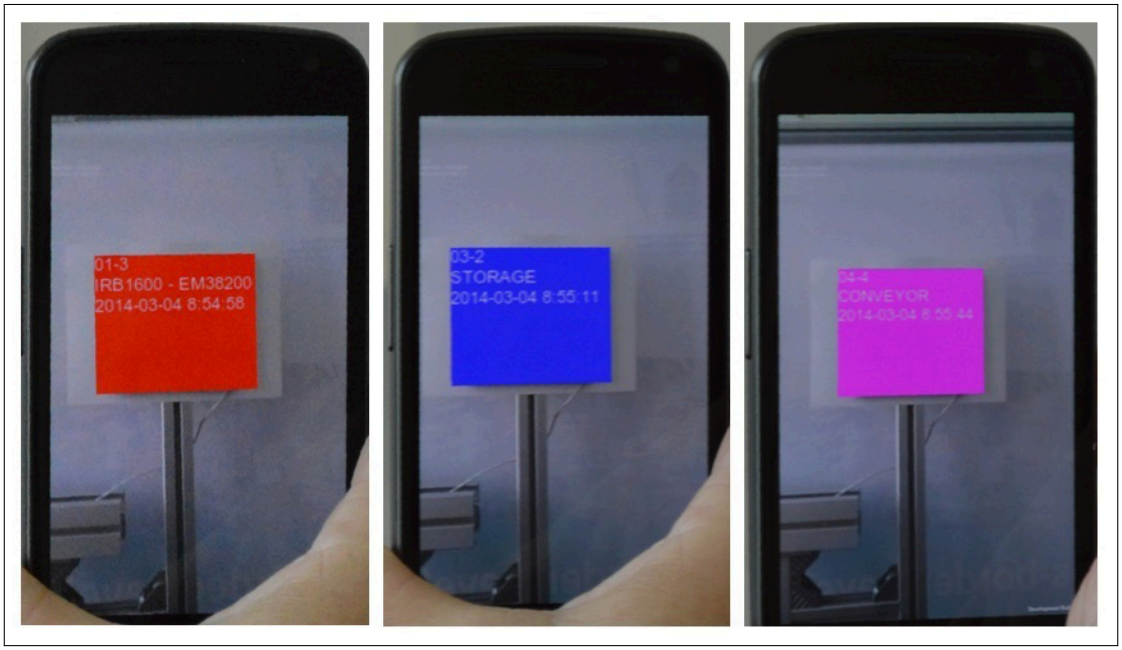

Figure 7: Errors types for different cases of failures

5 Conclusions and Future Works

The contribution of this paper is to propose an off-line version of the software framework using a frame marker device conceived by the authors, which can offer effectiveness control activities in the frame of a disturbance management system. The FMS components status is controlled by the software framework which transfers the information about the need of error troubleshooting from the FMS component to the operator, via a smartphone.

With the off-line error database we can create a more compact and network free error troubleshooting system. The only drawback of the system is the updates are not instant; they can be applied when the mobile system connects to the FMS control software when recharging.

The initial error database can be dynamically extended with new items corresponding to unpredictable errors developed during the manufacturing process.

Bibliography

[1] Csokmai,L.; Moldovan, O.; Tarca, I.; Tarca, R. (2013); Software Framework for Advanced Error Troubleshooting In Flexible Manufacturing System, *Applied Mechanics and Materials*, 397-400: 21-24.

[2] Borchelt, R. D., Thorson, J. (1997), Toward reusable hierarchical cell control software, *International Journal of Production Research*, 35(2):577-594.

[3] Kao, J.F., (1995), Optimal recovery strategies for manufacturing systems, *European Journal of Operational Research*, 80(2):252-263.

[4] Wu, H.J., (1999), Methodology of generating recovery procedures in a robotic cell, *Proceedings IEEE International Conference on Robotics and Automation*, 1:799-804.

[5] Toguyeni, A.K.A.; Craye, E.; Gentina, J.C. (1996); A framework to design a distributed diagnosis in FMS, *IEEE International Conference on Systems Man and Cybernetics*, 4:2774-2779.

[6] Bruccoleri, M.; Pasekb, Z.J.; Koren, Y. (2006); Operation management in reconfigurable manufacturing systems: Reconfiguration for error handling, *Int. J. Production Economics*, 100:87-100.

[7] Felea I, Dzitac S., Vesselenyi T., Dzitac I. (2014), Decision Support Model for Production Disturbance Estimation, *International Journal of Information Technology and Decision Making*, 13(3): 623-647.

[8] Qiang Ruan, Wensheng Xu, Gaoxiang Wang (2011); RFID and ZigBee Based Manufacturing Monitoring System, *2011 International Conference on Electric Information and Control Engineering (ICEICE)*, 1672-1675.

[9] Leito P. (2010); A holonic disturbance management architecture for flexible manufacturing systems, *International Journal of Production Research*, 49(5): 1269-1284.

[10] Leito, P., Restivo, F. (2006); ADACOR: A holonic architecture for agile and adaptive manufacturing control, *Computers in Industry*, 57 (2): 121-130.

[11] Bruccoleri, M., Renna, P., Perrone, G. (2005), Reconfiguration: a key to handle exceptions and performance deteriorations in manufacturing operations, *International Journal of Production Research*, 43(19):4125-4145.

[12] Bruccoleri, M. (2007), Reconfigurable control of robotized manufacturing cells, *Robotics and Computer-Integrated Manufacturing*, 23:94-106.

[13] Zhang X.L., Yan K., Ye J. ; Li J. (2012), A Remote Manufacturing Monitoring System Based on the Internet of Things, *Proceedings of 2012 2nd International Conference on Computer Science and Network Technology (ICCSNT 2012)*, 221-224.

[14] Dev Anand M., Selvaraj, T. Kumanan, S. (2012), Detection and Fault Tolerance Methods for Industrial Robot Manipulators Based on Hybrid Intelligent Approach, *Advances in Production Engineering and Management*, 7(4):225-236.

[15] Kumanan, S., Selvaraj, T.. Dev Anand, M., Janarthanan, J. (2008), Fault diagnosis system for a robot manipulator through neuro-fuzzy approach, *International Journal of Modelling, Identification and Control*, 3(2):181-192.

INTERNATIONAL JOURNAL OF COMPUTERS COMMUNICATIONS & CONTROL
ISSN 1841-9836, 10(1):38-48, February, 2015.

Intelligent Design Environment for Second-Order Positioning Systems

S. Dale, H. Silaghi, D. Zmaranda, U. Rohde

Sanda Dale, Helga Silaghi,
Doina Zmaranda*
University of Oradea
Romania, 410087 Oradea, Universitatii, 1
sdale@uoradea.ro, hsilaghi@uoradea.ro
*Corresponding author: dzmaranda@uoradea.ro

Ulrich Rohde
TUniversity of Technology Cottbus
Germany, 03048 Cottbus, Lipezker St. 47
ulrich.rohde@tu-cottbus.de

Abstract: From the designer perspective, in real-time applications as mechatronic systems - the control algorithm has to be easy to understand and to implement, easy to optimize and last but not least, to ensure the best possible behavior for the controlled system. The paper presents a design environment which provides the possibility to choose between a classical control algorithm (as state feedback stabilization represents) and a new approach (interpolative controllers) with the possibility to modify the designed parameters such as to obtain the optimum behavior for the controlled system. This opportunity is given through the inner structure and operating laws of the algorithm and exploited using genetic algorithm-based techniques. Interpolative-type controller category covers the controllers based on fuzzy, neural and pure interpolative algorithms, due to their common capability to make an approximate reasoning. The first ones, fuzzy and neural algorithms, are already well-known in the control area. A pure interpolative controller presumes to contain at least one block, placed no matter where in his structure, in which interpolation as mathematical operation to have place. The approach presented in the present paper uses this kind of blocks to reproduce and to optimize the behavior of an already existing controller (in this case the state feedback one) [1]. This type of controllers meets all the requirements stated at the beginning: they are easy to implement, easy to understand, they need reduced calculus time and gives notable results in specific cases. The above mentioned kind of controllers will be presented with all the necessary details in the paper. The design environment is presented as a collection of MATLAB functions, SIMULINK configurable schemes and a user interface. A case study ends the presentation with some experimental results obtained through a simulation for a specific second order positioning system.
Keywords: interpolative control algorithms, intelligent optimization, design environment, mechatronic positioning system.

1 Introduction

A mechatronic system is generally an electromechanical system equipped with sensors which detect the state of the environment, actuators which modify the state of the environment and a control system which controls the actuators based on the environment, as described by the sensors. Mechatronical systems are implemented in all kind of man-made machines as autonomous robots, industrial robots or flexible manufacturing cells.

In many mechatronical applications, the control functions are implemented through a microcontroller. If in the past microprocessors and microcontrollers have been used especially by the

electronic and automation engineers (due to the difficulties in design, programming, testing and usage and due to the fact that the amount of needed information for the applications was very large and the given degree of software and hardware integration), today the microcontroller can be used even by people that have minimum knowledge of electronics and programming. There are many brands that offers developing systems with integrated microcontrollers at good prices, well documented and with numerous applications in different fields. Some of them have an active policy in attracting the non-specialists in realization of applications with microcontrollers. The main advantage of such an evolution is the possibility to realize, in a relative easy way a sum of practical applications in various physical areas. In this context there isnt surprising the increasing amount of applications from the mechatronics field based on the usage of microcontrollers which implements various control techniques.

The actual approaching manner of such applications, focused on miniaturization, has stimulated the efforts in this direction. Nowadays, the microcontrollers have better and better performances (memory, speed etc). There is a need to continuous increase of the performances for those products, leading to a larger volume of software applications. Testing of the applications becomes more important. The usage of microcontrollers in mechatronical applications leads to the appearance of new directions of research in the field. Integrated systems based on microcontrollers are low cost solutions and have the advantage that can be used in applications where miniaturization (from the mass, volume, energy consumption point of view) is an important requirement. As a consequence, the researches on the implementation possibilities for control algorithms in applications from mechatronics as well as motion control, mini-robotics etc., constitutes a necessity. The main disadvantage of using the microcontroller in such applications (comparative with PLC's) its related to the potential difficulties in software development. In this context, development of performant control algorithms easy to use and to implement contributes to reduce and eventually eliminate this inconvenient: among them, some of those knew as intelligent control algorithms.

As it is well known, intelligent control is a class of control techniques, that use various AI computing approaches like Bayesian probability, approximate reasoning techniques based on expert knowledge or interpolative-type algorithms (as neural networks, fuzzy logic, pure interpolative algorithms), machine learning, evolutionary computation and genetic algorithms. In this branch of control engineering, the control techniques are extended beyond classical mathematical methods based on integral-differential calculus. Difficulties that appear in complex non-linear systems control with uncertain models can be eliminated by new approaches based on an operator experience. Hence, one way to develop control algorithms is to generate them based on expert knowledge. In that way, they are easier to understand for humans, and this can be considered as the second major requirement for the control algorithms used in mechatronic devices design. Intelligent control systems must treat information referring their own state and the environment state and that implies both heuristic and algorithmic programming methods. Intelligent control implies also a decisional strategy based on synthetic thesis from system theory, advanced mathematical modeling, computers and knowledge based linguistic methods, as in [2] and [7].

From both perspectives exposed above - which can be expressed as two major desiderates or requirements for the control algorithms implemented on microchips and designated to mechatronic devices there are a few categories of appropriate intelligent algorithms. Fuzzy and neural ones, due to their complexity, are not one of them. In [3] and [4] some comparative experimental studies was made from the implementation on microcontroller point of view, between PID, fuzzy and interpolative algorithms. The results allow to consider pure interpolative algorithms implemented as interpolative blocks and used in control structures as candidates for implementation on microcontrollers. One of the advantages of using such blocks are, mainly, based on simplifying the solutions (easier implementation and reduced calculus time, meaning the first requirement

is fulfilled) and the possibility to ensure for the control systems, in a relative easy way, some robustness properties [5]. In the same time, as in [4], [6] and [9], the controllers based on interpolation table, on the same form as in Drechsels RIP (Regelbasierte Interpolation) controllers introduced in [12], can be developed in much more situations than those based on linguistic rules. They can be conceived starting from solutions deducted in different ways, solutions that, finally, can be improved. From this perspective, interpolative algorithms meet the second requirement also, the possibility to be understood and designed by automation engineers or non-specialists with no loses from the control systems performances point of view.

The results achieved in this field in the last years authorise the answer at two major questions. Why an interpolative algorithm? Because these algorithms belong to the intelligent control techniques category, beeing one of the new-generation performant algorithms. On the other hand, due to the internal structure based on interpolation they are improvable, very simple to understand, use and implement, making them a good choice for the implementation on microcontrollers by specialist either non-specialist. In this way, the interpolative algorithms can present interes for the mechatronic applications field. Why a GA-based optimization technique? Because it seems to be very appropriate for optimizing the performances of the control structure with interpolative controllers, due to the fact that they represent themselves improvement methods based on natural and genetical mechanisms, which combine artificial surviving of best individuals with specific natural operators. Some procedural aspects of an intelligent design environment which combines interpolative control with GA-based optimization are presented in [1].

For the intelligibility of the presentation, in the second chapter interpolative algorithms will be presented from a large perspective, in a descriptive-conceptual manner. The functionality and the structure of the proposed design environment is described in the third chapter that ends with a case study made on a second order positioning system. Some relevant conclusions resume the presentation.

2 Design procedures for controllers with interpolative blocks optimized through GA-based algorithms

The controllers with interpolative blocks as introduced in [5] and [9] represents an alternative to the controllers obtained by various design procedures, that are replaced with controllers containing interpolation tables and algorithms and participate to the partial or integral control law elaboration. The idea of using interpolative blocks, named also table-type blocks its not a new one. They are frequently used in real time programs in order to reduce the calculus time in case of operating with multivariable complex functions. The interpolation technique is usual in robotic control systems.

The concept of controller with interpolative blocks brings as a new element the elaboration method of such a controller which can be implemented quite easy using digital techniques. These techniques allow the real time operation with complex tables. The concept maintains actual the design methods for the linear or non-linear control algorithms, whose results constitute the starting point for interpolative controller synthesis and at the same time improves their performances.

Those controllers are synthesized based on a very well known principle in the quality systems domain: continuous improvement of the activities flux of an already existing system, designated to ensure a specific quality function by which are expressed the system performances [10]. For the interpolative controllers this principle is translated as follows: to obtain, for a certain control system, a better controller than the initial one, designed through usual methods. The synthesis of an interpolation block (implemented by an interpolation table) is accomplished in two stages

(as in Figure 1):

- Primary synthesis stage necessits other two steps: initial control algorithm synthesis and interpolation table construction based on the command hyper-surface of the initial control algorithm
- Correction stage consists in one or more steps of on-line or off-line correction, operated on the interpolation table

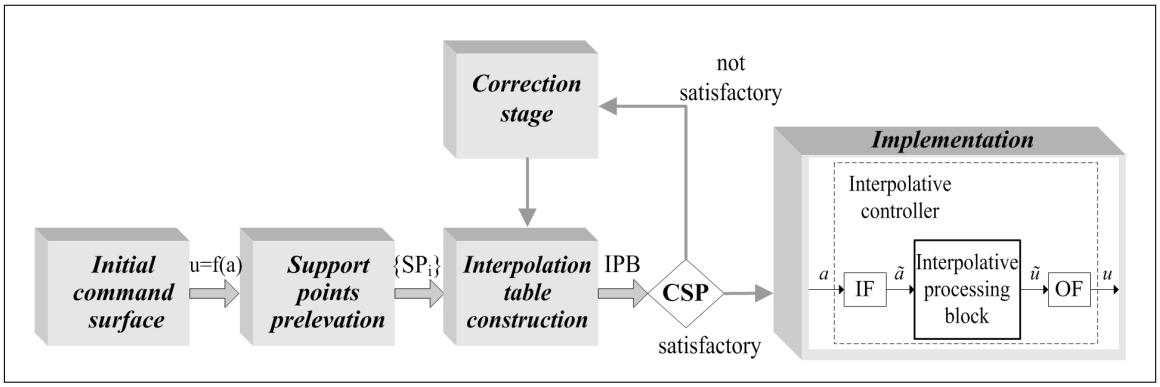

Figure 1: Interpolative controller synthesis

The interpolation table is determined through support points extraction from the initial controller hyper-surface. Support points set must be structurated as a Cartesian grid and has to cover all variations domain for the input variables. The support points ensemble has to embed, from a qualitative point of view, all the inflection points of the command hyper-surface. Support points generation is made point by point or based on an analytical function, when such a function is available. If the locations number on the table is too large, the support points extraction can be incomplete; the empty spaces will be filled by Shepard interpolation.

Once the interpolation table was obtained describing approximatively the behavior of the initial block it will replace the initial block, followed by a correction stage. The correction is realized by successive modifications operated on interpolation table with a specific aim: to improve the performance of the control system. The effective correction can be made by modification on the values in table locations and/or by granularity modification on the inputs and/or output and it is an iterative process.

At principle level, an interpolative controller contains an interpolative processing block (IPB), usually a non-dynamic non-linear block, implementing the relation in (1).

$$u = Int(a_1, ...a_n) \tag{1}$$

The input and output filters (IF and OF respectively) ensure together the controller dynamics and they adapt the inputs at the IPB and the outputs to the execution element connected after the controller. Control system performances (CSP) can be improved when an improvement criterion is chosen as in [10] or they can be optimized if an optimization, well defined criterion is considered, as in [6] and [8], where GA are used for a so-called *intelligent optimization.*

An IPB implementation is a digital one and its realized through n-dimensional interpolation tables, made in soft manner (programs capable to execute the operations corresponding to the association of table locations for input a and the calculus of command c based on an interpolation algorithm between the table values) or hard (using PLCs, microcontrollers or dSPACE modules). All implementation modalities offer the possibility of real-time operating.

Interpolative controller design has, starting from the correction stage, a heuristic character, mostly empirical. This fact represents in many cases an advantage: brings to the light the creative, innovative, intuitive side of the designer, without forcing him to manipulate a complex mathematical instrument, on models affected by uncertainties.

In the present paper the interpolative blocks will be synthesized through the method exposed above, as in [5] and [9], followed by off-line GA-based correction, as in [6] and [4]. GA-based techniques seems very appropriate in such cases due to the fact that GAs represent themselves improvement methods based on natural and genetic selection, compare and sorting mechanisms, which combine artificial surviving of best individuals with specific natural operators and form a searching mechanism, usable in various purposes.

For this kind of application optimization of an interpolation control table - a GA modifies a table population *Ti* which implements the control block for the interpolative structure (look-up table block). The starting point represents an initial set made from interpolation tables *Tinitial* capable to ensure command characteristics. During the synthesis operation the performances of the interpolative control systems are permanently evaluated by simulations made with the SIMULINK control schemes, for preset scenarios (eg. unit step response). A fitness function is used to provide a measure of performances related to the time requirements imposed to the control system. The adopted objectiv function induces the desired performances by using appropriate restrictions associated to the control system's response.

Through techniques which are specific to GA, at every generation are preserved a rising number of performant individuals, where the individual performance is associated with a rise in the system performance. At the time when the convergence criterion (CC) - consisting on minimization of the error between an imposed trajectory and the current trajectory of the system - is accomplished, the best individual is extracted and will be used in the effective implementation, being considered the optimal solution, regarded from the used criterion point of view. The entire process can be synthesized by the schema in Figure 2.

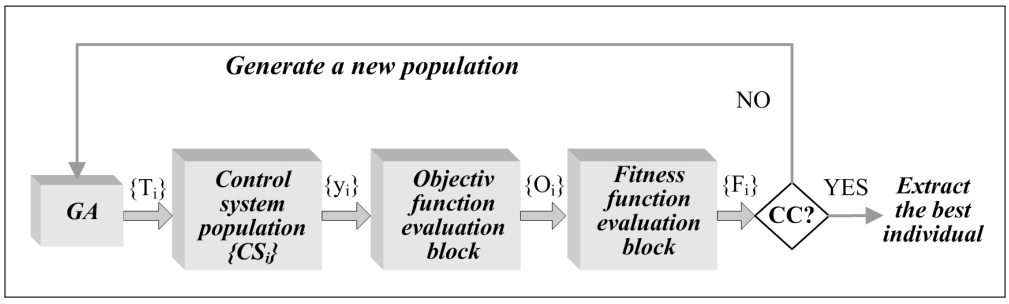

Figure 2: GA-based optimization

The main limitations of the interpolative controllers are represented by the fact that they cannot guarantee the robustness and stability for control structures during the operating regimes not provided (included) in their synthesis. This issue represents a common problem for all the systems with non-linear controllers [11].

3 Structure presentation of the intelligent design environment

The proposed design environment consists in a collection of MATLAB function and SIMULINK schemes managed through a user interface. SIMULINK schemes are configurable by user in order to correct and to justify some values or even to reconfigure some blocks if it is needed.

The environment addresses to second order positioning systems, as simple mechatronic ele-

ments, and offers the possibility to design an interpolative control structure in three stages: 1 - State feedback control structure design, 2 - Interpolative control structure design, 3 - Optimized GA-based interpolative structure design. Every stage, if the user considers it, can be viewed as a final and sufficient stage or it can be seen only as a step on a complex design issue, having as a final result the optimized interpolative structure. The functionality of the environment can be followed through the organigrame presented in Figure 3.

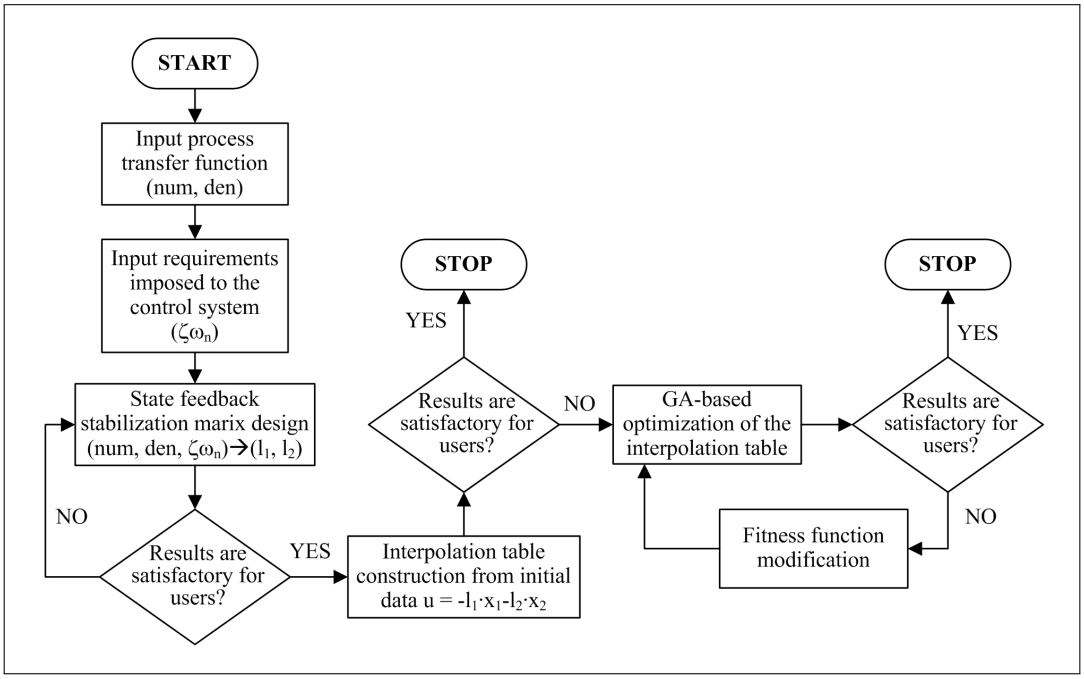

Figure 3: Intelligent design procedure

As depicted in the organigrame, the usage of the design environment presumes a sum of steps, described in detail in the following paragraphs.

3.1 Prelevation of process data

Transfer function of the positioning system and the requirements for the control systems, in terms of damp and rising time are introduced by the user. Based on that information, a preset SIMULINK scheme for the MM-ISI model of the second order system is updated.

3.2 Design of state feedback control structure

Consider the feedback state stabilization law with the folowing trajectory:

$$u(t) = L_c \cdot u_c + u_f(t) = L_c \cdot u_c - l_1 \cdot x_1(t) - l_2 \cdot x_2(t) \tag{2}$$

The calculus implied in state feedback control law design is implemented by a MATLAB function that use the Ackermann formula (for l_1 and l_2) and transmits the results to the SIMULINK scheme (see Figure 4) of the general state feedback control structure. With some manual corrections made on L_c parameter by trial-error efforts the results are evaluated through a step response.

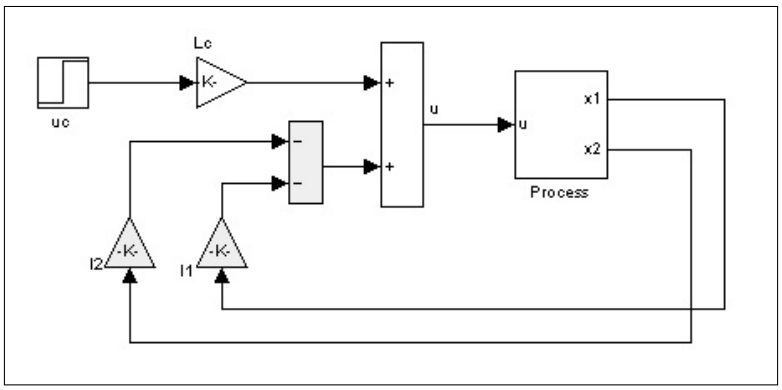

Figure 4: Initial state-feedback control loop (for second order processes)

3.3 Interpolative controller design

Based on initial data, significant information are extracted from the command characteristic of the state feedback control structure, as support points. A table which consists in a number of row and columns chosen by the user - with linguistic terms meaning for the variables $x_1(t)$ and $x_2(t)$ - is filled with the information organized as a Cartesian grid. The command law remains the same, only expressed through an interpolation table, as in Table 1.

Table 1: Interpolation table approximating the control law

x_1/x_2	$LT2_{-n}$	$LT2_{-n+1}$	....	$LT2_0$	....	$LT2_{n-1}$	$LT2_n$
$LT1_{-n}$ $LT1_{-n+1}$ ... $LT1_0$ ... $LT1_{n-1}$ $LT1_n$	$u_f = -l_1x_1 - l_2x_2$						

The interpolation table is implemented as a 2D look-up table in the SIMULINK scheme of the interpolative control structure, replacing the summation element with the irrespective coefficients (which implements the effective state feedback law) in control structure in Figure 4. The interpolative control structure can be seen in Figure 5. After some corrections made on L_c parameter and on table locations made by trial-error efforts the results are evaluated through a step response. If the user is satisfied with the results, the process can be stopped here.

3.4 Optimization of the interpolative control algorithm implemented as an interpolation table through GA-based techniques

As described in section 2 of the present paper, a GA is used to optimize the performances of the interpolative control structure, starting from a population of initial tables $\{Ti\}$ with the restriction: $Ti \in$ [-150% $\cdot$ $T_{initial}$ + 150% $\cdot$ $T_{initial}$], i.e. all the support values corresponding to the support points should not surpass, point by point, the Âą150% centered on the initial support values obtained at step 3 from the state feedback command surface. During the evolution of the algorithm (realized by MATLAB functions) the best individuals are stored as tables kept in especially created directories, out of which, in the end, one will replace the interpolation table $T_{initial}$. In this case, a target function was formed, by which was imposed that the system

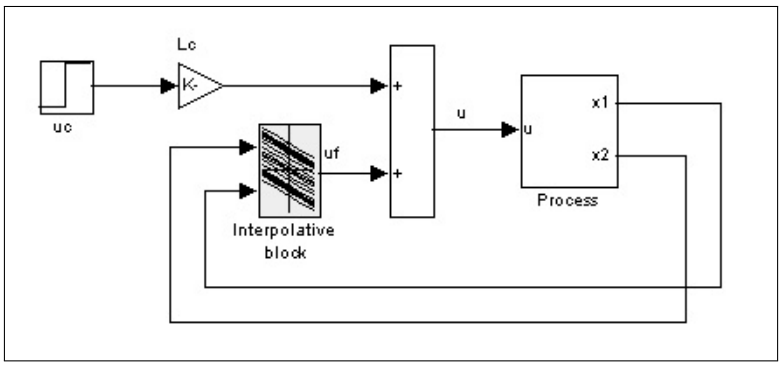

Figure 5: Interpolative control loop (for second order processes)

response to be ideal, meaning to be identical to the standard (unit step). From here appears the necessity of introducing the following criterion, which in fact is a minimizing one: the smaller the difference between ideal response and the tested system, the better the tested system will be.

$$Ji(T_i) = abs[\int_0^{+tmax} [y_i(t) - y_{ideal}]dt] \tag{3}$$

, where y_{ideal} is the standard. The genetic algorithm uses a fitness function that is a sum of conditions related to the error polarity, speed of the response, monotony a.s.o. The fitness function is implemented in MATLAB-SIMULINK, such that it allows the imposing of the above-mentioned conditions on the whole considered time, or only on certain intervals. At the end of the procedure, the results evaluation is made and if they are satisfactory to the user, the process stops here or. If the results are considered unsatisfactory, the fitness function implemented in the SIMULINK optimization scheme can be modified and the process can be resumed from the beginning of the 4th step.

The interpolation table considered as the best individual at step 3.3 will replace the look-up table in the interpolative control structure. With this action, the entire design process ends.

As it can be observed from the description above, the usage of the proposed design environment presumes that the user has some minimal knowledge about control systems and their performances evaluation (for reconfiguration of the schemes and parameters correction) without implying detailed knowledge regarding control system design. The user interface provides a friendly and easy communication and usage of the environment. A text containing instructions for the user is available, describing in detail minimum requirements, design steps, MATLAB functions and SIMULINK schemes involved in the designing process.

4 Case study: second order positioning system

As a study case a second order positioning system was chosen, given by the transfer function in (4) and the state-space model in (5).

$$H(s) = \frac{0.5}{s^2} \tag{4}$$

$$\begin{cases} x_1(t) = -0.5 \cdot x_2(t) \\ x_2(t) = -u(t) \\ y(t) = x_1(t) \end{cases} \tag{5}$$

The performance requirements for the control system were set at $\zeta = 0.9$ damping and $t_r = 0.8$ sec rising time. After the first step data introduction the design procedure begins with the first stage: state feedback stabilization structure design. For L matrix of the state controller calculus, the following results were provided: L=$[l_1\ l_2]$ = [0.8889 19.7531] . The value for the L_c coefficient of the trajectory following component was manually set on the SIMULINK scheme at $L_c = 39.5$. The simulation results of the step response in (6) are presented in Figure 6 (continuous line) and the command surface in Figure 7.

$$u_c(t) = 1,2 \cdot \sigma(t) \tag{6}$$

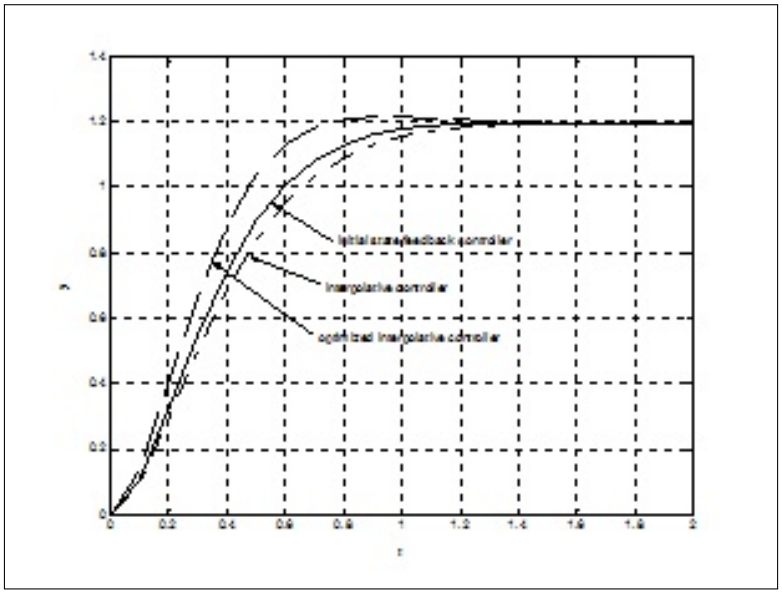

Figure 6: Step response

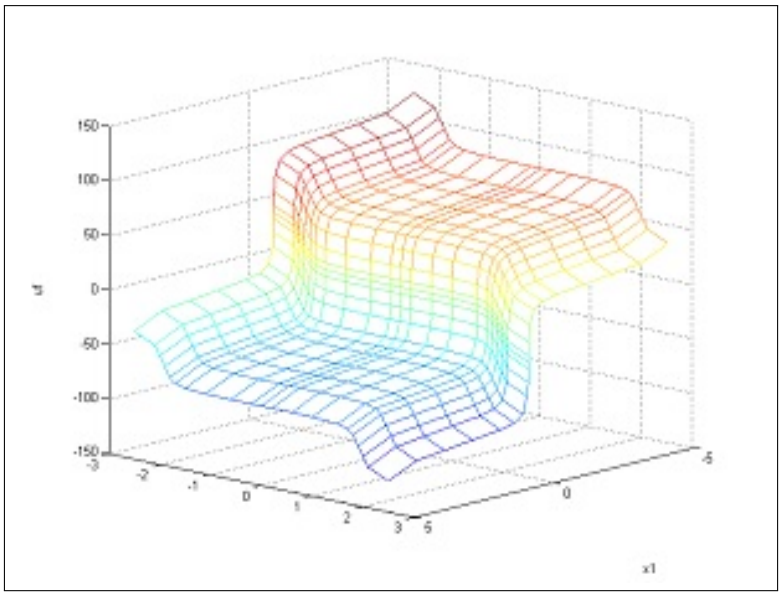

Figure 7: Command surface

In the next stage, significant support points from the command surface of the state feedback

controller were chosen and a 2D look-up table replaces the initial state feedback controller. The simulation results for the step response of the interpolative control system are depicted also in figure 6 (point-dashed line).

Finally, the GA-based optimization was applied to the interpolative controller. A simple GA was used tournament selection, simple crossing and uniform mutation. The size of the population was 50. The probability of crossing and mutation were considered 0.45 and 0.01 respectively, using the Grefenstelte references. The initial populations evolved for 50 generations. The simulation results for the step response of the optimized interpolative control system are depicted also in figure 6 (dashed line).

The results obtained through simulation for the three control structures, for the same scenario, present sensible differences between them, with a small advance for the optimized interpolative controller, that justify the demarche made by developing the design environment.

5 Conclusions and Future Works

An Intelligent design environment development can appear as a daring purpose. The result is a collection of MATLAB functions and SIMULINK schemes, unified by a quite explicit user interface that offers the possibility to design an optimized interpolative structure for any second order positioning system. The procedure is semi-automatic there are operations which have place in a non-transparent manner (they are done by the functions embeded in the environment without interacting with the user) and also other actions that involve the user in a more or less specialized interaction with the environment.

The design environment proposed in the article offers the possibility, for engineers and also for non-specialists, to design in three steps control systems for second order positioning systems and also to simulate their behavior. At the beginning, a state feedback stabilization algorithm can be designed which will constitute the base for a second step, the procedure to develop an interpolative structure. This one will be, in a third step, optimized through a GA-based technique. The environment consists in MATLAB functions, configurable SIMULINK schemes united by a user interface. The user can study and compare the behaviors of the system in each design stage, having hence the possibility to provide some conclusions related to feasibility, implementability and resources for the involved algorithms.

Some observations can be made based on the results obtained in previous work and on the study case from the present article: the combination interpolative algorithm plus GA-based optimization techniques offers easy to implement optimized controllers without loses in control performances and in specific cases even better from the performances point of view. Encouraged by the results obtained through simulation and dSPACE experiments, in future work, assisted with the proposed design environment, real-time applications on more complex systems will be developed.

Bibliography

[1] S. Dale, H. Silaghi, D. Zmaranda, U. Rohde (2014), Procedural Aspects Concerning Intelligent Design Environment for Real-Time Applications, *Abstracts of ICCCC Papers*, 5th International Conference on Computers, Communications & Control, ICCCC2014, Baile Felix, Romania, ISSN 1844-4334, 4:41.

[2] F.G. Filip (2012), A Decision-Making Perspective for Designing and Building Information Systems, *International Journal of Computers Communication & Control*, ISSN 1841-9836, 7(2):264-272.

[3] S. Dale, G. Gabor, C. Gyorodi, D. Zmaranda (2010), Interpolative Control Algorithm Applied on a 3D-Mechatronic System, *Proceedings of 4th International Workshop of Soft Computing Applications*, Arad, Romania, 2010, 229-233.

[4] A. Bara, S. Dale, T.Z. Nagy (2009), Comparative Real Time Experimental Study Case for Control Algorithms from the Implementation Point of View, *Proceedings of the 8th WSEAS International Conference on System Science and Simulation in Engineering (ICOSSSE09)*, Genova, Italy, 302-306.

[5] S. Dale, T.L. Dragomir (2009), Interpolative-type Control Solutions, *Studies in Computational Intelligence*, Berlin, Springer Verlag, 196: 169-203.

[6] S. Dale (2009), Interpolative Control for a d.c. Motor Drive with Genetic Algorithm-based Tuning, *Proceedings of EMES09 in Journal of Computer Science and Control Systems*, Oradea, 93-96.

[7] A. Bara (2006), An Algorithm for Fuzzy Relation Identification, *Proceedings IEEE-TTTC 2006*, Tome1, AQTR 2006, Cluj-Napoca, 96-102.

[8] T.L. Dragomir, E. Vladu, S. Dale (2003), Interpolative-type Controller Synthesis Using Genetic Algorithms, *Proceedings of CSCS14*, Bucuresti, 70-75.

[9] T.L. Dragomir, I. Silea, S. Nanu (2002), Control performances improving by interpolator controllers, *Proceedings of The 6th World Multiconference on Systemics, Cybernetics and Informatics*, July 14-18 2002 Orlando, Florida, 6: 208-213.

[10] G.F. Kamische, J.P.Brauer (1999), *Qualittsmanagement von A bis Z*, Hanser.

[11] M.M. Seron, et all (1997), *Fundamental limitation in filtering and control*, Springer-Verlag, 1997.

[12] D. Drechsel (1996), *Regelbasierte Interpolation und Fuzzy Control*, Vieweg, 1996.

INTERNATIONAL JOURNAL OF COMPUTERS COMMUNICATIONS & CONTROL
ISSN 1841-9836, 10(1):49-61, February, 2015.

Traffic Control Based on Contention Resolution in Optical Burst

E. Dhavarudha, C. Charoenlarpnopparut, S. Runggeratigul

Ekularn Dhavarudha*, Chalie Charoenlarpnopparut
School of Information, Computer, and Communication Technology
Sirindhorn International Institute of Technology,
Thammasat University - Rangsit Campus
P.O.Box 22, Pathum Thani 12121, Thailand
chalie@siit.tu.ac.th
*Corresponding author: ekularn.d@egat.co.th

Suwan Runggeratigul
Air Products Industry Co., Ltd.
84/8 Mu14 Petchakasem Rd., Nongkaem, Bangkok, 10160 Thailand
suwan@apithailand.com

Abstract: Traffic control based on contention resolution process (TCCR) is proposed in this study as a quality of service (QoS) mechanism to offer service level agreement (SLA) for optical burst switch (OBS). QoS of the high and the low priority classes are issued upon their SLA. The first one is defined for real-time application as Internet protocol television (IP TV) and voice over Internet protocol (VoIP) while the other is for soft real-time service as Internet protocol remote terminal unit (IP RTU) based on IEC 60870-5-101/104 protocol. A combination of burst aggregation (BA), extra offset time, and fiber delay line (FDL) is utilized in TCCR to offer absolute service differentiation QoS to the high priority class. The experiments show TCCR can offer the high priority class of its satisfied SLA for both blocking probability and delay. It also relatively improves the performances of the low priority class bounded in its SLA because TCCR does not force to drop this class. The performances of TCCR are compared with the other techniques such as no class isolation and bandwidth allocation processes. The comparisons show TCCR gives the best solution of the defined SLA which enhances OBS performances and properly differentiates class of services.
Keywords: optical burst switching, contention resolution, voice and video applications, telecontrol application, service level agreement.

1 Introduction

Optical burst switch (OBS) is all-optical switching which makes connection setup with out of band signaling. OBS is a promising and future proofed technology for backbone network since it can support tremendous bandwidth and eliminate drawbacks of optical-electrical-optical (OEO) switching. For illustration, OBS requires lower power consumption than OEO switching. Also, it is a protocol transparent and data rate independent which brings about network scalability. Nowadays, network bandwidth consumption has been dramatically increased due to the new Internet protocol (IP) applications such as high definition television, interactive games, triple plays, and so on. Although huge bandwidth is provided, consumer needs are not restrained. In order to maintain customers' requirement and network utilization, quality of service (QoS) is a crucial factor to support multiple classes of services. Implementing QoS to IP network can be categorized into two models which are the integrated service (Intserv) and the differentiated service (Diffserv) models. Intserv model is per-flow guaranteed QoS. On the Internet network there are plenty of information flows; therefore, Intserv requires enormous amount of state information for all flows causing unscalability to the network. On the other hand, Diffserv model

provides traffic differentiation based on per-hop QoS and specifies basic mechanisms on the way to treat packets. Difserv is defined into two services which are absolute service differentiation and relative service differentiation. The first one provides the worst case service to guarantee the application in each class whereas the second one relatively defines QoS based on other classes.

There are several research works in the area of OBS QoS based on contention resolution. Yoo et al. [1] propose offset time based QoS offering relative QoS for multi-class OBS. In this scheme, each class requires offset time differentiation for their class isolation. It also implements limited fiber delay line (FDL) for all classes to enhance each class's performance but not a purpose for class isolation. Although this scheme is effective to enhance network performances but it is not good enough to isolate multi-classes depending on their practical requirement. Therefore, more contention resolution mechanisms as burst aggregation (BA) or other techniques are required to provide the qualified QoS for multiple classes.

Shin and Yang [2] propose BA timer based scheme to isolate services between real-time and non real-time applications. In addition, Long et al. [3] also present BA adjustable timer and burst size based schemes to differentiate IP services into three classes. Both studies illustrate their schemes can offer relative QoS for the real-time application but they result in performance degradation of non real-time application. Moreover, both studies do not present FDL in OBS core nodes to reduce burst loss in the core network.

Cherif and Fatima [4] present a study of relative QoS oriented based on contention resolution by using FDL and deflection routing techniques. Although, they use various combinations of both schemes to reduce blocking probabilities of OBS; the major contribution come from FDL. The combinations of both schemes are also used as service differentiation of the two classes. However, the performances of the high classes are enhanced by those techniques but the low classes experience more contention due to the deflected bursts from the high class traffic. Moreover, lacking of BA and offset time schemes in this study yields limitation in OBS network enhancement. The study of absolute guaranteed QoS mechanism using BA timer and threshold based techniques is presented by Choi et al. [5]; however, this study is not proposed to isolate service differentiation classes. A proactive wavelength pre-emption technique supporting absolute QoS is proposed by Phuritatkul et al. [6] in order to guarantee QoS in absolute term for the high class. In contrast, the low class experiences more burst drops due to their wavelength preemption scheme. This scheme can guarantee the high class QoS but the mechanism is complex and it is not scalable for large networks.

Form the previous works, there are some openings based on providing QoS to OBS with contention resolution schemes. In this study, we focus on the study based on the two classes of traffic: the high and the low priority classes. We propose a new technique to offer absolute QoS with traffic control based on contention resolution (TCCR) applied to the high priority class. Because there is no electronic buffer device in OBS, the combination of the three contention resolution schemes in time domain as extra offset time, BA, and FDL are utilized in TCCR as QoS mechanisms to enhance OBS performances by reducing network blocking probabilities in both edge and core nodes. TCCR also gives distinctive service differentiation between the high and the low priority classes by allowing the high priority class to be controlled with the three mentioned mechanisms. Next, we compare our proposed schemes with an absolute QoS based on the IP QoS bandwidth allocation scheme [7] and also OBS implementing various contention resolution schemes with no class isolation.

We organize this research into four sections. The process of our proposed TCCR is demonstrated in the next section. Section 2 presents the proposed models and section 3 shows the experimental results. Lastly, the contribution is concluded in section 4.

2 Traffic Control Based on Contention Resolution Schemes

The technologies of optical memory and optical logic device are immature in this moment; therefore, contention resolution plays very important role for OBS to reduce burst losses in the network. Several contention resolution schemes are applied as QoS mechanisms. However, this paper highlights on the schemes in time domain which are extra offset time, BA, and FDL. Extra offset time scheme is a technique that allows extra timing accumulated to the original offset time for reducing burst losses in the network. BA electronically buffers several bursts at ingress node and smoothes burst traffics which lead to reduce network contention. FDL acts as a light buffer. It allows a contending burst traveling along optical fiber line in order to temporarily delay that burst before sending to an available channel. The detail of TCCR technique is illustrated in Fig.1. The high priority class (class 1) incoming traffics are queued in ingress buffers for BA

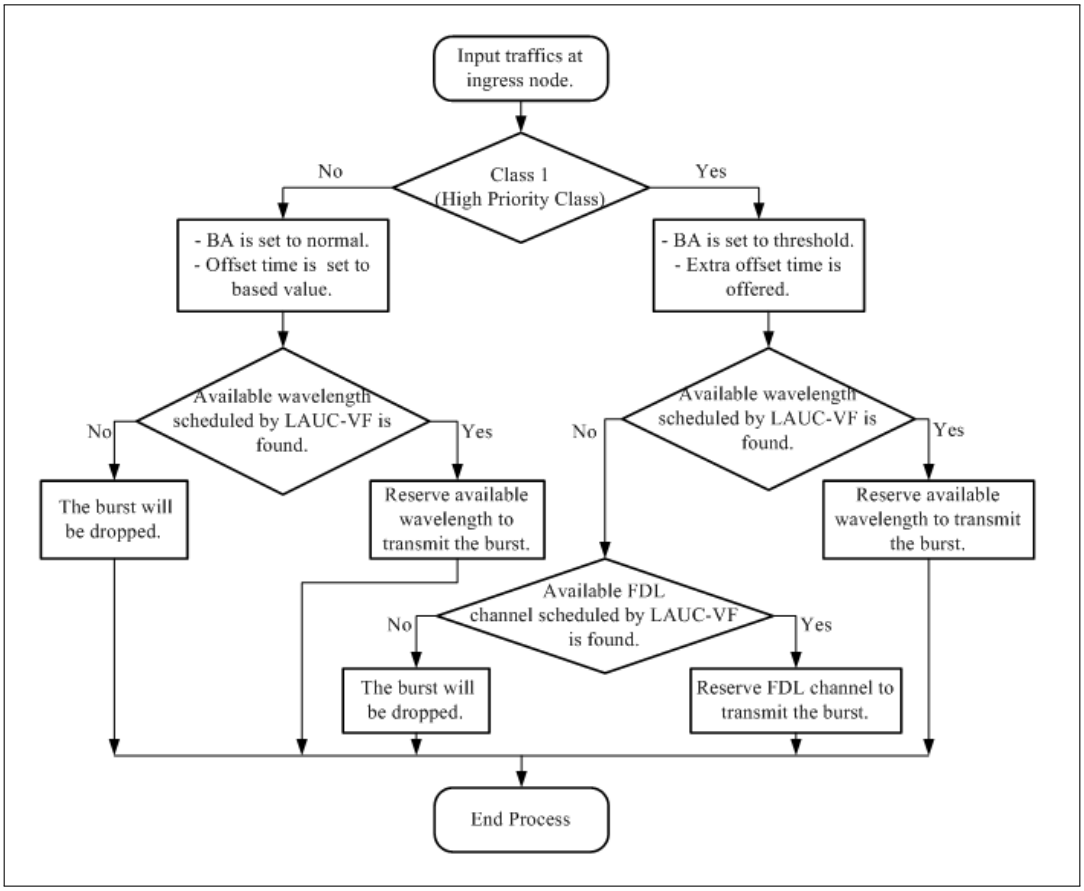

Figure 1: The process of TCCR

thresholds and their offset times are also set to be longer than their base values. In addition, at the intermediate nodes, if their control packets cannot reserve available channels for traffic class 1, then available FDL channels are selected. However, all mentioned contention resolution schemes are not provided for the low priority class (class 0) as to offer distinguished service differentiation between the two classes.

2.1 Quality of Service and Service Level Agreement

Service level agreement (SLA) is a key component of service level that service providers specify their performance agreement or QoS agreement to end users such as guaranteed delay

and guaranteed bandwidth. In this paper we consider the two agreements for the two classes according to their QoS as follows.

Firstly, traffic class 0 is IP remote terminal unit (IP RTU) traffic based on IEC 60870-5-101/104 protocol [8]. This application is IP based information of supervisory control and data acquisition (SCADA) system for remote controlling and monitoring utilized in utility business. This application is very important for power grids, water treatment, distribution utilities and other utilities such as oil and gas pipeline utilities. This application is one of smart grid applications provides data acquisitioning, remote monitoring and remote controlling of the equipment in power grids including power plants and substations. In addition, this kind of traffic becomes more important for remote sensor and remote control applications based on IP network. For QoS aspect, this application requires soft real-time communication. The latency requirement is less than 1 s [9]. As this service is a request and response communication and its nature is designed for client and server concept, one session consumes very low bandwidth. It is approximately 100 kbps for one session stream [9]. Because its nature is master/slave soft real-time communication, when the server detects communication failure the server is able to restart pooling and recollect the information from the client. Therefore, no requirement based on blocking probability is defined for this application. However, this application is critical for operational works; blocking probability of this case shall be as minimal as possible which shall not affect IP RTU operation and overall network performance.

Secondly, traffic class 1 is assumed to carry both IP television (IP TV) and voice over IP (VoIP) applications which are real-time services in IP networks. They require high QoS to offer satisfied quality to users. Normally high grade of service network for voice application requires blocking probability less than 0.03 [10]. For video traffic, it needs blocking probability below 0.02 [2] [10]. Therefore, setting SLA of traffic class 1 in term of blocking probability to 0.02 will give satisfied blocking agreement to both IP TV and VoIP applications.

The standardized recommendations recommend one way end-to-end packet delay for video service of 150 ms to 400 ms [2] [10] and for voice service of 150 ms [10]. However, these values are too high for backbone network; there are some extra delays causing from other elements such as queuing delay and processing delay produced by edge nodes. In addition, propagation delays shall be taken in to consideration for network designing. Therefore, the maximum SLA for delay aspect shall be set in order to allow the network can tolerate more compensation on other extra delay. As the Sprint IP backbone network and some OBS and public frame relay networks offer one way delay of 31 ms [11], we adopt this idea to our OBS network to offer 31 ms as a delay SLA of traffic class 1 which can support high QoS to both video and voice applications.

2.2 Traffic and Network Models

The network for our study is 14-node and 21-link NSFNET [12] of which the topology and link propagation delays in second (s) are illustrated in Fig.2. The traffic capacity for each node pair of this topology is generated from the uniform random distribution from [12]. These capacities are scaled in order to make the maximum value of t_{ij} (the traffic demand between node i and node j) to be 400 Gbps. The traffic of each pair is generated by Poisson process with arrival rates of t_{ij}/B. For our case, B is average burst length duration and we set to 8 Mbits [13]. For the class isolation experiments, we conduct simulations based on the two traffic scenarios. Scenario 1: the traffic demands of class 0 and class 1 are both 50 percent of t_{ij} . Scenario 2: the traffic demand for class 0 is 30 percent and 70 percent of overall traffic is for class 1. In both scenarios, the traffic is simulated varied by the demand coefficients (k) which is altered from 0 to 1 with each step of 0.1.

Based on our traffic and network models, we deploy routing and wavelength assignment

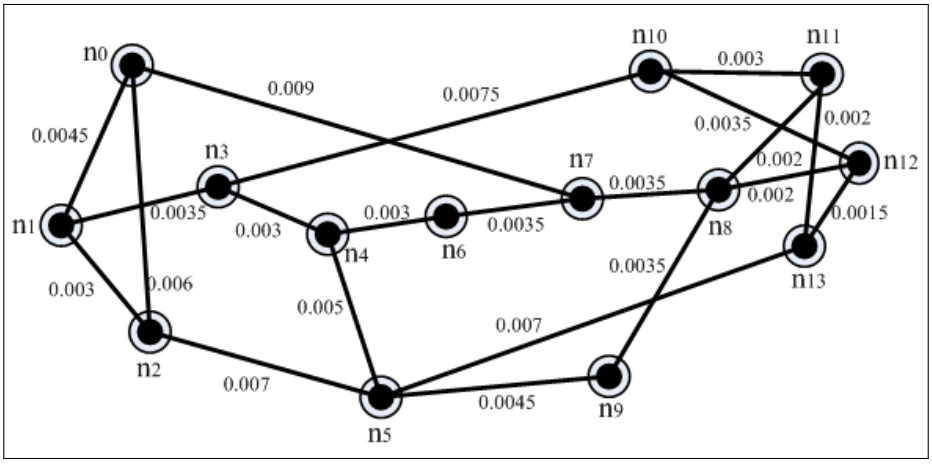

Figure 2: 14-node and 21-link NSFNET backbone network

(RWA) procedure from [14]. This network dimensioning procedure gives 98 wavelengths for unidirectional optical fiber cable as its optimum solution. We set 98 wavelengths for all data channels of this network and we assume the control channels' bandwidth is non-blocking. Each wavelength's capacity is 10 Gbps.

2.3 OBS Parameters and Simulation Models

Our OBS processing time is set to 80 μs [13] and the switching configuration time is 10 μs [5]. The simulation parameters are given as follows. BA is the first scheme of our consideration. BA is very important technique because it can smooth burst traffics and reduce burst losses which consequently improves link utilization [15]. Our BA is set by burst size threshold using burst length duration as it can ensure traffic smoothness and yields effectively reducing network blocking probability [15]. This scheme may introduce additional uncontrolled delay to the network when carrying light load traffics. However, this will not affect our study because we control the maximum delay in all experiments by controlling a target end-to-end delay below the offered SLA. Our basic burst size threshold is equal to the average burst length duration B in byte which is 1,000,000 bytes [13]. Each step of our BA experiment is varied with the multiple of B i.e. $1B$, $5B$ and etc. Our BA duration is quite high compared to the switching configuration time; therefore, link utilization of the network is not degraded [5]. In addition to BA, our based offset time of each route is the summation of total processing time of all nodes in that route and the switching configuration time [15]. Therefore, our extra offset time is varied incrementally from based offset time by multiple of b ($1b$, $2b$, and etc). We set $1b$ to the length of B in time domain (0.8 ms). Third, we implement FDL adopted from [16] to all nodes as illustrated in Fig.3. Each FDL parameter is varied with multiple of delay unit (D). $1D$ unit in time domain is set to 0.8 ms as same as $1b$ in the case of extra offset time scheme. The length of FDL is altered from $1D$ to $3D$. For $1D$ FDL in length, it takes a 160–km fiber cable; therefore, $3D$ is the maximum delay of 480–km fiber span implementing without an optical amplifier [17]. Lastly, all OBS experiments are simulated based on just enough time (JET) [18] and latest available unscheduled channel with void filling (LAUC–VF) scheduling [16] with shortest path routing. LAUC–VF requires full wavelength conversion; hence, our OBS is assumed full wavelength conversion [16].

From the literature reviews, Yoo et al. [1] propose the analytical formulations to calculate blocking probability of OBS implementing extra offset time and FDL schemes; however, they are applied for a single node analysis and do not give applicable results for the large network as our model. Du and Sbe [15] also propose analytical model to calculate network blocking probabilities

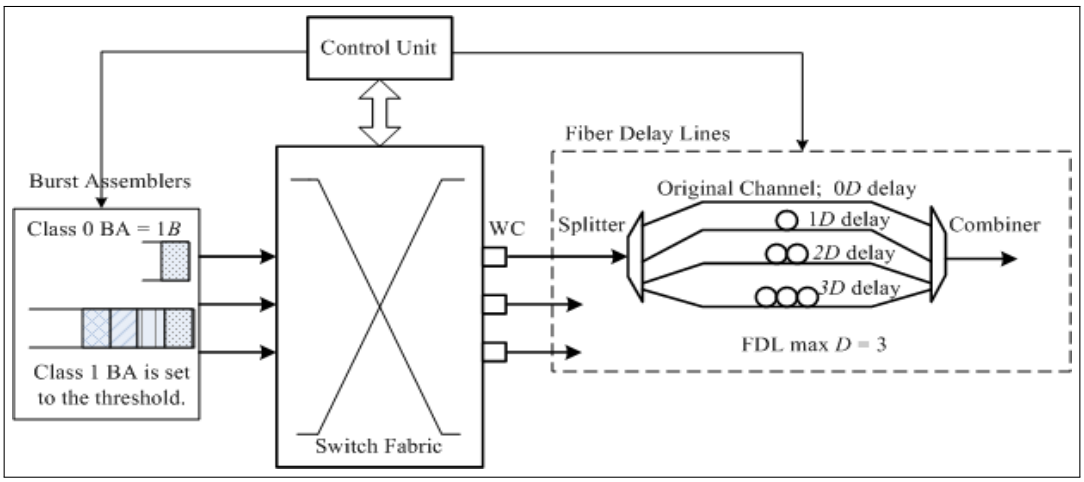

Figure 3: OBS node architecture

for BA in burst length threshold scheme. However, their analysis show variable BA thresholds do not affect network blocking probabilities because their offered loads remain the same. In contrast, they take a consideration of network blocking due to the congestion in control plane which is not applicable for our assumption. From those reasons, all experiments in this study are simulated based on ns-2 Simulator [19].

In order to demonstrate diverse aspects of our proposed TCCR process, we propose the performance comparisons between TCCR, bandwidth allocation service differentiation, and no class isolation models. In the bandwidth allocation service differentiation technique [7], the high priority class is offered dedicated network bandwidth just enough to give class 1 with its satisfied SLA. To illustrate, in scenario 1 both traffic class 0 and class 1 are 50 percent of total population in the network; however, 50 percent of all network bandwidth dedicated to traffic class 1 might not give the qualified blocking SLA to this class. Therefore, more reserved bandwidth for class 1 is required. However, the bandwidth given to traffic class 0 must be reduced because the bandwidth must be given to traffic class 1 to make it satisfied its SLA. Lastly, no class isolation model, all traffics are treated equally and their experiments are included based experiments (no contention resolution) and the simulations applied contention resolution schemes.

3 Experimental Results

Firstly, the repeated experiments are conducted for network provisioning to investigate the best parameters of our TCCR process with the results based on maximum load capacities ($k = 1$) shown in Table 1. The experiments are included the performances of class 1 applying each contention resolution scheme, the performances of class 0 with no contention resolution and also the simulations based on no class isolation comparable to those of service differentiation experiments are given.

Considering network condition in both scenarios 1 and 2, the studies in class isolation and no class isolation experiments show the same tendency. They can be concluded that BA is the best solution to reduce traffic class 1 blocking probabilities among the three techniques. FDL and extra offset time are the second and the third respectively. Although all schemes can enhance OBS performances, they introduce more delays to the network. If we compare the performances of traffic class 1 with the performances of traffic class 0, all contention resolution schemes can enhance the performances of traffic class 1 and it yields relatively reducing blocking probabilities

Table 1: Experimental results of one contention resolution schemes

Traffic Scenario 1									
Class	BA	Blocking Probability (x10^{-2})	Network Delay (ms)	Extra Offset Time	Blocking Probability (x10^{-2})	Network Delay (ms)	FDL	Blocking Probability (x10^{-2})	Network Delay (ms)
Class 0	-	2.76	10.72	-	3.00	10.35	-	2.95	10.35
Class 1	$5B$	2.38	14.46	$1b$	2.79	11.15	$1D$	2.77	10.36
Class 0	-	2.75	11.09	-	3.00	10.35	-	2.94	10.35
Class 1	$10B$	2.33	19.51	$2b$	2.78	11.95	$2D$	2.75	10.37
Class 0	-	2.71	11.46	-	3.00	10.35	-	2.93	10.35
Class 1	$15B$	2.16	24.55	$3b$	2.77	12.75	$3D$	2.74	10.37
Class 0	-	2.71	11.46	-	3.00	10.35	-	-	-
Class 1	$20B$	2.15	29.56	$4b$	2.77	13.55	-	-	-
Class 0	-	2.71	11.46	-	3.00	10.35	-	-	-
Class 1	$21B$	2.14	30.56	$5b$	2.77	15.15	-	-	-
Traffic Scenario 2									
Class	BA	Blocking Probability (x10^{-2})	Network Delay (ms)	Extra Offset Time	Blocking Probability (x10^{-2})	Network Delay (ms)	FDL	Blocking Probability (x10^{-2})	Network Delay (ms)
Class 0	-	2.82	10.42	-	3.00	10.35	-	2.97	10.35
Class 1	$5B$	2.44	14.21	$1b$	2.86	11.15	$1D$	2.84	10.36
Class 0	-	2.81	10.69	-	3.00	10.35	-	2.96	10.35
Class 1	$10B$	2.37	18.98	$2b$	2.85	11.95	$2D$	2.82	10.36
Class 0	-	2.80	11.06	-	3.00	10.35	-	2.95	10.35
Class 1	$15B$	2.34	23.73	$3b$	2.84	12.75	$3D$	2.81	10.37
Class 0	-	2.80	11.06	-	3.00	10.35	-	-	-
Class 1	$20B$	2.28	28.47	$4b$	2.84	13.55	-	-	-
Class 0	-	2.79	11.31	-	3.00	10.35	-	-	-
Class 1	$21B$	2.27	29.41	$5b$	2.84	14.35	-	-	-
Class 0	-	2.79	11.31	-	3.00	10.35	-	-	-
Class 1	22B	2.26	30.36	6b	2.84	15.15	-	-	-
No Class Isolation									
Class	BA	Blocking Probability (x10^{-2})	Network Delay (ms)	Extra Offset Time	Blocking Probability (x10^{-2})	Network Delay (ms)	FDL	Blocking Probability (x10^{-2})	Network Delay (ms)
-	-	3.01	10.35	-	3.01	10.35	-	3.01	10.35
	$5B$	2.52	13.57	$1b$	3.01	11.15	$1D$	2.89	10.35
	$10B$	2.45	17.58	$2b$	3.00	11.95	$2D$	2.87	10.35
	$15B$	2.43	21.58	$3b$	2.91	12.75	$3D$	2.86	10.36
	$20B$	2.42	25.58	$4b$	2.90	13.55	-	-	-
	$22B$	2.41	27.98	$5b$	2.90	14.35	-	-	-
	$23B$	2.41	28.77	$6b$	2.90	15.15	-	-	-

of traffic class 0 to be lower than the base experiment. In addition, the studies illustrate all contention resolution schemes can make traffic class 1 blocking probabilities lower than when we implement them to overall traffics with no class isolations. However, none of traffic class 0 blocking probability is better than those overall traffics treated by each contention resolution scheme. From the repeated experiments based on both class isolation and no class isolation, BA threshold is increased to the maximum limitation which produces the maximum delay just right under the defined delay SLA (31 ms). For the extra offset time scheme, the simulations are repeated with longer offset times until we hardly enhance network performance by this technique. In FDL, the experiments are simulated with the maximum limit of $3D$. Observing that the experiment based on the maximum threshold of each contention resolution is still unable to give class 1 satisfied blocking SLA (0.02); therefore, each two-combination of contention resolution schemes is conducted with the best solutions of which their delays are in boundaries learned from the experiences of one scheme implementations.

Table 2: Experimental results based on the combination of two contention resolution schemes

Traffic Scenario 1									
Class	BA	Blocking Probability (x10^{-2})	Network Delay (ms)	Extra Offset Time	Blocking Probability (x10^{-2})	Network Delay (ms)	FDL	Blocking Probability (x10^{-2})	Network Delay (ms)
Class 0	-	2.68	11.46	-	2.70	11.46	-	2.93	10.35
Class 1	$20B$ and $3D$	2.09	29.58	$20B$ and $3b$	2.14	31.06	$3b$ and $3D$	2.69	12.95
Traffic Scenario 2									
Class	BA	Blocking Probability (x10^{-2})	Network Delay (ms)	Extra Offset Time	Blocking Probability (x10^{-2})	Network Delay (ms)	FDL	Blocking Probability (x10^{-2})	Network Delay (ms)
Class 0	-	2.76	11.31	-	2.78	11.31	-	3.00	10.35
Class 1	$21B$ and $3D$	2.16	29.43	$21B$ and $3b$	2.25	30.72	$3b$ and $3D$	2.75	12.95
No Class Isolation									
Class	BA	Blocking Probability (x10^{-2})	Network Delay (ms)	Extra Offset Time	Blocking Probability (x10^{-2})	Network Delay (ms)	FDL	Blocking Probability (x10^{-2})	Network Delay (ms)
	-	3.01	10.35	-	3.01	10.35	-	3.01	10.35
	$22B$ and $3D$	2.28	28.10	$22B$ and $4b$	2.34	30.38	$4b$ and $3D$	2.83	13.56

To elaborate, the best solutions of traffic class 1, scenario 1 in the class isolation scheme of which their delays are in boundaries illustrated in Table 1 are the simulations applied with $21B$, $3b$, and $3D$ accordingly. For no class isolation, the best schemes are $23B$, $4b$, and $3D$. Thus, we conduct the experimentation of each two–combination scheme with those values. The results are presented in Table 2; however, these combinations are not able to make traffic class 1 meet blocking SLA requirement. However, there is some challenge for us to implement the third contention resolution scheme because there is some vacancy for extra delays. Therefore, the combination of the three contention resolution schemes based on TCCR is further conducted.

The parameters of the best results for all three schemes from Table 2 are selected for TCCR process. Their illustrations will be compared with the bandwidth allocation service differentiation technique (denoted BS). They are also compared with the experiments of no class isolation models (denoted No Class) which are the based experiment and the experiment applied contention resolution schemes. All mentioned simulations are conducted in both traffic scenario 1 (denoted

S1) and scenario 2 (denoted S2).

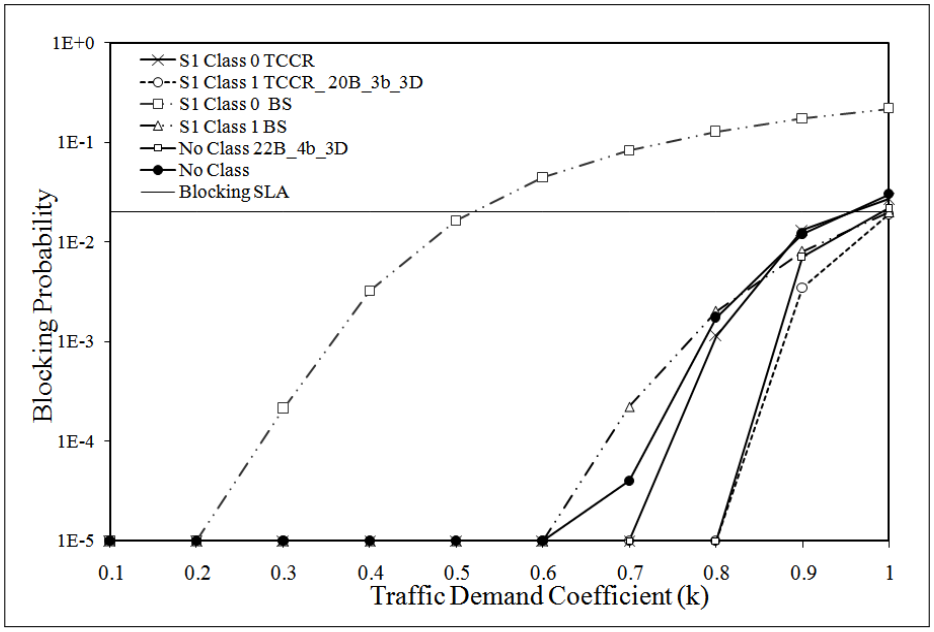

Figure 4: Average network blocking probabilities of TCCR, BS, and No Class for scenario 1

From the results illustrated in Table 2, traffic class 1 of scenario 1, the best solution is given by the combination of $20B$ and $3D$; however, this implementation is not be able to give satisfied blocking probability to traffic class 1. Therefore, the best solution of extra offset time scheme ($3b$) is combined to those two schemes in TCCR. As a result, TCCR with $20B$, $3b$, and $3D$ gives the most remarkable performance to this network as it can reduce blocking probability of the traffic class 1 under its SLA as illustrated in Fig.4. In addition, Fig.5 expresses the delay aspect of the results in Fig.4. The experiments show TCCR can very well improve services differentiation and class isolation between class 1 and class 0. Moreover, TCCR also indirectly improves blocking probability of traffic class 0 because the mechanism of TCCR does not make a decision to drop the low priority class but it selects various mechanisms to enhance the performance of the high priority class by utilizing network bandwidth, smoothing burst traffic and providing FDL channels for contending busts in the core network. Thus, more network resource can service traffic class 0 which leads to reduce this class's blocking probability. For BS, in order to give satisfied blocking SLA to traffic class 1, from the repeated experiments reffering to scenario 1, the simulations show it requires bandwidth of 57.70 percent of overall resource. Meanwhile the bandwidth of traffic class 0 is reduced to 42.30 percent. If we compare blocking probabilities of traffic class 1 between BS and TCCR processes, they have comparable performances at the maximum load capacity ($k = 1$). However, TCCR contributes better blocking probabilities than BS for all traffic capacities below that of $k = 1$. Moreover, blocking probability of traffic class 0 in TCCR process is very much better than in BS process. Also blocking probabilities of traffic class 0 in BS are higher than the base experiment because they are treated with very low amount of network bandwidth sharing.

Considering no class isolation with the three contention resolution schemes, it can enhance overall network performance. Form the experiences in Table 2, the combination of $22B$, $3D$ and, $4b$ is selected as they are the best solutions for this case. However, it cannot make overall network blocking SLA of class 1 within the limits. The repeated simulations with larger size of BA threshold and longer extra offset time are conducted to reduce blocking probability in this case but they introduce more delay beyond our delay limitation. Although traffic class 0

in TCCR process has little higher blocking probability than that of no class isolation deployed with the three contention resolution schemes, its blocking probability is acceptable. In contrast, blocking probability of traffic class 0 in BS process is quite high compared to no class isolation.

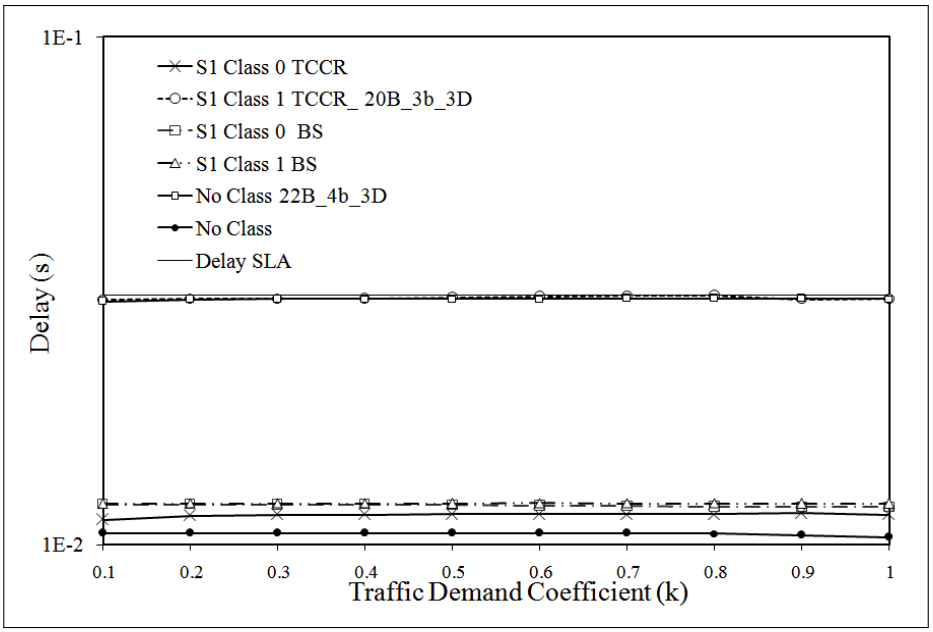

Figure 5: Average network delays of TCCR, BS, and No Class for scenario 1

In addition to the discussion of blocking performances, considering the delay aspect refering to Fig.5, traffic class 1 of both TCCR process and no class isolation with contention resolution experience highest average network delays but they are still under their delay SLA requirement. All extra delays are produced by the three contention resolution schemes. However, all traffic class 0 and class 1 in BS process including traffic class 0 of TCCR undertake very low delays because they are not deployed contention resolution scheme.

Fig.6 and Fig.7 illustrate the experiments of traffic scenario 2 based on the same experiments as scenario 1. In this scenario TCCR requires $21B$, $3b$, and $3D$ to give class1 satisfied blocking SLA. For BS, traffic class 1 requires 78.18 percent for the given class 1 blocking SLA which reduces offered bandwidth of traffic class 0 to 21.82 percent. In addition, the implementation of $22B$, $4b$, and $3D$ in no class isolation process is not able to give class 1 traffic with its satisfied blocking SLA. Also, traffic class 1 of TCCR process for scenario 2 has slightly higher blocking probability than in scenario 1 because of more traffic intensity but the results emphasize the same tendency conclusions as in scenario 1.

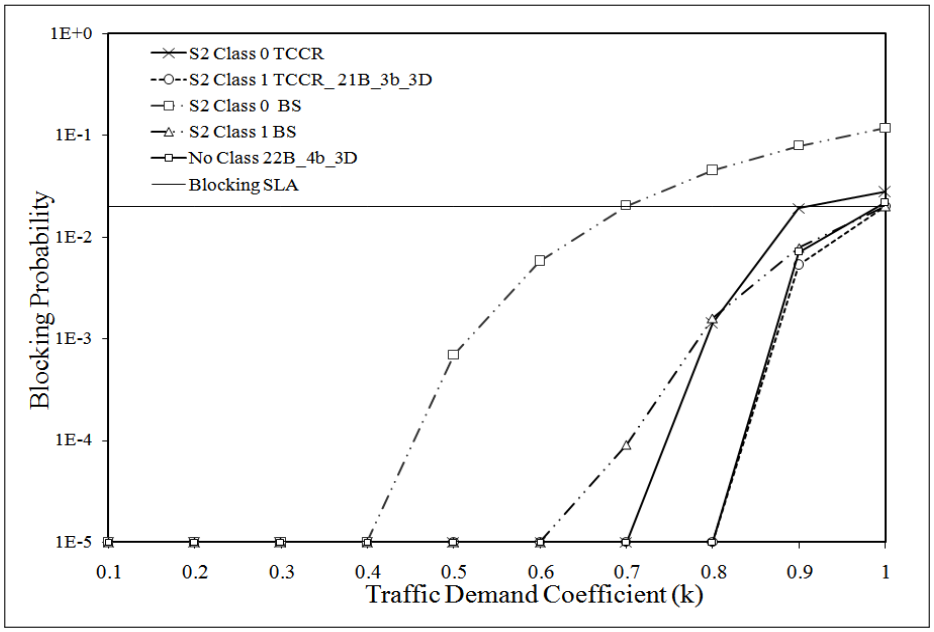

Figure 6: Average network blocking probabilities of TCCR, BS, and No Class for scenario 2

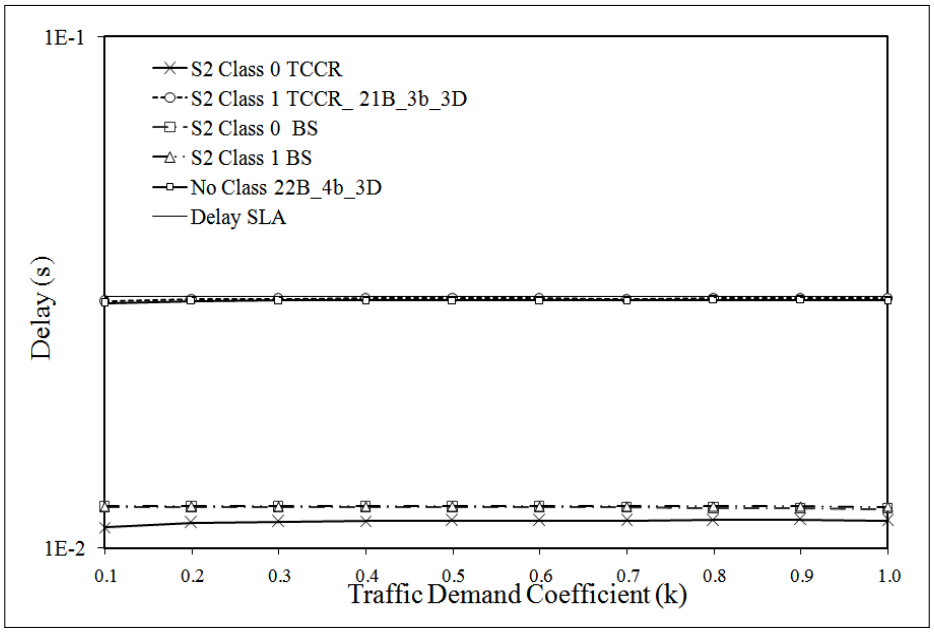

Figure 7: Average network delays of TCCR, BS, and No Class for scenario 2

4 Conclusions

This study proposes TCCR process which is a class isolation and service differentiation mechanism utilizing the three contention resolution schemes as BA, FDL, and extra offset time to control the performance of the high class traffic. This process can control the performance of this class very well by offering its satisfied SLA in both senses of network blocking probability and average network delay. In contrast, the illustrations of no class isolation deploying the three contention resolution schemes show they cannot offer the satisfied blocking SLA for the traffic in high class. In addition, BS process can give the traffic in high class satisfied its blocking SLA but this scheme results in very high blocking probability of the low class traffic. In summary, our OBS models require TCCR process to isolate the two classes and also differentiate their treatment according to their QoS. TCCR process can enhance the high class performance without dropping the low class packets; therefore, it yields indirect improvement of the low class traffic blocking probability which is also very well carried within its satisfied SLA. TCCR process can perform as an efficient QoS mechanism based on contention resolution and it can also give proper class isolation and service differentiation to both classes.

Bibliography

[1] Yoo, M. et al (2000); QoS Performance of Optical Burst Switching in IP over WDM Networks, *IEEE Journal of Selected Areas in Communications*, ISSN 0733-8716, 18(10):2062-2071.

[2] Shin, H.; Yang, F. (2007); ATCB: A QoS Guarantee Mechanism in the Optical Burst Switching Internet Backbone, *Proceedings of TENCON 2007 Conference*, Taipei, TW, ISBN 978-1-4244-1272-3, 1-4.

[3] Long, K. et al (2003); A New Framework and Burst Assembly for IP DiffServ over Optical Burst Switching Networks, *Proceedings of IEEE Global Telecommunications Conference (GLOBECOM '03)*, San Francisco, CA, USA, 3159-3164.

[4] Cherif, M.; Fatima, SGE. (2007); QoS Oriented Contention Resolution Technique for Optical Burst Switching Networks, *Proceedings of 9th International Conference on Telecommunications (ConTel 2007)*, Zagreb, HR, 81-88.

[5] Choi, JY. et al (2005); Dimension Burst Assembly Process in Optical Burst Switching, *IEICE TRANSACTIONS on Communications*, ISSN 0916-8516, E88-B(10):3855-3863.

[6] Phuritatkul, J. et al (2007); Proactive Wavelength Pre-Emption for Supporting Absolute QoS in Optical-Burst-Switched Networks, *Journal of Lightwave Technology*, ISSN 0733-8724, 25(5):1130-1137.

[7] Vegesna, S. (2011); IP Quality of Service, *Cisco Press*, USA, 69-103.

[8] IEC TC 57 (1990); IEC 60870-5-x Telecontrol equipment and systems - Part 5: Transmission protocols, *IEC Geneva*.

[9] Vaishnav, R. et al (2008); Using Public Mobile Phone Networks for Distribution Automation, *Power and Energy Society General Meeting - Conversion and Delivery of Electrical Energy in the 21st Century (IEEE 2008)*, Pittsburgh, PA, ISBN 978-1-4244-1905-0, 1-5.

[10] James, JH. et al (2004); Implementation VoIP a Voice Transmission Performance Progress Report, *IEEE Communications Magazine*, 42(7):36-41.

[11] Jeong, H. et al (2008); An Adaptive Loss-Aware Flow Control Scheme for Delay-Sensitive Applications in OBS Networks, *IEICE TRANSACTIONS on Communications*, ISSN 0916-8516, E91-B(7):2152-2159.

[12] Ramaswami, R.; Sivarajan, KN. (1996); Design of Logical Topology for Wavelength-routed Optical Networks, *IEEE Journal of Selected Areas in Communications*, 14(5):840-851.

[13] Kamiyama, N. (2004); Comparison of All-Optical Architectures for Backbone Networks, *IEICE TRANSACTIONS on Communications*, ISSN 0916-8516, E87-B(10):2877-2885.

[14] Schupke, DA.; Sellier, D. (2001); Lightpath Configuration of Transparent and Static WDM Networks for IP Traffic, *Proceedings of IEEE International Conference on Communications (ICC 2001)*, 2:494-498.

[15] Du, P.; Sbe, S. (2007); Traffic Analysis and Traffic-Smooth Burst Assembly Methods for the Optical burst Switching Network, *IEICE TRANSACTIONS on Communications*, ISSN 0916-8516, E90-B(7):1620-1630.

[16] Xiong, Y et al (2000), Control Architecture in Optical Burst-Switched WDM Networks, *IEEE Journal of Selected Areas in Communications*, 18(10):1838-1851.

[17] Simons, JM. (2006); Network in Realistic All-optical Backbone Networks, *IEEE Communications Magazine*, 44(11):88-94.

[18] Yoo, M.; Qiao, C. (1997); Just-Enough-Time (JET): a High Speed Protocol for Bursty Traffic in Optical Networks, *Proceedings of Vertical-Cavity Lasers, Technologies for a Global Information Infrastructure, WDM Components Technology, Advanced Semiconductor Lasers and Applications, Gallium Nitride Materials, Processing, and Devi*, Montreal, QC, CA, 26-27.

[19] DAWN Networking Research Labs (2006), The Network Simulator - ns-2 at September 15th 2006 http://www.isi.edu/nsnam/ns/.

INTERNATIONAL JOURNAL OF COMPUTERS COMMUNICATIONS & CONTROL
ISSN 1841-9836, 10(1):62-69, February, 2015.

Application of the Analysis of Self-similar Teletraffic with Long-range Dependence (LRD) at the Network Layer Level

G. Millán, G. Lefranc

Ginno Millán
Universidad Católica del Norte
Escuela de Ingeniería, Larrondo #1281, Coquimbo - Chile
gmillan@ucn.cl

Gastón Lefranc*
Pontificia Universidad Católica de Valparaíso
Escuela de Ingeniería Eléctrica, Avda. Brasil #2147, Valparaíso - Chile
*Corresponding author: glefranc@ucv.cl

Abstract: In a previous paper it was proposed, and theoretically confirmed, that analysis of self-similar traffic flows with long-range dependence may be restricted to the network layer. In this paper this novel concept is applied to the study of traffic recorded in an IEEE 802.3u network environment with the aim of proving its validity as a simple and efficient tool for high speed computer network traffic flow analysis.
Keywords: Long-range-dependence, network layer, traffic models, self-similar process.

1 Introduction

It is interesting to reflect on the idea that a purely random process is no more than a theoretical concept, but it is much more interesting to do so considering that no series is yet known whose characteristics correspond exactly to those of such processes. Likewise, it is of interest to explain that a given behavioral evolutionary singularity is widely attributable to two stationary stochastic processes without considering their origins, scope and implications.

To clarify the above two assertions, [1] made an exhaustive background review that includes research proposals and their results as well as the mathematical foundations underlying all of them. However, a basic idea remains unfinished: if all the arguments given do nothing more than highlight the benefits and advantages of the parsimonious modeling of traffic flow in current high speed network environments, then why is there dissent on its use?, and even more important yet, why do all the results deal with self-similarity as ubiquitous not only on the time scales, a fact that is certainly not put in doubt, but also with respect to the set of circumstances attributable to its origin?

With the purpose of answering these questions, that same paper states and then gives the foundation for the validity of the following working hypothesis: *"It is completely feasible to restrict the evolution of a statistically self-similar process to a well defined application setting without altering its nature and its more important properties, in that way highlighting the validity of its postulates and giving greater plausibility to its physical interpretation"*, clarifying that the plausibility refers to the action of conferring an admissible, and therefore worth considering, character to one or various parameters that compose an analytical model whose interpretations are not only mathematical idealizations, and that the theoretical proof of that hypothesis is based essentially on the proposal of Ryu and Lowen [2], which consists in making a distinction between the self-similarity observed at the application level and the self-similarity observed at the network level, but with the substantial difference of not considering any particular traffic model as in the case of the authors, in which the proposal is developed to support the analysis of the results obtained from using the fractal point process (FPP) model proposed in [3], to carry

out the characterization of traffic flow in high speed networks. It should be specified that the original proposal of Ryu and Lowen consists in establishing a difference based on the OSI level at which is found the source that gives origin to the traffic flows in which self-similarity is seen, and therefore explains its origin. In this way the authors conclude that it is more adequate to refer to application level fractal traffic and network level fractal traffic instead of encompassing under fractal traffic a whole range of dissimilar behaviors that find explanations precisely in the internal processes inherent to each of those levels. It is therefore clear that this division of fractal traffic into those two subcategories addresses effectively the profound differences that exist in the design as well as in the control processes of actual high speed networks at those levels.

Concretely, the application level self-similar traffic (fractal) has its origin in a source that exhibits self-similarity over a wide range of time and frequency scales without any interactions with the network. In other words, self-similarity is inherent to the source, while network level self-similar traffic (fractal), in contrast, exhibits self-similarity over a wide range of time and frequency scales as a result of numerous interactions with the network. An example of application level self-similar traffic source is the VBR video sequence of [4], while all the applications based on TCP of [5]-[8] are examples of network level self-similar traffic sources. It should be stated that actually the behavior of an application level traffic source can be affected by the network conditions, depending on the functionalities of the low level protocols used. This effect is insignificant, however, compared to what happens with a network level traffic source, such as an FTP client, under identical conditions, where the ratio of output to input data flow depends directly and critically on the conditions of the network and can largely be considered independent of the size of the files [9]. Also, application level self-similar traffic can be managed in the context of the resource assignment admission control subjected to service quality guarantees, since it is independent of the network conditions through which it is sent.

This paper presents an experimental application that validates the hypothesis of [1]. Considering a real network scenario implemented under IEEE standard 802.3u, traffic capture experiments are performed and then analyzed, restricting the results according to the precepts presented above as well as in [1]. This paper is therefore centered on showing the validity of the analysis of restricted self-similar traffic at the network layer level as a simple and efficient tool to study the behavior of traffic flow in present day high speed computer networks.

2 Traffic Measurements

2.1 Description of the network environment

Figure 1 is a diagram of the topology of the implemented experimental network scenario. It is a LAN IEEE 802.3u environment that has the following main operational characteristics:

- Ten workstations that uninterruptedly request an on-demand video service from the video server equipment provided for it. Both the client equipment as well as the server make use of the VLC Media Player application for that purpose. Continuous reproduction is achieved by predefining a video program in the server equipment. The ten stations keep an XML file with the page index of the web server. The state of the page index updating is consulted randomly by each of the stations with the purpose of always having the latest version of the file.

  The network monitoring equipment (tagged "Sniffer" in Figure 1) makes use of the Ethereal application to perform the traffic packet capture.

- The Internet access functions for the purpose of updating both the operating systems and the antivirus applications are enabled and automated in all the network's equipment.

2.2 Work Methodology

The procedure to carry out the experiment consists of the following steps:

- Program the algorithms to estimate the values and study the behavior of the Hurst parameter, of the variance-time (V-T), rescaled adjusted range or the R/S statistic, and spectral density analyses. All the programs were developed over MATLAB because of their availability. Verify the correct operation of the programmed algorithms. To perform this operation, use is made of the traffic sample normalized series of [5], BC-pAug89.TL, available for downloading in [10], and the values obtained are then compared with those reported in the literature by the authors.

  Capture traffic from the experimental network shown in Figure 1. It should be pointed out that the duration of each of the traffic capture periods is governed only by a criterion of availability of storage capacity in the Sniffer equipment, trying to capture the largest possible number of samples to face a possible decision scenario based on a figure of merit coming from the bias versus variance relation.

- Using the capabilities of the Ethereal application the filtering of the captured packets is carried out in such a way as to create time series of data that contain the length of the packets and the arrival times of each of them. These series are then stored in flat text files.

- Apply the V-T, R/S, and periodgram analyses over the data series previously specified.

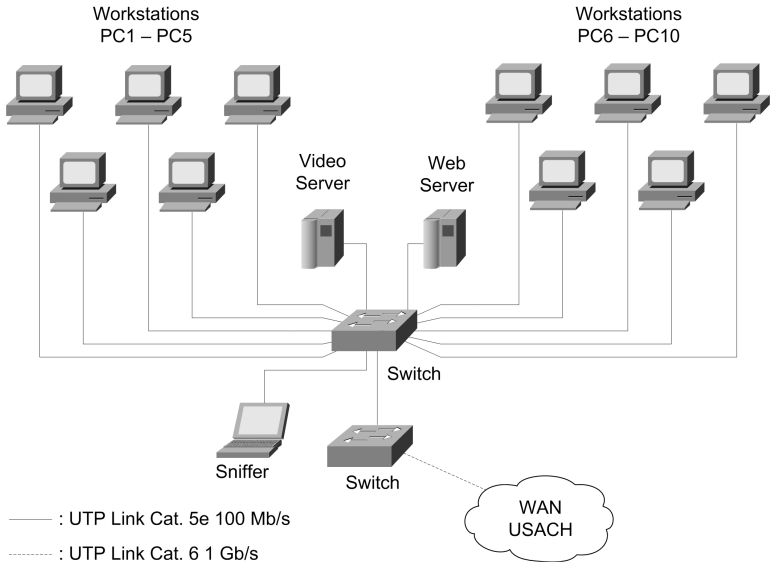

Figure 1: Experimental network connections

2.3 Simulations

Table 1 shows the detail of the captured Ethernet frames. In that respect the following aspects must be considered:

- The temporal resolution of the arrival times that are recorded by the Sniffer equipment is set in microseconds. This resolution is delivered as default measurement by the Ethereal application. The existence of time fluctuations that are not considered as those due to the latency of the circuits of the equipment's network card and those due to the code

processing time by the equipment is suggested. However, and in spite of the great impact that both can get to have on the finally recorded times, the option is taken to consider them anomalies belonging to the data processing systems, and they are therefore part of their behaviors.

The individual captures present a time resolution of 6 μs, which is the average recorded value.

- The data sets Trace-1 to Trace-4 contain the data of the time series representative of each capture process. In this respect, each series is composed of an ordered list of pairs of data: the arrival time of the packet, recorded according to the above considerations in floating point format with six positions, and the size of the captured Ethernet packet, which records the length of Ethernet data. The recorded value does not include the following fields: preamble, address of origin, destination address, length, and CRC or verification sequence. It must be recalled that the Ethernet protocol forces the frames to have a size with a minimum of 64 bytes and a maximum of 1518 bytes, so the recorded values are within that interval, with the 1518 bytes value as that recorded mostly in all the capture processes.
- 99.9% of the Ethernet PDUs are encapsulated in IP datagrams.
- With the purpose of testing the algorithms programmed for each method, whose mathematical expressions are given by (1)-(3), the analysis sequence begins using the series BC-pAug89.TL, from Figure 2, with the V-T, R/S and periodgram analyses, from left to right, respectively. Then, and in the same order, the analyses for each of the four data sets are shown.

Table 1: Qualitative description of the traffic capture sets

Measurement Period		**Data Set**	**Number of Packets**
November 2010	Total: 32 h		2118505
Start of Trace:	First Period:	Trace-1	918896
Nov. 29, 06:00 am	(06:00 am - 12:00 am)		
End of Trace:	Second Period:	Trace-2	1199609
Nov. 30, 08:00 pm	(08:00 am - 08:00 pm)		
December 2010	Total: 38 h		6096937
Start of Trace:	First Period:	Trace-3	1338789
Dec. 1, 08:00 am	(08:00 am - 08:00 pm)		
End of Trace:	Second Period:	Trace-4	4758148
Dec. 2, 10:00 pm	(12:00 am - 10:00 pm)		

$$\mathrm{Var}[X^{(m)}] \sim m^{-\beta},\ 0 < \beta < 1,\ H = 1 - \beta/2 \tag{1}$$

$$\frac{R(n)}{S(n)} = \frac{1}{S(n)}[\max(0, W_1, ..., W_n) - \min(0, W_1, ..., W_n)], \quad W_k = \sum_{i=1}^{k} X_i - k\bar{X}(n) \tag{2}$$

$$f(\lambda) \sim \lambda^{1-2H}, \quad \text{when } \lambda \to \infty \tag{3}$$

3 Discussion of Results

Table 2 summarizes the results obtained. It shows that the value of H for the BC-pAug89.TL data series using variance-time and R/S analyses is correct with respect to the value determined

by the authors, $H = 0.9$ using the R/S graphic method. It is also verified that all the values of H found for each of the experimental series (Trace-1, Trace-2, Trace-3, and Trace-4) are within the interval of interest $1/2 < H < 1$, which certainly implies an asymptotic behavior of the self-correlation function given by $r(k) \sim \ H(2H-1)k^{2H-2}$, when $k \to \infty$ [11], which ensures that these series present a hyperbolic type drop in the tails of their distributions, thereby reinforcing a behavior different from a typically exponential one.

Clearly, the central limit theorem reinforces the previous condition by considering that the self-covariance function of these processes in the interval $1/2 < H < 1$, depends on the value of the H in the approximate form $\gamma(k) \sim \ Ck^{2H-2}$, when $k \to \infty$, with C < 0 [12].

The presence of long-range time dependence is seen from $r(k) = r^m(k)$, $\forall k \geq 1$, $\forall m \geq 1$ [13], a fact that is evidenced from the linear type behavior of the relation subjacent between different levels of aggregation with respect to the variance, which becomes evident from the V-T graph analysis of the Figures 3, 4, 5, and 6.

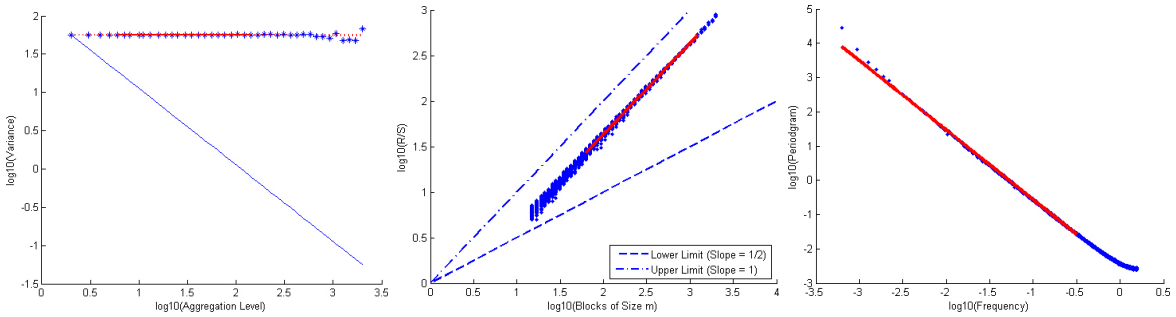

Figure 2: V-T, R/S, and periodgram for BC-pAug89.TL trace. $H = 0.9000$, $H = 0.8991$, and $H = 0.7681$

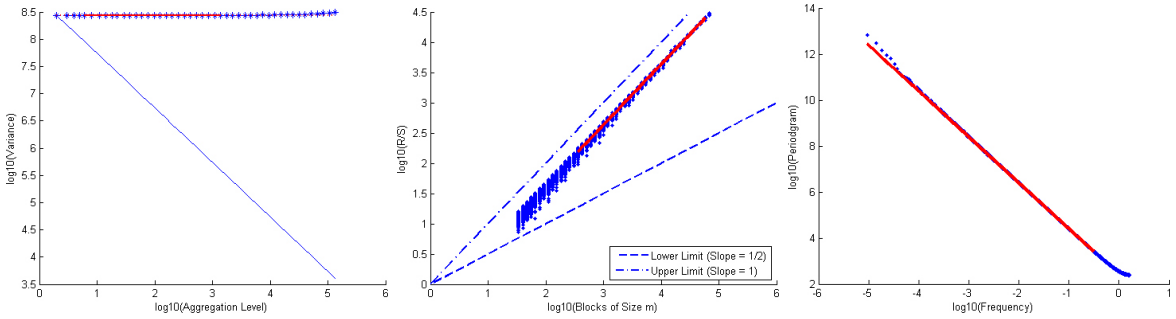

Figure 3: V-T, R/S, and periodgram for Trace-1. $H = 0.8999$, $H = 0.8986$, and $H = 0.7680$

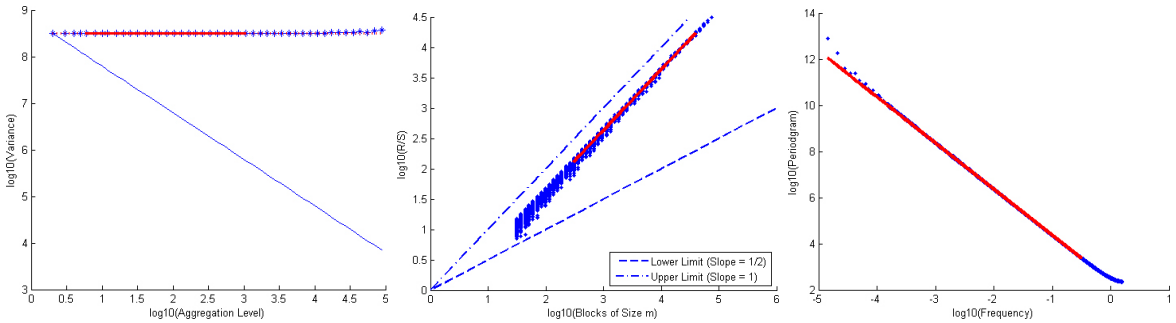

Figure 4: V-T, R/S, and periodgram for Trace-2. $H = 0.8999$, $H = 0.8982$, and $H = 0.7678$

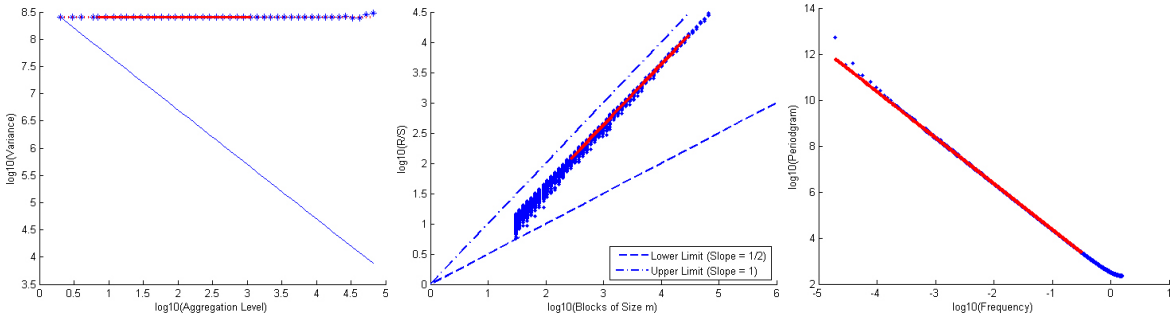

Figure 5: V-T, R/S, and periodgram for Trace-3. $H = 0.8999$, $H = 0.8985$, and $H = 0.7677$

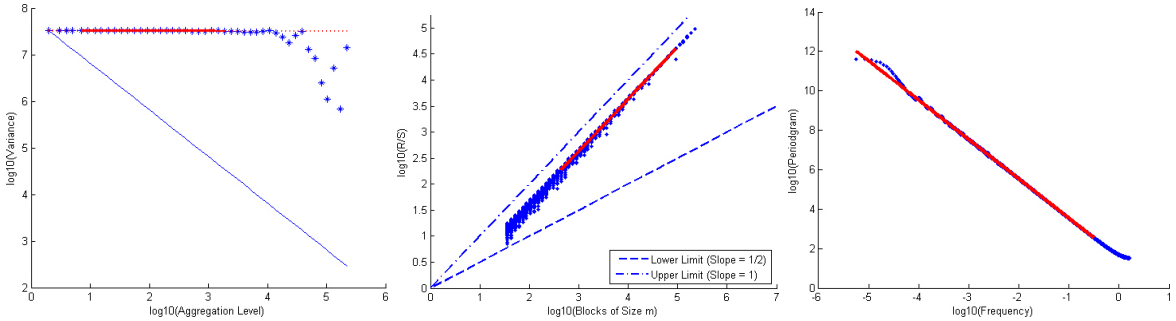

Figure 6: V-T, R/S, and periodgram for Trace-4. $H = 0.9000$, $H = 0.8994$, and $H = 0.7681$

Table 2: Results obtained for H after applying them to different methods of analysis

	Value of *H* for the Data series Measurement Period				
Method	**BC-pAug89.TL**	**Trace-1**	**Trace-2**	**Trace-3**	**Trace-4**
V-T	0.9009	0.8999	0.8999	0.8999	0.9007
R/S	0.8969	0.8996	0.8982	0.8985	0.9004
Periodgram	0.6603	0.6680	0.6678	0.6677	0.6681

The self-similar behavior of the different levels of aggregation, as well as its pronounced long-range dependence, are made evident from the linearity shown by the graphs of the size m blocks with respect to the R/S factor. See R/S graph analysis of the Figures 3, 4, 5, and 6.

The self-similar behavior of the different data series is also shown by the last row of Table 2, which considers the spectral estimation based on the periodgram of the series. The noticeable differences between the values of H for each of the series lie in the absence of confidence intervals. The analyses based on the R/S and variance-time graphs show simplified limiting cases that do not consider fine interactions between aggregate components when their differences are small, i.e., when considering, for example, two levels of immediately contiguous aggregation. In this respect, the frequency analysis does consider them, because the spectral handling is, most of the time, sufficiently exact to not omit the bias generated between the compromise of the representation of the singularities of each aggregation level and their general values in terms of the variance. Therefore, that is the reason to consider the aggregation of frequencies in relation to the periodgram, instead of the block sizes with respect to the variance. However, for the correct use of this method each result must go together with confidence intervals, which in general it is recommended to obtain from Whittle's Maximum Likelihood Estimator (MLE), but this goes beyond the objectives stated for this research, beside the fact that interest is focused on getting

a general view of the presence or absence of self-similarity characteristics, and not of their exact value, so the values obtained through the variance-time and R/S analyses as upper limits can therefore be considered with minimum error in the final interpretation of the results.

It is important to note that, even though no traffic model has been developed and it has only been assumed that the different arrivals are related to an On/Off model, as evidenced by the use of the variance-time and R/S statistics in terms of representing aggregations, parsimony is a provable characteristic based on the number of parameters needed to establish self-similarity and long-range dependence.

Finally, the proposal of restricting the results derived from representing the traffic flows as second order self-similar time series at the network level when necessary, certainly results not only feasible based on the set of arguments presented, but it is also useful for the correct understanding of and search for the origin of the self-similarity (fractality) and the long-range dependence that it may eventually exhibit. In that respect, it is undeniable that it is more adequate to interpret the presence of these singularities as the product of the internal processes subjacent in each OSI level in particular, instead of referring to them as intrinsic characteristics of the data flows because of the indetermination to which it leads. Therefore, the possibility of restricting a statistically self-similar process to a well defined application environment without altering its nature and its most important properties is true, thereby highlighting the validity of its postulates and adding greater plausibility to its physical interpretation, which is derived precisely from not forcing a reality to fit all the parameters of a given model, but on the contrary, it is taking care directly of a characteristic of the behavior of traffic flows that is exposed through its observation and mathematical interpretation.

4 Conclusions

A new point of view has been presented with respect to the systematic classification of self-similar processes with long-range dependence, whose purpose, applied to the parsimonious modeling of high speed computer networks, is to propose a common working framework for the interpretation of the results derived from the representation of traffic flows in the form of self-similar second order stationary time series.

Supported by the use of a set of four high time resolution traffic samples, it is shown that the behavior of traffic flow in a high speed computer network is self-similar and exhibits long-range dependencies over a wide range of time scales, which is evidenced when the dependence that exists among the different aggregation levels with respect to their second order statistics analyzed, and it is confirmed that regardless of the level considered, the trend reflects linearity. This linearity implies a behavior that does not depend on the time scales under consideration, but a behavior inherent to the data flows.

The mathematical models of current high speed computer networks must consider self-similarity as well as the long-range dependencies. Although it is true that the literature often proposes the equivalence of both concepts starting from an indistinct treatment, it happens that these concepts are actually independent, without one necessarily being the consequence of the other, and more profoundly, one not implying the existence of the other; these last two considerations are regardless of the direction in which they are taken.

To consider a restriction in the interpretation of the results derived from representing the traffic flows as self-similar stationary time series in relation to the OSI observation level results not only feasible, but it must be considered as a useful practice aimed at accuracy in determining the origins of self-similarity and long-term dependence, and for a better understanding of their implications, concretely when dealing with high speed computer networks where the protocol dependencies of the data flows require an adequate interpretation for their practical use in network

engineering. In this respect, it is doubtlessly a better practice to interpret these singularities as a product of the internal processes that underlie each OSI level in particular, than to interpret as the indetermination caused by referring to them as intrinsic characteristics of flows without an origin.

Bibliography

[1] Millán, G.; Kaschel, H.; Lefranc, G. (2010); Discussion of the Analysis of Self-similar Teletraffic with Long-range Dependence (LRD) at the Network Layer Level, *International Journal of Computers Communications & Control* , ISSN 1841-9836, 5(5): 799-812.

[2] Ryu, B.K.; Lowen, S.B. (1997); Point Process Approaches for Modeling and Analysis for Self-Similar Traffic. Part II: Applications, *Proc. 5th International Conference on Telecommunications Systems, Modeling and Analysis*, Nashville, TN.

[3] Ryu, B.K.; Lowen, S.B. (1996); Point Process Approaches for Modeling and Analysis for Self-Similar Traffic. Part I: Model Construction, *Proc. IEEE INFOCOM '96*, San Francisco.

[4] Garrett, M.W; Willinger, W. (1994); Analysis, Modeling and Generation of Self-Similar VBR Video Traffic, *Computer Communication Review*, 24(4):269-280.

[5] Leland, W.E.; Taqqu, M.S.; Willinger, W.; Wilson, D.V. (1994); On the Self-Similar Nature of Ethernet Traffic (Extended Version), *IEEE/ACM Trans. Netw.*, 2(1): 1-15, Feb. 1994.

[6] Paxson, V.; Floyd, S. (1995); Wide-Area Traffic: The Failure of Poisson Modeling, *IEEE/ACM Trans. Netw.*, 3(1):226-244.

[7] Ryu, B.K. (1996); Implications of Self-Similarity for Providing End-to-End QoS Euarantees in High-Speed Networks: A Framework of Application Level Traffic Modeling, *Lectures Notes in Computer Science (Proceedings of International Zurich Seminar on Digital Communications (IZS '96))*, Plattner, B. (ed.), Zurich, Switzerland: Springer-Verlag, (1044):65-79.

[8] Willinger, W.; Taqqu, M.S.; Sherman, R.; Wilson, D.V. (2007); Self-Similarity Through High-Variability: Statistical Analysis of Ethernet LAN Traffic at the Source Level, *IEEE/ACM Trans. Netw.*, 5(1):71-86.

[9] Aracil, J.; Edell, R.; Varaiya, P. (1997); A Phenomenological Approach to Internet Traffic Self-Similarity, *35th Annual Allerton Conference on Communication, Control and Computing*, Urbana-Champaign, IL.

[10] http://ita.ee.lbl.gov/html/contrib/BC.html.

[11] Park, K.; Willinger, W. (2000), Self-Similar Network Traffic: An Overview, *Self-Similar Network Traffic and Performance Evaluation*, Park, K.; Willinger, W. (eds.), New York: John Wiley & Sons.

[12] Sheluhin, O.I.; Smolski, S.M.; Osin, A.V. (2007); *Self-Similar Process in Telecommunications*, Chichester, UK: Wiley.

[13] Stallings, W. (2004); *Redes e Internet de Alta Velocidad. Rendimiento y Calidad de Servicio*, 2nd ed., Madrid, España: Pearson - Prentice Hall.

INTERNATIONAL JOURNAL OF COMPUTERS COMMUNICATIONS & CONTROL
ISSN 1841-9836, 10(1):70-77, February, 2015.

Fuzzy Euclidean Normed Spaces for Data Mining Applications

Sorin Nădăban*
Aurel Vlaicu University of Arad
Romania, 310330 Arad, Elena Dragoi, 2
*Corresponding author: snadaban@gmail.com

Abstract: The aim of this paper is to introduce some special fuzzy norms on $\mathbb{K}^n$ and to obtain, in this way, fuzzy Euclidean normed spaces. In order to introduce this concept we have proved that the cartesian product of a finite family of fuzzy normed linear spaces is a fuzzy normed linear space. Thus any fuzzy norm on $\mathbb{K}$ generates a fuzzy norm on $\mathbb{K}^n$. Finally, we prove that each fuzzy Euclidean normed space is complete. Fuzzy Euclidean normed spaces can be proven to be a suitable tool for data mining. The method is based on embedding the data in fuzzy Euclidean normed spaces and to carry out data analysis in these spaces.
Keywords: fuzzy norm, fuzzy Euclidean normed spaces, data mining.

1 Introduction

Data mining and information retrieval are two important components of the same problem: discovering new and relevant information and knowledge, through investigation of a large amount of data, through extracting the information and knowledge out of a very large databases or data warehouse.

In information retrieval the user knows what he is looking for, but sometimes it is very difficult to express this thing. The use of fuzzy sets in representing the knowledge proves to be successful on many occasions, allowing the user to express his expectations in a language close to the natural one. On the other hand, many times the matching between the requests of the user and the existing data in the databases is only an approximate one, thus, the use of fuzzy sets and the degrees of membership proves to be not only useful but also necessary.

In data mining, the user looks for new knowledge. The aim is to divide the data into homogeneous categories, in data classes. The use of the of fuzzy sets brings about flexibility both in representing knowledge and in interpreting the results as well.

The measures of similarity are the most used, at all levels in the data mining and information retrieval. The notion of similarity, or more general of the measures of comparison is the central point for all applications in the real world. The measure of similarity aims at quantifying the degree to which two objects are similar or dissimilar, offering a numeric value for this comparison.

Machine learning techniques use similarity measures. Machine learning represents an important method of extracting the knowledge out of very large databases. A study concerning fuzzy learning methods was realized by E. Hüllermeier [4].

In the last twenty years, the World Wide Web has become a major source of data and information for all domains. Web mining is the process of discovering useful knowledge and information through investigating the web structure and its content. Different web mining tasks and advanced artificial intelligence methods for information retrieval and web mining are discussed by I. Dzitac & I. Moisil [3].

Clustering and classification are both important tasks in data mining. Since clustering means the grouping of similar objects, we need some suitable measures on data sets. In order to determinate the similarity or dissimilarity between any pair of objects, the most used measures are distance measures.

If each data point is view as a n-dimensional vector $x = (x_1, x_2, \cdots, x_n) \in \mathbb{R}^n$, where each component x_i is the value of an attribute of the data, the distance between the two data instances can be calculated using Euclidean distance, Manhattan distance, Minkowski distance, Max distance, etc.

What will we do if the distance between the vectors x and y can not be precisely measured and thus we are not able to assign it, with certainty, the value $t \in \mathbb{R}_+$. There are probably different approaches enabling to handle somehow this situation. One of them, fuzzy approach, consists in using on $\mathbb{R}^n$ some fuzzy metrics, i.e. mappings $M : \mathbb{R}^n \times \mathbb{R}^n \times [0, \infty) \to [0, 1]$, where $M(x, y, t) = \alpha$ indicates the truth value of the statement "the distance between x and y is smaller than the real number t" and which belongs to $[0, 1]$. It will be better that such fuzzy metrics to come from fuzzy norms on $\mathbb{R}^n$, namely $M(x, y, t) = N(x - y, t)$, where $N : \mathbb{R}^n \times [0, \infty) \to [0, 1]$.

The aim of this paper is to introduce some special fuzzy norms on $\mathbb{K}^n$ and to obtain, in this way, fuzzy Euclidean normed spaces. In order to introduce this concept we have proved that the cartesian product of a finite family of fuzzy normed linear spaces is a fuzzy normed linear space. Thus any fuzzy norm on $\mathbb{K}$ generates a fuzzy norm on $\mathbb{K}^n$. Finally, we prove that each fuzzy Euclidean normed space is complete. Fuzzy Euclidean normed spaces can be proven to be a suitable tool for data mining. The method is based on embedding the data in fuzzy Euclidean normed spaces and to carry out data analysis in these spaces.

In studying fuzzy topological vector spaces, A.K. Katsaras [5] first introduced the notion of fuzzy norm on a linear space. Since then many mathematicians have introduced several notions of fuzzy norm from different points of view. Our definition looks similar, but it is more general, to the definitions introduced, almost in the same time, by T. Bag & S.K. Samanta (see [1], [2]) and R. Saadati & S.M. Vaezpour (see [7]). In 2006, R. Saadati & J.H. Park introduced the notion of intuitionistic fuzzy Euclidean normed space (see [8], [9]).

2 Preliminaries

Definition 1. [10] A binary operation $* : [0, 1] \times [0, 1] \to [0, 1]$ is called triangular norm (t-norm) if it satisfies the following conditions:

1. $a * b = b * a, (\forall) a, b \in [0, 1]$;
2. $a * 1 = a, (\forall) a \in [0, 1]$;
3. $(a * b) * c = a * (b * c), (\forall) a, b, c \in [0, 1]$;
4. If $a \leq c$ and $b \leq d$, with $a, b, c, d \in [0, 1]$, then $a * b \leq c * d$.

Example 2. Three basic examples of continuous t-norms are $\wedge, \cdot, *_L$, which are defined by $a \wedge b = \min\{a, b\}$, $a \cdot b = ab$ (usual multiplication in $[0, 1]$) and $a *_L b = \max\{a + b - 1, 0\}$ (the Lukasiewicz t-norm).

Remark 3. $* \leq \wedge$, i.e. $\wedge$ is stronger that any other t-norms.

Indeed, $a * b \leq a * 1 = a$, $a * b \leq 1 * b = b$. Thus $a * b \leq a \wedge b$.

Definition 4. Let $*, *\prime$ be two t-norms. We say that $*\prime$ dominates $*$ and we denote $*\prime \gg *$ if

$$(x_1 *\prime x_2) * (y_1 *\prime y_2) \leq (x_1 * y_1) *\prime (x_2 * y_2), (\forall) x_1, x_2, y_1, y_2 \in [0, 1].$$

Proposition 5. For any t-norm $*$ we have $\wedge \gg *$.

Proof: Let $x_1, x_2, y_1, y_2 \in [0,1]$.
Case 1. $x_1 \leq x_2, y_1 \leq y_2$. Then $x_1 * y_1 \leq x_2 * y_2$. Thus $(x_1 * y_1) \wedge (x_2 * y_2) = x_1 * y_1$. On the other hand $(x_1 \wedge x_2) * (y_1 \wedge y_2) = x_1 * y_1$. Therefore $(x_1 \wedge x_2) * (y_1 \wedge y_2) = (x_1 * y_1) \wedge (x_2 * y_2)$.
Case 2. $x_1 \leq x_2, y_2 \leq y_1$. As $x_1 \leq x_2$, we have $x_1 * y_2 \leq x_2 * y_2$. As $y_2 \leq y_1$, we have $x_1 * y_2 \leq x_1 * y_1$. Thus $x_1 * y_2 \leq (x_1 * y_1) \wedge (x_2 * y_2)$. Hence

$$(x_1 \wedge x_2) * (y_1 \wedge y_2) = x_1 * y_2 \leq (x_1 * y_1) \wedge (x_2 * y_2).$$

Case 3. $x_2 \leq x_1, y_1 \leq y_2$ and Case 4. $x_2 \leq x_1, y_2 \leq y_1$ are similar to previous cases. □

Definition 6. [6] Let X be a vector space over a field $\mathbb{K}$ (where $\mathbb{K}$ is $\mathbb{R}$ or $\mathbb{C}$) and $*$ be a continuous t-norm. A fuzzy set N in $X \times [0, \infty)$ is called a fuzzy norm on X if it satisfies:

(N1) $N(x,0) = 0, (\forall)x \in X$;

(N2) $[N(x,t) = 1, (\forall)t > 0]$ if and only if $x = 0$;

(N3) $N(\lambda x, t) = N\left(x, \frac{t}{|\lambda|}\right), (\forall)x \in X, (\forall)t \geq 0, (\forall)\lambda \in \mathbb{K}^*$;

(N4) $N(x+y, t+s) \geq N(x,t) * N(y,s), (\forall)x, y \in X, (\forall)t, s \geq 0$;

(N5) $(\forall)x \in X$, $N(x, \cdot)$ is left continuous and $\lim\limits_{t \to \infty} N(x,t) = 1$.

The triple $(X, N, *)$ will be called fuzzy normed linear space (briefly FNL-space).

Remark 7. a) T. Bag and S.K. Samanta [1], [2] gave a similar definition for $* = \wedge$, but in order to obtain some important results they assume that the fuzzy norm satisfies also the following conditions:

(N6) $N(x,t) > 0, (\forall)t > 0 \Rightarrow x = 0$;

(N7) $(\forall)x \neq 0, N(x, \cdot)$ is a continuous function and strictly increasing on the subset $\{t : 0 < N(x,t) < 1\}$ of $\mathbb{R}$.

The results obtained by T. Bag and S.K. Samanta can be found in this more general settings.
b) R. Saadati and S.M. Vaezpour [7] suppose that

1. $N(x,t) > 0, (\forall)t > 0$;
2. $N(x, \cdot)$ is a continuous function, $(\forall)x \neq 0$.

Remark 8. $N(x, \cdot)$ is nondecreasing, $(\forall)x \in X$.

Theorem 2.1. [6] Let $(X, N, *)$ be a FNL-space. For $x \in X, r \in (0,1), t > 0$ we define the open ball

$$B(x, r, t) := \{y \in X \ : \ N(x-y, t) > 1 - r\} .$$

Then

$$\mathcal{T}_N := \{T \subset X \ : \ x \in T \text{ iff } (\exists)t > 0, r \in (0,1) \ : \ B(x,r,t) \subseteq T\}$$

is a topology on X.

Moreover, if the t-norm $*$ satisfies $\sup\limits_{x \in (0,1)} x * x = 1$, then $(X, \mathcal{T}_N)$ is Hausdorff.

Theorem 2.2. [6] Let $(X, N, \wedge)$ be a FNL-space. Let

$$p_\alpha(x) := \inf\{t > 0 \ : \ N(x,t) > \alpha\}, \alpha \in (0,1) .$$

Then $\mathcal{P} = \{p_\alpha\}_{\alpha \in (0,1)}$ is an ascending family of semi-norms on X.

Moreover, for $x \in X, s > 0, \alpha \in (0,1)$ we have: $p_\alpha(x) < s$ if and only if $N(x,s) > \alpha$.

3 Convergence in FNL-spaces

Definition 9. [2] Let $(X, N, *)$ be a FNL-space and (x_n) be a sequence in X. The sequence (x_n) is said to be convergent if $(\exists)x \in X$ such that $\lim\limits_{n\to\infty} N(x_n - x, t) = 1$, $(\forall)t > 0$. In this case, x is called the limit of the sequence (x_n) and we denote $\lim\limits_{n\to\infty} x_n = x$ or $x_n \to x$.

Definition 10. [2] Let $(X, N, *)$ be a FNL-space and (x_n) be a sequence in X. The sequence (x_n) is called Cauchy sequence if $\lim\limits_{n\to\infty} N(x_{n+p} - x_n, t) = 1$, $(\forall)t > 0, (\forall)p \in \mathbb{N}^*$.

Remark 11. If $(X, N, *)$ is a FNL-space, then every convergent sequence is Cauchy sequence.

Definition 12. [2] Let $(X, N, *)$ be a FNL-space. $(X, N, *)$ is said to be complete if any Cauchy sequence in X is convergent to a point in X. A complete FNL-space will be called fuzzy Banach space.

Definition 13. Let $(X, N, *)$ be a FNL-space, $\alpha \in (0, 1)$ and (x_n) be a sequence in X. The sequence (x_n) is said to be α-convergent if exists $x \in X$ such that

$$(\forall)t > 0, (\exists)n_0 \in \mathbb{N} \ : \ N(x_n - x, t) > \alpha, (\forall)n \geq n_0 \ .$$

In this case, x is called the α-limit of the sequence (x_n) and we denote $x_n \overset{\alpha}{\to} x$.

Theorem 3.1. Let $(X, N, *)$ be a FNL-space and (x_n) be a sequence in X. The following sentences are equivalent:

1. (x_n) is convergent to x;
2. (x_n) is convergent to x in topology $\mathcal{T}_N$;
3. (x_n) is α-convergent to x, $(\forall)\alpha \in (0, 1)$;
4. $\lim\limits_{n\to\infty} p_\alpha(x_n - x) = 0, (\forall)\alpha \in (0, 1)$.

Proof: (2) $\Leftrightarrow$ (1)

$$x_n \to x \text{ in the topology } \mathcal{T}_M \Leftrightarrow$$

$$(\forall)r \in (0, 1), (\forall)t > 0, (\exists)n_0 \in \mathbb{N} \ : \ x_n \in B(x, r, t), (\forall)n \geq n_0 \Leftrightarrow$$

$$(\forall)r \in (0, 1), (\forall)t > 0, (\exists)n_0 \in \mathbb{N} \ : \ N(x_n - x, t) > 1 - r, (\forall)n \geq n_0 \Leftrightarrow$$

$$\lim_{n\to\infty} N(x_n - x, t) = 1 \ , \ (\forall)t > 0 \ .$$

(1) $\Leftrightarrow$ (3) It is obvious.
(4) $\Leftrightarrow$ (3)

$$\lim_{n\to\infty} p_\alpha(x_n - x) = 0 \Leftrightarrow (\forall)t > 0, (\exists)n_0 \in \mathbb{N} \ : \ p_\alpha(x_n - x) < t, (\forall)n \geq n_0$$

$$\Leftrightarrow (\forall)t > 0, (\exists)n_0 \in \mathbb{N} \ : \ N(x_n - x, t) > \alpha, (\forall)n \geq n_0 \Leftrightarrow x_n \overset{\alpha}{\to} x \ .$$

□

Theorem 3.2. Let $(X, N, *)$ be a FNL-space and (x_n) be a sequence in X. Then (x_n) is a Cauchy sequence if and only if $\lim\limits_{n\to\infty} p_\alpha(x_{n+p} - x_n) = 0, (\forall)\alpha \in (0, 1), (\forall)p \geq 1$.

Proof:

$$\lim_{n\to\infty} p_\alpha(x_{n+p}-x_n)=0,(\forall)\alpha\in(0,1),(\forall)p\geq 1$$
$$\Leftrightarrow(\forall)t>0,(\exists)n_0\in\mathbb{N}\ :\ p_\alpha(x_{n+p}-x_n)<t,(\forall)n\geq n_0,(\forall)\alpha\in(0,1),(\forall)p\geq 1$$
$$\Leftrightarrow(\forall)t>0,(\exists)n_0\in\mathbb{N}\ :\ N(x_{n+p}-x_n,t)>\alpha,(\forall)n\geq n_0,(\forall)\alpha\in(0,1),(\forall)p\geq 1$$
$$\Leftrightarrow(\forall)t>0,\lim_{n\to\infty} N(x_{n+p}-x_n,t)\geq\alpha,(\forall)\alpha\in(0,1),(\forall)p\geq 1$$
$$\Leftrightarrow(\forall)t>0,\lim_{n\to\infty} N(x_{n+p}-x_n,t)=1,(\forall)p\geq 1\Leftrightarrow(x_n)\text{ is a Cauchy sequence .}$$

□

Definition 14. Let $(X,N,*)$, $(X,N\prime,*\prime)$ be two FNL-space. The fuzzy norms N and $N\prime$ are said to be equivalent if for any sequence (x_n) in X, we have $x_n\to x$ in $(X,N,*)$ if and only if $x_n\to x$ in $(X,N\prime,*\prime)$.

4 Fuzzy Euclidean normed spaces

In this section we will denote by $\mathbb{K}$ the field of real numbers $\mathbb{R}$ or the field of complex numbers $\mathbb{C}$.

Theorem 4.1. Let $(X_1,N_1,*),(X_2,N_2,*),\cdots,(X_n,N_n,*)$ be FNL-spaces. Let $*\prime$ be a continuous t-norm such that $*\prime\gg *$. Let $N:X_1\times X_2\times\cdots X_n\times[0,\infty)\to[0,1]$,

$$N(x_1,x_2,\cdots,x_n,t)=N_1(x_1,t)*\prime N_2(x_2,t)*\prime\cdots*\prime N_n(x_n,t)\ .$$

Then $(X_1\times X_2\times\cdots X_n,N,*)$ is a FNL-space.

Proof: (N1) $N(x_1,x_2,\cdots,x_n,0)=N_1(x_1,0)*\prime N_2(x_2,0)*\prime\cdots*\prime N_n(x_n,0)=0$.
(N2)

$$N(0,0,\cdots,0,t)=N_1(0,t)*\prime N_2(0,t)*\prime\cdots*\prime N_n(0,t)=1\ .$$

Conversely, if $N(x_1,x_2,\cdots,x_n,t)=1,(\forall)t>0$, we obtain that

$$N_1(x_1,t)*\prime N_2(x_2,t)*\prime\cdots*\prime N_n(x_n,t)=1,(\forall)t>0.$$

As $*\prime\leq\wedge$, we have

$$1\leq\min\{N_1(x_1,t),N_2(x_2,t),\cdots,N_n(x_n,t)\},(\forall)t>0.$$

Thus $N_1(x_1,t)=1,N_2(x_2,t)=1,\cdots,N_n(x_n,t)=1,(\forall)t>0$. Hence $x_1=x_2=\cdots=x_n=0$.
(N3) For $\lambda\neq 0$, we have

$$N(\lambda x_1,\lambda x_2,\cdots,\lambda x_n,t)=N_1(\lambda x_1,t)*\prime N_2(\lambda x_2,t)*\prime\cdots*\prime N_n(\lambda x_n,t)=$$
$$=N_1\left(x_1,\frac{t}{|\lambda|}\right)*\prime N_2\left(x_2,\frac{t}{|\lambda|}\right)*\prime\cdots N_n\left(x_n,\frac{t}{|\lambda|}\right)=N\left(x_1,x_2,\cdots,x_n,\frac{t}{|\lambda|}\right).$$

(N4)

$$N(x_1+y_1,x_2+y_2,\cdots,x_n+y_n,t+s)=N_1(x_1+y_1,t+s)*\prime N_2(x_2+y_2,t+s)*\prime\cdots*\prime N_n(x_n+y_n,t+s)\geq$$
$$\geq(N_1(x_1,t)*N_1(y_1,s))*\prime(N_2(x_2,t)*N_2(y_2,s))*\prime\cdots*\prime(N_n(x_n,t)*N_n(y_n,s))\geq$$
$$\geq(N_1(x_1,t)*\prime N_2(x_2,t)*\prime\cdots*\prime N_n(x_n,t))*(N_1(y_1,s)*\prime N_2(y_2,s)*\prime\cdots*\prime N_n(y_n,s))=$$
$$=N(x_1,x_2,\cdots,x_n,t)*N(y_1,y_2,\cdots,y_n,s).$$

(N5) Let $x=(x_1,x_2,\cdots,x_n)\in X_1\times X_2\times\cdots X_n$. As $N_1(x_1,\cdot),N_2(x_2,\cdot),\cdots,N_n(x_n,\cdot)$ are left continuous and $*\prime$ is a continuous t-norm, we obtain that $N(x,\cdot)$ is left continuous. It is obvious that $\lim_{t\to\infty}N(x,t)=1$. □

Proposition 15. If $(X_1 \times X_2 \times \cdots X_n, N, *)$ is a FNL-space, then $(X_1, N_1, *)$, $(X_2, N_2, *)$, $\cdots$, $(X_n, N_n, *)$ are FNL-spaces, where $N_1(x_1, t) = N((x_1, 0, \cdots, 0), t), N_2(x_2, t) = N((0, x_2, \cdots, 0), t)$, $\cdots$, $N_n(x_n, t) = N((0, 0, \cdots, x_n), t)$.

Proof: We will prove that N_1 is a fuzzy norm. Similarly it can be shown that $N_2, \cdots, N_n$ are fuzzy norm.
(N1) $N_1(x_1, 0) = N((x_1, 0, \cdots, 0), 0) = 0$;
(N2) $N_1(x_1, t) = 1, (\forall)t > 0 \Leftrightarrow N((x_1, 0, \cdots, 0), t) = 1, (\forall)t > 0 \Leftrightarrow (x_1, 0, \cdots, 0) = 0 \Leftrightarrow x_1 = 0$;
(N3)

$$N_1(\lambda x_1, t) = N((\lambda x_1, 0, \cdots, 0), t) = N(\lambda(x_1, 0, \cdots, 0), t) =$$
$$= N\left((x_1, 0, \cdots, 0), \frac{t}{|\lambda|}\right) = N_1\left(x_1, \frac{t}{|\lambda|}\right) ;$$

(N4)

$$N_1(x_1 + y_1, t + s) = N((x_1 + y_1, 0, \cdots, 0), t + s) = N((x_1, 0, \cdots, 0) + (y_1, 0, \cdots, 0), t + s) \geq$$
$$\geq N((x_1, 0, \cdots, 0), t) * N((y_1, 0, \cdots, 0), s) = N_1(x_1, t) * N_1(y_1, s) ;$$

(N5) It is obvious. □

Example 16. Let $N : \mathbb{K} \times [0, \infty) \to [0, 1]$, defined by

$$N(x, t) := \begin{cases} e^{-\frac{|x|}{t}}, & \text{if} \quad t > 0 \\ 0, & \text{if} \quad t = 0 \end{cases} .$$

Then $(\mathbb{K}, N, \wedge)$ is a FNL-space.

Proof: (N1) It is obvious.
(N2) $N(x, t) = 1, (\forall)t > 0 \Leftrightarrow e^{-\frac{|x|}{t}} = 1, (\forall)t > 0 \Leftrightarrow -\frac{|x|}{t} = 0, (\forall)t > 0 \Leftrightarrow x = 0$.
(N3) Let $x \in \mathbb{R}, t > 0, \lambda \in \mathbb{R}*$. Then

$$N(\lambda x, t) = e^{-\frac{|\lambda x|}{t}} = e^{-\frac{|x|}{t/|\lambda|}} = N\left(x, \frac{t}{|\lambda|}\right) .$$

(N4) Fix $x, y \in \mathbb{R}, t, s > 0$. We assume, without restricting the generality, that $e^{-\frac{|x|}{t}} \leq e^{-\frac{|y|}{s}}$. Thus $-\frac{|x|}{t} \leq -\frac{|y|}{s}$, i.e. $|x|s \geq |y|t$. We will show that $e^{-\frac{|x+y|}{t+s}} \geq e^{-\frac{|x|}{t}}$, namely $-\frac{|x+y|}{t+s} \geq -\frac{|x|}{t}$, i.e. $|x + y|t \leq |x|(t + s)$. But

$$|x + y|t \leq (|x| + |y|)t = |x|t + |y|t \leq |x|t + |x|s = |x|(t + s) .$$

Therefore

$$N(x + y, t + s) = e^{-\frac{|x+y|}{t+s}} \geq \min\left\{e^{-\frac{|x|}{t}}, e^{-\frac{|y|}{s}}\right\} = N(x, t) \wedge N(y, s) .$$

(N5) It is obvious. □

Lemma 17. *Let $(\mathbb{K}, N, *)$ be a FNL-space. Then there exists $\alpha \in (0, 1)$ such that $p_\alpha(1) \neq 0$.*

Proof: $p_\alpha(1) = \inf\{t > 0 : N(1, t) > \alpha\}$. We suppose that $p_\alpha(1) = 0, (\forall)\alpha \in (0, 1)$. Then $N(1, t) > \alpha, (\forall)\alpha \in (0, 1), (\forall)t > 0$. Thus $N(1, t) = 1, (\forall)t > 0$. Therefore $1 = 0$, contradiction. □

Proposition 18. A sequence (x_n) is convergent in a FNL-space $(\mathbb{K}, N, *)$ if and only if (x_n) is convergent in $(\mathbb{K}, |\cdot|)$.

Proof: A sequence (x_n) is convergent to x in $(\mathbb{K}, N, *) \Leftrightarrow \lim\limits_{n\to\infty} p_\alpha(x_n - x) = 0, (\forall)\alpha \in (0,1)$ $\Leftrightarrow \lim\limits_{n\to\infty} |x_n - x| p_\alpha(1) = 0, (\forall)\alpha \in (0,1) \Leftrightarrow \lim\limits_{n\to\infty} |x_n - x| = 0 \Leftrightarrow (x_n)$ is convergent in $(\mathbb{K}, |\cdot|)$ $\square$

Corollary 19. Any two fuzzy norm on $\mathbb{K}$ are equivalent.

Definition 20. The triplet $(\mathbb{K}^n, N, *)$ is called fuzzy Euclidean normed space (briefly FEN-space) if $*$ is a continuous t-norm and $N : \mathbb{K}^n \times [0,\infty) \to [0,1]$ is a fuzzy norm defined by

$$N(x_1, x_2, \cdots, x_n, t) = N_1(x_1, t) \wedge N_2(x_2, t) \wedge \cdots \wedge N_n(x_n, t) ,$$

where $N_1, N_2, \cdots, N_n$ are fuzzy norms on $\mathbb{K}$ ((N4) is satisfied with the t-norm $*$, for all fuzzy norms $N_1, N_2, \cdots, N_n$).

Remark 21. Theorem 4.1 and the fact that $\wedge \gg *$ assure the accuracy of the previous definition, meaning that N is fuzzy norm on $\mathbb{K}^n$ indeed.

Proposition 22. A sequence (x_k) is convergent in a FEN-space $(\mathbb{K}^n, N, *)$ if and only if (x_k) is convergent in $(\mathbb{K}^n, ||\cdot||)$, where $||\cdot||$ denotes the Euclidean norm on $\mathbb{K}^n$.

Proof:

$$(x_k) \text{ is convergent to } x \text{ in } (\mathbb{K}^n, N, *) \Leftrightarrow \lim_{k\to\infty} N(x_k - x, t) = 1, (\forall)t > 0$$

$$\Leftrightarrow \lim_{k\to\infty} N_1(x_k^1 - x^1, t) \wedge N_2(x_k^2 - x^2, t) \wedge \cdots \wedge N_n(x_k^n - x^n, t) = 1, (\forall)t > 0$$

$$\Leftrightarrow \lim_{k\to\infty} N_i(x_k^i - x^i, t) = 1, (\forall)t > 0, (\forall)i = \overline{1,n} \Leftrightarrow |x_k^i - x^i| \to 0, (\forall)i = \overline{1,n} \Leftrightarrow ||x_k - x|| \to 0 .$$

$\square$

Theorem 4.2. Any FEN-space $(\mathbb{K}^n, N, *)$ is complete.

Proof: Let (x_k) be a Cauchy sequence in $(\mathbb{K}^n, N, *)$. Then

$$p_{\alpha,N}(x_{k+p} - x_k) = \inf\{t > 0 \ : \ N(x_{k+p} - x_k, t) > \alpha\} =$$

$$= \inf\{t > 0 \ : \ N_1(x_{k+p}^1 - x_k^1, t) \wedge N_2(x_{k+p}^2 - x_k^2, t) \wedge \cdots \wedge N_n(x_{k+p}^n - x_k^n, t) > \alpha\} =$$

$$= \inf\{t > 0 \ : \ N_1(x_{k+p}^1 - x_k^1, t) > \alpha, N_2(x_{k+p}^2 - x_k^2, t) > \alpha, \cdots, N_n(x_{k+p}^n - x_k^n, t) > \alpha\} \geq$$

$$\geq \inf\{t > 0 \ : \ N_i(x_{k+p}^i - x_k^i, t) > \alpha\}, (\forall)i = \overline{1,n} .$$

Thus

$$p_{\alpha,N}(x_{k+p} - x_k) \geq p_{\alpha,N_i}(x_{k+p}^i - x_k^i) = |x_{k+p}^i - x_k^i| p_{\alpha,N_i}(1), (\forall)i = \overline{1,n} .$$

By Lemma 4.4, applied to fuzzy norm N_i, we obtain that there exists $\alpha_i \in (0,1)$ such that $p_{\alpha_i,N_i}(1) \neq 0$. Therefore

$$p_{\alpha_i,N}(x_{k+p} - x_k) \geq |x_{k+p}^i - x_k^i| p_{\alpha_i,N_i}(1), (\forall)i = \overline{1,n} .$$

As (x_k) is a Cauchy sequence in $(\mathbb{K}^n, N, *)$, we obtain that (x_k^i) is a Cauchy sequence in $(\mathbb{K}, |\cdot|), (\forall)i = \overline{1,n}$. Thus (x_k^i) is convergent to $x^i, (\forall)i = \overline{1,n}$. Therefore (x_k) is convergent to $x = (x^1, x^2, \cdots, x^n)$ in $(\mathbb{K}^n, ||\cdot||)$ and previous proposition implies that (x_k) is convergent to x in $(\mathbb{K}^n, N, *)$. $\square$

5 Conclusion

In this paper some special fuzzy norms on $\mathbb{K}^n$ is given in order to obtain, in this way, fuzzy Euclidean normed spaces. These spaces can be proven to be a suitable tool for data mining. The method is based on embedding the data in fuzzy Euclidean normed spaces and to carry out data analysis in these spaces.

Bibliography

[1] Bag, T., Samanta, S.K. (2003); Finite dimensional fuzzy normed linear spaces, *Journal of Fuzzy Mathematics*, 11(3): 687–705.

[2] Bag, T., Samanta, S.K. (2005); Fuzzy bounded linear operators, *Fuzzy Sets and Systems*, 151: 513–547.

[3] Dzitac, I., Moisil, I. (2008); Advanced AI techniques for web mining, *Proceedings of the 10th WSEAS international conference on Mathematical methods, computational techniques, non-linear systems, intelligent systems*, 343–346.

[4] Hüllermeier, E. (2005); Fuzzy methods in machine learning and data mining: Status and prospects. *Fuzzy Sets and Systems*, 156(3): 387–406.

[5] Katsaras, A.K. (1984); Fuzzy topological vector spaces II, *Fuzzy Sets and Systems*, 12: 143–154.

[6] Nădăban, S., Dzitac, I. (2014); Atomic Decompositions of Fuzzy Normed Linear Spaces for Wavelet Applications, *Informatica*, (in press).

[7] Saadati, R., Vaezpour, S.M. (2005); Some results on fuzzy Banach spaces, *J. Appl. Math. & Computing*, 17(1-2): 475–484.

[8] Saadati, R., Park, J.H. (2006); Intuitionistic fuzzy Euclidean normed spaces, *Communications in Mathematical Analysis*, 1(2): 85–90.

[9] Saadati, R., Park, J.H. (2006); On the intuitionistic fuzzy topological spaces, *Chaos, Solitons and Fractals*, 27: 331–344.

[10] Schweizer, B., Sklar, A. (1960); Statistical metric spaces, *Pacific J. Math.*, 10: 314–334.

INTERNATIONAL JOURNAL OF COMPUTERS COMMUNICATIONS & CONTROL
ISSN 1841-9836, 10(1):78-88, February, 2015.

Real-time Monitoring of Tectonic Displacements in the Pacific Northwest through an Array of GPS Receivers

R. Popovici, R. Andonie, W.M. Szeliga, T.I. Melbourne, C.W. Scrivner

Răzvan Popovici
1. Altair Engineering Inc.
Troy, MI, USA
rp@miravtech.com
2. School of Engineering and Computer Science, Oakland University
Rochester, MI, USA

Răzvan Andonie*
1. Computer Science Department, Central Washington University
Ellensburg, WA, USA
2. Electronics and Computers Department, Transilvania University
Braşov, Romania
*Corresponding author:andonie@cwu.edu

Walter M. Szeliga, Timothy I. Melbourne, Craig W. Scrivner
Department of Geological Sciences, Central Washington University
Ellensburg, WA, USA
walter@geology.cwu.edu, tim@geology.cwu.edu, scrivner1@cwu.edu

Abstract: The Pacific Northwest Geodesic Array at Central Washington University collects telemetered streaming data from 450 GPS stations. These real-time data are used to monitor and mitigate natural hazards arising from earthquakes, volcanic eruptions, landslides, and coastal sea-level hazards in the Pacific Northwest. The displacement measurements are performed at millimeter-scale, and require stringent analysis and parameter estimation techniques. Recent improvements in both accuracy of positioning measurements and latency of terrestrial data communication have led to the ability to collect data with higher sampling rates, of up to 1 Hz. For seismic monitoring applications, this means 1350 separate position streams from stations located across 1200 km along the West Coast of North America must be able to be both visually observed and analyzed automatically. We aim to make the real-time information from GPS sensors easily available, including public access via interfaces for all intelligent devices with a connection to the Internet.
Our contribution is a dashboard application that monitors the real-time status of the network of GPS sensors. We are able to visualize individual and multiple sensors using similar time series scales. We are also able to visualize groups of sensors based on time-dependent statistical similarity, such as sensors with the the highest variance, in real-time. In addition to raw positioning data, users can also display derived quantities, such as the Allan variance or the second derivative of a data stream.
Keywords: Real time dashboard, signal analysis, data streaming, GPS, slow earthquake.

1 Introduction

The Pacific Northwest Geodesic Array (PANGA) Geodesy Laboratory at Central Washington University (CWU) has a primary scientific role to support high precision geodetic measurements using Global Positioning System (GPS) observations in order to characterize crustal deformation, plate tectonic motions, coastal and earthquake hazards, and other environmental science applications. Under contracts from the National Science Foundation, the National Aeronautics and Space Administration, the U.S. Geological Survey, and UNAVCO, Inc., the Laboratory

analyses all publicly shared GPS data within the Cascadia subduction zone [1] and greater Pacific Northwest. The Geodesy Laboratory analyzes data from roughly 1000 GPS stations that comprise the EarthScope Plate Boundary Observatory, whose stations span the Pacific-North American tectonic plate boundary from Alaska to Mexico. Fig. 1 is a map of all stations currently analyzed by CWU. In addition to serving as the Data Analysis Facility for the PANGA, the Geodesy Laboratory also supports field experiments on Cascades volcanoes and in mainland Mexico, Baja California, California, Idaho, Montana, Oregon, and Washington. CWU also operates a continuous GPS network in Nepal.

Data from 450 GPS stations are telemetered in real-time back to CWU, where they are processed, also in real-time, using both NASA Jet Propulsion Lab's RTG [2] software as well as Trimble's RTKNet Integrity Manager software to provide relative positioning of several mm resolution across the Cascadia subduction zone and its metropolitan regions. These real-time data are used to monitor and mitigate natural hazards arising from earthquakes, volcanic eruptions, landslides, and coastal sea-level hazards. In addition, they are also used to monitor man-made structures such as Seattle's sagging Alaska Way Viaduct, WA SR-520 and I-90 floating bridges and power-generation/drinking-water-supply dams throughout the Cascadia subduction zone, including those along the Columbia River.

The data streams from these 450 receivers is continuously downloaded, analyzed, archived and disseminated, as part of the existent geophysics and tectonics research programs within the Department of Geological Sciences, CWU. These tectonic displacement measurements are performed at millimeter-scale, and requires stringent analysis and parameter estimation techniques. The Geodesy Laboratory uses NASA's GIPSY OASIS (GPS Inferred Positioning SYstem, Orbital Analysis and SImulation Software) software to translate GPS satellite phase observables into position time series, and in-house parameter estimation and modeling software to quantify crustal deformation caused by plate tectonics, earthquakes, landslides and volcanic eruptions.

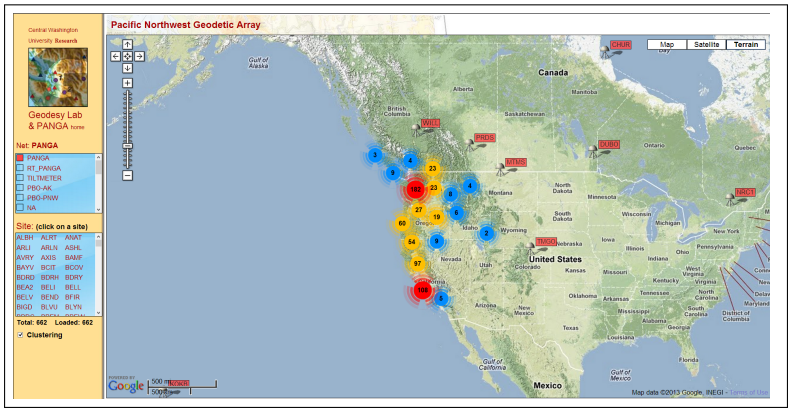

Figure 1: Panga sensor placement.

The position of a GPS station is estimated from a combination of satellite range and carrier phase measurements, with the position accuracy being heavily dependent on the accuracy of the satellite ephemerides, stability of the Cesium time standards on board the orbiting satellites, and the realism of models for both the tropospheric water content and electron density of the ionosphere. In the early days of GPS positioning, when none of these variables were particularly well-determined, long-duration observations were necessary to properly constrain models of each error source, with typically a single position estimated daily. These daily solutions have enabled the study of long term crustal deformation and even earthquake source processes, but only well after the observations were recorded.

At it's inception, the GPS receivers networks were designed to monitor tectonic displacements

with a coarse-grained temporal resolution, with data reductions to one measurement per day. However, over the intervening two decades, real- or near-real time estimates of ephemerides and real-time estimations of satellite clock behavior and atmospheric delays have enabled positioning estimates to be made at rates as rapid as once per second. Moreover, the widespread implementation of real-time data telemetry systems have enabled these high-rate position estimates to be computed nearly in real-time. This, combined with increased precision in all aspects of GPS position estimations, essentially transforms a continuously-operating, real-time networks of GPS receivers into a seismic network capable of detecting the strong ground motion that accompanies large earthquakes in real-time. For example, Fig. 2, shows data from one component of motion at a single site due to the well known M9 2011 Tōhoku earthquake in Japan. This time series is comparable to data from traditional seismic instrumentation for the event but is free from data artifacts common to seismic instruments, such as "clipping" of a time series due to physical limitations of the instrument response. Thus real-time high-sample-rate GPS solutions can provide useful data to determine the magnitude of large earthquakes in the immediate quake aftermath when the size of the event is still being determined and emergency response is being organized.

Ground deformation due to a major earthquake leads to a sudden change in the positions of sensors across a wide zone. One outstanding problem in monitoring any large network of continuously operating instruments is facile observation and analysis of its data streams. In the case of the Pacific Northwest Geodetic Array, the 450 GPS stations each output three continuous data channels: latitude, longitude and vertical position. For seismic monitoring applications, this means 1350 separate position streams from stations located across 1200 km along the West Coast of North America must be able to be both visually observed and analyzed automatically. One of the characteristics of seismic events is spatial coherence of the observed earthquake deformation, which requires that station behavior be monitored in spatially-clustered groups.

There are two conflicting factors which motivate our present work. One is the potentially valuable information which can be extracted from the GPS sensors' data stream for detecting major earthquakes. Obviously, such data is valuable when extracted and processed in real-time. This takes us to the second factor, which is the challenge posed by mining big datasets of streaming data: we are more concerned about the abundance, not the lack of data. The recent advancements in data collection, such as data streams from sensors, exceed the ability of the data scientists to really put data in context of the questions and extract usable knowledge.

Our final goal is to make the real-time information from GPS sensors easily available. This includes wider public access via interfaces for all intelligent devices with a connection to the Internet. Practically, a geologist with mobile phone access, should have real-time access to streaming GPS position data. When combined with other measurements and information, this would help him to detect a major earthquake.

Our contribution is a dashboard application that monitors the real-time status of a network of GPS sensors. We are able to visualize individual and multiple sensors using similar time series scales. We are also able to visualize groups of sensors based on time-dependent statistical similarity, such as sensors with the the highest variance, in real-time. In addition to raw positioning data, users can also display derived quantities, such as the Allan variance or the second derivative of a data stream.

Section 2 describes our interface to the PANGA data stream. Section 3 introduces our main contribution, the dashboard application, whereas in Section 4 we discuss our results. In Section 5, we conclude with final remarks and open problems.

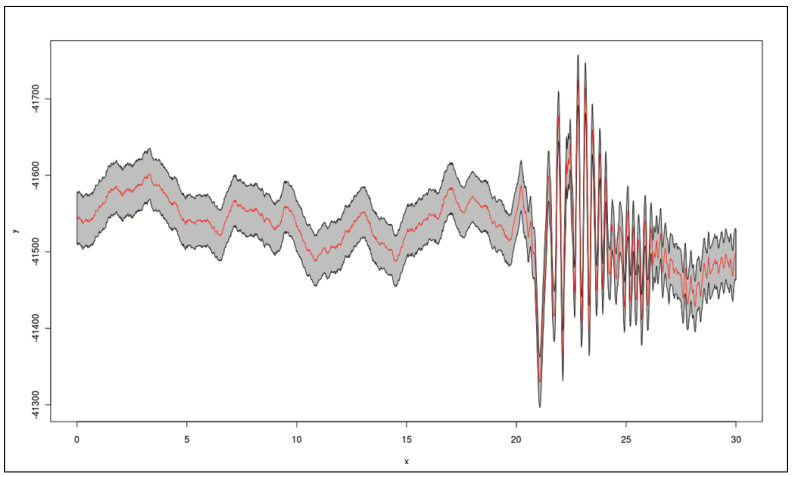

Figure 2: Longitudinal movement of a GPS receiver located in Japan, during the Tōhoku earthquake. The read line is the reading and the gray area is one standard deviation border around the reading.

2 The PANGA data output stream interface

The dashboard input data is the output of the PANGA network, and it consists of a list of streams with active/inactive status. Each stream contains a set of samples, each containing the North/West/Elevation displacements, as well as quality statistics. Although not used by the dashboard, it is possible to compute the correlation between each pair of any of the three dimensions with displacement. We first will describe the PANGA data structure and our interface to the resulted output data stream.

The PANGA network aims to precisely measure the displacement of multiple locations organized in a network. Physically, the network is composed of a number of GPS receivers, which receive signals from satellites and regularly send that data to a processing center using a cellular radio network. In our data model, such a receiver is called a 'site'. Each site provides one or more streams of processing solutions, which are displacement values and quality information. Depending on the type of, the streams can contains raw solutions, or they are processed further using a Kalman filter. Some streams provide data points every second, other streams provide an aggregation of the data over a longer time span. Each stream contain a record payload storing the time stamp, as well as the variations of the position with respect of north, east and elevation relative to a reference position. It is possible for a stream to miss some points in time and it is not guaranteed that all the data is available at every sampling time stamp. Fig. 3 depicts the conceptual entities, described above, as well as the querying mechanism.

A large data repository[1] is available, as well as the diverse real time data streams we focus on. The challenge is to visualize and exploit the historical data to increase the accuracy of current readings or to efficiently categorize a major earthquake. Literature examples, such as [3], show that big data can overwhelm the analyst, either if the right algorithm is not in place, or if the nature of the data does not address, directly or indirectly, the research questions.

The system can be interrogated using a RESTful Web interface[2] that returns data serialized in JSON. RESTful (Representational State Transfer) [4], although known for more a decade, is a recently embraced concept in the architecture of web services that excludes the presence of an established session between client and server, as opposite to the classical dynamic web

[1] `http://www.geodesy.cwu.edu/data_ftp_pub/data/`
[2] `http://www.panga.org/realtime/data/api`

approach of a shared state encompassed by the session. The advantages of the new approach are the possibility to spread the server requests over a number of cluster nodes, as well as simplicity in the implementation of both server and client, since it is eliminated the need to implement system states and shared session. JSON (JavaScript Object Notation) [5] is an emerging standard for structured data encoding, designed to replace XML in lightweight implementations, such as browsers and mobile applications. Initiated by JavaScript, it can be used under most of the modern platforms, including (in our case) Java.

The interface is composed of a set of query verbs and parameters. We use the verb `sitelist` to acquire the list of the sites available. For each site, the response provides site attributes and the streams associated with the site, including the status (active or inactive) of the stream.

The `records` verb provides access to the position data for a stream. The stream name is given as a required parameter. The response is composed of the current set of positions for the stream, the time stamp of the last record and current server time. The last record time stamp can be used as an option parameter to constrain the next query for that stream. If the time stamp of the last record of the previous query is included, then the response will only include records newer than those received previously. In this way, the client maintains the state necessary to avoid the unnecessary download of records that were already contained within a previous interrogation.

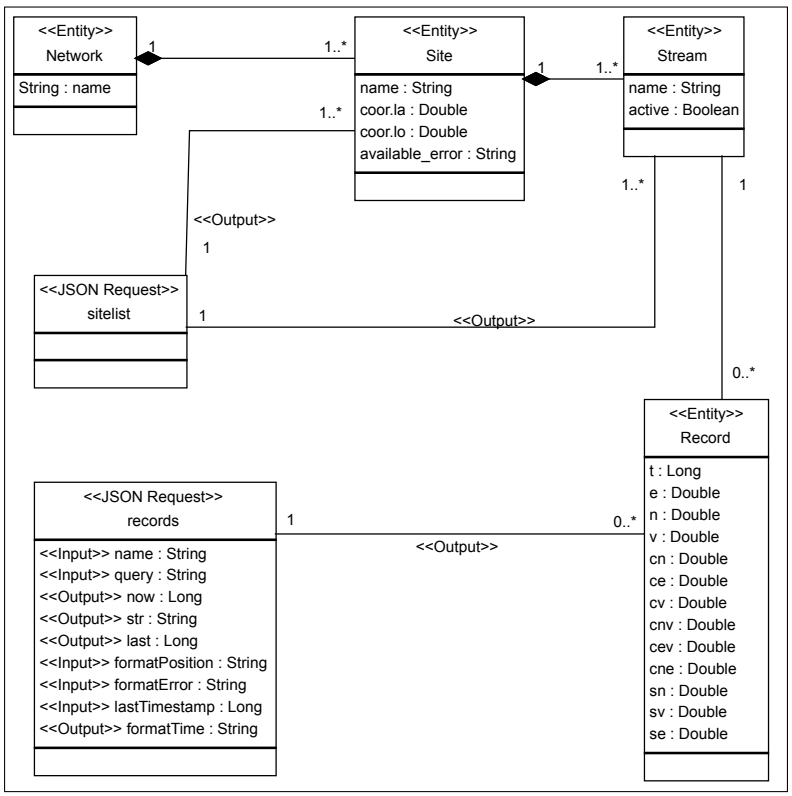

Figure 3: PANGA data model and web interrogation structure.

In the UML diagram of Fig. 3, conceptual classes are labeled with "Entity" stereotype, so that they differentiate of JSON requests. Within a request, each attribute can be either input or output. The associations of JSON requests are also of "Output" stereotype, since they are part of the reply.

Multiple networks could be theoretically represented in the system. This is the reason why we introduce the "Network" class. However, multiple networks may have different data models and different querying systems For example, the network that captured the Tōhoku earthquake [6],

only provides the standard deviation value for each of the three dimensions of displacement, as a measure of precision, rather than the fill covariance of the solution.

For each data stream PANGA provides multiple "queues", with different sampling intervals. This is a convenience for charting applications, which do not need to perform analysis, but for our application we only request data from at the full sample rate.

3 The dashboard application

Our dashboard is oriented on stream processing, which facilitates the visualization of PANGA data. The application is J2EE compliant, developed in two layers: the server layer consists of a EJB singleton that downloads PANGA data, stimulated by a timer, while the second layer is a web front end, which connects to the first layer and receives the instantaneous state of the data. This way, independently of the number of the web dashboard, the PANGA server is only queried once. As shown in Fig. 4, the implementation is divided into three logical layers: the interface layer, the J2EE middle layer, and the data layer. Since the data layer is highly volatile and it does not need to be persisted into a database, it is not implemented as an EJB entity. The J2EE layer is responsible for scheduling of the downloads of PANGA data, as well as for the storage of user configuration settings within the user session.

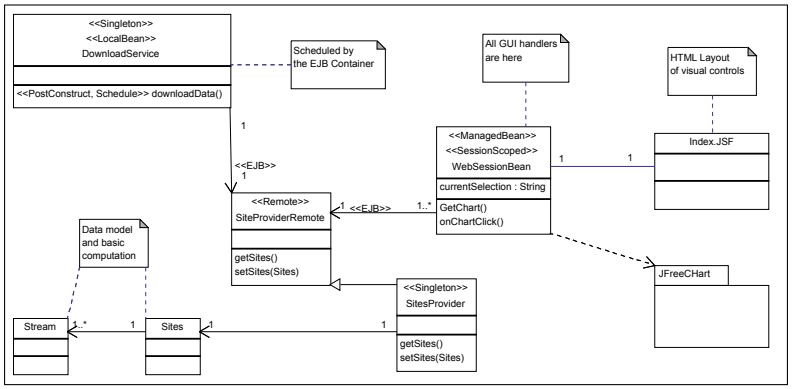

Figure 4: Interface-centric class diagram of EJB components.

We run our application with the Oracle Glassfish application server [7], but it can be deployed most of the J2EE application servers. Opposite to most of the J2EE applications, we don't mandate the existence of a back-end database, since we don't persist any data outside the user session scope. For future analysis, we save the JSON content downloaded by the application in a local directory. Since this infringes the J2EE requirements, the option is only designated to be used in a testing environment and shall be subject of scrutiny in case of deploying the application on a cluster.

The application runs on both Windows and Linux server (with untested possibility to run on Apple computers). We have tested all major browsers: Microsoft Internet Explorer, Mozilla Firefox, Chrome, and Safari, with different screen resolutions. The best resolution to visualize the dashboard is High Definition Television (HDTV) 1920×1080, resolution common to most of the TV screens available on the market. It is possible to access the dashboard with mobile devices, through the browser capability, as shown in Fig. 5.

The user interface layer is based on the PrimeFaces library [8], using Google Maps [9] for spatial display of sensors (see Fig. 5). The selected sensors are displayed yellow, the active ones green and the inactive transmitters are black. We extend the capabilities of the control, provided by PrimeFaces, to allow replacement of map icons without the need for full reload of

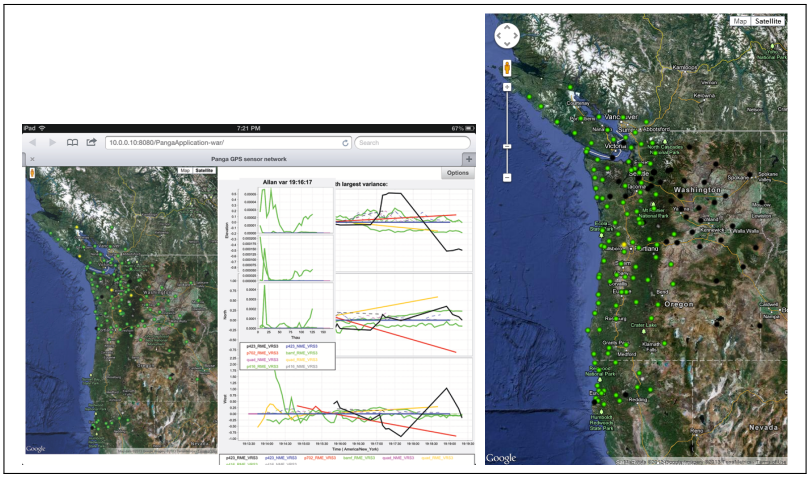

Figure 5: left: Screenshot of the dashboard on Apple IPad; right: Map of the sensors.

the control's content. This way, we avoid flickering the map if the data has been changed. We use the JFreeCharts library [10] to render the charts. The rendering occurs on the server side, within the servlet container, JFreeCharts is able to render SVG content to a Java stream, by receiving a Graphical Context object compatible with Java AWT drawing system. Using this technique we render the main chart and Allan variance chart, shown in Fig. 6.

The PrimeFaces library was not designed with real time charts in mind. Particularly, it is difficult to refresh the content of a chart without performing a full control refresh; even it technologies like Ajax allow the discriminative refresh of specific controls on a page, refreshing the image will cause it to disappear on the duration of the download, and then it reappears again. Since a regular HTTP web transaction takes between 20-300 milliseconds, there are at least a few frames when the image is missing. For this reason, we use a technique similar to the double buffering: we load the content of the new chart in a hidden IMG element, then, once load is completed, the content of the hidden image is moved to the visible image control. Since this last operation is performed on the user browser, its duration is in sub-millisecond range, hence no flickering occurs.

A similar challenge has been observed for the map control. When a new set of sensor data is available, the Google Map control requires a complete refresh, in order to accommodate the new changes in the way envisioned by the authors of PrimeFaces. We had to access the control at JavaScript level, remove the existing markups layers and add the newly available points. This way, we retain the position of latitude and longitude, as well as the zoom level of the map, established by the user on the local browser.

Fig. 7 shows a sensor plot, as well as the numeric second derivative of the signal, and the local Allan variance.

4 Discussion

We used the second derivative and the Allan variance [11] to characterize the GPS data streams. The Allan variance is a statistical measure of the stability of a series of observations over various periods. This statistic was initially developed to investigate the stability of the atomic oscillators that comprise most high-precision frequency standards [12, 13]. The Allan variance is uniquely suited to identifying not only the frequency-dependency of noise in a time series, but over what periods that noise operates.

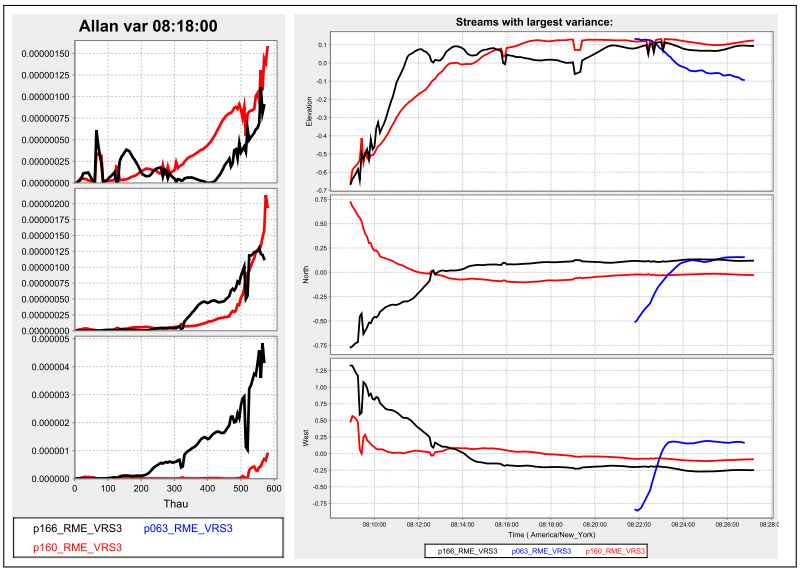

Figure 6: Allan variance chart.

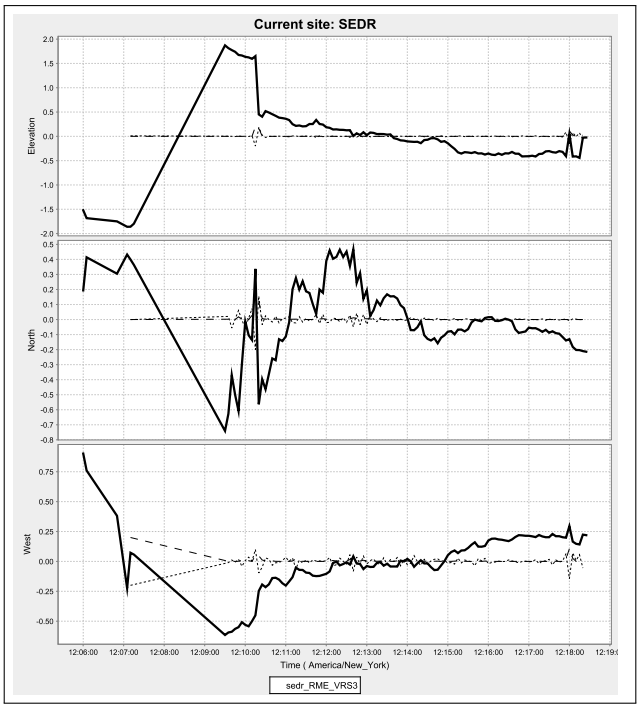

Figure 7: Chart of sensor plot together with Allan variance and second derivative.

GPS position time series are often composed of daily aggregates of higher-rate observations. This aggregation is typically performed to improve the noise characteristics of the resulting geodetic time series. Still, these daily aggregate time series are known to be contaminated by colored noise [14]. In the past decade, time series composed of the higher-rate observations themselves have begun to provide crucial measurements of absolute ground deformation, both static and dynamic, due to earthquakes [15]. However, the noise characteristics of position time series at sampling intervals shorter than one day are poorly known and are likely to be strongly dependent on the subtleties of each GPS processing methodology [16]. The characterization of the noise content of these high-rate GPS measurements is essential for their future use in the study of earthquake deformation [17].

Previous authors [16,18,19] have used the Allan variance statistic to study the noise characteristics of various geodetic time series, such as Earth Orientation Parameters, GPS position time series, and VLBI baseline time series. With the advent of streaming of near-real-time, high-rate GPS time series, we are provided with the opportunity to study not only the frequency characteristics of high-rate geodetic time series, but their evolution with time. This ability to monitor the evolution of the noise characteristic of each individual instrument in a network has implications not only for the observation of near-real-time earthquake deformation and thus earthquake early warning, but also for instrument and network state-of-health.

To compute the second derivative, we first determine the sampling rate of data (different streams may have a different sampling rate) and then we apply eq. (1):

$$\begin{aligned} &f''(x_1) = \frac{f(x_0) - 2f(x_1) + f(x_2)}{h^2} \\ &\text{where} \\ &h = x_2 - x_1 = x_1 - x_0 \end{aligned} \tag{1}$$

In our case, if any of $f(x)|x \in \{x_0, x_1, x_2\}$ does not exist, the second derivative for the point x_1 is not being computed.

The Allan variance is computed by eq. (2), where $\sigma_y^2(x,\tau)$ is the computed Allan variance, y is the signal function, and τ is the time interval considered to compute the function.

$$\sigma_y^2(x,\tau) = \frac{(y(x-\tau) - 2y(x) + y(x+\tau))^2}{2\tau^2} \tag{2}$$

Since we took the value of τ to be equal with the sampling rate, we observe that:

$$\sigma_y^2(x,\tau) = \frac{(\tau y'')^2}{2} \tag{3}$$

According to eq. (3), the Allan variance and the second derivative are equivalent in meaning. More specifically, the Allan variance is always positive and it differs from the second derivative by a constant.

We plot eq. (2) by choosing a fixed x and letting the τ vary. The fixed x is provided by the user, as a result of a mouse click in the chart. Based on chart scaling, we depict the variation of time coordinate x in Fig. 6.

5 Conclusion and Open Problems

Our application runs on both Windows and Linux server, on all major browsers. Through the web interface, we made PANGA data accessible the to a plurality of remote users. To cover

a wider range of users, we plan to implement the same dashboard as a native Android and Apple iOS (iPhone and iPad) application, so that availability of PANGA data to be truly ubiquitous.

One challenge to producing a fast and reliable classification technique of earthquakes is the lack of training data. Major earthquakes large enough to produce significant ground deformation across a large region are rare and at this time the only set of data of with high sampling rates from a large and densely-instrumented GPS network is from the 2011 Tōhoku event sequence. Therefore, it is of major interest to record the displacement data measurement in order to be used for future data mining applications.

Another challenge is that there are significant noise and data quality issues with GPS data streams. Some problems are common with those of seismic networks, such as telecommunications glitches and outages. Others are unique to GPS data acquisition and processing. For example, some atmospheric phenomenon can perturb GPS signals. Correlation with seismographs and atmospheric sensors may be key elements in a system to identify earthquakes and perform a rapid computation of an event's magnitude.

It is an open problem to implement a classifier for these big noisy data GPS streams. Such a classifier should be able to monitor and disseminate in real-time especially slow landslides, hard to detect by seismographs, arising from earthquakes, volcanic eruptions, and other hazards.

Bibliography

[1] A.C. Aguiar, T.I. Melbourne, and C.W. Scrivner (2009), Moment release rate of Cascadia tremor constrained by GPS, *Journal of Geophysical Research*, Jul. 2009, 114:1-11.

[2] W. Bertiger, S.D. Desai, B.Haines, N. Harvey, A.W. Moore, S. Owen, J.P. Weiss (2010), Single receiver phase ambiguity resolution with GPS data, *Journal of Geodesy*, May 2010, 84:327–337.

[3] B. Franks (2012), *Taming The Big Data Tidal Wave: Finding Opportunities in Huge Data Streams with Advanced Analytics*, Wiley and SAS Business Series, Wiley.

[4] R.T. Fielding (2000), *Architectural styles and the design of network-based software architectures*, Ph.D. dissertation.

[5] D. Crockford (2006), The application/json Media Type for JavaScript Object Notation (JSON), IETF, RFC 4627, 7.

[6] M. Simons, S.E. Minson, A. Sladen, F. Ortega, J. Jiang, S.E. Owen, L. Meng, J.-P. Ampuero, S. Wei, R. Chu, D. V. Helmberger, H. Kanamori, E. Hetland, A. W. Moore, and F. H. Webb (2011), The 2011 magnitude 9.0 Tohoku-Oki earthquake: Mosaicking the megathrust from seconds to centuries, *Science*, Jun. 2011, 332(6036):1421–1425.

[7] A. Goncalves (2010), *Beginning Java EE 6 with GlassFish 3 (Expert's Voice in Java Technology)*, Apress.

[8] O. Varaksin, M. Caliskan (2013), *PrimeFaces Cookbook*, Packt Publishing.

[9] G. Svennerberg (2010), *Beginning Google Maps API 3 (Expert's Voice in Web Development)*, Apress.

[10] S. Weidler (2008), *Statistiken für Warehouse Management Systeme: Entwicklung eines Statistiktools mit Hilfe des JAVA-Frameworks JFreeChart*, Vdm Verlag Dr. Müller.

[11] D.W. Allan, J.H. Shoaf, D. Halford (1974), Statistics of Time and Frequency Data Analysis, in *Time and Frequency: Theory and Fundamentals*, B. E. Blair (Ed.).

[12] D. Allan (1965), *Statistics of Atomic Frequency Standards*, University of Colorado.

[13] H. Hellwig (1972), I. for Basic Standards (U.S.). Time, and F. Division, *Frequency standards and clocks: a tutorial introduction*, ser. NBS technical note, Dept. of Commerce, National Bureau of Standards, Institute for Basic Standards, Time and Frequency Division.

[14] A. Mao, C.G.A. Harrison, T.H. Dixon (1999), Noise in GPS coordinate time series, *Journal of Geophysical Research: Solid Earth*, 104(B2):2797–2816.

[15] K. Larson, GPS seismology (2009), *Journal of Geodesy*, 83(3-4):227–233.

[16] Z. Malkin, A. Voinov (2001), Preliminary results of processing euref network observations using a non-fiducial strategy, *Physics and Chemistry of the Earth*, Part A: Solid Earth and Geodesy, 26(68):579 –583.

[17] P. Elósegui, J. L. Davis, D. Oberlander, R. Baena, G. Ekström (2006), Accuracy of high-rate GPS for seismology, *Geophysical Research Letters*, 33(11):1-4.

[18] C. Roberts, P. Morgan, C. Rizos (2002), Allan variance applied to time series baseline results for gps-based deformation monitoring applications, in *Proceedings of the 2nd symposium on geodesy for geotechnical and structural applications, Berlin, May 2002*, 299–311.

[19] Z. Malkin (2011), Study of astronomical and geodetic series using the allan variance, *Kinematics and Physics of Celestial Bodies*, 27(1):42–49.

INTERNATIONAL JOURNAL OF COMPUTERS COMMUNICATIONS & CONTROL
ISSN 1841-9836, 10(1):89-99, February, 2015.

An Approximate Algorithm Combining P Systems and Active Evolutionary Algorithms for Traveling Salesman Problems

X. Song, J. Wang

Xiaoxiao Song*
School of Electrical and Information Engineering
Xihua University, Chengdu, Sichuan, P.R. China, 610039
*Corresponding author: sxx_pippen@163.com

Jun Wang
School of Electrical and Information Engineering
Xihua University, Chengdu, Sichuan, P.R. China, 610039
745257101@qq.com

Abstract: An approximate algorithm combining P systems and active evolutionary algorithms (AEAPS) to solve traveling salesman problems (TSPs) is proposed in this paper. The novel algorithm uses the same membrane structure, subalgorithms and transporting mechanisms as Nishida's algorithm, but adopts two classes of active evolution operators and a good initial solution generating method. Computer experiments show that the AEAPS produces better solutions than Nishida's shrink membrane algorithm and similar solutions with an approximate optimization algorithm integrating P systems and ant colony optimization techniques (ACOPS) in solving TSPs. But the necessary number of iterations using AEAPS is less than both of them.
Keywords: P systems, active evolutionary algorithms, traveling salesman problems.

1 Introduction

Membrane computing, a milestone in natural computing, was introduced by Gheorghe Păun [1] in 1998. This computational model, which was inspired by the structure and the behavior of living cells, was proposed. In the following more than ten years, a sizeable group of researchers were seduced by membrane computing. Membrane algorithm is one of the research hotspots after Nishida [2–4] first proposed this concept by combining P systems and meta-heuristic search methodologies. Huang [5, 6] and Cheng [7] combined genetic algorithm and differential evolution with membrane systems to solve some single- and multi-objective optimization problems. Quantum-inspired evolutionary algorithm based on P systems was proposed to solve some classical theoretical [8,9] and practical problems [10–17]. Also some novel membrane algorithms based on particle swarm optimization [18] and artificial fish swarm algorithm [19] were proposed.

Evolutionary algorithm is based on survival of the fittest. Creatures do not have ability to decide their mutation directions and choose advantageous gene to their offspring. But based on the researches in biology, this stochastic evolution theory could not explain some problems in creature's adaptability. The modern biology research shows that the evolution process is not completely stochastic [20–22]. So called stress-induced mutation mechanisms were proposed. Specifically, when creatures are maladapted to their environment, that is, when they are stressed, stress-induced mutation mechanisms produce mutations [23–26]. These facts have been considered in evolutionary algorithm for solving optimization problems [27].

In this paper an approximate algorithm combining P systems and active evolutionary algorithms (AEAPS) is proposed in order to solve traveling salesman problems (TSPs) in the special case of complete graphs with Euclidean distance. It follows the nested membrane structure adopted by Nishida [2], and adopts genetic algorithm (GA), tabu search and active evolutionary algorithms (AEA) as the subalgorithms. Experiment results are compared with Nishida's

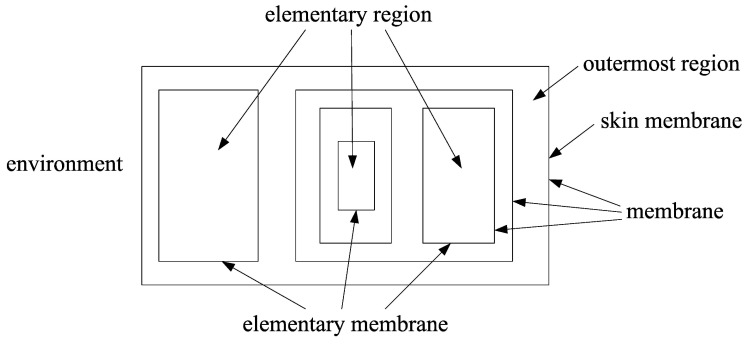

Figure 1: The membrane structure of a cell-like P system

algorithm and an approximate optimization algorithm integrating P systems and ant colony optimization techniques (ACOPS) [28, 29].

In Section 2, a brief introduction of P systems and Nishida's membrane algorithm for TSPs is given. Details of AEA designed for TSPs and AEAPS is discussed in Section 3. The experiment results and analysis are mentioned in Section 4. Conclusions are drawn in Section 5.

2 P Systems and membrane algorithm

2.1 P Systems

P systems could be divided into three groups: cell-like P systems, tissue-like P systems and neural-like P systems [30]. The structure of cell-like P systems is the basic structure of other P systems. The membrane structure of a cell-like P system is shown in Fig. 1. The outermost membrane is the skin membrane. Outside of the skin membrane is the environment. Usually, there are some other membranes inside the skin membrane. We call the spaces between membranes regions. The region just inside the skin membrane is the outermost region, and the region in an elementary membrane is an elementary region. In membrane computing, regions contain multisets of objects and sets of evolution rules.

A cell-like P system is formally defined as follows [1, 31]:

$$\Pi = [V, T, \mu, w_1, \ldots, w_m, R_1, \ldots, R_m, i_0]\,. \tag{1}$$

where:
(i) V is an alphabet; its elements are called objects;
(ii) $T \subseteq V$ is the output alphabet;
(iii) μ is a membrane structure consisting of m membranes; m is called the degree of Π;
(iv) w_i, $1 \leq i \leq m$, is a string representing the initial multiset over V associated with region i, $1 \leq i \leq m$;
(v) R_i, $1 \leq i \leq m$, is a finite set of evolution rules associated with region i, $1 \leq i \leq m$;
(vi) i_0 is a number between 1 and m which specifies the output membrane of Π.

The rules of R_i, $1 \leq i \leq m$, have the form $a \to v$, where $a \in V$ and $v \in (V \times \{here, out, in\})^*$. The multiset v consists of pairs (b,t), $b \in V$ and $t \in \{here, out, in\}$. *here* means when the rule is used in one region, b will stay in the region; *out* means that b exits the region and *in* means that b will be communicated to one of the membranes contained in the current region.

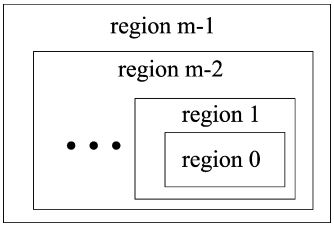

Figure 2: Membrane structure of membrane algorithm

2.2 The membrane algorithm for TSPs

Membrane algorithm is designed with the hierarchical or network structure of membranes and rules of P systems, and the concepts and principles of meta-heuristic search methodologies. It is a new kind of parallel-distributed framework for solving optimization problems. Nishida first proposed a membrane algorithm using cell-like P systems (nested membrane structure) [2] to solve TSPs. Nishida also proposed some improved membrane algorithms based on tissue-like P systems, such as compound membrane algorithm [3] and shrink membrane algorithm [4]. All the basic concepts of improved algorithms are based on the membrane algorithm. For example, compound membrane algorithm has two phases. The first phase is using membrane algorithm generating good initial solutions for phase 2; and the second phase is also similar to membrane algorithm but using good initial solutions. The shrink membrane algorithm incorporates dynamic membrane structure into compound membrane algorithm. The membrane algorithm with nested membrane structure is a special case of multi-deme evolutionary algorithm [32]. In this paper, we only research membrane algorithm with this structure.

In Nishida's membrane algorithm, nested membrane structure, rules in membrane separated regions and transporting mechanisms through membrane from P systems are adopted. The structure of the membrane algorithm is shown in Fig. 2.

In solving TSPs, the membrane algorithm can be described as follows:
1. Generate one initial solution in region 0 and two initial solutions in all regions from 1 to $m-1$ respectively;
2. In one iteration, the solution in region 0 is updated by tabu search and the solutions in regions from 1 to $m-1$ are updated by genetic algorithm, simultaneously;
3. Regions from 1 to $m-2$ send the best solution to adjacent inner region, and the worst solution to adjacent outer respectively. Region 0 sends the worst solution to region 1 and region $m-1$ sends the best solution to region $m-2$.
4. Erases solutions but the best two in regions from 1 to $m-1$ and the best one in region 0.
5. Jump to step 2 if the termination condition is not satisfied; otherwise the output of the algorithm is the solution in region 0.

3 AEAPS for TSPs

In active evolution organisms adapt their behaviour to changing environment. In TSPs, the "environment" means the structure characteristics of a solution, like without crossings in its path of traveling. If a solution is maladapted to the "environment", some active mutation mechanisms should be considered to improve it. In this section we propose two classes of active evolution conditions and show how to deal with these conditions; then we give a simple method of obtaining good initial solutions; finally, every step of AEAPS is described.

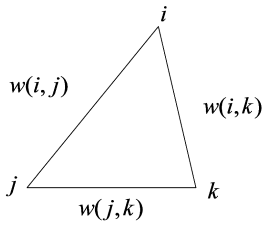

Figure 3: Triangle inequality for (G, w)

3.1 1^{st} class active evolution condition

TSP is one of the well-known combinatorial optimization problems. The TSP problem is about finding the Hamilton cycle. i.e., the optimum shortest path of a given weighted undirected and connected graph (G, w) with N nodes and where w is a distance metric. This distance is symmetric, which means $w(i, j) = w(j, i)$. In the two dimensional space, the distance between vertex i and vertex j is

$$w(i, j) = \sqrt{(x_i - x_j)^2 + (y_i - y_j)^2}. \tag{2}$$

where i and j have the coordinates (x_i, y_i) and (x_j, y_j), respectively.

The value of one solution is

$$V = \sum_{i=1}^{N-1} w(i, i+1) + w(N, 1). \tag{3}$$

Since w is a distance, then it satisfies the triangle inequality, i.e., $w(i, j) \leq w(i, k) + w(j, k)$, for any vertices $i \neq j$, and $k \neq i, j$ (see Fig. 3).

It has been shown that 2-Opt iterative improvement method [10, 33, 35] leads to optimum solutions for the TSP without any crossings. This means that any optimal path contains edges of the graph that do not intersect each other. If we consider four nodes. The total graph associated with these four nodes shows convex and concave quadrilaterals. When the convex quadrilateral is considered, any two edges are disjoint (they do not intersect each other). This is no longer true for the concave quadrilateral. In Fig. 4, we select a as the starting node, and there can be 6 possible solutions. Solutions *abcda* and *adcba* have no crossings, and solutions *abdca*, *acbda*, *acdba* and *adbca* have crossings. One can easily show that the solutions without crossings are better than those with crossings, by referring to the triangle inequality. For example, the path *abdca*, has two edges, (a, b) and (d, c), overlapping the path *abcda* ($(d, c) = (c, d)$). For the path *abdca*, we have $w(b, d) = w(b, o) + w(o, d)$ and $w(c, a) = w(c, o) + w(o, a)$. According to the triangle inequality, we have

$$\begin{aligned} w(b, d) + w(c, a) &= w(b, o) + w(o, d) + w(c, o) + w(o, a) \\ &= w(b, o) + w(c, o) + w(o, d) + w(o, a) \\ &\geq w(b, c) + w(a, d) \end{aligned} \tag{4}$$

So we found solution *abcda* without crossings is better than solution *abdca* with crossings. With this method, other solutions with crossings can also be transformed into a better ones without crossings. One can conclude stating that for the TSP problem, with Euclidian distance, for any solution with crossings there is always a better one without crossings.

In our AEAPS method we use a specific stress-induced mutation to the current solution. This mutation operator is different from the usual one theory of evolution. This is an active evolution

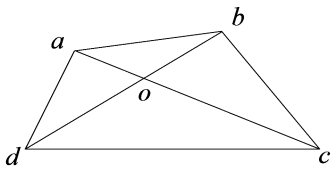

Figure 4: Example with four nodes

$$\text{Old solution}: \quad 1,2,\cdots,i-1,i,i+1,\cdots,j-1,j,j+1,\cdots N$$
$$\Downarrow 1^{\text{st}} \text{ class active evolution}$$
$$\text{New solution}: \quad 1,2,\cdots,i-1,j+1,j,j-1,\cdots,i+1,i,\cdots N$$

Figure 5: A 1^{st} class active evolution condition applied

operator. If in the current path there is an edge from i to $i+1$ that crosses other existing edge in the path, then i is called a 1^{st} class active evolution node. The method of revising the path according to a 1^{st} class active evolution node is the following:
1. Find the nearest N_1 nodes to i and denote by A the set consisting of these nodes;
2. Select one node from the set A and name it j;
3. Find out node $j+1$ which is the next node after j in the solution;
4. Swap the nodes i and $j+1$ in the solution;
5. If the value V of the new solution is less than the old one, keep the new one, otherwise keep the old one.

An illustration of the method is provided in Fig. 5.

3.2 2^{nd} class active evolution condition

If the distance from i to the next node, $i+1$, is larger than some value D, i is called a 2^{nd} class active evolution node. In this case insert a new node between i and $i+1$. Also compute$D_i = e \times total_distance_i/(N-1)$, where e is a parameter, $total\_distance_i$ is the total distance between i and the other nodes and N is the number of nodes.

In AEAPS we consider an approach similar to 2.5-Opt iterative improvement scheme [36] for dealing with 2^{nd} class active evolution nodes. This method is described below, where i is a 2^{nd} class active evolution node and $i+1$ is the next node after i in the current solution:
1. Find the nearest N_2 nodes to i and put them all into a set A; similarly build the set B for $i+1$;
2. Select one element from $A \cap B$ and name it j;
3. Eliminate j from the solution and insert it between i and $i+1$;
4. If the value of the new solution is less than the old one, keep the new one, otherwise keep the old one.

An illustration of the use a 2^{nd} class active evolution node is shown in Fig. 6.

3.3 Initial solutions

Nishida proposed a membrane algorithm, called compound membrane algorithm, which has two phases. The function of the first phase is producing good solutions which are used as initial

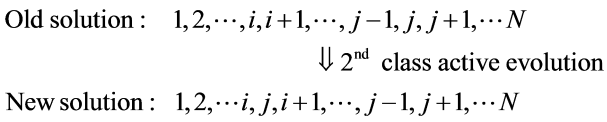

Figure 6: A 2^{nd} class active evolution condition applied

solutions for phase two. The better initial solutions can improve the final output solution. As Nishida said the computation time of compound membrane algorithm is quite prohibitive. We propose a simpler and faster method for generating good initial solutions. The method is as follows:
1. Select one node randomly as the starting node, and name it current node;
2. Find the nearest neighbour of the current node which is not selected, and name it current node;
3. Repeat step 2 until all nodes are selected; a good initial solution has been then found.

If we repeat the above steps for $2 \times m - 1$ times, we get enough initial solutions for each region of the P system. We have one solution in region 0 and two solutions in each of the regions 1 to $m - 1$.

3.4 AEAPS algorithm

AEAPS uses the basic idea of the membrane algorithm proposed by Nishida; a nested membrane structure with m regions is considered. We still use tabu search in region 0 and genetic algorithms in regions 1 to $m-1$ as sub-algorithms. Finally, the same communication mechanisms between adjacent regions are used; the best and worst solutions are sent to adjacent inner and outer regions, respectively. Unlike the Nishida's algorithm, AEAPS adds two classes of active evolution operators in every region and use a new initial solution generation method.

The overall membrane algorithm can be described as follows:
1. Generate initial solutions by using the method mentioned in Section 3.3, one for region 0 and two for each of the regions from 1 to $m - 1$;
2. Modify solutions simultaneously in each of the regions 1 to $m-1$ by using genetic algorithms, simultaneously;
3. Find out all 1^{st} class active evolution nodes in every solution and revise them; then find out all 2^{nd} class active evolution nodes and also revise them all;
4. Use tabu search in region 0;
5. Use the communication mechanisms between adjacent regions (as proposed by Nishida);
6. Remove all solutions but the best one from region 0 and best two in each of the regions 1 to $m - 1$;
7. Jump to step 2 if the number of iterations is not satisfied; otherwise the output of the algorithm is the solution in region 0.

4 Experiments and Results

We have tested the searching efficiency of AEAPS on two benchmark problems, eil51, with 51 nodes, and kroA100, with 100 nodes, from TSPLIB [37], running 10 times each. The parameters in experiments are chosen as follows: $m = 50$, $e = 0.1$, $N_1 = 25$, $N_2 = 35$. The number of iterations is 300. Table 1 shows the results. A comparison of simulated annealing (SA), shrink

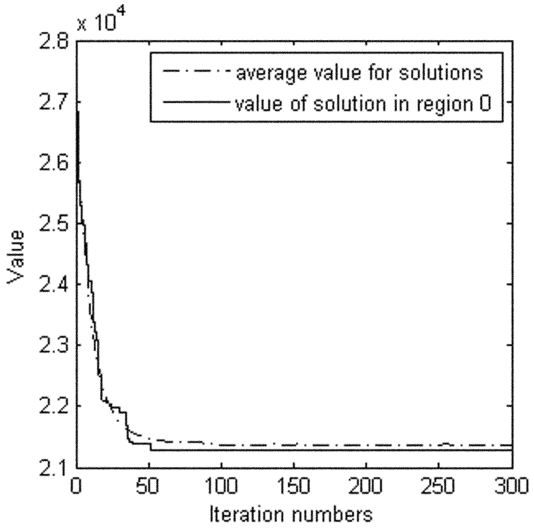

Figure 7: Curves of solving kroA100 problem by AEAPS

membrane algorithm (SMA) and AEAPS is shown in Table 2. We have implemented AEAPS in C and tested the algorithm on a Microsoft Visual C++ 6.0 platform with Windows 7 and using a computer with 2.4GHz CPU and 2G RAM.

Table 1. Results of AEAPS for eil51 and kroA100

	1	2	3	4	5	6	7	8	9	10
$eil51$	431	429	428	428	426	430	429	428	429	427
$kroA100$	21282	21282	21320	21282	21389	21282	21373	21379	21282	21282

Table 2. A comparison of SA, SMA and AEAPS

	SA			SMA			$AEAPS$		
	$Best$	$Average$	$Worst$	$Best$	$Average$	$Worst$	$Best$	$Average$	$Worst$
$eil51$	430	438	445	429	430	433	426	429	431
$kroA100$	21369	21763	22564	21299	21504	21750	21282	21315	21389

Results of SA and SMA from [4] are shown in the tables. From Table 1 and 2, one can see that AEAPS gets better results than SA and SMA for both eil51 and kroA100. Fig. 7 shows the curves of average values for all the solutions and the average value of the solution in region 0 for the kroA100 problem solved by AEAPS. For initial solutions which are generated by the method in Section 3.3, the average value of the initial solutions in AEAPS is much smaller than those using the membrane algorithm [4]. Compared to Nishida's algorithm for solving the same problem by the 50 membranes, AEAPS converges to remarkably fast to good solutions, in approximately 50 steps.

Zhang [28, 29] proposed ACOPS for TSP, which uses a smaller number of function evaluations to achieve better solutions. Experimental comparisons between Nishida's algorithm, ACOPS and AEAPS are listed in Table 3 and Table 4. Results of Nishida's algorithm and ACOPS are from [28]. The results of Nishida's algorithm were calculated by using 50 membranes and 10000 iterations. In ACOPS the number of function evaluations (NoFE) is the

stopping criterion. An equivalent number of iterations was obtained by using the product of average iterations for elementary membranes $(g_{min}+g_{max})/2$ and the number of communications $2*(g_{min}+g_{max})*\text{NoFE}/(N+m)$. In solving ulysses22, eil51, eil76, eil101 and kroA100 problems, the parameters of AEAPS have the values: $m = 50$, $e = 0.1$, $N_1 = 25$, $N_2 = 35$, and the maximal number of iterations is 300. In solving ch150, gr202 and tsp225 problems, the parameters of AEAPS are: $m = 50$, $e = 0.1$, $N_1 = 40$, $N_2 = 50$, and the maximal number of iterations is 500. The results of the AEAPS are obtained from 10 independent runs.

Table 3. Number of iterations in Nishida's algorithm, ACOPS and AEAPS with 8 TSPs

	Nishida's algorithm	*ACOPS*	*AEAPS*
*ulysses*22	1.0e+5	7.7e+2	3.0e+2
*eil*51	1.0e+5	7.3e+2	3.0e+2
*eil*76	1.0e+5	7.5e+2	3.0e+2
*eil*101	1.0e+5	7.6e+2	3.0e+2
*kroA*100	1.0e+5	9.6e+2	3.0e+2
*ch*150	1.0e+5	7.8e+2	5.0e+2
*gr*202	1.0e+5	6.8e+2	5.0e+2
*tsp*225	1.0e+5	3.1e+2	5.0e+2

Table 4. Results of Nishida's algorithm, ACOPS and AEAPS with 8 TSPs

	Nishida's algorithm			*ACOPS*			*AEAPS*		
	Best	*Average*	*Worst*	*Best*	*Average*	*Worst*	*Best*	*Average*	*Worst*
*ulysses*22	75.31	75.31	75.31	75.31	75.32	75.53	75.31	75.31	75.31
*eil*51	429	434	444	429	431	434	426	429	431
*eil*76	556	564	575	546	551	558	543	545	547
*eil*101	669	684	693	641	647	655	631	638	643
*kroA*100	21651	22590	24531	21285	21320	21427	21282	21315	21389
*ch*150	7073	7320	7633	6534	6560	6584	6549	6554	6565
*gr*202	509.7	520.1	528.4	489.2	492.7	497.1	491.3	496.1	498.9
*tsp*225	4073.1	4153.6	4238.9	3899.6	3938.2	4048.2	3938.7	3992.3	4034.1

As compared with Nishida's algorithm, AEAPS uses much smaller number of iterations to achieve better solutions. As compared with ACOPS, AEAPS uses smaller number of iterations only except for the *tsp*225 and gets better results for the first 5 TSPs, similar results for ch150 problem and slightly worse results for the last 2 TSPs.

5 Conclusions

This work is the first attempt to discuss the role of active evolutionary operators in membrane algorithms. We present an approximate algorithm combining nested membrane structure, rules within regions and communication mechanisms of the P systems, and two classes of active

evolution operators and a good initial solution generating method. AEAPS is used to solve Euclidian TSPs, well-known NP-hard problems. The experiment results show that AEAPS performs better than SA and Nishida's membrane algorithm and similar with ACOPS, which requires a smaller number of iterations. In order to improve the performance of AEAPS, especially in solving large scale TSPs, our future studies will focus on other membrane structure options and communication mechanisms.

Acknowledgments.

This work is supported by the National Natural Science Foundation of China (Grant No. 61170030), the Chunhui Plan of Ministry of Education of China (Grant No. Z2012025), the Open Research Fund of Key Laboratory of Xihua University (Grant No. SZJJ2012-002), the Research Projects of Eduction Department of Sichuan Province (Grant No. 13ZB0017) and the Key Scientific Research Foundation of Xihua University (Grant No. Z1120943). The authors also gratefully acknowledge helpful comments and suggestions made by reviewers, which have significantly improved the presentation.

Bibliography

[1] Păun, G. (2000); Computing with membranes, *Journal of Computer and System Sciences*, ISSN 0022-0000, 61(1): 108–143.

[2] Nishida, T.Y. (2004); An application of P-system: A new algorithm for NP-complete optimization problems, *Proceedings of the 8th World Multi-Conference on Systems, Cybernetics and Informatics*, V: 109–112.

[3] Nishida, T.Y. (2005); An approximate algorithm for NP-complete optimization problems exploiting P-systems, *Proceedings of the 6th International Workshop on Membrane Computing*, ISBN 978-3-540-30948-2, 26–43.

[4] Nishida, T.Y. (2006); Membrane algorithms: Approximate algorithms for NP-complete optimization problems, *Applications of Membrane Computing*, ISBN 978-3-540-29937-0, 303–314.

[5] Huang, L.; He, X.X.; Wang, N.; Xie, Y. (2007); P systems based multi-objective optimization algorithm, *Progress in Natural Science*, ISSN 1002-0071, 17(4): 458–465.

[6] Huang, L.; Wang, N. (2006); An optimization algorithm inspired by membrane computing, *ICNC 2006, LNCS*, ISBN 3-540-45901-4, 4222: 49–52.

[7] Cheng, J.X.; Zhang, G.X.; Zeng, X.X. (2011); A novel membrane algorithm based on differential evolution for numerical optimization, *International Journal of Unconventional Computing*, ISSN: 1548-7199, 7(3): 159–183.

[8] Zhang, G.X.; Liu, C.X.; Gheorghe, M.; Ipate, F. (2009); Solving satisfiability problems with membrane algorithm, *Proceedings of the 4th International Conference on Bio-Inspired Computing: Theories and Applications*, ISBN 978-1-4244-3866-2, 29–36.

[9] Zhang, G.X.; Gheorghe, M.; Wu, C.Z. (2008); A quantum-inspired evolutionary algorithm based on P systems for knapsack problem, *Fundamenta Informaticae*, ISSN 0169-2968, 87(1): 93–116.

[10] Liu, C.X.; Zhang, G.X.; Zhu, Y.H.; Fang, C.; Liu, H.W. (2009); A quantum-inspired evolutionary algorithm based on P systems for radar emitter signals, *Proceedings of the 4th International Conference on Bio-Inspired Computing: Theories and Applications*, ISBN 978-1-4244-6438-8, 1–5.

[11] Liu, C.X.; Zhang, G.X.; Liu, L.W.; Gheorghe, M.; Ipate, F. (2010); An improved membrane algorithm for solving time-frequency atom decomposition, *WMC 2009. LNCS*, ISSN 0302-9743, 5957: 371–384.

[12] Liu, C.X.; Zhang, G.X.; Liu, H.W. (2009); A memetic algorithm based on P systems for IIR digital filter design, *Proceedings of the 8th IEEE International Conference on Pervasive Intelligence and Computing*, ISBN: 978-0-7695-3929-4, 330–334.

[13] Huang, L.; Suh, I.H. (2009); Controller design for a marine diesel engine using membrane computing, *International Journal of Innovative Computing Information and Control*, ISSN 1349-4198, 5(4): 899–912.

[14] Zhang, G.X.; Liu, C.X.; Rong, H.N. (2010); Analyzing radar emitter signals with membrane algorithms, *Mathematical and Computer Modelling*, ISSN 0895-7177, 52(11-12): 1997–2010.

[15] Yang, S.P.; Wang, N. (2012); A P systems based hybrid optimization algorithm for parameter estimation of FCCU reactor-regenerator model, *Chemical Engineering Journal*, ISSN 1385-8947, 211: 508–518.

[16] Zhang, G.X.; Gheorghe, M.; Li, Y.Q. (2012); A membrane algorithm with quantum-inspired subalgorithms and its application to image processing, *Natural Computing*, ISSN 1567-7818, 11(4): 701–717.

[17] Zhang, G.X.; Cheng, J.X.; Gheorghe, M.; Meng, Q. (2013); A hybrid approach based on differential evolution and tissue membrane systems for solving constrained manufacturing parameter optimization problems, *Applied Soft Computing*, ISSN 1568-4946, 13(3): 1528–1542.

[18] Zhang, G.X.; Zhou, F.; Huang, X.L. (2012); A Novel membrane algorithm based on particle swarm optimization for optimization for solving broadcasting problems, *Journal of Universal Computer Science*, ISSN 0948-695X, 18(13): 1821–1841.

[19] Tu, M.; Wang, J.; Song, X.X.; Yang, F.; Cui, X.R. (2013); An artificial fish swarm algorithm based on P systems, *ICIC Express Letters, Part B: Applications*, ISSN 1881-803X, 4(3): 747–753.

[20] Cairns, J.; Overbaugh, J.; Miller, S. (1988); The origin of mutations, *Nature*, ISSN 0028-0836, 335: 142–145.

[21] Hall, B.G. (1988); Adaptive evolution that requires multiple spontaneous mutations. I. Mutations involving an insertion sequence, *Genetics*, ISSN 0016-6731, 120(4): 887–897.

[22] Hall, B.G. (1991); Is the occurrence of some spontaneous mutations directed by environmental challenges?, *The new biologist*, ISSN 1043-4674, 3(8): 729–733.

[23] Ponder, R.G.; Fonville, N.C.; Rosenberg, S.M. (2005); A switch from high-fidelity to error-prone DNA double-strand break repair underlies stress-induced mutation, *Molecular Cell*, ISSN 1097-2765, 19(6): 791–804.

[24] Slack, A.; Thornton, P.C.; Magner, D.B.; Rosenberg, S.M.; Hastings, P.J. (2006); On the mechanism of gene amplification induced under stress in Escherichia coli, *Plos Genetics*, ISSN 1553-7390, 2(4): 385–398.

[25] Galhardo, R.S.; Hastings, P.J.; Rosenberg, S.M. (2007); Mutation as a stress response and the regulation of evolvability, *Critical Reviews in Biochemistry and Molecular Biology*, ISSN 1040-9238, 42(5): 399–435.

[26] Rosenberg S.M.; Shee, C.; Frisch, R.L.; Hastings, P.J. (2012); Stress-induced mutation via DNA breaks in Escherichia coli: a molecular mechanism with implications for evolution and medicine, *Bioessays*, ISSN 0265-9247, 34(10): 885–892.

[27] Shi, L.; Li, H.Y.; Yang, J.A. (2004); Active evolution based genetic algorithm, *Mini-micro Systems*, ISSN 1000-1220, 5(25): 790–793.

[28] Zhang, G.X.; Cheng, J.X.; Gheorghe M. (2010); An approximate algorithm combining P systems and ant colony optimization for traveling salesman problems, *Proceedings of the 8th Brainstorming Week on Membrane Computing*, ISBN 978-84-614-2357-6, 321–340.

[29] Zhang, G.X.; Cheng, J.X.; Gheorghe M. (2011); A membrane-inspired approximate algorithm for traveling salesman problems, *Romanian Journal of Information Science and Technology*, ISSN 1453-8245, 14(1): 3–19.

[30] Păun, G. (2007); Tracing some open problems in membrane computing, *Romanian Journal of Information Science and Technology*, ISSN 1453-8245, 10(4): 303–314.

[31] Păun, G.; Rozenberg, G. (2002); A guide to membrane computing, *Theoretical Computer Science*, ISSN 0304-3975, 287(1): 73–100.

[32] Erick, C.P. (1998); A survey of parallel genetic algorithms, *Calculateurs Paralleles*, ISSN 1260-3198, 10(2): 141–171.

[33] Croes, G.A. (1958); A method for solving traveling salesman problems, *Operations Research*, ISSN 0030-364X, 6(6): 791–812.

[34] Lin, S.; Kernighan, B.W. (1973); An Effective Heuristic Algorithm for the Traveling-Salesman Problem, *Operations Research*, ISSN 0030-364X, 21(2): 498–516.

[35] Helsgaun K. (2000); An effective implementation of the Lin-Kernighan traveling salesman heuristic, *European Journal of Operational Research*, ISSN 0377-2217, 126(1): 106–130.

[36] Bentley, J.J. (1992); Fast algorithm for geometric traveling salesman problems, *Informs Journal on Computing*, ISSN 1091-9856, 4(4): 387–411.

[37] http://www.iwr.uni-heidelberg.de/groups/comopt/software/TSPLIB95/

INTERNATIONAL JOURNAL OF COMPUTERS COMMUNICATIONS & CONTROL
ISSN 1841-9836, 10(1):100-111, February, 2015.

Routing Optimization for Delay Tolerant Networks in Rural Applications Using a Distributed Algorithm

C. Velásquez-Villada, F. Solano, Y. Donoso

Carlos Velásquez-Villada
Universidad de los Andes
Bogotá D.C., Colombia, South America
c.velasquez@ieee.org

Fernando Solano
Warsaw University of Technology
Poland, Nowowiejska 15/19, Warsaw
fs@tele.pw.edu.pl

Yezid Donoso*
Universidad de los Andes
Bogotá D.C., Colombia, South America
*Corresponding author: ydonoso@uniandes.edu.co

Abstract: Internet access can improve people's life quality by helping them to reduce and overcome the poverty and educational gaps. However, most rural communities in the world, specially in underdeveloped countries, do not have access to the Internet. Delay/Disruption Tolerant Networking (DTN) is a recent low-cost technology now being used to provide connectivity to rural towns were some transportation means periodically arrive. DTNs can be implemented to connect communities to Internet, since this technology takes advantage of the existing people's transportation infrastructure using it to move packets and messages to and from Internet.
This paper proposes a DTN mathematical optimization model that maximizes the availability probabilities of the paths from sources to destinations. We also present an opportunistic forwarding algorithm that takes into account the availability probability of a node's neighbors to decide if a node should forward a message or store the message until a node with a higher availability probability contacts it. This algorithm was tested in five different scenarios and in all of them it found a path to the destination.
Keywords: Disruption-Tolerant, Delay-Tolerant, availability probability, opportunistic forwarding, ICT for rural development, Rural telecommunications.

1 Introduction

Most rural communities in the world have scarce or non-existent Internet availability [1]. According to the ITU [1], only 38.8% of the world's population have access to Internet, either fixed or mobile. Most of these connections are concentrated in the main cities, leaving most of the world's surface with almost no Internet availability. Several governments are increasing the availability of Internet in their territories, showing an increase of 145.57% from 2006 to 2013, as can be seen in the Internet penetration figures from ITU [1]. The initiatives to bring Internet to more people include optical fiber deployments, satellite connectivity solutions, electronic devices for people in remote towns and training for them to use these new devices and connections.

Even with these efforts, many people will still be left behind without constant Internet connectivity or without connectivity at all. The Delay/Disruption Tolerant Networking (DTN) architecture proposed in [2] is a new technology that can connect users in rural and disconnected places. This DTN technology can give disconnected users access to information that can help them overcome the digital divide and become net citizens taking full advantage of the information,

education and opportunities that Internet can provide. Benefits of this connectivity include access to learning materials like Wikipedia, distance learning courses or even offline versions of Massive Online Open Courses (MOOCs) that gives them the same education contents that their urban counterparts receive; thus, helping them to reduce the poverty gap [1, 3, 4].

There are also benefits when the local infrastructure is created in the communities where people can create contents and share them with others. Local news can be reported on a local website, people can share their music, documents, videos or libraries. In some communities, people have created local websites for their businesses and even local radio stations over the net. These applications depend on a strong deployment of a local infrastructure and the presence of people willing to train and educate locals. Even without the community network, the opportunities that can arise from a connection point and information distribution in an asynchronous way can bring many benefits for the inhabitants around these deployments. Applications that show the benefits of giving ICT to people in remote communities and accompanying these technologies with the respective knowledge, training and following can be found in many fields: Healthcare [5–7], banking opportunities [8, 9], agriculture development [10–12], businesses creation and growing [8, 13], politics accountability and participation [14], and education [15].

Although there are many studies about DTN architectures and technologies (as can be seen in Section 2), research and developments in application software and specially in routing protocols are still missing. Most current applications and protocols fail when implemented in a DTN environment, due to long delays or frequent disruptions. The focus of this work is on developing a routing algorithm that can be used in a real application to bring Internet connectivity to rural communities around the world.

This paper introduces a mathematical model to represent the best path choices in a Delay/Disruption Tolerant network designed for rural connectivity scenarios. This model is built based on previous models developed by the authors [28–30]. The model uses the availability probabilities of the network's links and their changes through time to calculate the best paths from the information sources to their destination. The model gives, as a result, the optimal decisions that the nodes can make to send their information to the destination (when should a node send a message to a neighbor and to which neighbor and when should this node store the message in its buffer to send it later instead). This paper also introduces a distributed heuristic algorithm to make forwarding decisions. This algorithm is implemented at each node in the simulation, and it decides whether to forward or store the messages based on the availability probability of a node's neighbors (if this availability probability is good enough will be decided via a variable parameter that will be used and tested in the simulation).

This paper extends paper [31]. The key additions of this journal version are as follows. First, Section 2 includes and describes more related works, the DTN Architecture, and DTN implementations for rural solutions. Secondly, this paper contains an extended explanation of the mathematical model presented in Section 3 and of the heuristic algorithm from Section 4. Finally, this paper contains additional results for the simulated scenarios.

This paper is organized as follows: Previous and related works are summarized in Section 2; Section 3 introduces the mathematical model used to calculate the optimal forwarding decisions; Section 4 describes the distributed heuristic algorithm implemented for the simulation; Section 5 shows and discusses optimization and simulation results; finally, conclusions and possible directions for future research are summarized at the end of the document.

2 Related Work and DTN Architecture

Delay/Disruption Tolerant Networks (DTN) are a relatively new kind of network that work in challenging environments [2, 16–23]. These networks have been developed with new protocols

tailored to their needs, which can make them incompatible between different applications and even with the Internet. Each one of these networks works within its own boundaries with known and relatively homogeneous delays and error rates, and some have trusted boundary devices to translate inner messages to different protocols for external communications.

The initial application for the DTN, where the name appeared, was the Interplanetary Internet Project [17], an idea from NASA to interconnect devices in space. It was motivated from the Pathfinder mission to Mars (1997), but it was tested in the Spirit and Opportunity missions in Mars (2004) due to a failure in the communication solution implemented in one of these rovers. After this experience, NASA started working and researching for an InterPlanetary Internet with the idea of connecting most of the devices in the space to provide a reliable store and forward network for all current and future missions. They also imagined a future where different spatial agencies could use these protocols and extend the reach of this InterPlanetary Network (IPN) for further spatial exploration.

Earthly DTN protocols face other challenges, mainly high rates of disruptions or failures. They must enable interconnectivity between different networking technologies in order to allow these technologies–used for wireless sensor networks, unmanned vehicular networks, battlefield monitoring and smart infrastructure–to communicate through the Internet and with each other. Protocols must account for variable delays, variable error rates, network disruptions and attacks.

The architecture for DTN proposed in [2] tries to change or at least relax some assumptions built into the Internet architecture. These assumptions are that there are end-to-end paths between source and destination; that retransmissions based on feedback from data receivers are effective for errors correction; that end-to-end loss is relatively small; that all network nodes support the TCP/IP protocols; that applications does not need to be aware of the communications performance; that security can be achieved through mechanisms on end nodes; that packet switching is the most appropriate abstraction for interoperability and performance; and, that a single route is sufficient for acceptable performance. The DTN architecture relaxes most of these assumptions using variable-length messages; a naming syntax that supports a wide range of naming and addressing; store-and-forward over multiple paths; security mechanisms against unauthorized use; classes of service; delivery options; and a way to express the useful lifetime of data.

The DTN architecture [2] uses a Bundle layer [21] that serves as middleware between the application layer and lower layers. This bundle layer shows a transparent interface for applications that can go through the Internet or DTN. However, applications for DTN must follow some design principles: they should minimize the number of round-trip exchanges, cope with restarts after failure while network transactions remain pending, and inform the network of the useful life and relative importance of data to be delivered. The bundle layer provides unacknowledged, prioritized (but not guaranteed) unicast message delivery. It also provides two options for enhancing delivery reliability: end-to-end acknowledgments and custody transfer. Applications can use these end-to-end acknowledgments for reliability. The custody transfer option allows a node to give the responsibility for reliable transfer of messages to other node, a "custodian". Nodes in the DTN can be custodians or can choose not to be based on available resources and network congestion. A custodian-to-custodian acknowledgement mechanism is implemented in the bundle layer.

The Bundle Protocol defines a convergence layer where underlying protocols will function to provide successful end-to-end communications. These convergence layers accomplish communications between nodes and can comprise a whole network stack with transport and network protocols that can run on top of existing networking technologies. Many protocols can exist in these convergence layers (the protocols themselves are called convergence layers), but they must provide at least two services to the bundle protocol agent: "sending a bundle to all bundle

nodes in the minimum reception group of the endpoint identified by a specified endpoint ID that are reachable via the convergence layer protocol; and delivering to the bundle protocol agent a bundle that was sent by a remote bundle node via the convergence layer protocol." [21].

Demmer [24] presents a full implementation of the previous architecture with storage and routing developments and an available simulation environment. Daknet [25] is a project developed by MIT researchers that tackles the problem of Internet connectivity in rural or remote communities and is the closest one to the idea presented here. Daknet aims to provide connectivity to remote villages were some wireless networking devices have been installed (kiosks) in strategic places and in buses or public service vehicles (Mobile Access Points, MAPs) that eventually will go to this and other villages and bigger towns, delivering messages between these disconnected networks and also accessing Internet (for non-real time access) at some moment and delivering and retrieving requested information. Authors in [20], [26] and [27] present developments on DTNs for underdeveloped regions concluding that providing full reliability and good strategies for data forwarding are difficult objectives in these scenarios.

3 Optimization Problem

Topology of DTNs is usually unreliable and constantly changes due to their nodes movement. However, we can use these same node movements to transmit messages in the network and to Internet. In this section, we present the problem of finding the best path in the network from one or more sources to a destination (it can be a node connected to Internet) based on the availability probabilities of the links between the nodes. The mathematical model takes into account that the availability probability of a link can change from one instant of time to another. The model has complete information over the network and can decide whether to send a message over a link or wait (storing the message in an internal buffer) until there is a link with a better availability probability. Thus, the network model presented in this paper maximizes the availability probability of the paths from sources to destinations, see Fig. 1. The model assumes that every node has storage capabilities, that it can serve as a relay for messages from other nodes and that it can send a message at any moment of time. The links between the nodes are given as are given their availability probabilities that serve to model the movement of the nodes, these probabilities are assumed to be independent and following an uniform distribution for testing purposes.

Table 1: Mathematical model parameters

Parameter	Definition
P	Set of candidate paths
T	Set of discrete time intervals
c_{ij}	Capacity of edge $(i,j) \in E$.
c_{ii}	Storage capacity of node i
$a_{ij}(t)$	Availability Probability of edge $(i,j) \in E$ at time t
	It is assumed that the availability probability of the edge (i,j)
	is the same as the one for the edge (j,i)
t	discrete time interval, where $t \in T$
δ_t	Time interval duration

The model starts with a network represented by a graph $G = (N, E)$, where N is the nodes set and E is the edges set. The edges set has the connections between the nodes. The graph G is extended in a new graph $G\prime = (N\prime, E\prime)$ that contains a copy of the original graph for every change

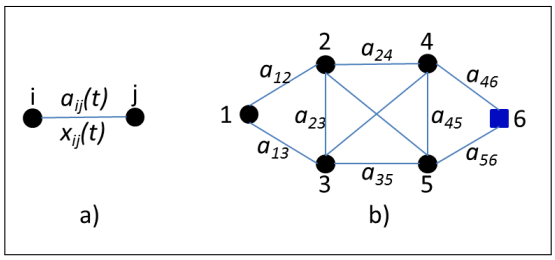

Figure 1: Network representation (a) two-node graph; (b) six-node graph

in a link's availability probability. The extended graph $G\prime$ is used by the optimization algorithm to make decisions on forwarding or storing the messages, since it has all the information about the network changes, see Fig. 2. Table 1 shows the main parameters used in the mathematical model. Set T contains the time intervals t that define the validity of the links' availability probabilities. These time intervals have a duration equal to δ_t. We are assuming that all time intervals have the same extent and that this time period lasts long enough to send a message between two neighboring nodes. Capacities are assumed to be constant, since they depend on the hardware of the nodes and because of this are not so easily changed.

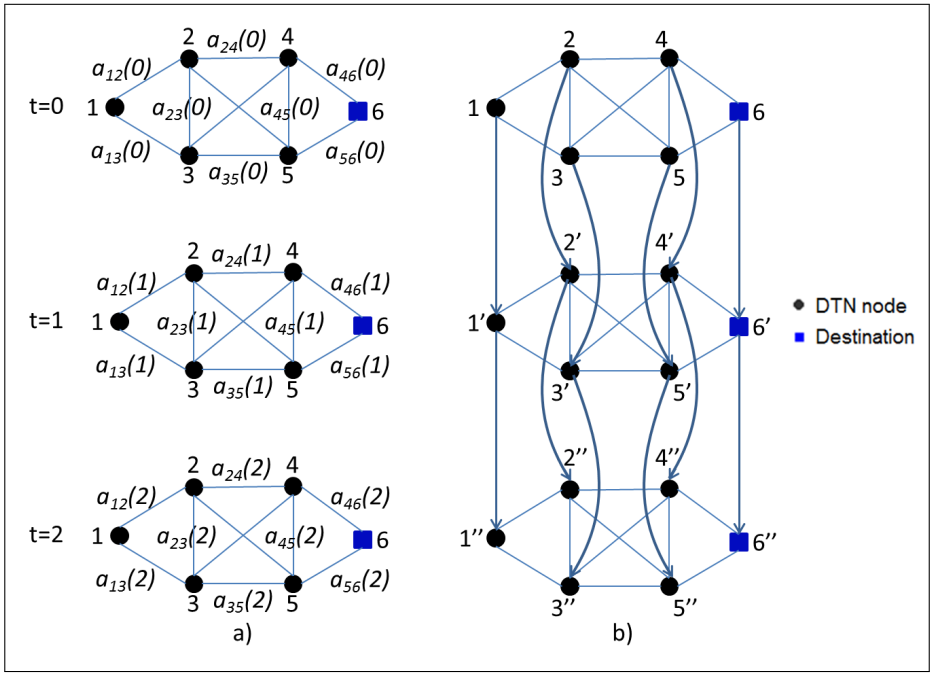

Figure 2: Network graph (a) original graph changes through time; (b) extended graph with the availability probabilities through time represented at once

$$\max \prod_{(i,j)\in P} a_{ij}(t)x_{ij}(t) \tag{1}$$

$$\max \sum_{(i,j)\in E} \log\left(a_{ij}(t)\right) x_{ij}(t) \tag{2}$$

Constraints

$$\sum_{j \in N} x_{ij}(t) - \sum_{j \in N} x_{ji}(t) + x_{ii}(t) - x_{ii}(t-1) = b_i(t) \qquad \forall (i,j) \in E, i \neq j \tag{3}$$

$$x_{ij}(t) \leq c_{ij}\delta_t \qquad \forall (i,j) \in E \tag{4}$$

$$x_{ij}(t) \in \mathbb{Z}_{\geq 0} \qquad \forall (i,j) \in E, p \in P \tag{5}$$

Equation (1) shows the objective function that maximizes the network availability probability of the paths from sources to destination. This objective function multiplies the availability probabilities of the links in a path, since we are dealing with probabilities and we want to obtain the path that maximizes these availability probabilities. We are assuming that the internal buffer is always available, so this availability probability (to store a message in its buffer) is always 1. A linear approximation of the objective function is shown in Equation (2). Decision variable $x_{ij}(t)$ determines the amount of information that flows through the link (i, j) using positive integers (5). $x_{ij}(t)$ is greater or equal than 1 if the link (i, j) is in the path p for a source to a destination, and 0 otherwise.

Constraints (3) and (4) are data-flow constraints and they keep the information flow below the channels and buffers capacities and guarantee that the messages reach their destinations.

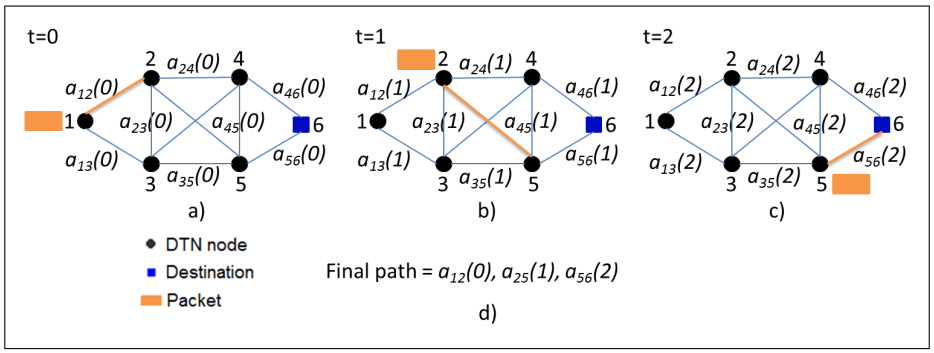

Figure 3: Network routing solution (a) decision taken at time 0; (b) decision taken at time 1; (c) decision taken at time 2; (d) final path through time

Fig. 3 shows an example of the optimization algorithm at work. At time 0 node 1 creates a message to be sent to node 6 and all availability probabilities have their initial values. At this moment, node 1 chooses the highest availability probability to its neighbors and decides to send the message to node 2. Then, at time 1, all availability probabilities can change and node 2 have to decide where it should send the message or if the message should be stored in its internal buffer to be sent later. Node 2 decides to send the message to its neighbor with the highest availability probability, Node 5. Finally, node 5 sends the message towards its destination, node 6, at time 2.

4 Proposed Forwarding Heuristic

This section describes the forwarding heuristic implemented for the results section based on the mathematical optimization algorithm. The heuristic internal working is explained in Fig. 4 and the pseudocode is shown in Algorithm 1. The heuristic works as a distributed optimization algorithm in which each node has to decide by its own and with local information whether it can send a message to a neighbor or it should store the message in its local buffer until a better path becomes available, see Fig. 4. For a node running the heuristic to decide if a link has a

good enough availability probability it has to compare it against a set parameter (*alpha*). This forwarding heuristic can be used in a rural scenario that has at least one central, fixed wireless distribution point (AP), at least one mobile distribution point (MAP) that can be in contact with the local APs periodically (once a day or less in many cases, depending on the transportation means to the town). The APs and MAPs must have reasonable storage capabilities. The scenario has users in each village where at least an AP is deployed and users requests for information are not real-time ones and can wait for one or more MAP-AP contacts to be satisfied. Users must have the necessary technology to access the network and the appropriate training to use that technology and the applications given to them.

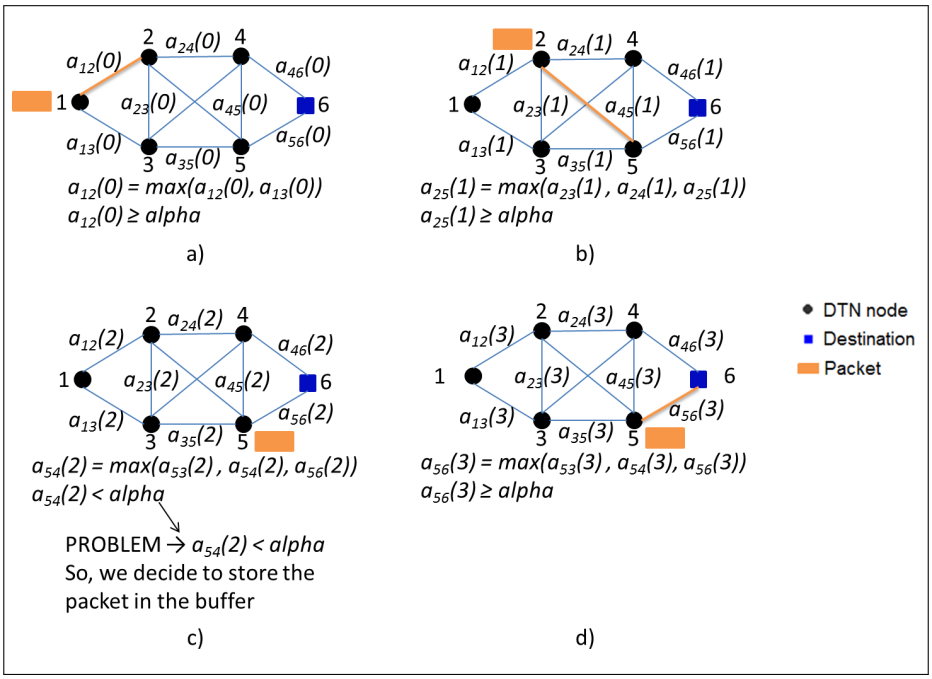

Figure 4: Network distributed heuristic (a) first step at time 0; (b) time 1 (c) time 2 (d) time 3

The forwarding algorithm, shown in Algorithm 1, is based on the assumption that every node knows the availability probability of its neighbors at any instant of time, and that if that probability is high enough (over a certain *alpha*) it can communicate with such neighbor. The alpha parameter is the threshold to take a forwarding action. If an availability probability is below this threshold (*alpha*) the node can assume that its neighbor is unreachable. Nodes do not have access to the whole network graph but they can discover which one is the destination or gateway in the network in order to send their requests to Internet. Nodes can create a request at any instant of time. In our forwarding strategy we take into account the information available at the node that is taking the forwarding decision; i.e., the availability probabilities of its neighbors. And we also take into account that the node should not return the packet to the node that sent it to him (but it can send it to another node, even if the packet visited that other node earlier).

5 Results

The proposed heuristic described in Section 4 was implemented using Java in a 64-bit CPU. Five different network configurations, from 6 to 10 nodes, as can be seen in Fig. 5, were simulated. In each scenario the last node received messages from all the previous nodes. These nodes created a message to be delivered through the path with the best availability probability but using only

```
node start (initialization)
send ID
listen for neighbors' IDs
if IDs received then
  | save them (IDs) in neighbors list
else
  | wait for messages()
end
if message received in queue then
  | if final destination = my ID then
  |   | read message and delete it from queue
  | else if message for other node then
  |   | check neighbors' availability probability, except previous node
  |   | if max(availability probability) ≥ alpha then
  |   |   | Send message to node with max(ap)
  |   | else
  |   |   | Store message in buffer until next time
  |   | end
  | end
else
  | wait for messages()
end
```

Algorithm 1: Distributed algorithm for every node in the network

local information. All nodes served as relays to convey messages to the destination (i.e., to the final node). Nodes had access to the availability probabilities of their links to their neighbors and they had to make a decision (send or store a message) based on this information and the parameter *alpha* (the threshold to decide if an availability probability is good enough). *alpha* was varied from 0.1 to 0.9 with 0.1 increases between each simulation run. We ran 10,000 simulations for each scenario and for every alpha to increase the confidence in the averaged results. The results, shown in Fig. 6, included the averaged values of all the availability probabilities of the paths from sources to destinations; the hop count and the time steps count until the last message was delivered to the final node. All these variables were measured for every alpha and plotted in a single graph for each scenario shown in Fig. 5 (see Fig. 6).

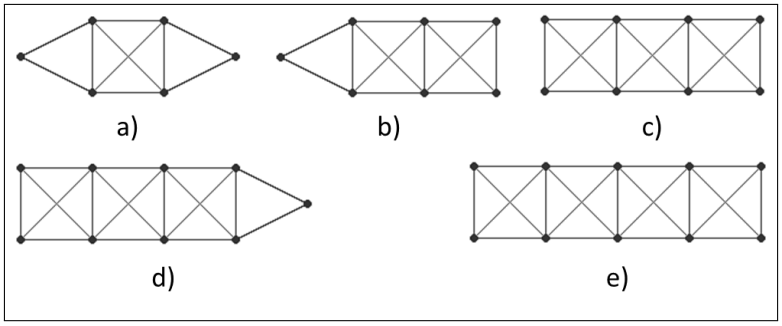

Figure 5: Scenarios used for the simulations with (a) 6; (b) 7; (c) 8; (d) 9; e) 10 nodes

As can be seen in Fig. 6, for *alpha* values between 0.1 and 0.6 there are no significant differences in all variables. The average hop count does not change; the time to deliver the messages presents an increase of around 7 steps (or a 30% increase); and the average availability probability shows an increase of around 0.1 (or a 30% increase). For *alpha* values from 0.7 to 0.9 the hop count remains steady but the time steps and the availability probability increase exponentially. The change in time steps from 0.6 to 0.9 alpha is around 200%; and the increase in availability probability is around 0.3 (an increase of around 77%). These results show that choosing an adequate *alpha* value is a critical decision and that choosing an *alpha* between 0.6 and 0.8 most likely provides the best trade-off between time to deliver the messages and availability probability of the paths. From Fig. 6 we can also see that the hop count does not change with alpha variations and that it depends on the network size (number of nodes) and

network topology.

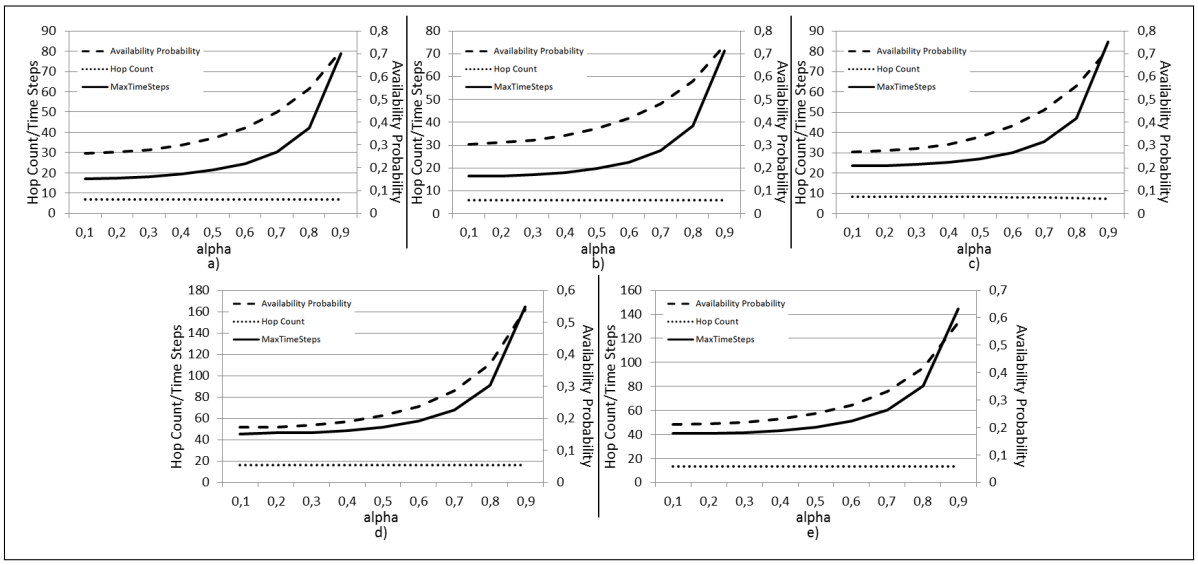

Figure 6: Results for the scenarios with (a) 6; (b) 7; (c) 8; (d) 9; (e) 10 nodes

6 Conclusions and Future Work

We have proposed a mathematical model for a Delay/Disruption Tolerant Network in a rural application based on the dynamic availability probabilities of the links between neighboring nodes. These availability probabilities model the movement of nodes and the opportunistic behavior of the solution. We used a linear approximation of the objective function through a logarithmic function that allows a faster implementation and solution.

For an application that can be implemented in a real scenario, we presented a distributed heuristic algorithm where nodes only have access to local information to make decisions. This heuristic was simulated for all the scenarios and it was able to deliver all the messages. The performance of the heuristic regarding the value of the *alpha* parameter was evaluated. From the results it can be seen that an *alpha* between 0.6 and 0.8 must be chosen in order to achieve a better availability probability of the paths without a notorious increase in the time needed to deliver all the packets. The hop count is independent of the *alpha* chosen, it is related to the number of nodes in the network but it also depends on the geometry of the graph and each node's degree.

The DTN implementation proposed here can be used in a rural environment to give Internet connectivity to the people living there using any transportation mean available to them. We have shown that the distributed algorithm used to decide whether to forward or store a message works as expected and can deliver all messages in the scenarios tested; however, this algorithm can benefit from recording previous contacts between nodes and sharing this information with other nodes to create a historical record of contacts and choose the nodes that are most likely to deliver the message in short time.

For future work we are working with the non-lineal model and the subproblem of path generation to evaluate those paths in the master problem (i.e., find the optimal path based on the availability probabilities of the links in it).

Acknowledgments

The research leading to these results has received funding from the European Union Seventh Framework Programme (FP7/2007-2013) under grant agreement no. 269985. The author Carlos Velásquez-Villada received funding by the Colombian "Departamento Administrativo de Ciencia, Tecnología e Innovación - Colciencias Conv. 528/2011".

Bibliography

[1] (2013), *Measuring the Information Society*, International Telecommunication Union. [Online]. Available: http://www.itu.int/en/ITU-D/Statistics/Pages/default.aspx

[2] Cerf, V.; Burleigh, S.; Hooke, A.; Torgerson, L.; Durst, R.; Scott, K.; Fall, K. & Weiss, H. (2007), Delay-tolerant networking architecture, *RFC4838*, April, 1-35.

[3] Andrew T. & Petkov, D. (2003) The need for a systems thinking approach to the planning of rural telecommunications infrastructure, *Telecommunications Policy*, 27:75-93.

[4] Johnson D. L. & Roux, K. (2008), Building rural wireless networks: Lessons learnt and future directions, *Proceedings of the 2008 ACM workshop on Wireless networks and systems for developing regions. ACM*, 17-22.

[5] Ruxwana, N. L.; Herselman, M. E. & Conradie, D. P. (2010), ICT applications as e-health solutions in rural healthcare in the Eastern Cape Province of South Africa, *Health information management journal*, Health Information Management Association of Australia, Limited, 39(1):17-26.

[6] De Savigny, D.; Kasale, H.; Mbuya, C. & Reid, G. (2008), Fixing health systems: linking research, development, systems, and partnerships, *IDRC*.

[7] Donner, J. (2004), Innovations in mobile-based public health information systems in the developing world: an example from Rwanda, *Workshop on mobile technologies and health: benefits and risks*.

[8] De Blasio, G. (2008), Urban-rural differences in internet usage, e-commerce, and e-banking: Evidence from Italy, *Growth and Change*, 39(2): 341-367.

[9] (2013) *Care*, [Online]. Available: http://www.care.org

[10] Warren, M. (2002), Adoption of ICT in agricultural management in the United Kingdom: the intra-rural digital divide, *ZEMEDELSKA EKONOMIKAPRAHA*, 48(1), pp. 1-8.

[11] (2013) *Fair trade USA*, [Online]. Available: http://www.fairtradeusa.org/

[12] Sohoo, S. (2008), ICT initiative of SAARC agriculture centre in the SAARC region, *Computer Science and Information Technology. ICCSIT 08. International Conference on. IEEE*, 923-929.

[13] Steinfield, C.; LaRose, R.; Chew, H. E. & Tong, S.T. (2012), Small and medium-sized enterprises in rural business clusters: The relation between ICT adoption and benefits derived from cluster membership, *The Information Society*, 28(2):110-120.

[14] Kannabiran, G.; Xavier, M. & Banumathi, T. (2008), E-governance and ICT enabled rural development in developing countries: critical lessons from RASI project in India, *International Journal of Electronic Government Research (IJEGR)*, 4(3): 1-19.

[15] Cheng, A.; Sinha, A.; Shen, J.; Mouakkad, S.; Joseph, L. & Mehta, K. (2012), Opportunities for social innovation at the intersection of ICT education and rural supply chains, *Global Humanitarian Technology Conference (GHTC), IEEE*, 328-335.

[16] Scott, K. (2009) Delay/disruption tolerant networking, *LISA09 Invited Talk*, USENIX. [Online]. Available: http://static.usenix.org/events/lisa09/stream1/scott.htm

[17] Warthman, F. (2012), Delay- and Disruption-Tolerant Networks (DTNs). A Tutorial. V. 2.0, *Interplanetary Internet Special Interest Group*, 2012.

[18] Burleigh, S.; Cerf, V.; Durst, R.; Hooke, A.; Rumeau, R.; Scott, K.; Travis, E. & Weiss, H. (2001), The Interplanetary Internet: The Next Frontier in Mobility, *Internet Global Summit*, June, 2001.

[19] Durst, R. C.; Feighery, P. D. & Scott, K. L. (2000), Why not use the standard internet suite for the interplanetary internet, *InterPlanetary Internet (IPN) Technical Information.*

[20] Fall, K. (2003), A delay-tolerant network architecture for challenged internet, *Proceedings of the 2003 conference on Applications, technologies, architectures, and protocols for computer communications*, 27–34.

[21] Scott, K. L. & Burleigh, S. (2007), Bundle protocol specification, *RFC5050*, November, 1-50.

[22] Akyildiz, I. F.; Akan, O. B.; Chen, C.; Fang, J. & Su, W. (2003), InterPlaNetary Internet: state-of-the-art and research challenges, *Computer Networks*, 43(2):75–112.

[23] Khabbaz, M. J.; Assi, C. M. & Fawaz, W. F. (2012), Disruption-tolerant networking: A comprehensive survey on recent developments and persisting challenges, *Communications Surveys & Tutorials, IEEE*, 14(2), 607–640.

[24] Demmer, M. J. (2008), *A Delay Tolerant Networking and System Architecture for Developing Regions*, PhD thesis, University of California at Berkeley.

[25] Pentland, A.; Fletcher, R. & Hasson, A. (2004), Daknet: Rethinking connectivity in developing nations, *Computer*, 37(1):78–83.

[26] Seth, A.; Kroeker, D.; Zaharia, M.; Guo, S. & Keshav, S. (2006), Low-cost communication for rural internet kiosks using mechanical backhaul, *Proceedings of the 12th annual international conference on Mobile computing and networking*, 334–345.

[27] (2013), *Technology and Infrastructure for Emerging Regions*, University of California at Berkeley. [Online]. Available: http://tier.cs.berkeley.edu/drupal/

[28] Montoya, G. A.; Velasquez-Villada, C. & Donoso, Y. (2013), Energy Optimization in Mobile Wireless Sensor Networks with Mobile Targets Achieving Efficient Coverage for Critical Applications, *International Journal of Computers Communications & Control*, 8(2), 247–254.

[29] Velasquez-Villada, C. & Donoso, Y. (2013), Multipath Routing Network Management Protocol for Resilient and Energy Efficient Wireless Sensor Networks, 1st International Conference on Information Technology and Quantitative Management (ITQM), Suzhou, China, May 16-18, 2013, *Procedia Computer Science*, 17:387-394.

[30] Montoya, G. A. & Donoso, Y. (2013), Energy Load Balancing Strategy to Extend Lifetime in Wireless Sensor Networks, 1st International Conference on Information Technology and Quantitative Management (ITQM), Suzhou, China, May 16-18, 2013, Procedia Computer Science, 17:395-402

[31] Velasquez-Villada, C.; Solano, F. & Donoso, Y. (2014), Opportunistic Forwarding Algorithm for Delay Tolerant Networks in Rural Applications, International Conference on Computers Communications & Control, Romania, Oradea, Baile Felix, May 6-10, 2014, *Abstracts of ICCCC 2014*, ISSN 1844-4334.

INTERNATIONAL JOURNAL OF COMPUTERS COMMUNICATIONS & CONTROL
ISSN 1841-9836, 10(1):112-122, February, 2015.

Energy-Efficient Design for Relay-Aided MIMO-OFDM Cognitive Radio Networks

B. Wu, J. Zuo, L. Zhao, C. Zou

Bin Wu*, Jiakuo Zuo, Li Zhao, Cairong Zou
School of Information Science and Engineering,
Southeast University, Nanjing, 210096, China
njwubin@seu.edu.cn, zuojiakuo85418@gmail.com
zhaoli@seu.edu.cn, cairong@seu.edu.cn
*Corresponding author:njwubin@seu.edu.cn

Abstract: With the explosive growth of high-rate multimedia services and promptly boomed energy consumption in wireless networks, energy-efficient design is become more and more important. In this paper, we investigate energy-efficient design for relay-aided multiple-input multiple-output-orthogonal frequency division multiplexing (MIMO-OFDM) cognitive radio networks. We formulate an energy-efficient power allocation problem, which takes a form of nonlinear fractional programming. To solve the problem, we first make a joint concave approximation to the original problem which facilitates the optimal algorithm development. Then, we derive an equivalent parametric optimization problem of the approximated problem. Finally, an iteration energy-efficient power allocation algorithm is presented. Numerical results reveal that the proposed algorithm can improve energy efficiency over traditional capacity maximization method.
Keywords: cognitive radio, power allocation, MIMO, relay, fractional programming.

1 Introduction

Cognitive radio (CR) and multiple-input multiple-output-orthogonal frequency division multiplexing (MIMO-OFDM) communications have been considered as a promising scheme to solve the spectrum scarcity problem and improve the quality of wireless communications [1]. Recently, to reduce the multi-path fading and improve the channel capacity, cooperative relaying technique is considered as a potent means to be adopted in the CR networks. Thus, the researches of relay aided MIMO CR networks are being received a growing attention in recent years [2, 3].

In [4], the relay selection and beamforming problem for the non-regenerative MIMO cognitive multi-relay network was considered and an optimal scheme was proposed via maximizing the capacity of the SUs by selecting the best cognitive MIMO relay. [5] studied a new paradigm for CR networks, which allowed the secondary users (SUs) to cooperatively relay the traffic for the primary users (PUs) while simultaneously transmitting their own traffic, and proposed a novel MIMO cooperative cognitive radio networks framework. [6] considered the power allocation problem for MIMO two-way CR sytem under a specturm sharing scenario, and presented an analytical expression of the optimal power allocation to each antenna of the treminals. [7] studied the power and channel allocation, and relay assignment for MIMO-OFDM based cooperative CR networks and proposed an optimal complexity algorithm and a sub optimal low complexity algorithm. [8] investigated subcarrier pairing and power allocation for MIMO-OFDM relay-aided CR networks and used environmental learning algorithm to mitigate the interference of the PUs. In the previous works, most researches intend to improve the throughput of relay aided CR systems. However, the energy efficiency (EE) has been considered more and more important in future wireless communication networks. The wireless devices and equipments consume about 9% of the total energy of information technology, the communication and information technology already contributes to about 2% of the global carbon dioxide emissions [9, 10]. Therefore green

communication, which emphasizes on EE in wireless communication networks, is attracting more and more attention [11, 12]. A large amount of work has bee reported on energy-efficient design for CR networks [13-15]. For MIMO CR networks, [16] studies EE optimization problem of MIMO CR broadcast channels to improve the system throughput for unit energy consumption. In [17], the throughput and energy efficiency optimization under quality-of-service (QoS) constraints for MIMO CR systems are studied. In [18], a promising framework of spectrum sharing strategy selection based on EE is proposed for MIMO CR interference channels.

In this paper, we focus on energy-efficient power allocation for relay-aided MIMO-OFDM CR networks. We formulate an optimization problem related to maximization of EE of the consider network under total power constraints of cognitive source node and cognitive relay node, and interference constraints of primary users. Since the original optimization problem is difficult to solve directly, we first get an approximated problem of the original problem, and then transform the approximated problem into an equivalent convex optimization problem. A new iterative energy-efficient power allocation scheme is presented at last. The rest of this paper is organized as follows: In Section 2, we introduce the system model and formulate an energy-efficient power allocation problem. In Section 3, the double-loop iterative method is presented. Finally, simulation results and Conclusions are presented in Section 4 and 5.

The following notations are used in this paper, $\mathbb{C}^{M\times N}$ denotes $M \times N$ complex matrix, $(\cdot)^H$ denotes the conjugate transpose, $(\cdot)^+$ means $\max(0, \cdot)$, the distribution of a circularly symmetric-complex-Gaussian vector with mean vector x and covariance matrix y is denoted by $CN(x, y)$, $diag(\cdot)$ returns a square matrix with the elements of $(\cdot)$ on the diagonal.

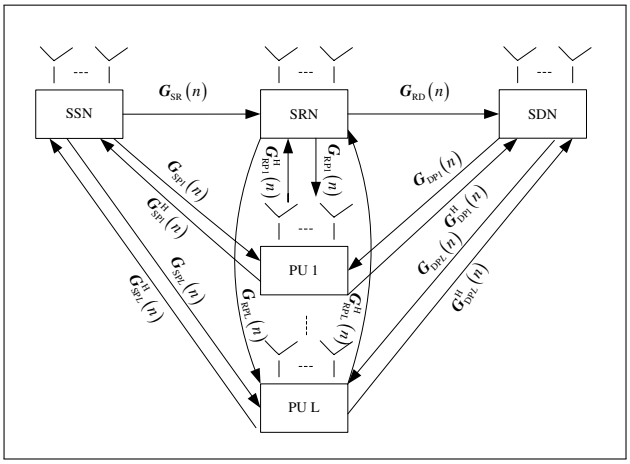

Figure 1: Relay-aided MIMO-OFDM cognitive radio network

2 Signal Model and Problem Statement

Consider a two-hop relay-aided cognitive radio (CR) network shown in Fig.1, there are a secondary source node (SSN), a secondary destination node (SDN), and a secondary relay node (SRN). The relay-aided CR network coexists with L licensed primary users (PUs). The SSN communicates with SDN through SRN, and they share the whole spectrum with PU. SSN, SDN, and SRN are equipped with M_S antennas, each PU is equipped with M_P ($M_P \leq M_S$)antennas. The relay-aided CR network adopts OFDM modulation for transmission, and the total number of available subcarriers for CR network is N. Let $\boldsymbol{G}_{SR}(n) \in \mathbb{C}^{M_S\times M_S}$ and $\boldsymbol{G}_{RD}(n) \in \mathbb{C}^{M_S\times M_S}$ denote the channel matrices from SSN to SRN and SRN to SDN over the n-th subcarrier respectively. Let $\boldsymbol{G}_{SPl}(n) \in \mathbb{C}^{M_p\times M_S}$, $\boldsymbol{G}_{RPl}(n) \in \mathbb{C}^{M_p\times M_S}$ and $\boldsymbol{G}_{DPl}(n) \in \mathbb{C}^{M_p\times M_S}$ denote the

channel matrices from SSN to l-th PU, from SRN to l-PU, and from SDN to l-PU, respectively. The channel matrix from l-th PU to SSN, SDN, and SRN are $\boldsymbol{G}_{SPl}^{H}(n)$, $\boldsymbol{G}_{RPl}^{H}(n)$ and $\boldsymbol{G}_{DPl}^{H}(n)$.

Assume there is no cooperation between CR network and PUs, environmental learning (EL) method [19] is performed to control the interference to the PUs. Via EL learning method, secondary nodes estimate the null space information of the channels between secondary nodes and PU. Assume the cognitive beamforming (CB) matrices at SSN, SRN, SDN for the n-th subcarrier are $\boldsymbol{U}_{SPl}(n) \in \mathbb{C}^{M_S\times(M_S-M_P)}$, $\boldsymbol{U}_{RPl}(n) \in \mathbb{C}^{M_S\times(M_S-M_P)}$ and $\boldsymbol{U}_{DPl}(n) \in \mathbb{C}^{M_S\times(M_S-M_P)}$, respectively. These CB matrices satisfy $\boldsymbol{U}_{SPl}^{H}(n)\boldsymbol{G}_{SPl}(n) = 0$, $\boldsymbol{U}_{RPl}^{H}(n)\boldsymbol{G}_{RPl}(n) = 0$ and $\boldsymbol{U}_{DPl}^{H}(n)\boldsymbol{G}_{DPl}(n) = 0$. However, the accurate CB matrices are difficult to be acquired, therefore in practical applications, the estimated CB matrices $\tilde{\boldsymbol{U}}_{SPl}(n)$, $\tilde{\boldsymbol{U}}_{RPl}(n)$ and $\tilde{\boldsymbol{U}}_{DPl}(n)$ are used.

In the first hop, the received signal at CRN in the n-th subcarrier is given by:

$$\boldsymbol{y}_R(n) = \boldsymbol{G}_{SR}(n)\tilde{\boldsymbol{U}}_{SPl}(n)\boldsymbol{x}_S + \boldsymbol{G}_{RPl}^{H}(n)\boldsymbol{w}_P^1 + \boldsymbol{z}_R(n) \tag{1}$$

where $\boldsymbol{x}_S$ is the transmitted signal of SSN, $\boldsymbol{w}_P^1$ is the PU interference to SRN in the first hop. $\boldsymbol{z}_R(n) \sim CN\left(0, \sigma_R^2\boldsymbol{I}_{M_S}\right)$ is the additive white Gaussian noise (AWGN) at SRN.

In the second hop, SRN first filters received signal $\boldsymbol{y}_R(n)$ with $\tilde{\boldsymbol{U}}_{RPl}^{H}(n)$, and then precodes the filtered signal by forwarding matrix $\boldsymbol{B}(n)$, finally precodes the resultant signal by $\tilde{\boldsymbol{U}}_{DPl}(n)$. Therefore, the received signal at SDN in the n-th subcarrier is:

$$\boldsymbol{y}_D(n) = \boldsymbol{G}_{RD}(n)\tilde{\boldsymbol{U}}_{RPl}(n)\boldsymbol{B}(n)\tilde{\boldsymbol{U}}_{RPl}^{H}(n)\boldsymbol{y}_R(n) + \boldsymbol{G}_{DPl}^{H}(n)\boldsymbol{w}_P^2 + \boldsymbol{z}_D(n) \tag{2}$$

where $\boldsymbol{w}_P^2$ is the PU interference to SDN in the second hop, $\boldsymbol{z}_D(n) \sim CN\left(0, \sigma_D^2\boldsymbol{I}_{M_S}\right)$ is additive white Gaussian noise (AWGN) at SDN in the n-th subcarrier.

Finally, the CR-DN does receive CB by filtering $\boldsymbol{y}_D(n)$ with $\tilde{\boldsymbol{U}}_{DPl}^{H}(n)$, we have

$$\boldsymbol{y} = \boldsymbol{D}_2(n)\boldsymbol{B}(n)\boldsymbol{D}_1(n)\boldsymbol{x}_S + \boldsymbol{D}(n)_2\boldsymbol{B}(n)\boldsymbol{n}_1(n) + \boldsymbol{n}_2(n) \tag{3}$$

where $\boldsymbol{D}_1(n) = \tilde{\boldsymbol{U}}_{DPl}^{H}(n)\boldsymbol{G}_{RD}(n)\tilde{\boldsymbol{U}}_{RPl}(n)$ and $\boldsymbol{D}_2(n) = \tilde{\boldsymbol{U}}_{RPl}^{H}(n)\boldsymbol{G}_{SR}(n)\tilde{\boldsymbol{U}}_{SPl}(n)$, $\boldsymbol{n}_1(n) = \Delta\boldsymbol{U}_{RPl}^{H}(n)\boldsymbol{G}_{RPl}^{H}(n)\boldsymbol{w}_P^1 + \tilde{\boldsymbol{U}}_{RPl}^{H}(n)\boldsymbol{z}_R(n)$, $\boldsymbol{n}_2(n) = \Delta\boldsymbol{U}_{DPl}^{H}(n)\boldsymbol{G}_{DPl}^{H}(n)\boldsymbol{w}_P^2 + \tilde{\boldsymbol{U}}_{DPl}^{H}(n)\boldsymbol{z}_D(n)$, $\Delta\boldsymbol{U}_{RPl}^{H}(n) = \tilde{\boldsymbol{U}}_{RPl}^{H}(n) - \boldsymbol{U}_{RPl}^{H}(n)$, $\Delta\boldsymbol{U}_{DPl}^{H}(n) = \tilde{\boldsymbol{U}}_{DPl}^{H}(n) - \boldsymbol{U}_{DPl}^{H}(n)$ denote the first-order perturbations of the CB matrices due to imperfect environmental learning [8, 19].

Let the singular value decomposition of $\{\boldsymbol{D}_k(n)\}_{k=1,2}$ be $\boldsymbol{D}_k(n) = U_k(n)\boldsymbol{\Lambda}_k(n)\boldsymbol{V}_k^{H}(n)$ $(k = 1, 2)$, and define $q_{m,n} = \sqrt{\frac{p_{m,n}^R}{p_{m,n}^S\lambda_{m,n}^{SR}+\sigma_R^2}}$, where $p_{m,n}^S$ and $p_{m,n}^R$ are the transmit power of SSN and SRN, $\lambda_{m,n}^{SR}$ is the eigenvalue of $\boldsymbol{G}_{SR}(n)$. Thus, the forwarding matrix can be defined as $\boldsymbol{B}(n) = \boldsymbol{V}_2^{H}(n)\boldsymbol{Q}(n)\boldsymbol{U}_1(n)$. Multiplying y with $U_{2,n}^{H}$ at SDN , we have

$$\boldsymbol{y} = \boldsymbol{\Lambda}_2(n)\boldsymbol{\Sigma}(n)\boldsymbol{\Lambda}_1(n)\boldsymbol{V}_1(n)\boldsymbol{x}_S + \boldsymbol{\Lambda}_2(n)\boldsymbol{\Sigma}(n)\boldsymbol{U}_1^{H}(n)\boldsymbol{n}_1(n) + \boldsymbol{U}_2^{H}(n)\boldsymbol{n}_2(n) \tag{4}$$

where $\boldsymbol{\Sigma}_n = diag(q_{1,n}, q_{2,n}, \cdots, q_{M,n})$.

According to formula (4), the MIMO-OFDM channel between SSN and SDN can be decomposed into $N \times M_S$ parallel independent channels, therefore, the throughput of the Relay-aided MIMO-OFDM network is

$$C_{tp}(\mathrm{p}) = \frac{1}{2}\sum_{m=1}^{M}\sum_{n=1}^{N}\log_2\left(1 + \frac{p_{m,n}^S\alpha_{m,n}p_{m,n}^R\beta_{m,n}}{1 + p_{m,n}^S\alpha_{m,n} + p_{m,n}^R\beta_{m,n}}\right) \tag{5}$$

where $\alpha_{m,n} = \frac{\lambda_{m,n}^{SR}}{\sigma_R^2+\psi_1}$, $\beta_{m,n} = \frac{\lambda_{m,n}^{RD}}{\sigma_D^2+\psi_2}$, $\lambda_{m,n}^{RD}$ is the eigenvalue of $\boldsymbol{G}_{RD}(n)$, ψ_1 and ψ_2 are constants and linear with $\frac{1}{N_{EL}}$ (N_{EL} is the number of samples in EL stage), $\mathrm{p} = \left\{p_{m,n}^S, p_{m,n}^R\right\}$ is power

vector. The overall power consumption at SSN and SDN can be expressed respectively as follows:

$$P^{SSN} = \tau^S \sum_{m=1}^{M}\sum_{n=1}^{N} p_{m,n}^S + P_c^S \tag{6a}$$

$$P^{SRN} = \tau^R \sum_{m=1}^{M}\sum_{n=1}^{N} p_{m,n}^R + P_c^R. \tag{6b}$$

where τ^S and P_c^S are the reciprocal of drain efficiency of power amplifier and circuit power at SSN. τ^R and P_c^R are the reciprocal of drain efficiency of power amplifier and circuit power at SDN.

The EE of the cognitive relay network while selecting the l-th CRN for transmitting is defied as:

$$\xi^{EE}(\mathrm{p}) = \frac{\frac{1}{2}\sum\limits_{m=1}^{M}\sum\limits_{n=1}^{N}\log_2\left(1+\frac{p_{m,n}^S\alpha_{m,n}p_{m,n}^R\beta_{m,n}}{1+p_{m,n}^S\alpha_{m,n}+p_{m,n}^R\beta_{m,n}}\right)}{\tau^S\sum\limits_{m=1}^{M}\sum\limits_{n=1}^{N}p_{m,n}^S+\tau^R\sum\limits_{m=1}^{M}\sum\limits_{n=1}^{N}p_{m,n}^R+P_c^S+P_c^R} \tag{7}$$

Since we use the estimated CB matrices, the interferences to PUs cased by SSN and SRN are inevitably, the interferences cased by SSN and SRN to l-th PU are

$$I_l^{SP} = \frac{\mu_S}{\sigma_l^2}\sum_{m=1}^{M}\sum_{n=1}^{N} p_{m,n}^S \tag{8a}$$

$$I_l^{RP} = \frac{\mu_R}{\sigma_l^2}\sum_{m=1}^{M}\sum_{n=1}^{N} p_{m,n}^R. \tag{8b}$$

where μ_S and μ_R are constants and linear with $\frac{1}{N_{EL}}$, σ_l^2 is the transmit power of the l-th PU signal.

From (7), the objective of energy-efficient power allocation problem for the relay-aided MIMO-OFDM CR network can be expressed as:

$$\mathrm{OP1}\ \max_{p_{m,n}^S,p_{m,n}^R\geq 0}\ \frac{\frac{1}{2}\sum\limits_{m=1}^{M}\sum\limits_{n=1}^{N}\log_2\left(1+\frac{p_{m,n}^S\alpha_{m,n}p_{m,n}^R\beta_{m,n}}{1+p_{m,n}^S\alpha_{m,n}+p_{m,n}^R\beta_{m,n}}\right)}{\tau^S\sum\limits_{m=1}^{M}\sum\limits_{n=1}^{N}p_{m,n}^S+\tau^R\sum\limits_{m=1}^{M}\sum\limits_{n=1}^{N}p_{m,n}^R+P_c^S+P_c^R} \tag{9}$$

subject to

$$\begin{cases} C1: \sum\limits_{m=1}^{M}\sum\limits_{n=1}^{N} p_{m,n}^S \leq P_{th}^S \\ C2: \sum\limits_{m=1}^{M}\sum\limits_{n=1}^{N} p_{m,n}^R \leq P_{th}^R \\ C3: \frac{\mu_S}{\sigma_l^2}\sum\limits_{m=1}^{M}\sum\limits_{n=1}^{N} p_{m,n}^S \leq I_{th}, l=1,2,\cdots,L \\ C4: \frac{\mu_R}{\sigma_l^2}\sum\limits_{m=1}^{M}\sum\limits_{n=1}^{N} p_{m,n}^R \leq I_{th}, l=1,2,\cdots,L. \end{cases}$$

where P_{th}^S and P_{th}^R are the total power budgets of SSN and SRN respectively, I_{th} is the interference threshold of PUs. C1 and C2 are transmission power constraints of SSN and SDN, C3 and C4 are the interference constraints of the PUs.

Duo to lack of convexity, it is difficult to solving OP1 directly. In the following, we make a joint concave approximation to OP1 and introduce a new equivalent optimization problem via nonlinear fractional programming (NFP) [21].

3 Energy Efficient Power Allocation Algorithm

To make OP1 more tractable, the throughput C_{tp} can be approximated at the high signal-to-noise ratio (SNR) as

$$\tilde{C}_{tp}\left(\mathrm{p}\right)=\frac{1}{2}\sum_{m=1}^{M}\sum_{n=1}^{N}\log_2\left(1+\frac{p_{m,n}^{S}\alpha_{m,n}p_{m,n}^{R}\beta_{m,n}}{p_{m,n}^{S}\alpha_{m,n}+p_{m,n}^{R}\beta_{m,n}}\right) \tag{10}$$

Note: As in [20], $\tilde{C}_{tp}\left(\mathrm{p}\right)$ is joint concave with $p_{m,n}^{S}$ and $p_{m,n}^{R}$.

Thus, we can also get the approximation of EE as:

$$\tilde{\xi}^{EE}\left(\mathrm{p}\right)=\frac{\tilde{C}_{tp}\left(\mathrm{p}\right)}{P_{total}\left(\mathrm{p}\right)} \tag{11}$$

where $P_{total}\left(\mathrm{p}\right)=P^{SSN}+P^{SRN}$.

Substitute $\tilde{\xi}^{EE}$ into OP1, we get the approximated optimization problem

$$\mathrm{OP2}\ \max_{p_{m,n}^{S},p_{m,n}^{R}\geq 0}\ \tilde{\xi}^{EE}\left(\mathrm{p}\right) \tag{12}$$

subject to

$$C1\sim C4$$

For notational simplicity, we define $\aleph$ as the set of feasible solution of OP2, and let $\mathrm{p}=\left\{p_{m,n}^{S},p_{m,n}^{R}\right\}$ be variable vector. Define the maximum EE ρ^{*} of network as follows:

$$\rho^{*}=\frac{\tilde{C}_{tp}\left(\mathrm{p}^{*}\right)}{P_{total}\left(\mathrm{p}^{*}\right)}=\max_{p\in\aleph}\frac{\tilde{C}_{tp}\left(\mathrm{p}\right)}{P_{total}\left(\mathrm{p}\right)} \tag{13}$$

where p^{*} is the optimal solution of OP2.

Introducing a new parametric optimization problem OP3

$$\mathrm{OP3}\ \max_{p_{m,n}^{S},p_{m,n}^{R}\geq 0}\ \left\{\tilde{C}_{tp}\left(\mathrm{p}\right)-\rho P_{total}\left(\mathrm{p}\right)\right\} \tag{14}$$

subject to

$$C1\sim C4$$

where ρ is non-negative parameter. Since $\tilde{C}_{tp}\left(p\right)$ is joint concave with $p_{m,n}^{S}$ and $p_{m,n}^{R}$, for a given ρ, OP3 is a convex optimization problem.

Next, introduce a theorem based on NFP [21]: **Theorem** The optimal solution achieve the maximum EE if and only if

$$\begin{aligned}&\max_{p\in\aleph}\left\{\tilde{C}_{tp}\left(\mathrm{p}\right)-\rho^{*}P_{total}\left(\mathrm{p}\right)\right\}\\ =\ &\tilde{C}_{tp}\left(\mathrm{p}^{*}\right)-\rho^{*}P_{total}\left(\mathrm{p}^{*}\right)\\ =\ &0\end{aligned} \tag{15}$$

with $\tilde{C}_{tp}\left(\mathrm{p}\right)\geq 0$, $P_{total}\left(\mathrm{p}\right)>0$.

Proof: Similar proof can be found in [21].

The Theorem implies that for fractional OP2, there is an equivalent problem whose objective function is in subtractive form, e.g. $\tilde{C}_{tp}\left(\mathrm{p}\right)-\rho^{*}P_{total}\left(\mathrm{p}\right)$. Therefore, solving OP2 is equivalent to solve problem OP3 for a given ρ and then update ρ until the Theorem is satisfied.

An alternative method solving OP3 is through deriving the Lagrange dual [22] of the optimization problem OP3. The Lagrange function of OP3 is defined as bellow:

$$\begin{aligned} L_{ag}\left(p,\theta_1,\theta_2,\{\chi_l\}_{l=1}^{L},\{\eta_l\}_{l=1}^{L}\right) &= \tfrac{1}{2}\sum_{m=1}^{M}\sum_{n=1}^{N}\log_2\left(1+\tfrac{p_{m,n}^{S}\alpha_{m,n}p_{m,n}^{R}\beta_{m,n}}{p_{m,n}^{S}\alpha_{m,n}+p_{m,n}^{R}\beta_{m,n}}\right) \\ &-\rho\left[\tau^{S}\sum_{m=1}^{M}\sum_{n=1}^{N}p_{m,n}^{S}+\tau^{R}\sum_{m=1}^{M}\sum_{n=1}^{N}p_{m,n}^{R}+P_C^{S}+P_C^{R}\right] \\ &-\theta_1\left(\sum_{m=1}^{M}\sum_{n=1}^{N}p_{m,n}^{S}-P_{th}^{S}\right)-\theta_2\left(\sum_{m=1}^{M}\sum_{n=1}^{N}p_{m,n}^{R}-P_{th}^{R}\right) \\ &-\sum_{l=1}^{L}\chi_l\left(\tfrac{\mu_S}{\sigma_l^2}\sum_{m=1}^{M}\sum_{n=1}^{N}p_{m,n}^{S}-I_{th}\right)-\sum_{l=1}^{L}\eta_l\left(\tfrac{\mu_R}{\sigma_l^2}\sum_{m=1}^{M_S}\sum_{n=1}^{N}p_{m,n}^{R}-I_{th}\right) \end{aligned} \tag{16}$$

where θ_1, θ_2 , χ_l and η_l are the Lagrange multipliers.

Therefore, the Lagrange dual function of the primal problem OP3 can be written as:

$$D_{ual}\left(\theta_1,\theta_2,\{\chi_l\}_{l=1}^{L},\{\eta_l\}_{l=1}^{L}\right)=\max_{p\geq 0}L_{ag}\left(p,\theta_1,\theta_2,\{\chi_l\}_{l=1}^{L},\{\eta_l\}_{l=1}^{L}\right) \tag{17}$$

The corresponding Lagrangian dual problem of OP3 can be expressed as:

$$\min_{\theta_1,\theta_2,\chi_l,\eta_l\geq 0}D_{ual}\left(\theta_1,\theta_2,\{\chi_l\}_{l=1}^{L},\{\eta_l\}_{l=1}^{L}\right) \tag{18}$$

The problem (17) is convex, according to the Karush-Kuhn-Tucker condition: $\frac{\partial L_{ag}}{\partial p_{m,n}^{S}}=0$ and $\frac{\partial L_{ag}}{\partial p_{m,n}^{R}}=0$, then we have:

$$\frac{1}{2\ln 2}\frac{\alpha_{m,n}\beta_{m,n}^{2}\left(p_{m,n}^{R}\right)^{2}}{\left(p_{m,n}^{S}\alpha_{m,n}+p_{m,n}^{R}\beta_{m,n}\right)\left(p_{m,n}^{S}\alpha_{m,n}+p_{m,n}^{R}\beta_{m,n}+p_{m,n}^{S}p_{m,n}^{R}\right)}=\rho\tau^{S}+\theta_1+\mu_S\sum_{l=1}^{L}\frac{\chi_l}{\sigma_l^2} \tag{19}$$

$$\frac{1}{2\ln 2}\frac{\alpha_{m,n}^{2}\beta_{m,n}\left(p_{m,n}^{S}\right)^{2}}{\left(p_{m,n}^{S}\alpha_{m,n}+p_{m,n}^{R}\beta_{m,n}\right)\left(p_{m,n}^{S}\alpha_{m,n}+p_{m,n}^{R}\beta_{m,n}+p_{m,n}^{S}p_{m,n}^{R}\right)}=\rho\tau^{R}+\theta_2+\mu_R\sum_{l=1}^{L}\frac{\eta_l}{\sigma_l^2} \tag{20}$$

Solving the above two equations, we get the optimal power allocation solutions as:

$$p_{m,n}^{S}=\frac{1}{\sqrt{\alpha_{m,n}x_1}\left(\sqrt{\frac{x_1}{\alpha_{m,n}}}+\sqrt{\frac{x_2}{\beta_{m,n}}}\right)}\left(1-\left(\sqrt{\frac{x_1}{\alpha_{m,n}}}+\sqrt{\frac{x_2}{\beta_{m,n}}}\right)^{2}\right)^{+} \tag{21}$$

$$p_{m,n}^{R}=\frac{1}{\sqrt{\beta_{m,n}x_2}\left(\sqrt{\frac{x_1}{\alpha_{m,n}}}+\sqrt{\frac{x_2}{\beta_{m,n}}}\right)}\left(1-\left(\sqrt{\frac{x_1}{\alpha_{m,n}}}+\sqrt{\frac{x_2}{\beta_{m,n}}}\right)^{2}\right)^{+} \tag{22}$$

where $[x]^{+}=\max(0,x)$, $x_1=\rho\tau^{S}+\theta_1+\mu_S\sum_{l=1}^{L}\frac{\chi_l}{\sigma_l^2}$ and $x_2=\rho\tau^{R}+\theta_2+\mu_R\sum_{l=1}^{L}\frac{\eta_l}{\sigma_l^2}$. Note: (21) and (22) show that $p_{m,n}^{S}$ and $p_{m,n}^{R}$ are either both positive or both zero, this implies that if power allocated to the n-th subcarrier in the first hop is zero, then no power is allocated to its corresponding subcarrier in the second hop, which meets the intuition very well.

Table 1:

	Algorithm: **approximated** energy-efficient power allocation
1	**Initialization**: initial ρ, ϖ_1^θ, ϖ_2^θ, ϖ_l^χ and ϖ_l^η, the maximum tolerance δ
2	**repeat**
3	**repeat**
4	update $p_{m,n}^S$ and $p_{m,n}^R$ according to (21) and (22)
5	update ϖ_1^θ, ϖ_2^θ, ϖ_l^χ and ϖ_l^η according to (23)
6	**until** ϖ_1^θ, ϖ_2^θ, ϖ_l^χ and ϖ_l^η converge
7	Update $\rho = \tilde{\xi}^{EE}(p)$ via (11)
8	**until** $\left\|\tilde{C}_{tp}(p) - \rho P_{total}(p)\right\| \leq \delta$

The optimal dual variables can be obtained from the dual problem (18) using the subgradient method[23]. The dual variables could be updated as:

$$\theta_1 = \left(\theta_1 + \varpi_1^\theta \left(P_{th}^S - \sum_{m=1}^{M}\sum_{n=1}^{N} p_{m,n}^S\right)\right)^+ \tag{23a}$$

$$\theta_2 = \left(\theta_2 - \varpi_2^\theta \left(P_{th}^R - \sum_{m=1}^{M}\sum_{n=1}^{N} p_{m,n}^R\right)\right)^+ \tag{23b}$$

$$\chi_l = \left(\chi_l - \varpi_l^\chi \left(I_{th} - \frac{\mu_S}{\sigma_l^2}\sum_{m=1}^{M}\sum_{n=1}^{N} p_{m,n}^S\right)\right)^+ \tag{23c}$$

$$\eta_l = \left(\eta_l - \varpi_l^\eta \left(I_{th} - \frac{\mu_R}{\sigma_l^2}\sum_{m=1}^{M}\sum_{n=1}^{N} p_{m,n}^R\right)\right)^+ \tag{23d}$$

where ϖ_1^θ, ϖ_2^θ, ϖ_l^χ and ϖ_l^η are the step length. According to the aforementioned analysis, we propose a two loop iterative algorithm to solve the approximated energy-efficient power allocation problem OP2, which is termed as AEE-PA and tabulated as in Table 1.

Note: [23] shows that the subgradient algorithm can converge to the optimal solution of convex optimization problems within a small range. Therefore, the inner loop can converge to the optimal solution of the dual problem (18) with in a small range. Since OP3 is convex optimization problem, the duality gap for OP3 is zero, the inner loop also converges to the optimal solution of OP3 within a small range. The detailed proves of the convergence of the outer loop, i.e. NFP can be found in [21].

4 Performance Simulations

We perform numerical simulations to evaluate the present some numerical experiments to evaluate the performance of our proposed scheme. Without loss of generality, the channel gains are assumed to be Rayleigh fading with an average power gain of 1dB, and set the parameters $N = 10$, $L = 2$, $M_S = 4$, $M_P = 2$, $\sigma_R^2 = \sigma_D^2 = 10^{-6}W$, $\sigma_l^2 = 1W$, $\tau^S = \tau^R = 1$, $P_c^S = P_c^R = 10^{-2}W$, $P_{th}^S = P_{th}^R = P_{\max}$. Since ψ_1, ψ_2, μ_S and μ_R are linear with $\frac{1}{N_{EL}}$, for

simplicity, let , , and are equals with . All the results have been averaged over 500 iterations. We compare the proposed algorithm with the traditional throughput maximum problem. Change the objective function $\xi^{EE}(\mathrm{p})$ in OP1 with the throughput $C_{tp}(\mathrm{p})$ in (5) and change the approximated objective function $\tilde{\xi}^{EE}(\mathrm{p})$ in OP2 with the approximated throughput $\tilde{C}_{tp}(\mathrm{p})$ in (10), then we formulate the traditional throughput maximum problem. Since $\tilde{C}_{tp}(\mathrm{p})$ is joint concave in with $p_{m,n}^{S}$ and $p_{m,n}^{R}$, the throughput maximum problem is convex problem which can be solved by many standard convex optimization algorithms [22]. We name the method to solve the throughput maximum problem as TM-PA. In the following, we compare the proposed algorithm with the TM-PA scheme.

Since the proposed AEE-PA consists of two loops, we only consider the affect of the number of outer loop iterations t_O and set the number of inner iterations large enough to guarantee that the inner loop can find the optimal solution of OP3. Fig.2 shows the EE versus the outer loop iterations t_O for different total power budget under $I_{th} = 1W$, $N_{EL} = 500$. It can be observed in Fig.2 that AEE-PA converges to the optimal value within eleven iterations for all considered value of total power budgets. The maximum EE can be improved when there are more total power budgets.

Fig.3 depicts the EE versus total power budget $P_{\max}$ for different interference thresholds under $N_{EL} = 500$. As shown in Fig.3, the EE of the both algorithms increases with the increasing of the total power budget, however the proposed AEE-PA has a higher EE than the non energy efficiency scheme TM-PA. The EE versus interference threshold I_{th} for different total power budgets under $N_{EL} = 500$ is evaluated in Fig.4. It is shown in Fig.4 that the EE of the both algorithms grows with the growth of the interference threshold. This is because that the lower the interference threshold is, the more the CR network suffers outage.

We also evaluate the impact of N_{EL} (the number of samples in EL stage) on the proposed algorithm. In Fig.5, EE versus interference threshold I_{th} for different N_{EL} under $P_{\max} = 0.5W$ is depicted. Obviously, the algorithm has a better performance with lager N_{EL} than small N_{EL}. This is because smaller N_{EL} performs poor learning and yields large interference to PUs.

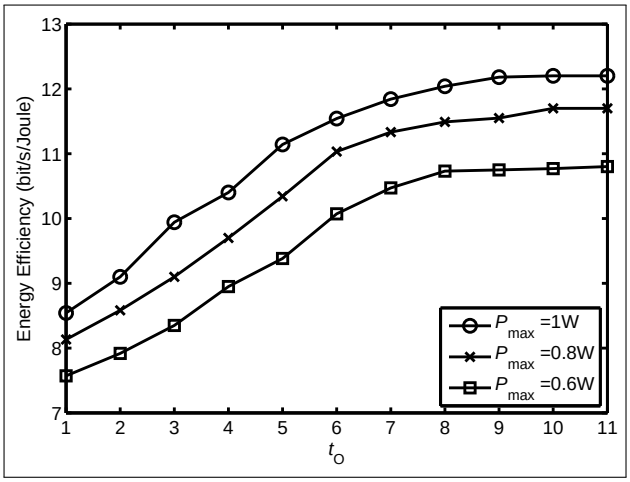

Figure 2: Energy efficiency versus the outer iterations for different total power budget

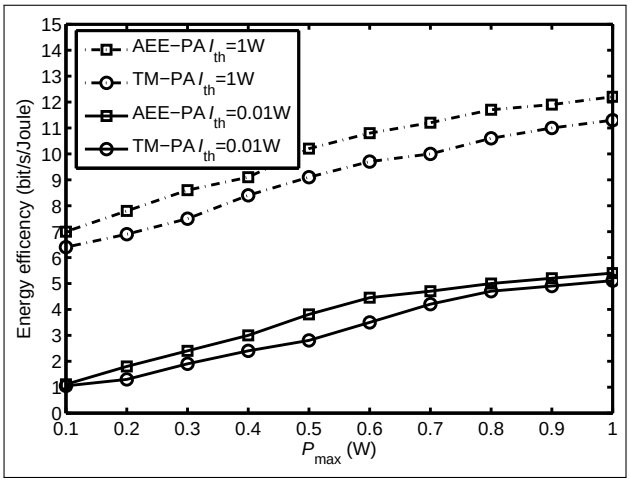

Figure 3: Energy-efficiency versus total power budget for different interference threshold

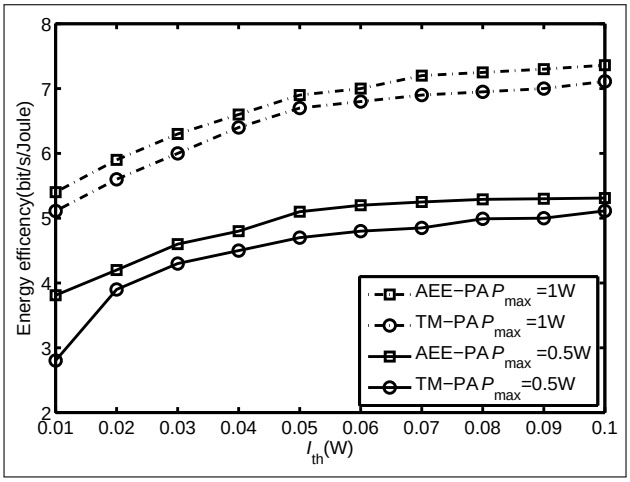

Figure 4: Energy efficiency versus interference threshold for different total power budget

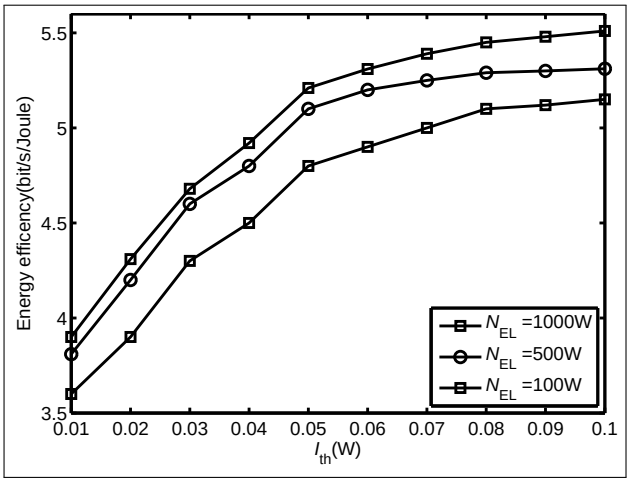

Figure 5: Energy efficiency versus interference threshold for different N_{EL}

5 Conclusions

In this paper, we investigated the power allocation for relay-aided MIMO-OFDM cognitive radio networks from energy efficiency perspective. Different from traditional throughput maximizing methods, we solve the power allocation problem via maximizing the energy efficiency measured by "Joule per bit" metric. However, the formulated problem is nonconvex. To make it solvable, we first make an approximation to the original problem. Indeed, the approximated problem is a fractional programming problem. Then, the approximated problem is transformed into a parametric convex optimization problem. Finally, we give closed form solutions to the parametric convex optimization problem and proposed a two loop iterative energy-efficient power allocation algorithm. To show the improvement in energy efficiency, we compared the proposed algorithm with the traditional throughput maximizing method. From the simulation results, we observed that the proposed new scheme have a better performance than conventional capacity maximization scheme in energy efficiency.

Bibliography

[1] L. Lu, G.Y. Li, A. Maaref, et. al. (2014), Opportunistic transmission exploiting frequency- and spatial-domain degrees of freedom, *IEEE Wireless Communications*, April 2014, 21(2):91-97.

[2] Muhammad Naeem, Alagan Anpalagan, Muhammad Jaseemuddin, et. al. (2014), Resource allocation techniques in cooperative cognitive radio networks, *IEEE Communications Surveys & Tutorials*, Second Quarter 2014, 16(2):729-744.

[3] Mehdi Ghamari Adian and Hassan Aghaeinia (2014), Optimal and sub-optimal resource allocation in multiple-input multiple-output-orthogonal frequency division multiplexing-based multi-relay cooperative cognitive radio networks, *IET Communications*, March 2014, 8(5):646-657.

[4] Quanzhong Li, Qi Zhang, Renhai Feng, et. al. (2013), Optimal relay selection and beamforming in MIMO cognitive multi-relay networks, *IEEE Communications Letters*, June 2013, 17(6):1188-1191.

[5] Sha Hua, Hang Liu, Xuejun Zhuo, et.al. (2014), Exploiting multiple antennas in cooperative cognitive radio networks, *IEEE Transactions on Vehicular Technology*, February 2014, 99: 1-12.

[6] Ahmad Alsharoa, Hakinm Ghazzai and Mohamed-Slim Alouini (2014), Optimal transmit power allocation for MIMO two-way cognitive relay networks with multiple relays using AF strategy, *IEEE Wireless Communications Letters*, February 2014, 3(1):30-33.

[7] Mehdi Ghamari Adian and Hassan Aghaeinia (2014), Resoure allocation in MIMO-OFDM based cooperative cognitive radio networks, *IEEE Transactions on Communications*, May 2014, 99: 1-11.

[8] Shou Li, Bingquan Li, Chengwen Xing, et. al.(2013), Joint resource allocation for learning-based cognitive radio networks with MIMO-OFDM relay-aided transmissions, *2013 IEEE Wireless Communications and Networking Conference*, 7-10 April 2013, Shanghai, 3271-32676.

[9] G. P. Fettweis and E. Zimmermann (2008), ICT energy consumption-trends and challenges, *Proceedings in 11-th International Symposiums Wireless Personal Multimedia Communications*, Lapland, Finland, September 2008, 1-4.

[10] Chunlong He, Geoffrey Ye Li, Fu-Chun Zheng, et.al (2014), Energy-efficient resource allocation in OFDM Systems with distributed antennas, *IEEE Transactions on Vehicular Technolgoy*, March 2014, 63(3):1223-1231.

[11] Geoffrey Ye Li, Zhikun Xu, Cong Xiong, et.al.(2011), Energy-efficient wireless communications: tutorial, survey, and open issues, *IEEE Wireless Communications*, December 2011, 18(6):28-35.

[12] Cong Xiong, Lu Lu and Geoffery Ye Li (2014), Energy-efficient specturm access in cognitive radios, *IEEE Journal of Selected Areas in Communicatinos*, March 2014, 32(3):550-562.

[13] Cong Xiong, Geoffery Ye Li, Yalin Liu, et.al. Energy-efficient design for downlink OFDMA with delay-sensitive traffic, *IEEE Transactions on Wireless Communications*, June 2013, 12(6):3085-3095.

[14] Suzan Bayhan and Fatih Alagoz (2013), Schedulign in centralized cognitive radio networks for energy efficiency, *IEEE Transactions on Vehicular Technolgoy*, February 2013, 62(2):582-595.

[15] Seonwook Kim, Byeong Gi Lee (2014), Energy-per-bit minimized radio resource allocation in heterogeneous networks, *IEEE Transactions on Wireless Communications*, April 2014, 13(4):1862-1873.

[16] Junling Mao, Gang Xie, Jinchun Gao, et al.(2013), Energy efficiency optimization for cognitive radio MIMO broadcast channels, *IEEE Communications Letters*, February 2013, 17(2):337-340.

[17] Sami Akin and Mustafa Cenk Gursoy (2013), On the throughput and energy efficiency of cognitive MIMO transmissions, *IEEE Transactions on Vehicular Technology*, March 2013, 62(7):3245-3260.

[18] Wei Zhong, and Jiaheng Wang (2013), Energy efficient spectrum sharing strategy selection for cognitive MIMO interference channels, *IEEE Transactions Signal Processing*, July 2013, 61(14):3705-3717.

[19] Feifei Gao, Rui Zhang, Ying-Chang Liang, et.al.(2010), Design of learning-based MIMO cognitive radio systems, *IEEE Transactions on Vehicular Technology*, May 2010, 59(4):1707-1720.

[20] Ingmar Hammerstrom and Armin Wittneben (2007), Power allocation schemes for amplify-and-forward MIMO-OFDM relay links, *IEEE Transactions on Wireless Communications*, August 2007, 6(8):2798-2802.

[21] Werner Dinkelbach (1967), On Nonlinear Fractional Programming, *Management Science*, March 1967, 13(7):492-498.

[22] Stephen Boyd and Lieven Vandenberghe (2014), *Convex Optimization*, Cambridge University Press, 2004.

[23] Stephen Boyd, L. Xiao and A. Mutapcic, Subgradient Methods, Online: https://web.stanford.edu/class/ee392o/subgrad_method.pdf.

INTERNATIONAL JOURNAL OF COMPUTERS COMMUNICATIONS & CONTROL
ISSN 1841-9836, 10(1):123-135, February, 2015.

Tractable Algorithm for Robust Time-Optimal Trajectory Planning of Robotic Manipulators under Confined Torque

Q. Zhang, S.-R. Li, J.-X. Guo, X.-S. Gao

Qiang Zhang, Shu-Rong Li
Automation Department
China University of Petroleum(East China)
E-mail:zhangqiangupc@gmail.com, lishuron@upc.edu.cn

Jian-Xin Guo, Xiao-Shan Gao*
Academy of Mathematics and Systems Science
Chinese Academy of Sciences
E-mail:guojianxin@amss.ac.cn
*Corresponding author: xgao@mmrc.iss.ac.cn

Abstract: In this paper, the problem of time optimal trajectory planning under confined torque and uncertain dynamics and torque parameters along a predefined geometric path is considered. It is shown that the robust optimal solution to such a problem can be obtained by solving a linear program. Thus a tractable algorithm is given for robust time-optimal path-tracking control under confined torque.
Keywords: robust optimal control, time minimum trajectory planning, parameter uncertainties, tractable algorithm.

1 Introduction

In order to maximize productivity, the problem of minimum time motion planning of robotic manipulators is widely studied. In practical applications, the motion planning problem can be solved by two kinds of methods: the coupled method and the decoupled method [1]. As the name implies, the coupled methods determine the geometric path and the velocity along the path simultaneously. On the other hand, the decoupled methods determine the geometric path first according to certain criteria, and then determine the velocity along the path to minimize the path traversal time. This paper follows the decoupled approach due to the following reasons. Simultaneous optimization of the geometric path and the velocity is computationally difficult [2], especially when one wants to find a tractable algorithm. Also, in many industrial applications, the geometric path is predefined and does not need to be optimized.

Many efficient approaches for the time minimum trajectory planning (TMTP) problem along a predefined geometric path have been proposed, including the phase plane analysis approaches [3–6], the Pontryagin maximum principle and shooting algorithms [7], the convex optimization [2, 10], the path reshaping [8], and the direct search method [9]. The recent works [2, 11] are significant in which general and efficient methods are proposed. In [2], the second-order cone program is applied to solve the corresponding convex optimization problem. In [11], the sequential linear programming is used to solve the TMTP, which has better computational complexity than that of the phase plane method given in [4].

The above approaches assume that the dynamics model of the robotic manipulator is precisely known and equal to some nominal values. In practice, the dynamic model always has uncertainties. For example, to simplify the solution procedure, the viscous friction is often neglected and the uncertainties caused by the payload variation are often ignored. Many robust trajectory planning methods were proposed to handle these uncertainties. One of the commonly used approach is the min-max optimization approach which obtains the time minimum solution in the case of worst disturbances [12–14]. Due to its bi-level structure, min-max optimization problems pose

challenges for efficient numerical solution in many cases. Other interesting approaches include the stochastic optimization approach [15] and the predictive control [16, 17].

In this paper, a tractable offline algorithm is given for the robust TMTP of robotic manipulators under torque limits and bounded dynamic parameter uncertainties and torque disturbances based on the min-max optimization approach. To solve the problem, it is shown that the TMTP problem for robotics under confined torque is equivalent to a linear optimal control problem meaning that both the objective function and the constraints are linear in the control and state variables. When disturbances are added, a robust linear optimal control problem is obtained, which is formulated as a min-max optimization problem. Furthermore, it is shown that when the trajectory is approximated with a quadratic B-spline curve, the min-max optimization problem is reduced to a min-max linear optimization problem which in turn can be reduced to a plain linear programming problem and thus is tractable, meaning that the problem can be solved in polynomial time. Numerical simulations are used to show that the method gives high precision approximate solutions to the robust TMTP very efficiently.

Comparing to existing approaches [12–14], the proposed method seems to be the first to convert the robust TMTP for robotics into a linear program. Linear program was also used in [12], where the objective function is not equivalent to time-minimality.

The rest of the paper is organized as follows. In Section 2, the nominal TMTP problem is reduced to a linear control problem. In Section 3, methods of parametrization is given. In Section 4, a tractable algorithm for the robust TMTP problem is given. In Section 5, numerical examples are presented. Conclusions are presented in Section 6.

2 Linear Formulation for TMTP under Confined Torque

In this section, we will show that the TMTP problem can be formulated as a linear optimal control problem meaning that the objective function and the constraints of the problem are linear in the control and state variables.

Consider an n DOF robotic manipulator satisfying the following dynamic equation [2]

$$\tau = \mathbf{M}(\mathbf{q})\,\ddot{\mathbf{q}} + \dot{\mathbf{q}}^T \mathbf{C}(\mathbf{q})\,\dot{\mathbf{q}} + \mathbf{G}(\mathbf{q}), \tag{1}$$

where $\tau \in \mathbf{R}^n$ is the vector of actuator torques, $\mathbf{q} \in \mathbf{R}^n$ is the vector of joint angular positions, $\mathbf{M}(\mathbf{q}) \in \mathbf{R}^{n\times n}$ is the inertia matrix of the manipulator, $\mathbf{C}(\mathbf{q}) \in (\mathbf{R}^n)^{n\times n}$ is a matrix, whose elements are in $\mathbf{R}^n$, representing the coefficients of the centrifugal and Coriolis forces, and $\mathbf{G}(\mathbf{q}) \in \mathbf{R}^n$ is the vector of gravitational torques.

In this paper, the given path to be tracked in task space is denoted by

$$\mathbf{r}(s) = [x(s), y(s), z(s)]^{\mathrm{T}}, s \in [0, 1], \tag{2}$$

and the corresponding joint path $\mathbf{q}(s)$ in the joint space is also assumed to be determined by considering task requirement, obstacle avoidance, singularity avoidance, etc. Hence, a kinematics map between $\mathbf{r}(s)$ and $\mathbf{q}(s)$ exists. Here the path singularity problem is not considered since it can be avoided by properly adjusting the joint path.

Following [4], each element of $\mathbf{r}(s)$ is assumed to be a piecewise analytic real-valued function and has at least C^1 continuity at the connection points. Furthermore, $\mathbf{r}$ is assumed to be non-singular, that is, for any $s \in [0, 1]$ there exists at least one $l \in \{x, y, z\}$ such that $\frac{\mathrm{d}l(s)}{\mathrm{d}s} \neq 0$.

Denote $' = \frac{\mathrm{d}}{\mathrm{d}s}$ and $\dot{} = \frac{\mathrm{d}}{\mathrm{d}t}$, where t represents time. Then the joint velocity and joint acceleration can be formulated as

$$\dot{\mathbf{q}} = \mathbf{q}'\dot{s}, \quad \ddot{\mathbf{q}} = \mathbf{q}'\ddot{s} + \mathbf{q}''\dot{s}^2. \tag{3}$$

Following (1) and (3), the dynamics model can be written as a linear function in $\ddot{s}$ and $\dot{s}^2$:

$$\tau = \mathbf{m}(s)\,\ddot{s} + \mathbf{c}(s)\,\dot{s}^2 + \mathbf{g}(s), \tag{4}$$

where $\mathbf{m}(s) = \mathbf{M}(\mathbf{q}(s))\,\mathbf{q}'(s) \in \mathbf{R}^n, \mathbf{c}(s) = \mathbf{M}(\mathbf{q}(s))\,\mathbf{q}''(s) + \mathbf{q}'(s)^T\mathbf{C}(\mathbf{q}(s))\,\mathbf{q}'(s) \in \mathbf{R}^n$, $\mathbf{g}(s) = \mathbf{G}(\mathbf{q}(s)) \in \mathbf{R}^n$.

The TMTP problem can be described as the following optimal control problem [2]:

$$\begin{aligned} &\min_{b(s)} \; J_T = \textstyle\int_0^1 \frac{1}{\sqrt{a(s)}}\mathrm{d}s \\ \text{s.t.} \quad &a'(s) = 2b(s), \; \forall s \in [0,1], \\ &a(s) > 0, \; \forall s \in (0,1), a(0) = a_0, a(1) = a_1, \\ &\mathbf{m}(s)\,b + \mathbf{c}(s)\,a + \mathbf{g}(s) = \tau(s), \\ &\tau_{\min} \le \tau(s) \le \tau_{\max}, \end{aligned} \tag{5}$$

where $a = \dot{s}^2$, $b = \ddot{s}$, $\tau_{\min}$ and $\tau_{\max}$ are the bound vectors for the torque, and the boundary values $a(0)$ and $a(1)$ can be obtained from (3) and the boundary values of the joint velocities: $\dot{\mathbf{q}}(0) = \dot{\mathbf{q}}_0, \dot{\mathbf{q}}(1) = \dot{\mathbf{q}}_{\mathrm{f}}$. When $b(s) = \ddot{s}$ is known, $\dot{s}$ and $\mathbf{q}(t)$ can be uniquely determined.

Problem (5) has the following important property.

Theorem 1. *The optimal solution $\dot{s}_o(s), s \in [0,1]$ of problem (5) is unique and is maximum at any parameter value. That is, let $\dot{s}_f(s)$ be another parameter velocity satisfying the constraints of (5). Then, $\dot{s}_f(s) \le \dot{s}_o(s)$ for all $s \in [0,1]$.*

Theorem 1 follows from the proof of Theorem 2 in [3] and the proof of Theorem 3 in [4]. In both cases, an admissible parameter velocity $\dot{s}_o(s), s \in [0,1]$ is first constructed. To show $\dot{s}_o(s)$ is a solution to problem (5), the authors actually proved that $\dot{s}_o(s)$ is maximum at any parameter value.

The constraints of problem (5) are linear in a and b. It will be shown that the nonlinear objective function of problem (5) can be replaced with a linear function in a. The idea is to *maximize the total feedrate* for the end effector of the robots instead of minimizing the traversing time. The feedrate of the end effector of the robot is $F_d(s) = \|\mathbf{r}'(s)\|\sqrt{a(s)}$, where $\|\mathbf{r}'(s)\| = \sqrt{x'^2(s) + y'^2(s) + z'^2(s)}$.

Consider the optimal control problem.

$$\begin{aligned} &\max_{b(s)} \; J_F = \textstyle\int_0^1 \|\mathbf{r}'(s)\|^2 a(s)\mathrm{d}s \\ \text{s.t.} \quad &a'(s) = 2b(s), \; \forall s \in [0,1], \\ &a(s) > 0, \; \forall s \in (0,1), a(0) = a_0, a(1) = a_1, \\ &\mathbf{m}(s)\,b + \mathbf{c}(s)\,a + \mathbf{g}(s) = \tau(s), \\ &\tau_{\min} \le \tau(s) \le \tau_{\max}. \end{aligned} \tag{6}$$

Since the objective function of the above problem is linear in $a(s)$, problem (6) is a linear optimal control problem meaning that both the objective function and the constraints are linear in a and b. We thus have

Theorem 2. *Problem* (6) *and problem* (5) *have the same unique optimal solution.*

Proof: From [3] and [4], problem (5) has an optimal solution $a_o(s) = \dot{s}_o(s)^2, s \in [0,1]$. Since the two problems have the same constraints, $a_o(s)$ is also an admissible pseudo feedrate to problem (6). From Theorem 1, $a_o(s)$ achieves maximum values among all $a(s)$ satisfying the constraints of (6) at any parametric value. Since the parametric path $\mathbf{r}(s)$ is assumed to be non-singular, $\|\mathbf{r}'(s)\|^2 > 0$ for all $s \in (0,1)$. Thus $a_o(s)$ is also the optimal solution to problem (6). □

3 Parametrization and Tractable Algorithm for Nominal TMTP

In this section, a method of parametrization is given to reduce the infinite dimensional optimal control problem (6) to a linear program. The parametrization method will also be used in the next section to solve the robust TMTP.

The first step is to use a special type quadratic B-spline function to approximate the function $a(s)$.

We first define the B-splines used in this paper. Let K and p be positive integers and $s_i = \frac{i}{K-p+2}, i = 0, \ldots, K-p+2$. Consider the following knot sequence with the first $p+1$ and last $p+1$ knots "clamped".

$$\mathbf{s} = \left[\underbrace{0, \ldots, 0}_{p+1}, s_1, \ldots, s_i, \ldots, s_{K-p+1}, \underbrace{1, \ldots, 1}_{p+1}\right]. \tag{7}$$

The B-spline curve of degree p in the parameter interval $[0, 1]$ is defined as

$$\tilde{a}(s) = \sum_{i=0}^{K+1} N_{i,p}(s)\hat{a}_i, \tag{8}$$

where $\hat{a}_i$ are parameters and $N_{i,p}(s)$ is the i-th spline basis function of degree p defined as

$$\begin{aligned} N_{i,0}(s) &= \begin{cases} 1 & \text{if } \mathbf{s}(i) \le s < \mathbf{s}(i+1) \\ 0 & \text{otherwise} \end{cases}, i = 0, \ldots, K+p+1 \\ N_{i,k}(s) &= \frac{s - \mathbf{s}(i)}{\mathbf{s}(i+k) - \mathbf{s}(i)} N_{i,k-1}(s) + \frac{\mathbf{s}(i+k+1) - s}{\mathbf{s}(i+k+1) - \mathbf{s}(i+1)} N_{i+1,k-1}(s), \\ & \quad k = 1, \ldots, p; i = 0, \ldots, K+p-k+1. \end{aligned}$$

The derivative of the B-spline basis function is given below

$$N'_{i,p}(s) = \frac{\mathrm{d}}{\mathrm{d}s} N_{i,p}(s) = \frac{p}{\mathbf{s}(i+p) - \mathbf{s}(i)} N_{i,p-1}(s) - \frac{p}{\mathbf{s}(i+p+1) - \mathbf{s}(i+1)} N_{i+1,p-1}(s). \tag{9}$$

Now, function $a(s)$ is approximated by a quadratic B-spline function $a(s) \approx \tilde{a}(s)$ where $\tilde{a}(s)$ is from (8) for $p = 2$. Set $\hat{a}_0 = a_0$, $\hat{a}_{K+1} = a_1$. Due to the multiple knots in the B-splines, we have have $\tilde{a}(0) = \hat{a}_0$ and $\tilde{a}(1) = \hat{a}_{K+1}$ [18]. The control points $\mathbf{X} = [\hat{a}_1, \ldots, \hat{a}_K]^T$ will be optimized. The variable $b(s)$ is

$$b(s) = a\prime(s)/2 \approx \frac{1}{2} \sum_{i=0}^{K+1} N'_{i,p}(s)\hat{a}_i, \tag{10}$$

where $N'_{i,p}(s)$ is given in (9).

The second step is to reduce the continuous optimal control problem (6) to a finite state optimal problem by using pointwise constraints to replace the continuous torque constraints. The constraint knot points are

$$\bar{s}_j = \begin{cases} \frac{1}{2} s_1, j = 1 \\ \frac{1}{2}(s_{j-1} + s_j), j = 2, \ldots, K-1 \\ \frac{1}{2}(s_{K-1} + 1), j = K \end{cases} \tag{11}$$

With these knot points, the objective function can be approximated as

$$J_F = \int_0^1 \|\mathbf{r}\prime(s)\|^2 a(s) \mathrm{d}s \approx \mathbf{BX} \tag{12}$$

where $\mathbf{B} = (B_1, \ldots, B_K)$ with $B_i = \sum_{j=1}^{K} \|\mathbf{r}\prime(\bar{s}_j)\|^2 N_{i,p}(\bar{s}_j)\,\Delta\bar{s}_j$ for $\Delta\bar{s}_j = s_j - s_{j-1} = 1/K$.

From (4), (8), and (10), the torques of the l-th joint at the knot points are

$$\hat{\tau}_l = \mathbf{A}_l\mathbf{X} + \hat{\mathbf{g}}_l, l = 1, \ldots, n, \tag{13}$$

where $\hat{\tau}_l = [\tau_l(\bar{s}_1), \ldots, \tau_l(\bar{s}_K)]^T$ with $\tau_l(\bar{s}_j) = \frac{1}{2}m_l(\bar{s}_j)\sum_{i=0}^{K+1} N'_{i,p}(\bar{s}_j)\ \hat{a}_i + c_l(\bar{s}_j)\sum_{i=0}^{K+1} N_{i,p}(\bar{s}_j)\ \hat{a}_i + g_l(\bar{s}_j)$, $\mathbf{A}_l \in \mathbf{R}^{K\times K}$ with $A_{lji} = \frac{1}{2}m_l(\bar{s}_j)N'_{i,p}(\bar{s}_j) + c_l(\bar{s}_j)N_{i,p}(\bar{s}_j)$, and $\hat{\mathbf{g}}_l = [\ g_l(\bar{s}_1) + \xi_1, \ldots, g_l(\bar{s}_K) + \xi_K]^T$ with $\xi_j = \frac{1}{2}m_l(\bar{s}_j)(N'_{0,p}(\bar{s}_j)a_0 + N'_{K+1,p}(\bar{s}_j)a_1) + c_l(\bar{s}_j)(N_{0,p}(\bar{s}_j)\ a_0 + N_{K+1,p}(\bar{s}_j)a_1)$.

With the above parametrization, problem (6) is reduced to the following linear program

$$\begin{aligned} &\max_{\mathbf{X}}\ \mathbf{B}\mathbf{X} \\ \text{s.t.}\quad &\tilde{a}(\bar{s}_j) = \mathbf{N}_j\mathbf{X} + N_{0,p}(\bar{s}_j)a_0 + N_{K+1,p}(\bar{s}_j)a_1 > 0, j = 1, \ldots, K, \\ &\tau_{l,\min}\mathbf{I} \le \mathbf{A}_l\mathbf{X} + \hat{\mathbf{g}}_l \le \tau_{l,\max}\mathbf{I}, l = 1, \ldots, n, \end{aligned} \tag{14}$$

where $\mathbf{I} = (1, \ldots, 1)^T \in \mathbf{R}^K$, $\mathbf{B}$ is from (12), $\mathbf{N}_j = [N_{1,p}(\bar{s}_j), \ldots, N_{K,p}(\bar{s}_j)]$, and $\mathbf{A}_l, \hat{\mathbf{g}}_l$ are from (13). Note that the boundary conditions $a(0) = \hat{a}_0 = a_0$ and $a(1) = \hat{a}_{K+1} = a_1$ are automatically satisfied. Properties of the above problem will be discussed in the next section.

4 Tractable Algorithm for Robust TMTP

In this section, we will show that the robust TMTP can be reduced to a linear program by using proper parametrization and methods of robust optimization.

Suppose that the dynamics model (4) has uncertainties and the real dynamics model is

$$\tau(s) = (\mathbf{m}(s) + \Delta\mathbf{m}(s))\,\ddot{s} + (\mathbf{c}(s) + \Delta\mathbf{c}(s))\,\dot{s}^2 + (\mathbf{g}(s) + \Delta\mathbf{g}(s)) - \Delta\mathbf{d}(s), \tag{15}$$

where $\Delta\mathbf{m}(s), \Delta\mathbf{c}(s), \Delta\mathbf{g}(s)$, and $\Delta\mathbf{d}(s)$ are the disturbances for $\mathbf{m}(s), \mathbf{c}(s), \mathbf{g}(s)$, and the torque, respectively. The disturbances are assumed to satisfy the following constraints:

$$\mathcal{D}(\Delta\mathbf{m}, \Delta\mathbf{c}, \Delta\mathbf{g}, \Delta\mathbf{d}) : \left\{ \begin{array}{l} |\Delta m_l(s)| \le B_m(l,s), l = 1, \ldots, n \\ |\Delta c_l(s)| \le B_c(l,s), l = 1, \ldots, n \\ |\Delta g_l(s)| \le B_g(l,s), l = 1, \ldots, n \\ |\Delta d_l(s)| \le B_d(l,s), l = 1, \ldots, n \end{array} \right\} \tag{16}$$

where $\Delta m_l(s), \Delta c_l(s), \Delta g_l(s)$, and $\Delta d_l(s)$ are the elements of the vectors $\Delta\mathbf{m}(s), \Delta\mathbf{c}(s), \Delta\mathbf{g}(s)$, and $\Delta\mathbf{d}(s)$, respectively.

Using the min-max approach [12, 13], the robust TMTP can be formulated as the following bi-level optimization problem:

$$\begin{aligned} &\max_{b(s)}\ J_F = \int_0^1 \|\mathbf{r}\prime(s)\|^2 a(s)\mathrm{d}s \\ &\text{s.t. } a\prime(s) = 2b(s), a(s) > 0, s \in (0,1),\ a(0) = a_0,\ a(1) = a_1, \\ &\max_{\mathcal{D}(\Delta\mathbf{m},\Delta\mathbf{c},\Delta\mathbf{g},\Delta\mathbf{d})} \left(\ (\mathbf{m}(s) + \Delta\mathbf{m}(s))\,b(s) + (\mathbf{c}(s) + \Delta\mathbf{c}(s))\,a(s) + (\mathbf{g}(s) + \Delta\mathbf{g}(s)) - \Delta\mathbf{d}(s)\ \right) \le \tau_{\max} \\ &\min_{\mathcal{D}(\Delta\mathbf{m},\Delta\mathbf{c},\Delta\mathbf{g},\Delta\mathbf{d})} \left(\ (\mathbf{m}(s) + \Delta\mathbf{m}(s))\,b(s) + (\mathbf{c}(s) + \Delta\mathbf{c}(s))\,a(s) + (\mathbf{g}(s) + \Delta\mathbf{g}(s)) - \Delta\mathbf{d}(s)\ \right) \ge \tau_{\min} \end{aligned} \tag{17}$$

where $\mathcal{D}(\Delta\mathbf{m}, \Delta\mathbf{c}, \Delta\mathbf{g}, \Delta\mathbf{d})$ is defined in (16).

Using the parametrization procedure presented in Section 3, the robust TMTP problem (17) is reduced to the following bi-level optimization problem

$$\begin{aligned}
&\max_{\mathbf{X}} \ \mathbf{BX}\\
\text{s.t.}\quad &\mathbf{N}_j\mathbf{X} + N_{0,p}(\bar{s}_j)a_0 + N_{K+1,p}(\bar{s}_j)a_1 > 0, j = 1,\ldots,K\\
&\max_{\Delta\mathbf{Am}_l,\Delta\mathbf{Ac}_l,\Delta\mathbf{g}_l,\Delta\mathbf{d}_l} \ \mathbf{A}_l\mathbf{X} + \hat{\mathbf{g}}_l + \Delta\mathbf{Am}_l\mathbf{Y} + \Delta\mathbf{Ac}_l\mathbf{X} + \Delta\hat{\mathbf{g}}_l - \Delta\hat{\mathbf{d}}_l \le \tau_{l,\max}\mathbf{I},\\
&\min_{\Delta\mathbf{Am}_l,\Delta\mathbf{Ac}_l,\Delta\mathbf{g}_l,\Delta\mathbf{d}_l} \ \mathbf{A}_l\mathbf{X} + \hat{\mathbf{g}}_l + \Delta\mathbf{Am}_l\mathbf{Y} + \Delta\mathbf{Ac}_l\mathbf{X} + \Delta\hat{\mathbf{g}}_l - \Delta\hat{\mathbf{d}}_l \ge \tau_{l,\min}\mathbf{I},\\
&l = 1,\ldots,n,
\end{aligned} \tag{18}$$

where $\mathbf{Y} = [\mathbf{N}'_1,\ldots,\mathbf{N}'_K]^T\mathbf{X}$ is a newly defined variable with $\mathbf{N}'_j = \left[N'_{1,p}(\bar{s}_j),\ldots,N'_{K,p}(\bar{s}_j)\right]$, $\mathbf{B}$, $\mathbf{N}_j$, $\mathbf{A}_l$, and $\hat{\mathbf{g}}_l$ are the same as in (14), $\Delta\hat{\mathbf{g}}_l = [\Delta g_l(\bar{s}_1),\ldots,\Delta g_l(\bar{s}_K)]^T$ is the disturbance of the gravitational torque, $\Delta\hat{\mathbf{d}}_l = [\Delta d_l(\bar{s}_1),\ldots,\Delta d_l(\bar{s}_K)]^T$ is the torque disturbances, $\Delta\mathbf{Am}_l \in \mathbf{R}^{K\times K}$ and $\Delta\mathbf{Ac}_l \in \mathbf{R}^{K\times K}$ are the uncertainty matrixes of the l-th joint with elements $\Delta Am_{lji} = \frac{1}{2}\Delta m_l(\bar{s}_j)$ and $\Delta Ac_{lji} = \Delta c_l(\bar{s}_j)N_{i,p}(\bar{s}_j)$ respectively. And the uncertainty constraints are

$$\Delta\mathbf{Am}_l \ : \ |\Delta m_l(\bar{s}_j)| \le B_m(l,\bar{s}_j), \tag{19}$$

$$\Delta\mathbf{Ac}_l \ : \ |\Delta c_l(\bar{s}_j)| \le B_c(l,\bar{s}_j), \tag{20}$$

$$\begin{aligned}
\Delta\mathbf{g}_l \ &: \ |\Delta g_l(\bar{s}_j)| \le B_g(l,\bar{s}_j),\\
\Delta\mathbf{d}_l \ &: \ |\Delta d_l(\bar{s}_j)| \le B_d(l,\bar{s}_j), j = 1,\ldots,K.
\end{aligned}$$

Based on a result of Soyster about robust optimization [19], the bi-level optimization problem (18) can be relaxed to the following linear program

$$\begin{aligned}
&\max_{\mathbf{X},\mathbf{Z_1},\mathbf{Z_2}} \ \mathbf{BX}\\
\text{s.t.}\quad &\mathbf{N}_j\mathbf{X} + N_{0,p}(\bar{s}_j)a_0 + N_{K+1,p}(\bar{s}_j)a_1 > 0, j = 1,\ldots,K,\\
&\mathbf{A}_l\mathbf{X} + \hat{\mathbf{g}}_l + \Delta\mathbf{Bm}_l\mathbf{Z_1} + \Delta\mathbf{Bc}_l\mathbf{Z_2} + \Delta\mathbf{B}_{gl} + \Delta\mathbf{B}_{dl} \le \tau_{l,\max}\mathbf{I},\\
&\mathbf{A}_l\mathbf{X} + \hat{\mathbf{g}}_l - \Delta\mathbf{Bm}_l\mathbf{Z_1} - \Delta\mathbf{Bc}_l\mathbf{Z_2} - \Delta\mathbf{B}_{gl} - \Delta\mathbf{B}_{dl} \ge \tau_{l,\min}\mathbf{I},\\
&-\mathbf{Z_2} \le \mathbf{X} \le \mathbf{Z_2}, -\mathbf{Z_1} \le \mathbf{Y} \le \mathbf{Z_1}, \mathbf{Z_1} \ge \mathbf{0}, \mathbf{Z_2} \ge \mathbf{0},\\
&\mathbf{Y} = [\mathbf{N}'_1,\ldots,\mathbf{N}'_K]^T\mathbf{X},\\
&l = 1,\ldots,n,
\end{aligned} \tag{21}$$

where $\mathbf{Z}_1 \in \mathbf{R}^K$ and $\mathbf{Z}_2 \in \mathbf{R}^K$ are new sets of variables, $\Delta\mathbf{Bm}_l \in \mathbf{R}^{K\times K}$ and $\Delta\mathbf{Bc}_l \in \mathbf{R}^{K\times K}$ are matrixes with elements $\Delta Bm_{lji} = \frac{1}{2}B_m(l,\bar{s}_j)$ and $\Delta Bc_{lji} = N_{i,p}(\bar{s}_j)B_c(l,\bar{s}_j)$ respectively, $\Delta\mathbf{B}_{gl} = [B_g(l,\bar{s}_1),\ldots,B_g(l,\bar{s}_K)]^T$, and $\Delta\mathbf{B}_{dl} = [B_d(l,\bar{s}_1),\ldots,B_d(l,\bar{s}_K)]^T$.

The number of variables in problem (21) is $3K$ and the number of constraints is $(2n+7)K$. According to Karmarkar's result [20], problem (21) can be solved with $O((nK)^{3.5})$ floating point arithmetic operations.

We briefly discuss the convergency of the method, that is, whether the solutions of the linear programs (14) and (21) convert to the optimal solutions of the optimal control problems (6) and (17), respectively, when K becomes sufficiently large. From the approximation theory, quadratic splines can approximate the solution of optimal control problems to any given precision when K is large enough [21]. Notice that the method of using quadratic splines to approximate the control variable is a special case of the Ritz method, the convergence of which has been proved only for special types of constraints [21–23]. Convergency for problems like the one in this paper seems open. In the next section, numerical results will be used to demonstrate that the method gives the optimal solution with very high precision in less than one second.

5 Numerical Examples

The experimental robot is a six-DOF Puma 560 manipulator which is modeled using the *Robotics Toolbox for Matlab* [24]. The torque limits of the six joints are set to be $[97.6; 186.4; 89.4; 24.2; 20.1; 21.3] N.m$. Initial and end feedrates of the end effecter are zeros. The path to be traced in the robot work space is shown in Fig.1(a) with the following parametric formula

$$\begin{cases} x(s) = 0.5, \\ y(s) = 0.25\left(\cos(2a\pi s) - \cos(2b\pi s)^3\right), \\ z(s) = 0.25\left(\sin(2a\pi s) - \sin(2b\pi s)^3\right), \end{cases} \quad s \in [0,1].$$

where $a = 2, b = 1$. The corresponding joint path is shown in Fig.1(b).

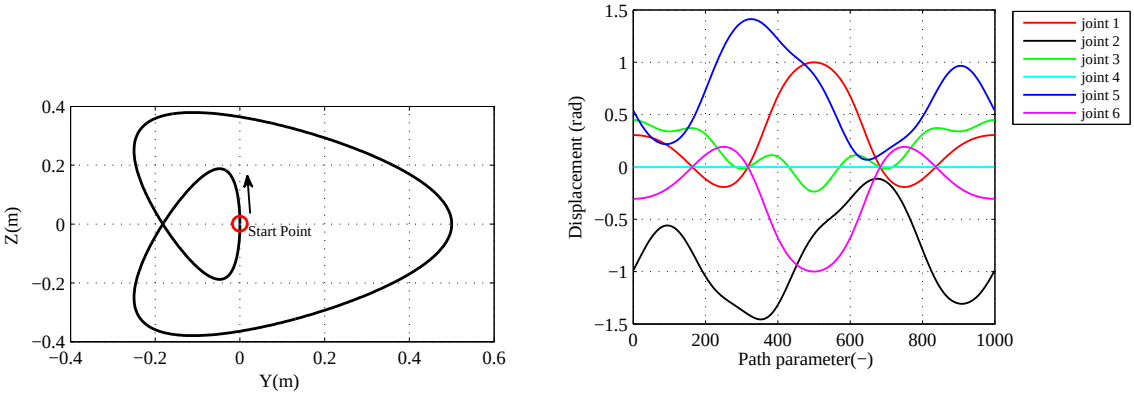

(a) (b)

Figure 1: (a): The task path on Y-Z plane. (b): The corresponding joint path.

First, problem (14) is used to show that the proposed method is efficient and correct. The proposed linear program (LP) approach will be compared to the convex optimization (CP) approach [2] for efficiency. The approach in [2], which is realized by executing the second order cone program (SOCP), was the fastest existing numerical method by now. Both algorithms are implemented by using optimization software package *Sedumi* [25] in Matlab on a PC with a 2.6GHz CPU and 2G memory.

Table 1: Comparison of computation times for different K

Number K	CPU time(s)		Optimal motion time(s)	
	LP	CP in [2]	LP	CP in [2]
100	0.3964	1.2460	1.6473	1.6449
200	0.6830	2.2970	1.6495	1.6491
500	0.4630	3.6260	1.6506	1.6506
700	0.9048	4.2620	1.6508	1.6507
1000	0.9300	3.4430	1.6508	1.6508
2000	1.1960	6.3440	1.6508	1.6508

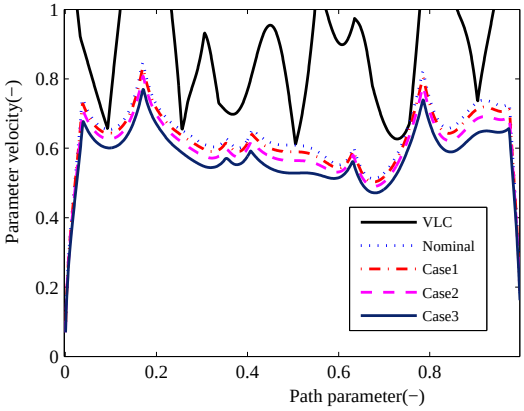

Figure 2: Optimized parameter velocity curves of all four cases for K=1000.

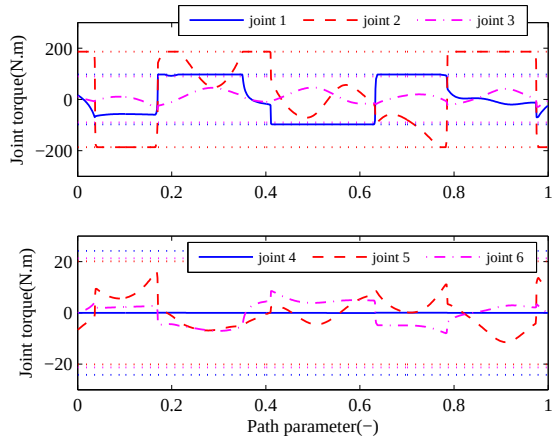

Figure 3: Joint torques of the planned nominal minimum time motion for K=1000.

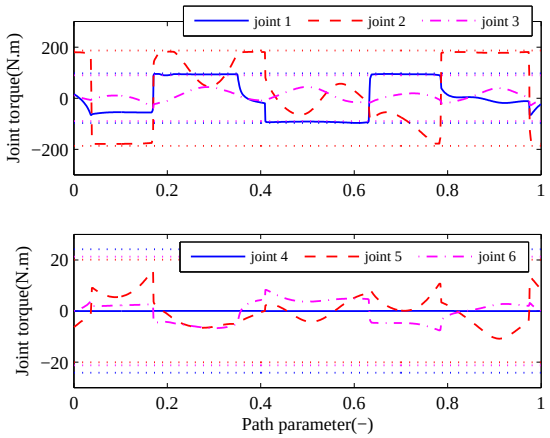

Figure 4: Joint torques of robust minimum time motion in case 1 for K=1000.

In Table 1, the computation time and the robot motion time are given for different values of K. From Table 1, we can see that the optimal motion times based on formulation (6) and formulation (5) are almost the same, which is consistent with Theorem 2. However, the computation time of our approach is faster than that of [2]. Also note that the actually computational complexity of our approach is sub-linear, meaning less than $O(K)$, which might be due to the special structure of $\mathbf{A}_l$ in (14). The practical computational complexity of this approach is better than the complexity $O(K^2)$ of the method given in [11].

The planned joint torques are given in Fig. 3. From [3], the optimal solution of problem (5) is *bang-bang-singular* in the sense that for any $s \in [0, 1]$, the torque of at least one joint reaches its boundary values in the constraint $\tau_{\min} \leq \tau(s) \leq \tau_{\max}$. This property is often used to verify whether a numerical solution is the optimal solution and whether K is large enough. In Fig. 3, the torque is clearly bang-bang-singular: the torques of joints 2, 1, 2, 1, and 2 reach their maximal or minimal values in the intervals $[0, 0.17], [0.17, 0.35], [0.35, 0.41], [0.41, 0.78], [0.78, 1]$, respectively. This indicates that for $K = 1000$, the solution obtained with our method most probably gives high precision approximation to the optimal solution of the original problem (5).

Now, it will be shown that the solution of problem (21) is indeed robust. Suppose that the payload holden by the end effector is the only uncertain parameter. As mentioned in [24], the maximum payload capability of the Puma 560 is 2.5 kg. In this section, the robust trajectory

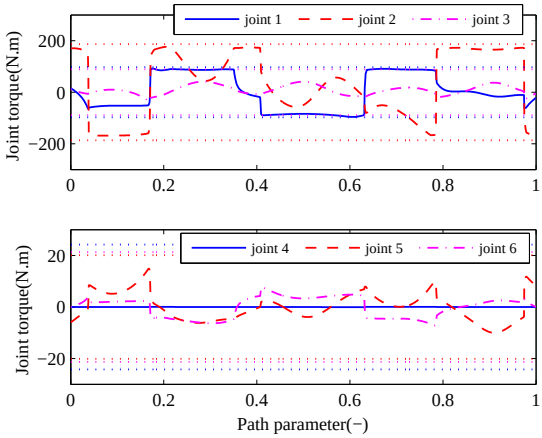

Figure 5: Joint torques of robust minimum time motion in case 2 for K=1000.

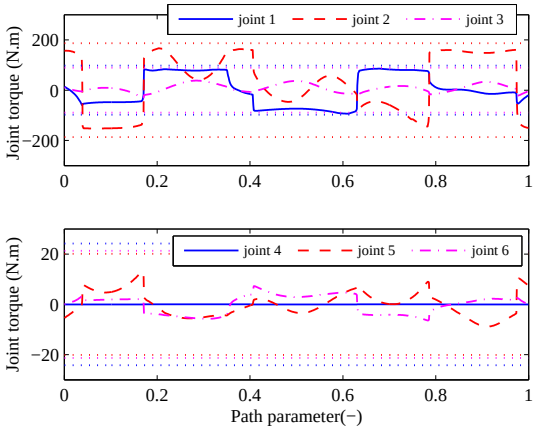

Figure 6: Joint torques of robust minimum time motion in case 3 for K=1000.

planning is implemented under three cases of maximum payload uncertainty assumptions, respectively. The assumptions are 0.5kg for case 1, 1.25kg for case2, and 2.5kg for case 3. The disturbed $\mathbf{\Delta m}$, $\mathbf{\Delta c}$, and $\mathbf{\Delta g}$ are estimated by using the dynamics computation function of the Robotic Toolbox for Matlab.

The computation performance of the proposed robust trajectory planning algorithm is tested by implementing case 2 under different values of K. The results are listed in Table 2. From this table, we can see that the calculated optimal solution is convergent when K increases. Also in this example, the actually computational complexity of our approach is less than $O(K)$.

Table 2: Computation performance of robust algorithm for Case 2 with different K

	Number (K)					
	100	200	500	700	1000	2000
CPU time	0.4330	0.7080	1.0720	1.1290	1.6920	2.6680
Optimal motion time	1.7355	1.7395	1.7407	1.7408	1.7409	1.7409

The planned joint torques of the robust minimum time motions in case 1, case 2, and case 3 are given in Fig. 4, Fig. 5, and 6, respectively. The optimized parameter velocities $\dot{s}$ for all four cases are shown in Fig. 2. Comparing to Fig. 3, the torques for the robust time-minimum motion are reduced to reserve enough space to reject uncertainties and disturbances without causing torque saturation.

To demonstrate the robustness of the obtained trajectories compared to the nominal one, consider 10 equidistantly distributed mass values of payload in $[0, 2.5]kg$. The planned feedrates in the cases of Fig. 3, Fig. 4, Fig. 5, and Fig. 6 are used to traverse the path, and the corresponding torques are given in Fig. 7, Fig. 8, Fig. 9, and Fig. 10, respectively.

Note that the torque bounds are $[97.6; 186.4; 89.4; 24.2; 20.1; 21.3]$ $N.m$. From Fig. 7, Fig. 8 and Fig. 9, we can see that the actual torques pass the given bounds for about 25%, 19% and 11%, respectively. From Fig. 10, it can be seen that the actual torques are all within the given bound, which is consistent with the fact that the robust trajectory in this case is planned under the condition of maximum 2.5kg payload.

The robust trajectories for the three cases of uncertainty assumptions are used to traverse

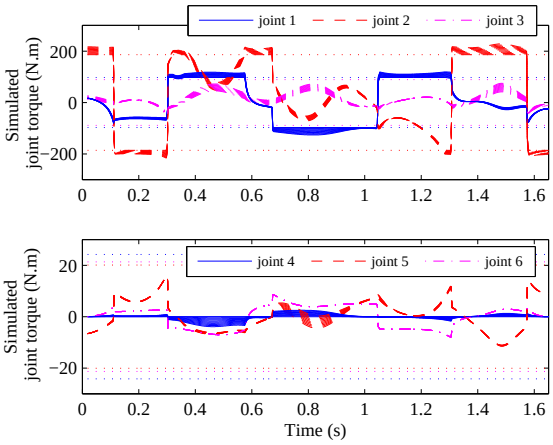

Figure 7: Joint torques for 10 difference payload masses along the nominal reference trajectory.

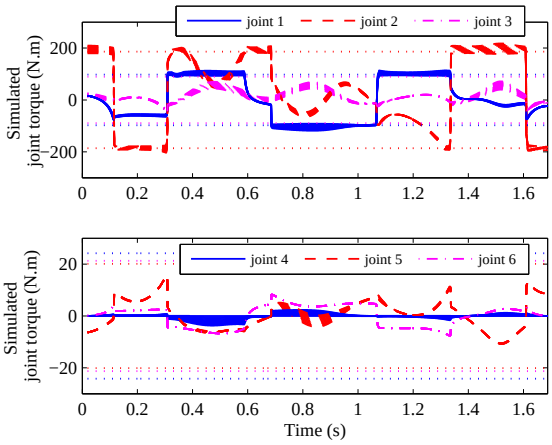

Figure 8: Joint torques for 10 difference payload masses along the robust reference trajectory of case 1.

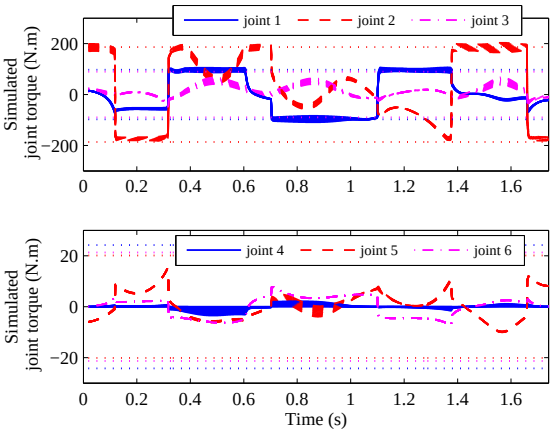

Figure 9: Joint torques for 10 difference payload masses along the robust reference trajectory of case 2.

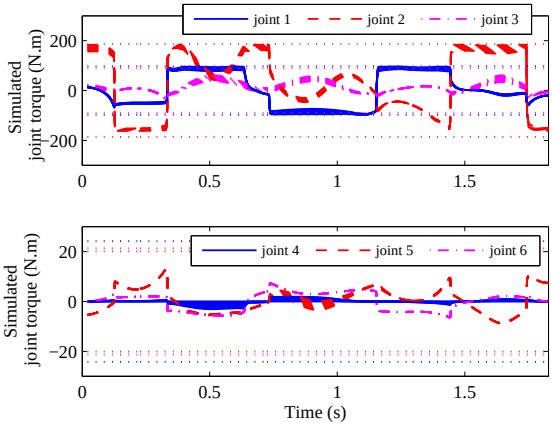

Figure 10: Joint torques for 10 difference payload masses along the robust reference trajectory of case 3.

the path using the ten values of the payload. Detailed data of the experiments are given in Table 3, where Ctime stands for the computation time, Mtime stands for the optimal motion time, RTI stands for the rate of time increase compared with the nominal case, MTV stands for the maximum torque violation, ATV stand for the average torque violation, and RTV stands for the rate of torque violation.

From Table 3, we can see that when the 2.5kg payload uncertainty assumption is used, along the generated robust trajectory, the actual torques do not pass the given bounds. By contrast, along the non robust nominal trajectories, at almost all times at least one actual torque passes the given bound and the maximum torque violation reaches 25% of the given bound. The optimal motion time of this robust trajectory increases about 10.7% compared with the nominal case, which is a reasonable price to pay for robustness.

Table 3: Results of trajectory robustness test for K=1000

	Ctime(s)	Mtime(s)	RTI(%)	MTV(N.m)	ATV(N.m)	RTV(%)
Nominal	1.4508	1.6508	0	46.39	3.99	99.16
Case 1	1.9810	1.6872	2.2	35.65	2.87	98.96
Case 2	1.6920	1.7409	5.5	21.04	1.75	82.35
Case 3	1.8600	1.8281	10.7	None	None	0

6 Conclusions

In this paper, a linear program based robust time minimum trajectory planning approach is presented. The robust version of the TMTP problem is constructed to overcome the parameter uncertainties and torque disturbances of the dynamic system. To make our approach tractable, the TMTP problem is proven to be equivalent to a linear optimal control problem by considering the total motion feedrate of the end-effector of the robot as the objective function. Quadratic B-spline curves are used to parameterize the linear optimal control problem into a linear program which can be solved in polynomial time. The approach theoretically ensures that the generated velocity is time optimal and for every possible realization of the uncertainties and disturbances within the bound, the robust trajectory will not violate any joint torque constraints. Though the proposed algorithm is designed to execute offline, online use is also possible because of the good computation performance.

Acknowledgment

This research was partially supported by a National Key Basic Research Project of China (2011CB302400), a grant from NSFC (60821002) and a grant from UPC (120501A).

Bibliography

[1] Katzschmann, R.; Kroger, T.; Asfour, T.; Khatib O.(2013); Towards Online Trajectory Generation Considering Robot Dynamics and Torque Limits, in *Intelligent Robots and Systems (IROS), 2013 IEEE/RSJ International Conference on*, ISSN 2153-0858, Tokyo, 5644 - 5651.

[2] Verscheure, D.; Demeulenaere, B.; Swevers, J.; De Schutter, J.; Diehl, M.(2009); Time-optimal path tracking for robots: a convex optimization approach, *IEEE Trans. on Automatic Control*, ISSN 0018-9286, 54(10): 2318-2327.

[3] Bobrow, J.E.; Dubowsky, S.; Gibson, J.(1985); Time-optimal control of robotic manipulators along specified paths, *International Journal of Robotics Research*, ISSN 0278-3649, 4(3): 3-17.

[4] Shin, K.; McKay, N.(1985); Minimum-time control of robotic manipulators with geometric path constraints, *IEEE Trans. on Automatic Control*, ISSN 0018-9286, 30(6): 531-541.

[5] Timar, S.D.; Farouki, R.T.(2007); Time-optimal traversal of curved paths by Cartesian CNC machines under both constant and speed-dependent axis acceleration bounds, *Robotics and Computer-Integrated Manufacturing*, ISSN 0736-5845, 23(5): 563-579.

[6] Yuan, C.; Zhang, K.; Fan, W.(2013); Time-optimal Interpolation for CNC Machining along Curved Tool Pathes with Confined Chord Error, *Journal of Systems Science and Complexity*, ISSN 1559-7067, 26(5): 836-870.

[7] Chen, Y.; Desrochers, A.A.(1989); Structure of minimum-time control law for robotic manipulators with constrained paths, in *Robotics and Automation, IEEE International Conference on*, ISBN 0-8186-1938-4, Scottsdale, USA, 971-976.

[8] Guo, J.X.; Zhang, Q.; Gao, X.S.(2013); Tracking Error Reduction in CNC Machining by Reshaping the Kinematic Trajectory, *Journal of Systems Science and Complexity*, ISSN 1559-7067, 26(5), 800-817.

[9] Zhang, K.; Yuan, C.M.; Gao, X.S.(2013); Efficient algorithm for feedrate planning and smoothing with confined chord error and acceleration for each axis, *The International Journal of Advanced Manufacturing Technology*, ISSN 0268-3768 , 66(9): 1685-1697.

[10] Ardeshiri, T.; Norrlof, M.; Lofberg, J.; Hansson, A.(2011); Convex optimization approach for time-optimal path tracking of robots with speed dependent constraint, in *Proceedings of the 18th IFAC World Congress*, ISSN 1474-6670, Milano, Italy, 14648-14653.

[11] Hauser, K.(2013); Fast Interpolation and Time-Optimization on Implicit Contact Submanifolds, in *Proceedings of Robotics: Science and Systems*, ISSN 2330-765X, Berlin, Germany.

[12] Shin, K.G.; McKay, N.D.(1987); Robust trajectory planning for robotic manipulators under payload uncertainties, *IEEE Trans. on Automatic Control*, ISSN 0018-9286, 32(12): 1044-1054.

[13] Kieffer, J.; Cahill, A.J.; James, M.R.(1997); Robust and accurate time-optimal path-tracking control for robot manipulators, *IEEE Trans. on Robotics and Automation*, ISSN 1042-296X, 13(6): 880–890.

[14] Diehl, M.; Gerhard, J.; Marquardt, W.; Monnigmann, M.(2008); Numerical solution approaches for robust nonlinear optimal control problems, *Computers & Chemical Engineering*, ISSN 0098-1354, 32(6): 1279-1292.

[15] Marti, K.; Aurnhammer, A.(2002); Robust optimal trajectory planning for robots by stochastic optimization, *Mathematical and Computer Modelling of Dynamical Systems*, ISSN 1744-5051, 8(1): 75-116.

[16] Chisci, L.; Rossiter, J.A.; Zappa, G.(2001); Systems with persistent disturbances: Predictive control with restrictive constraints, *Automatica*, ISSN 0005-1098, 37(7): 1019-1028.

[17] Mayne, D.Q.; Seron, M.M.; Rakovic, S.V.(2005); Robust model predictive control of constrained linear systems with bounded disturbances, *Automatica*, ISSN 0005-1098, 41(2): 219-224.

[18] Patrikalakis, N.M.; Maekawa, T.(2010); *Shape Interrogation for Computer Aided Design and Manufacturing*, ISBN 978-3-642-04074-0, Springer Berlin, Heidelberg.

[19] Bertsimas, D.; Brown, D.B.; Caramanis, C.(2011); Theory and applications of robust optimization, *SIAM Review*, ISSN 0036-1445, 53(3): 464–501.

[20] Karmarkar, N.(1984); A new polynomial time algorithm for linear programming, *Combinatorica*, ISSN 0209-9683, 4(4): 373-395.

[21] Sirisena, H.R.; Chou, F.S.(1979); Convergence of the control parameterization Ritz method for nonlinear optimal control problems, *Journal of Optimization Theory and Applications*, ISSN 0022-3239, 29(3): 369-382.

[22] Daniel, J.W.(1973); The Ritz-Galerkin method for abstract optimal control problems, *SIAM Journal on Control*, ISSN 0036-1402, 11(1): 53-63.

[23] Schwartz, A.L.(1996); *Theory and Implementation of Numerical Methods Based on Runge-Kutta Integration for Solving Optimal Control Problems*, Ph.D. Thesis, Univ. of California at Berkeley.

[24] Corke, P.(1996); A robotics toolbox for MATLAB, *IEEE Robotics and Automation Magazine*, ISSN 1070-9932, 3(1): 24-32.

[25] Sturm, J.F.(1999); Using SeDuMi 1.02, A Matlab toolbox for optimization over symmetric cones, *Optimization Methods and Software*, ISSN 1055-6788, 11(1-4): 625-653.

INTERNATIONAL JOURNAL OF COMPUTERS COMMUNICATIONS & CONTROL
ISSN 1841-9836, 10(1):136-146, February, 2015.

Design of Robust Fuzzy Sliding-Mode Controller for a Class of Uncertain Takagi-Sugeno Nonlinear Systems

X.Z. Zhang, Y.N. Wang

X.Z. Zhang*
1. School of Electrical and Information Engineering
Hunan University
China, 410082 Changsha, Yuelushan
2. Cooperative Innovative Center of Wind Power
Hunan Institute of Engineering
China, 411104 Xiangtan, Fuxing Road 88
*Corresponding author: zxz@hnie.edu.cn

Y.N. Wang
School of Electrical and Information Engineering
Hunan University
China, 410082 Changsha, Yuelushan
yaonan@hnu.edu.cn

Abstract: This paper presents the fuzzy design of sliding mode control (SMC) for nonlinear systems with uncertainties, which can be represented by a Takagi-Sugeno (T-S) model. There exist the parameter uncertainties in both state and input matrices, as well as the matched external disturbance. The key feature of this work is the great ability of the controller to deal with systems without assuming that the control matrices of each local T-S model to be same and knowing the priori information of the upper norm-bounds of uncertainties. A sufficient condition for the existence of the desired fuzzy SMC is obtained by solving a set of linear matrix inequalities (LMIs). The reachability of the specified sliding surface is proven. A numerical example is illustrated in order to show the validity of the proposed scheme.
Keywords: uncertain T-S nonlinear system, sliding mode control, linear matrix inequalities (LMI), system stabilitybooks, examples.

1 Introduction

It has been shown that Takagi Sugeno (T-S) fuzzy model is a powerful and efficient tool to handle complex nonlinear system, and be employed in most model-based fuzzy analysis approaches [1, 2]. Since the Parallel Distributed compensation (PDC) approach is formulated by Tanaka and Wang [3], the stability analysis and stabilized controller design for T-S fuzzy systems become achievable and have been applied in a wide range of areas such as electrical/mechanical systems [4, 5], process control [6], robot [7] and time-delayed systems [8]. A lot of research outcomes on this field have been appeared in literatures. Practically, a real nonlinear system may contain various kinds of uncertainties such as parameter variations, modeling errors and external disturbances, etc. In this case, the PDC-based controllers [3] may perform well no longer. Then, the robustly stabilized control to uncertainties of nonlinear fuzzy systems is required. Based on the T-S fuzzy model, Wu studied the robust H_2 fuzzy observer-based control problem for discrete-time nonlinear systems with parametric uncertainties [9]. Lin, et.al, investigated the mixed H_2/H_∞ controller for uncertain T-S fuzzy systems with discrete time-varying delay [10].

It's well known that the sliding mode control (SMC) is an effective means to design robust controllers for nonlinear systems with uncertainties bounded by known scalar-valued functions. Recently, the SMC has been successfully applied into solving the stabilization problems for uncertain fuzzy systems [11, 12]. Specially, under the SMC control the state trajectories would

enter into the pre-designed sliding-mode motion within finite time and after that keep staying on it; thus, the system dynamics is not sensitive to parameter variations and external disturbances any more [9, 13]. Basically, the feedback gains of the SMC control are often determined by the feasible solution of a set of Linear Matrix Inequalities (LMI). Choi presented a robust stabilization of uncertain fuzzy systems using SMC system approach [14]. Zhang and Wang proposed a mixed SMC-H_∞ controller for time-delay system with unmatched uncertainties [15].

Although many researchers have proposed a variety of T-S fuzzy SMC-based methods [4, 7–10, 14], by far there still two problems yet remained to be well-solved: (1) the suitable relaxation on the assumption that all the control matrices of the nominal sub-systems' models are identical; It is practically difficult to satisfy this assumption. In practice, this assumption is very strict and insufficient to model various uncertainties/nonlinearities in most of actual systems such as nonlinear stirred tank reactor, fourth-order cart-pole system, and active queue management in TCP networks and two-link robot manipulator; (2) the reasonable assumption that the system uncertainties/perturbations are unknown but norm-bounded. For the SMC-based methods, if uncertainties are known, it's easy to choose proper switching gains, which are bigger than the upper norm-bounds of uncertainties, to ensure the reachability of sliding-mode motion. Unfortunately, the information of the upper bound of uncertainties/perturbations may not easily be obtained in practice. Therefore, it's supposed to adopt parameter identification or adaptive control approach to estimate the bounds of uncertainties on-line [16].

Motivated by the above discussion, it is meaningful to design fuzzy variable structure controller in this paper such that the closed-loop system is asymptotically stable without (1) assuming the control matrices of each local linear model to be same; and (2) knowing the priori information of the upper norm-bounds of uncertainties. The existence condition of linear sliding surfaces and the asymptotical stability of the reduced-order equivalent sliding-mode dynamics are firstly derived by the LMI optimization technique. After the establishment of the local T-S model, the upper norm-bounds of uncertainties and modeling errors between the original and local systems are estimated. Then, the designed SMC controller composes of a state-feedback control term and an adaptive switching-feedback control term, which are achieved based on the Lyapunov function method. As a result, the aforementioned problems are well solved in the proposed scheme. Finally, a numerical example is illustrated in order to show the effectiveness of the proposed methods.

2 Problem formulation and preliminaries

As stated in Introduction, T-S fuzzy models can provide an effective representation of complex nonlinear systems in terms of fuzzy sets and fuzzy reasoning applied to a set of linear input output sub-models. Hence, in this work, a class of nonlinear systems is represented by a T-S model. As in [3], the T-S fuzzy system with uncertainties is described by fuzzy IF THEN rules, which locally represent linear input-output relations of nonlinear systems.

The i-th rule of the fuzzy model is formulated in the following equation:

Plant rule i: IF z_1 is M_1^i and z_2 is M_2^i $\cdots$ and z_p is M_1^p, THEN

$$\dot{\boldsymbol{x}}(t) = \boldsymbol{A}_i \boldsymbol{x}(t) + \boldsymbol{B}_i \boldsymbol{u}(t) \tag{1}$$

where M_j^i is the fuzzy set, $\boldsymbol{z}(t) = [z_1(t), z_2(t), \cdots, z_p(t)]^T$ is the premise variable vector, r is the number of rules of this T-S fuzzy model. $\boldsymbol{x}(t) \in \mathbb{R}^n$ is the state vector, $\boldsymbol{u}(t) \in \mathbb{R}^m$ is the control input vector. $\boldsymbol{A}_i$,$\boldsymbol{B}_i$ are known real constant matrices with appropriate dimensions.

The overall fuzzy model achieved by fuzzy blending of each plant rule is represented as follows:

$$\dot{\boldsymbol{x}}(t) = \sum_{i=1}^{r} h_i(\boldsymbol{z})[\boldsymbol{A}_i\boldsymbol{x}(t) + \boldsymbol{B}_i\boldsymbol{u}(t)] \tag{2}$$

where $h_i(\boldsymbol{z}(t)) = \frac{w_i(\boldsymbol{z}(t))}{\sum_{j=1}^{r} w_i(\boldsymbol{z}(t))}$,$w_i(\boldsymbol{z}(t)) = \prod_{j=1}^{p} M_j^i(\boldsymbol{z}(t))$, in which $M_j^i(\boldsymbol{z}(t))$ is the membership grade of $z_j(t)$ in M_j^i. According to the theory of fuzzy sets, we have $M_j^i(\boldsymbol{z}(t)) \geq 0$. Therefore, it implies that $h_i(\boldsymbol{z}(t)) \geq 0$ and $\sum_{i=1}^{r} h_i(\boldsymbol{z}(t)) = 1$.

In practical applications, the system (2) usually exists the parameters variation and the external disturbances. After considering the perturbation, the global fuzzy model of system (2) can be rewritten as

$$\dot{\boldsymbol{x}}(t) = \sum_{i=1}^{r} h_i(\boldsymbol{z})[(\boldsymbol{A}_i + \Delta\boldsymbol{A}_i)\boldsymbol{x}(t) + (\boldsymbol{B}_i + \Delta\boldsymbol{B}_i)\boldsymbol{u}(t) + d_i(t, \boldsymbol{x}, \boldsymbol{u})] \tag{3}$$

where $\Delta\boldsymbol{A}_i$, $\Delta\boldsymbol{B}_i$ are unknown time-varying matrices representing parameter uncertainties, and $d_i(t, \boldsymbol{x}, \boldsymbol{u})$ denotes the external disturbance.

In this work, the control matrices doesn't satisfy $\boldsymbol{B}_1 = \boldsymbol{B}_2 = ... = \boldsymbol{B}_r$ and we define the weighted nominal matrix as $\boldsymbol{B} = \sum_{i=1}^{r} h_i(\boldsymbol{z})\boldsymbol{B}_i$. Moreover, it is required that $\boldsymbol{B}$ is a non-zero matrix with full-column (or full-row) rank. The uncertain matrices are assumed to be matched, i.e. there exist certain functions $\boldsymbol{D}(t)$, $\boldsymbol{E}(t)$ and $\boldsymbol{F}(t)$ such that $\Delta\boldsymbol{A}_i(t) = \boldsymbol{B}_i\boldsymbol{D}(t)$, $\Delta\boldsymbol{B}_i(t) = \boldsymbol{B}_i\boldsymbol{E}(t)$ and $d_i(t, \boldsymbol{x}, \boldsymbol{u}) = \boldsymbol{B}_i\boldsymbol{F}(t)$ hold. As a result, the system (3) can be rewritten as

$$\dot{\boldsymbol{x}}(t) = \sum_{i=1}^{r} h_i(\boldsymbol{z})\boldsymbol{A}_i\boldsymbol{x}(t) + \boldsymbol{B}[\boldsymbol{u}(t) + g(t, \boldsymbol{x}, \boldsymbol{u})] \tag{4}$$

where the time-varying function $g(t, \boldsymbol{x}, \boldsymbol{u}) = \boldsymbol{D}(t)\boldsymbol{x}(t) + \boldsymbol{E}(t)\boldsymbol{u}(t) + \boldsymbol{F}(t)$, then $g(t, \boldsymbol{x}, \boldsymbol{u})$ contains all the perturbation in system (3). Before proceeding, some assumptions and lemmas are given as following, which are useful for the development of our result.

(Assumption.1) The time-varying uncertainties $g(t, \boldsymbol{x}, \boldsymbol{u})$ is assumed to be norm-bounded, that is, $\|g\| \leq \sum_{k=0}^{N-1} \gamma_k \|\boldsymbol{x}(t)\|^k$, where γ_k is unknown coefficient and N is a positive integer.

Remark 1: Assumption 1 is a standard assumption in the study of variable structure control.

(Lemma.1 Choi [14]): Give any matrix X, Y, Z with appropriate dimensions, and $Y > 0$. Then we have $-X^TZ - Z^TX \leq X^TYX + Z^TY^{-1}Z$.

(Lemma.2 Schur's Complement [3]): Given the matrix inequality $\begin{bmatrix} S_{11} & S_{12} \\ S_{12}^T & S_{22} \end{bmatrix} < 0$, where S_{11} and S_{22} are invertible symmetrical matrices, it's equal to each of the following inequalities:

(i) $S_{11} < 0$, $S_{22} - S_{12}^T S_{11}^{-1} S_{12} < 0$; (ii) $S_{22} < 0$, $S_{11} - S_{12} S_{22}^{-1} S_{12}^T < 0$.

3 Controller design

The objective of this work is to design an SMC law such that the desired control performance for the resulting closed-loop system is obtained despite of parameter uncertainties and unmatched external disturbance. In this section, an SMC law is synthesized such that the closed-loop systems are robustly asymptotically stable. It is also proven that the reachability of the specified switching (sliding) surface $S(t) = 0$ can be ensured by the proposed SMC law. Thus, it is concluded that the synthesized SMC law can guarantee the state trajectories of uncertain system (4) to be driven onto the sliding surface, and asymptotically tend to zero along the specified sliding surface.

3.1 Design of the sliding function and stability analysis of the sliding motion

Essentially, a VSC design is composed of two phases: hyper-plane design and controller design [9]. There are various methods for designing hyper-plane, however in this paper the switching surface is defined as

$$S(t, \boldsymbol{x}) = \boldsymbol{C}\boldsymbol{x}(t) \tag{5}$$

where $\boldsymbol{C} \in \mathbb{R}^{m\times n}$ is the designed coefficient. According to the previous works [2], for the system (2), there are two prerequisites to find the switching surface (5) that is

(P-1): The matrix $\boldsymbol{CB}$ is invertible for any $h_i(\boldsymbol{z})$ satisfying $h_i(\boldsymbol{z}) \geq 0$ and $\sum_{i=1}^{r} h_i(\boldsymbol{z}) = 1$.

(P-2): The reduced sliding-mode motion of the system dynamics restricted on the switching surface is asymptotically stable to all admissible uncertainties.

In this part, we analyze the dynamic performance of the system described by (4), and derives some sufficient conditions for the asymptotically stability of the sliding dynamics via LMI method. The following theorem shows that system (4) with the switching surface as in (5) is asymptotically stable.

Theorem 1. *Consider the fuzzy uncertain systems (4) with Assumptions (1). The switching function is given by (5). If there is feasible solution Q such that the LMIs shown in (6) hold for $\forall i, j, k \in 1, ..., r$, the proper sliding-mode coefficient C exists and $C = (B^T Q^{-1} B)^{-1} B^T$.*

$$\begin{bmatrix} \boldsymbol{A}_i\boldsymbol{Q} + \boldsymbol{Q}\boldsymbol{A}_i^T & \boldsymbol{Q}\boldsymbol{B}_j^T & \boldsymbol{A}_i^T \\ \boldsymbol{B}_j^T\boldsymbol{Q} & -\boldsymbol{B}_j^T\boldsymbol{B}_k & 0 \\ \boldsymbol{A}_i & 0 & -\boldsymbol{I} \end{bmatrix} < 0 \tag{6}$$

where the invertible matrix $Q \in \mathbb{R}^{n\times n}$ is decisive variable.

Proof: First, the existence of the coefficient C is proved. Since Q is designed to be invertible, the inequalities $\boldsymbol{B}^T\boldsymbol{B} \neq 0$ and $\boldsymbol{B}^T\boldsymbol{Q}^{-1}\boldsymbol{B} \neq 0$ hold; thus, its easy to prove that the achieved matrix $\boldsymbol{CB}$ is invertible and $(\boldsymbol{CB})^{-1} = (\boldsymbol{B}^T\boldsymbol{B})^{-1}(\boldsymbol{B}^T\boldsymbol{Q}^{-1}\boldsymbol{B})$. That is to say, if the coefficient is chosen as $\boldsymbol{C} = (\boldsymbol{B}^T\boldsymbol{Q}^{-1}\boldsymbol{B})\boldsymbol{B}^T$, both the sliding surface and the equivalent control exist. With the chosen sliding surface, once the n-order system enters the m-order sliding surface $S = \boldsymbol{C}\boldsymbol{x}(t)$, the system dynamic of (4) is equivalent to the $(n-m)$-order sliding motion, and the system states will asymptotically converge to zero with proper switching gains. In the following, we will derive the equivalent control and the sliding mode as well as the stability analysis.

Now, the linear transformation $\boldsymbol{T}$ is carried on the states to separate the m-th sliding-mode states and the reduced $(n-m)$-order states

$$\boldsymbol{T} = \begin{bmatrix} T_1 \\ T_2 \end{bmatrix} = \begin{bmatrix} (\boldsymbol{K}^T\boldsymbol{Q}\boldsymbol{K})^{-1}\boldsymbol{K}^T\boldsymbol{Q} \\ (\boldsymbol{B}^T\boldsymbol{Q}^{-1}\boldsymbol{B})^{-1}\boldsymbol{B}^T \end{bmatrix} \tag{7}$$

where $T_1 \in \mathbb{R}^{(n-m)\times n}$, $T_2 \in \mathbb{R}^{m\times n}$ and $\boldsymbol{K} \in \mathbb{R}^{n\times(n-m}$ is an orthonormal basis for the null space of $\boldsymbol{B}^T$ such that $\boldsymbol{B}^T\boldsymbol{K} = 0$ and $\boldsymbol{K}^T\boldsymbol{K} = \boldsymbol{I}$ satisfy. We have

$$\boldsymbol{z} = \boldsymbol{T}\boldsymbol{x}(t) = \begin{bmatrix} z_1 \\ z_2 \end{bmatrix} \tag{8}$$

In (8), it's obvious that $z_2 = (\boldsymbol{B}^T\boldsymbol{Q}^{-1}\boldsymbol{B})\boldsymbol{B}^T\boldsymbol{x}(t) = \boldsymbol{C}\boldsymbol{x}(t)$ is the sliding-mode state and z_1 is the reduced-order state. Its easy to obtain the inverse transformation $\boldsymbol{T}^{-1} = [\boldsymbol{K}, \boldsymbol{Q}^{-1}\boldsymbol{B}]$.

By differentiating the above transformation, we can obtain

$$\begin{aligned}\dot{z} &= \boldsymbol{T}\boldsymbol{x}(t) = \sum_{i=1}^{r} h_i(\boldsymbol{z}) \begin{bmatrix} \boldsymbol{T}_1 \\ \boldsymbol{T}_2 \end{bmatrix} \boldsymbol{A}_i \begin{bmatrix} \boldsymbol{K} & \boldsymbol{Q}^{-1}\boldsymbol{B} \end{bmatrix} \boldsymbol{T}\boldsymbol{x}(t) + \begin{bmatrix} \boldsymbol{T}_1 \\ \boldsymbol{T}_2 \end{bmatrix} \boldsymbol{B}[\boldsymbol{u} + g(t, \boldsymbol{x}, \boldsymbol{u})] \\ &= \sum_{i=1}^{r} h_i(\boldsymbol{z}) \begin{bmatrix} \boldsymbol{T}_1\boldsymbol{A}_i\boldsymbol{K} & \boldsymbol{T}_1\boldsymbol{A}_i\boldsymbol{Q}^{-1}\boldsymbol{B} \\ \boldsymbol{T}_2\boldsymbol{A}_i\boldsymbol{K} & \boldsymbol{T}_2\boldsymbol{A}_i\boldsymbol{Q}^{-1}\boldsymbol{B} \end{bmatrix} \begin{bmatrix} z_1 \\ z_2 \end{bmatrix} + \begin{bmatrix} \boldsymbol{T}_1\boldsymbol{B} \\ \boldsymbol{T}_2\boldsymbol{B} \end{bmatrix} [\boldsymbol{u} + g(t, \boldsymbol{x}, \boldsymbol{u})] \end{aligned} \tag{9}$$

In (9), it's not difficult to verify that $\boldsymbol{T}_1\boldsymbol{B} = (\boldsymbol{K}\boldsymbol{Q}^{-1}\boldsymbol{K})\boldsymbol{K}^T\boldsymbol{B} = 0$ and $\boldsymbol{T}_2\boldsymbol{B} = \boldsymbol{C}\boldsymbol{B}$. According to the sliding mode theory, let $\dot{S} = S = \dot{z}_2 = 0$, we have

$$\begin{aligned}\dot{z}_2 &= \sum_{i=1}^{r} h_i(\boldsymbol{z})(\boldsymbol{T}_2\boldsymbol{A}_i\boldsymbol{K}z_1 + \boldsymbol{T}_2\boldsymbol{A}_i\boldsymbol{Q}^{-1}\boldsymbol{B}z_2) + \boldsymbol{T}_2\boldsymbol{B}[\boldsymbol{u} + g(t, \boldsymbol{x}, \boldsymbol{u})] \\ &= \sum_{i=1}^{r} h_i\boldsymbol{C}\boldsymbol{A}_i\boldsymbol{x}(t) + \boldsymbol{T}_2\boldsymbol{B}[g(t, \boldsymbol{x}, \boldsymbol{u})] \end{aligned} \tag{10}$$

From (16), the following equivalent control can be derived

$$\boldsymbol{u}_{eq}(t) = -g(t, \boldsymbol{x}, \boldsymbol{u}) - \sum_{i=1}^{r} h_i((z)(t))(\boldsymbol{C}\boldsymbol{B})^{-1}\boldsymbol{C}\boldsymbol{A}_i\boldsymbol{x}(t) \tag{11}$$

Substitute $\boldsymbol{u}_{eq}(t)$ in (11) into (10), the reduced-order sliding motion in the switching surface can be obtained as

$$\dot{z}_1 = \sum_{i=1}^{r} h_i(\boldsymbol{z}(t))(\boldsymbol{K}^T\boldsymbol{Q}\boldsymbol{K})^{-1}\boldsymbol{K}^T[\boldsymbol{I} - \boldsymbol{B}(\boldsymbol{C}\boldsymbol{B}^{-1}\boldsymbol{C})]\boldsymbol{A}_i\boldsymbol{K}z_1 \tag{12}$$

To analyze the stability of the sliding-mode dynamics (8), we consider the fuzzy uncertain system (4) with LMIs in (6) and choose the Lyapunov functional candidate $V_1 = z_1^T\boldsymbol{P}z_1$, where $\boldsymbol{P} = \boldsymbol{K}^T\boldsymbol{Q}\boldsymbol{K}$ is a positive matrix.

By differentiating the function $\boldsymbol{V}_1$, we obtain the differential along the trajectories as

$$\begin{aligned}\dot{V}_1 &= z_1^T\boldsymbol{P}\dot{z}_1 + \dot{z}_1^T\boldsymbol{P}z_1 \\ &= \sum_{i=1}^{r} h_i(z)\big[z_1^T\boldsymbol{P}\boldsymbol{T}_1(\boldsymbol{I} - \boldsymbol{B}(\boldsymbol{C}\boldsymbol{B})^{-1}\boldsymbol{C}\boldsymbol{A}_i)\boldsymbol{K}z_1 + z_1^T\boldsymbol{K}^T\boldsymbol{A}_i^T(\boldsymbol{I} - \boldsymbol{B}(\boldsymbol{C}\boldsymbol{B})^{-1}\boldsymbol{C})^T\boldsymbol{T}_1^T\boldsymbol{P}^T z_1\big] \\ &= \sum_{i=1}^{r} h_i(z)\big[z_1^T\boldsymbol{K}^T\boldsymbol{Q}(\boldsymbol{I} - \boldsymbol{B}(\boldsymbol{C}\boldsymbol{B})^{-1}\boldsymbol{C})\boldsymbol{A}_i\boldsymbol{K}z_1 + (*)\big] \\ &= \sum_{i=1}^{r} h_i(z)\big[w^T(t)\boldsymbol{Q}(\boldsymbol{I} - \boldsymbol{B}(\boldsymbol{C}\boldsymbol{B})^{-1}\boldsymbol{C})\boldsymbol{A}_i\boldsymbol{K}w(t) + (*)\big] \\ &= \sum_{i=1}^{r} h_i(z)w^T(t)\Big\{\big[\boldsymbol{Q}\boldsymbol{A}_i + (*)\big] - \big[\boldsymbol{Q}\boldsymbol{B}(\boldsymbol{C}\boldsymbol{B})^{-1}\boldsymbol{C}\boldsymbol{A}_i + (*)\big]\Big\}w(t) \end{aligned} \tag{13}$$

where the defined new state vector $w(t) = \boldsymbol{K}z_1 \in \mathbb{R}^{n\times 1}$.

By now, the stability of the states $\boldsymbol{x}(t)$ in the switching surface is equivalent to the stability of the news states $\boldsymbol{w}(t)$. Noticing that $\boldsymbol{B}(\boldsymbol{C}\boldsymbol{B})^{-1}\boldsymbol{C} = \boldsymbol{B}(\boldsymbol{B}^T\boldsymbol{B})^{-1}\boldsymbol{B}^T$, it is easy to have $\dot{V}_1 < 0$ if the following inequality holds

$$\big[\boldsymbol{Q}\boldsymbol{A}_i + (*)\big] - \boldsymbol{Q}\boldsymbol{B}(\boldsymbol{B}^T\boldsymbol{B})^{-1}\boldsymbol{B}^T\boldsymbol{A}_i - \boldsymbol{A}_i^T\boldsymbol{B}(\boldsymbol{B}^T\boldsymbol{B})^{-1}\boldsymbol{B}^T\boldsymbol{Q} \le 0 \tag{14}$$

According to Lemma 2, let $\boldsymbol{X} = \boldsymbol{QB}(\boldsymbol{B}^T\boldsymbol{B})^{-1}\boldsymbol{B}^T$, $\boldsymbol{Z} = \boldsymbol{A}_i$ and $\boldsymbol{Y} = \boldsymbol{I} > 0$, the inequality in (21) implies that

$$\big[\boldsymbol{QA}_i + (*)\big] + \boldsymbol{QB}(\boldsymbol{B}^T\boldsymbol{B})^{-1}\boldsymbol{B}^T + \boldsymbol{A}_i^T\boldsymbol{A}_i \leq 0 \tag{15}$$

According to the inequalities (14), (15), we have

$$\big[\boldsymbol{QA}_i + (*)\big] - \big[\boldsymbol{QB}(\boldsymbol{B}^T\boldsymbol{B})^{-1}\boldsymbol{B}^T\boldsymbol{A}_i + \boldsymbol{A}_i^T\boldsymbol{B}^T(\boldsymbol{B}^T\boldsymbol{B})^{-1}\boldsymbol{B}^T\boldsymbol{Q}\big] \leq 0 \tag{16}$$

By using Schur's complement formula and noticing that $\boldsymbol{B}^T\boldsymbol{B} \geq 0$, we can rewrite the above inequality as

$$\begin{bmatrix} \boldsymbol{A}_i\boldsymbol{Q} + \boldsymbol{Q}\boldsymbol{A}_i^T & \boldsymbol{QB} & \boldsymbol{A}_i^T \\ \boldsymbol{B}^T\boldsymbol{Q} & -\boldsymbol{B}^T\boldsymbol{B} & 0 \\ \boldsymbol{A}_i & 0 & -\boldsymbol{I} \end{bmatrix} < 0 \tag{17}$$

From (17) and noticing the definition of the matrix $\boldsymbol{B}$ and $\boldsymbol{B}^T\boldsymbol{B} = \sum_{j=1}^{r}\sum_{k=1}^{r} h_j(z)h_k(z)\boldsymbol{B}_j^T\boldsymbol{B}_k$, we can deduce the following inequality

$$\dot{V}_1 = \sum_{i=1}^{r}\sum_{j=1}^{r}\sum_{k=1}^{r} h_i(z)h_j(z)h_k(z)w^T(t)\begin{bmatrix} \boldsymbol{A}_i\boldsymbol{Q} + \boldsymbol{Q}\boldsymbol{A}_i^T & \boldsymbol{Q}\boldsymbol{B}_j^T & \boldsymbol{A}_i^T \\ \boldsymbol{B}_j^T\boldsymbol{Q} & -\boldsymbol{B}_j^T\boldsymbol{B}_k & 0 \\ \boldsymbol{A}_i & 0 & -\boldsymbol{I} \end{bmatrix} w(t) \leq 0 \tag{18}$$

and this leads to for $\forall i, j, k \in 1, ..., r$

$$\begin{bmatrix} \boldsymbol{A}_i\boldsymbol{Q} + \boldsymbol{Q}\boldsymbol{A}_i^T & \boldsymbol{Q}\boldsymbol{B}_j^T & \boldsymbol{A}_i^T \\ \boldsymbol{B}_j^T\boldsymbol{Q} & -\boldsymbol{B}_j^T\boldsymbol{B}_k & 0 \\ \boldsymbol{A}_i & 0 & -\boldsymbol{I} \end{bmatrix} w(t) \leq 0 \tag{19}$$

This means that the sliding surface (5) and the equivalent control (11) for the fuzzy system (4) with Assumption 1 exist and the sliding motion is asymptotically stable. □

3.2 Design of controller and adaptive laws

As the last step of design procedure, we will further design the VSC controller ensures the reachability of the specified switching surface. The adaptive VSC controller is represented in a set of fuzzy rules as following
Controller rule i: IF z_1 is M_1^i and z_2 is M_2^i $\cdots$ and z_p is M_p^i, THEN

$$\boldsymbol{u}(t) = -(\boldsymbol{CB})^{-1}\big[\boldsymbol{CA}_i\boldsymbol{x}(t) + \|N(t)\|\|\dot{h}_\alpha\|\|\boldsymbol{x}(t)\|sgn(\boldsymbol{S}) + \|\boldsymbol{CB}\|(\hat{\rho}_0 + \hat{\rho}_1\|\boldsymbol{x}(t)\|)sgn(\boldsymbol{S}) + \varepsilon sgn(\boldsymbol{S})\big] \tag{20}$$

The global fuzzy VSC and the adaptation laws are designed as

$$\boldsymbol{u}(t) = -\sum_{i=1}^{r} h_i(z)(\boldsymbol{CB})^{-1}\big[\boldsymbol{CA}_i\boldsymbol{x}(t) + \hat{\varphi}(t, \boldsymbol{x})sgn(\boldsymbol{S})\big] \tag{21}$$

with the following adaptive laws

$$\begin{cases} \hat{\varphi}(t,\boldsymbol{x}) = \|N(t)\|\|\dot{h}_\alpha\|\|\boldsymbol{x}(t)\| + \sum_{k=0}^{1}\hat{\rho}_k\|\boldsymbol{CB}\|\|\boldsymbol{x}(t)\|^k + \varepsilon \\ \dot{\hat{\rho}}_0 = \gamma_0\|\boldsymbol{S}^T(t)\|\big\|\sum_{i=1}^{r} h_i(z)\boldsymbol{CB}_i\big\| \\ \dot{\hat{\rho}}_1 = \gamma_1\|\boldsymbol{S}^T(t)\|\big\|\sum_{i=1}^{r} h_i(z)\boldsymbol{CB}_i\big\|\|\boldsymbol{x}(t)\| \end{cases} \tag{22}$$

where the adaptation rates $\gamma_i > 0$, the constant $\varepsilon > 0$, and the functions $N(t)$, h_α will be defined in the following theorem, which gives the stability analysis when the controller (30) is enforced on the system (4) and the reachability of the specified sliding surface $\boldsymbol{S}(t) = 0$ can be obtained.

Theorem 2. *For the uncertain fuzzy systems (4) with the switching function (5), $\boldsymbol{Q}$ is the feasible solution of LMIs (6). Then it can be shown that the state trajectories of the system (4) will be driven onto the switching surface $\boldsymbol{S}(t) = 0$ and asymptotically converge to zero by the adaptive SMC law in (20),(21) and (22).*

Proof: For purpose of design integrity, a simple stability analysis based on Lyapunov direct method is carried out. Define the Lyapunov function candidate

$$V_2(t) = \frac{1}{2}\boldsymbol{S}^T\boldsymbol{S} + \sum_{k=0}^{1}\frac{1}{2\gamma_k}\tilde{\rho}_k^2 \geq 0 \tag{23}$$

where the estimation error $\tilde{\rho}_k = \hat{\rho}_k - \rho_k$.

By differentiating the switching surface $\boldsymbol{S}(t)$, we have

$$\dot{\boldsymbol{S}}(t) = \boldsymbol{C}(t)\dot{\boldsymbol{x}}(t) + \dot{\boldsymbol{C}}(t)\boldsymbol{x}(t) \tag{24}$$

In (24), by following from Lemma 1 we have

$$\dot{\boldsymbol{C}}(t) = \frac{d}{dt}(h_\alpha^T\boldsymbol{P}h_\alpha)^{-1}\boldsymbol{B}_\alpha h_\alpha = N(t)\dot{h_\alpha}(t) \tag{25}$$

where $h_\alpha(t) = [h_1, ..., h_r]$, $\boldsymbol{B}_\alpha(t) = [\boldsymbol{B}_1, ..., \boldsymbol{B}_r]^T$, $\boldsymbol{P} = \boldsymbol{B}_\alpha\boldsymbol{Q}^{-1}\boldsymbol{B}_\alpha^T$, $N(t) = \big[-(h_\alpha^T\boldsymbol{P}h_\alpha)^{-1}h_\alpha^T(\boldsymbol{P}+\boldsymbol{P}^T)(h_\alpha^T\boldsymbol{P}h_\alpha)^{-1}\boldsymbol{B}_\alpha h_\alpha + (h_\alpha^T\boldsymbol{P}h_\alpha)^{-1}\boldsymbol{B}_\alpha\big]$

Then, it follows from (4) that we have

$$\dot{\boldsymbol{S}}(t)\boldsymbol{S}(t) = \boldsymbol{C}(t)\dot{\boldsymbol{x}}(t)\boldsymbol{C}(t)\boldsymbol{x}(t) + N(t)\dot{h_\alpha}(t)\boldsymbol{x}(t)\boldsymbol{C}(t)\boldsymbol{x}(t) \tag{26}$$

By substituting the controller (21) into (26), we have

$$\begin{aligned} \boldsymbol{S}^T(t)\dot{\boldsymbol{S}}(t) &= \boldsymbol{S}^T(t)\big[\sum_{i=1}^{r} h_i(z)\boldsymbol{CA}_i\boldsymbol{x}(t) + \boldsymbol{CBu}(t) + N(t)\dot{h}_\alpha(t)\boldsymbol{x}(t) + \sum_{i=1}^{r} h_i(z)\boldsymbol{CB}_i g(t,\boldsymbol{x},\boldsymbol{u})\big] \\ &= \boldsymbol{S}^T(t)\big[N(t)\dot{h}_\alpha(t)\boldsymbol{x}(t) + \boldsymbol{CB}g(t,\boldsymbol{x},\boldsymbol{u}) - \hat{\varphi}(t,\boldsymbol{x})sgn(\boldsymbol{S}(t))\big] \\ &\leq \|\boldsymbol{S}^T(t)\|\|N(t)\|\|\dot{h}_\alpha\|\|\boldsymbol{x}(t)\| + \|\boldsymbol{S}^T(t)\|\|\boldsymbol{CB}\|\sum_{k=0}^{1}\rho_k\|\boldsymbol{x}(t)\|^k - \hat{\varphi}(t,\boldsymbol{x})\|\boldsymbol{S}(t)\| \\ &= \|\boldsymbol{S}^T(t)\big[\|\boldsymbol{CB}\|\sum_{k=0}^{1}\rho_k\|\boldsymbol{x}(t)\|^k - \|\boldsymbol{CB}\|\sum_{k=0}^{1}\hat{\rho}_k\|\boldsymbol{x}(t)\|^k - \varepsilon\big] \end{aligned} \tag{27}$$

By differentiating the function V_2 and substituting the adaptive laws (22) into (27), the simplified expression of (27) can be obtained as

$$\dot{V}_2(t) = \boldsymbol{S}^T\dot{\boldsymbol{S}} + \frac{\dot{\hat{\rho}}_0}{\gamma_0}(\hat{\rho}_0 - \rho_0) + \frac{\dot{\hat{\rho}}_1}{\gamma_1}(\hat{\rho}_1 - \rho_1) = -\varepsilon\|\boldsymbol{S}^T(t)\| \tag{28}$$

Noticing that $\epsilon > 0$, thus the derivative $\dot{V}_2(t) < 0$ when $\boldsymbol{S}(t) \neq 0$, which implies that under the controller (21) and (22) the reachability of the specified switching surface is guaranteed, and the trajectories of the fuzzy uncertain system (3) are globally driven onto the specified switching surface $\boldsymbol{S}(t) \neq 0$. Moreover, it is seen that the estimation error $\tilde{\rho}_k$ will converge to zero.

□

4 Numerical Simulation

To show the effectiveness of the proposed controller design techniques, the inverted pendulum with parametric uncertainties, which is taken from Wu and Juang [16], is formulated for simulation. The control objective is to drive its state trajectories to the origin. The equations of motion for the inverted pendulum device are

$$\begin{cases} \dot{x}_1(t) = x_2(t) \\ \dot{x}_2(t) = \dfrac{-f_1 mlx_2 cosx_1 - m^2gl^2 sinx_1 cosx_1 + (J+ml^2)[mlx_2^2 sinx_1 - f_0x_4 + u(t) + d(t)]}{\bar{M}(J+ml^2) - m^2l^2cos^2x_1} \\ \dot{x}_3(t) = x_4(t) \\ \dot{x}_4(t) = \dfrac{-f_1\bar{M}x_2^2 - m^2l^2x_2^2 sinx_1 cosx_1 + f_0 mlx_4 cosx_1 + \bar{M}mgsinx_1 - mlcosx_1[u(t) + d(t)]}{\bar{M}(J+ml^2) - m^2l^2cos^2x_1} \end{cases}$$

where x_1 denotes the angle (rad) of the pendulum from the vertical,x_2 is the angular velocity (rad/s), x_3 is the displacement (m) of the cart, and x_4 is the velocity of the cart.$g = 9.8m/s^2$ is the gravity constant, m is the mass (kg) of the pendulum, M is the mass (kg) of the cart, f_0 is the friction factor (N/m/s) of the cart, f_1 is the friction factor (N/rad/s) of the pendulum, l is the length (m) from the center of the mass of the pendulum to the shaft axis,J is the moment of inertia (kg.m2) of the pendulum round its center of mass, and $u(t)$ is the force (N) applied to the cart. The model parameters are given as: $\bar{M} = M + m$,$M = 1.3282$kg, $m = 0.22$kg, $f_0 = 22.915$N/m/s, $f_1 = 0.007056$N/rad/s, $l = 0.304$m, $J = 0.004963$kg.m2 in the numerical simulation. It's assumed that $d(t)$ is bounded by $d(t) \leq \rho_0 + \rho_1\|\boldsymbol{x}\|$, where ρ_i is unknown parameter. The fuzzy model of system is described as the following two rules:

Plant rule i: IF $x_1(t)$ is M_1^i, THEN $\dot{\boldsymbol{x}}(t) = \boldsymbol{A}_i + \boldsymbol{B}_i\big[u(t) + g(t,\boldsymbol{x})$.

The model parameters are given as $\boldsymbol{A}_1 = \begin{bmatrix} 0 & 1 & 0 & 0 \\ 29.2529 & -0.3149 & 0 & 44.1811 \\ 0 & 0 & 0 & 1 \\ -1.2637 & 0.0136 & 0 & -16.7096 \end{bmatrix}$, $\boldsymbol{A}_2 = \begin{bmatrix} 0 & 1 & 0 & 0 \\ 22.0587 & -0.2872 & 0 & 20.1425 \\ 0 & 0 & 0 & 1 \\ -0.4765 & 0.0062 & 0 & -15.2361 \end{bmatrix}$, $\boldsymbol{B}_1 = \begin{bmatrix} 0 \\ -1.9280 \\ 0 \\ 0.7292 \end{bmatrix}$, $\boldsymbol{B}_2 = \begin{bmatrix} 0 \\ -0.8790 \\ 0 \\ 0.6649 \end{bmatrix}$. The membership functions are selected as $M_1(\boldsymbol{x}) = [1 - 1/(1 + e^{-7(x_1 - \pi/24)})]/(1 + e^{-7(x_1 + \pi/24)})$, $M_2(\boldsymbol{x}) = 1 - M_1(\boldsymbol{x})$.Due to $\boldsymbol{B}_2 \leq \boldsymbol{B}_1$, the stabilization result (Zheng et al., 2002) is invalid. The perturbation is set to be $g(t,\boldsymbol{x}) = [0.1sint, 0.05sint]^T$, the initial states $\boldsymbol{x}(0) = [\pi/3, 0, \pi/5, 0]$. To assess

the effectiveness of our fuzzy controller, we apply the controller to the original system (12) with nonzero $d(t)$. We choose the adaptation parameters $\gamma_0 = 0.001$, $\gamma_1 = 0.1$.Via LMI optimization with (19), we obtain the feasible solutions and the switching suafrace.

The simulation results are given in Figures 1-2. It is seen that the reachability of the sliding motion can be guaranteed. The system enters sliding-mode motion after about t=0.8 second. From Figure 1, one can see that the system states converge to zero fast, furthermore, the simulation results also show that our present design effectively attenuates the effect of both parameter uncertainties and external disturbances. In Figure 2, the control effort is shown and approaches to be stable after a short-term adjustment in the initial stage.

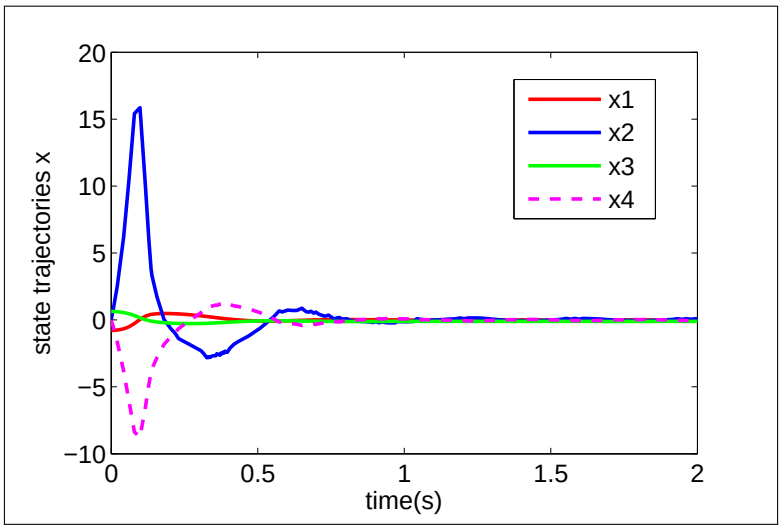

Figure 1: Trajectories of states x_1, x_2, x_3 and x_4

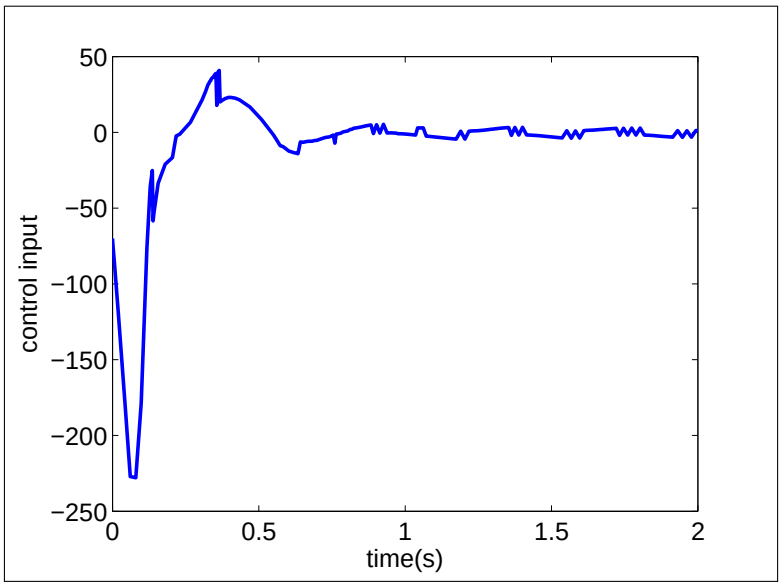

Figure 2: Control input

5 Conclusions and Future Works

This paper has generalized the T-S fuzzy model to represent a class of nonlinear systems which includes parameter uncertainties or external disturbances. A novel adaptive VSC control scheme has been proposed for the uncertain model, which relaxes the restrictive assumption that the input matrices of the local sub-models are identical and needs no information of uncertainties. The overall fuzzy VSC controller of the system is achieved by fuzzy blending of the local VSC controller. The existence condition of linear sliding surfaces guaranteeing asymptotic stability of the equivalent dynamics is derived as well as the stability analysis. Finally, a numerical design example is illustrated in order to show the effectiveness of our scheme.

Acknowledgment

The authors are grateful to the support of the National Natural Science Foundation of China (61203019), the China Postdoctoral Science Foundation funded project (2012M521518), the Key Projects of Chinese Ministry of Education (No.212122), the Department of Education (14A032) and Innovative Research Team in Higher Educational Institutions of Hunan Province, and the Natural Science Foundation of Hunan Provincial (No.13JJ9019).

Bibliography

[1] Takagi, T.; Sugeno, M. (1985); Fuzzy identification of systems and its applications to modeling and control, *IEEE Trans. Syst., Man, Cybern.*, ISSN 0018-9472, 15(1): 116-132.

[2] Feng, G. (2006); A survey on analysis and design of model-based fuzzy control systems, *IEEE Trans. Fuzzy Syst.*, ISSN 1063-6706, 14(5): 676-697.

[3] Tanaka, K.; Ikeda, T.; Wang, H.O. (1998); Fuzzy regulators and fuzzy observers: Relaxed stability conditions and LMI-based designs, *IEEE Trans. Fuzzy Syst.*, ISSN 1063-6706, 6(2): 250-265.

[4] Zhang, X. Z.; Wang, Y. N. (2009); Fuzzy variable structure control based on a Takagi-Sugeno model for permanent magnet synchronous motors, *Journal of Systems and Control Engineering*, ISSN 0959-6518, 223(6): 773-783.

[5] Besheera, A. H.; Emarab, H. M.; Azizb, M. M. A.(2009); Wind energy conversion system regulation via LMI fuzzy pole cluster approach, *Electric Power System Research*, ISSN 0378-7796, 79(6): 531-538.

[6] Aouaouda, S.; Chadli, M.et.al.(2012); Robust fault tolerant tracking controller design for unknown inputs TS models with un-measurable premise variables, *Journal of Process Control*, ISSN 0959-1524, 22(5): 861-872.

[7] Liang, Y. W.; Xu, S. D.; Liaw, D. C.et.al.(2008); A study of T-S model-based SMC scheme with application to robot control, *IEEE Trans. Ind.Electron.*, ISSN 0278-0046, 55(11): 3964-3971.

[8] Tian, E. G.; Peng, C.(2006); Delay dependent stability analysis and synthesis of uncertain TS fuzzy systems with time-varying delay, *Fuzzy Sets and Systems*, ISSN 0165-0114, 157(4): 544-559.

[9] Wu, H. N.(2007); Robust H2 fuzzy output feedback control for discrete-time nonlinear systems with parametric uncertainties, *International Journal of Approximate Reasoning*, ISSN 0888-613X, 46(1): 151-165.

[10] Lin, Y.C.; Lo, J.C.(2005); Robust mixed H2/H∞ filtering for discrete-time delay fuzzy systems, *International Journal of System Science*, ISSN 1841-9836, 36(15): 993-1006.

[11] Wang Y.N.; Zhang X.Z.et.al.(2011); Position-sensorless hybrid sliding mode control of electric vehicles with brushless DC motor, *IEEE Trans. Veh. Technol.*, ISSN 0018-9545, 60(2): 421-432.

[12] Zheng, F.; Wang, Q. G. et.al.(2002); Output tracking control of MIMO fuzzy nonlinear systems using variable structure control approach, *IEEE Trans. Fuzzy Syst.*, ISSN 1063-6706, 10(3): 686-697.

[13] Cao, W. J.; Xu, J. X.(2004); Nonlinear integral-type sliding surface for both matched and unmatched uncertain systems, *IEEE Trans. Automat. Contr.*, ISSN 0018-9286, 49(8): 1355-1360.

[14] Choi, H. H.(2008); Robust stabilization of uncertain fuzzy systems using variable structure system approach, *IEEE Trans. Fuzzy Syst.*, ISSN 1063-6706, 16(3): 715-724.

[15] Zhang, X.Z.; Wang, Y.N.et.al.(2010); H∞ robust T-S fuzzy design for uncertain nonlinear systems with state delays based on sliding-mode control, *International Journal of Computers Communications & Control*, ISSN 1841-9836, 5(4): 592-602.

[16] Wu, T.Z.; Juang, Y.T.(2008); Design of variable structure control for fuzzy nonlinear systems, *Expert Systems with Applications*, ISSN 0957-4174, 35(3): 1496-1503.

Author index